Laboratory Astrochemistry of Dust and Ice

Skandar Mahmmood Taj

Submitted for the Degree of Doctor of Philosophy

Heriot-Watt University

School of Engineering and Physical Sciences

2019

Abstract

Thin film growth and desorption behaviour of simple molecules on interstellar dust grain analogue surfaces has been investigated using a range of surface science techniques including temperature programmed desorption (TPD), reflection-absorption infrared (RAIR) and reflection-adsorption UV-Visible spectroscopy. The systems investigated use amorphous silica ($aSiO_2$) as a mimic for bare interstellar dust grains and thin adsorbed films of ammonia (NH_3), benzene (C_6H_6), carbon monoxide (CO), compact and porous amorphous solid water (c-ASW and p-ASW) crystalline solid water (CSW), methanol (CH_3OH) and methyl formate ($HCOOOCH_3$, MF).

The optical properties for benzene (C_6H_6) were investigated using a newly designed and constructed UV/Visible spectrometer. Preliminary measurements of C_6H_6 on a highly-orientated pyrolytic graphite (HOPG) surface give the refractive index (n) as 1.43 ± 0.07 for a film of thickness (d) 261±5 nm.

MF on $aSiO_2$ was investigated using TPD, RAIRS and ab initio calculations. The TPD of MF is consistent with wetting of the $aSiO_2$ surface. The binding energy of the monolayer was found to be 29.8±0.1 kJ mol^{-1} and that of the multilayer is 26.4±5.5 kJ mol^{-1}. This indicates that MF coupling to the $aSiO_2$ surface is weak and only slightly stronger than the MF interaction with itself. Below 95 K, MF is in an amorphous phase and above 95 K, it is crystalline. A combination of measurements of spontaneous dipole orientation and RAIR spectra with computational chemistry supports the idea that the basis motif of the lattice in crystalline cis-MF is a ring dimer structure.

A simple method was developed to synthesise the vibrational line profile of CO on a heterogeneous surface. The procedure developed allows the conversion of a distribution of binding energies, E_{des}, into a continuous distribution of vibrational frequencies, which can in turn be compared with experimental RAIRS data. The interaction of CO with a range of astrophysically surfaces including CH_3OH, CSW, c-ASW, amorphous silica and NH_3 on the $aSiO_2$ substrate was investigated using TPD. Extended Inversion Analysis was used to determine the pre-exponential factor, distribution of E_{des} and the entropy of activation ($\Delta^{\ddagger}S$) for desorption of CO from each surface.

Acknowledgements

The work that has gone into this thesis, both experimental and written, could not have been done without the help, advice and guidance of many people. Firstly, I would like thank Prof. Martin McCoustra for the opportunity to work with him and his group. My time at Heriot-Watt University has been filled with joy and frustration when the experimental equipment worked or needed repair. Whatever the situation in the laboratory, Prof. Martin McCoustra was always there with help, guidance and encouragement.

I am also very grateful to Alex Rosu-Finsen for all help in and out of the laboratory. Alex had the patience to teach me how to work with the different experimental setups in the laboratories.

I would like to thank my family for their support; Hassan, Sophie and especially my brother Tariq who has supported me through good and bad times in my life. I am especially grateful to my father who has always been there for me no matter what the problem was. I would never have been able to complete this thesis, and achieved as much in my life and academic career, without my beloved father's support, guidance and help.

During my PhD, I have come up against a range of problems. I am grateful to my friends Chris, Philippa, Samara and Chiara for all their help, support, encouragement and just being there for shoulder to cry on. I am especially grateful to my dear friend Martin for all his support and advice over the years and for just being there.

A life outside my PhD has been important to me. I am so grateful to Joanne for all her support, advice, hugs, cups of tea and just for being there for me through the good and bad times. Joanne support throughout this PhD has been amazing and I am so great full to her for everything she has done for me.

Research Thesis Submission

Please note this form should be bound into the submitted thesis.

Name*:*	Skandar Mahmmood Taj		
School:	EPS		
Version: *(i.e. First, Resubmission, Final)*	Final	Degree Sought:	PhD

Declaration

In accordance with the appropriate regulations I hereby submit my thesis and I declare that:

1. The thesis embodies the results of my own work and has been composed by myself
2. Where appropriate, I have made acknowledgement of the work of others
3. Where the thesis contains published outputs under Regulation 6 (9.1.2) these are accompanied by a critical review which accurately describes my contribution to the research and, for multi-author outputs, a signed declaration indicating the contribution of each author (complete Inclusion of Published Works Form – see below)
4. The thesis is the correct version for submission and is the same version as any electronic versions submitted*.
5. My thesis for the award referred to, deposited in the Heriot-Watt University Library, should be made available for loan or photocopying and be available via the Institutional Repository, subject to such conditions as the Librarian may require
6. I understand that as a student of the University I am required to abide by the Regulations of the University and to conform to its discipline.
7. Inclusion of published outputs under Regulation 6 (9.1.2) shall not constitute plagiarism.
8. I confirm that the thesis has been verified against plagiarism via an approved plagiarism detection application e.g. Turnitin.

* *Please note that it is the responsibility of the candidate to ensure that the correct version of the thesis is submitted.*

Signature of Candidate*:*		Date:	

Submission

Submitted By *(name in capitals):*	Skandar Mahmmood Taj
Signature of Individual Submitting:	
Date Submitted:	

For Completion in the Student Service Centre (SSC)

Received in the SSC by *(name in capitals):*			
Method of Submission *(Handed in to SSC; posted through internal/external mail):*			
E-thesis Submitted (**mandatory for final theses)**			
Signature:		Date:	

Inclusion of Published Works

Declaration

This thesis contains one or more multi-author published works. In accordance with Regulation 6 (9.1.2) I hereby declare that the contributions of each author to these publications is as follows:

Citation details	Assigning a Structural Motif using Spontaneous Molecular Dipole Orientation in Thin Films, *Physical Chemistry Chemical Physics*, 2018, **20**, 29038.
Author 1	M. Roman (10%) – Analysis of Data
Author 2	A. Dunn (10%) – Experimental Measurements
Author 3	S. Taj (10%) – Experimental Measurements
Author 4	Z. G. Keolopile (15%) – Computational Input
Author 5	M. Gutowski (15%) – Computational Input
Author 6	M. R. S. McCoustra (30%) – Initial Idea and Draft of Paper
Author 7	A. M. Cassidy (5%) – Provision of Underpinning Understanding
Author 8	D. Field (5%) – Provision of Underpinning Understanding
Signature:	
Date:	

Citation details	Non-linear and Non-local Behaviour in Spontaneously Electrical Solids, *Physical Chemistry Chemical Physics*, 2018, **20**, 5112.
Author 1	M. Roman (10%) – Analysis of Data
Author 2	S.Taj (10%) – Experimental Measurements
Author 3	M. Gutowski (10%) – Computational Input
Author 4	M. R. S. McCoustra (20%) – Draft of Paper
Author 5	A. C. Dunn (10%) – Experimental Measurements
Author 6	Z. G. Keolopile (10%) – Computational Input

Author 7	A. Rosu-Finsen (5%) – Experimental Measurements
Author 8	A. M. Cassidy (5%) – Provision of Underpinning Understanding
Author 9	D. Field (20%) – Draft of Paper
Signature:	
Date:	

Citation details	A Fibre-Coupled UHV-Compatible Variable Angle Reflection-Absorption UV/Visible Spectrometer, *Rev. Sci. Inst*., 2018, **89**, 054102.
Author 1	J. W. Stubbing (30%) – Experimental Measurements and Initial Draft of Paper
Author 2	T. L. Salter (10%) – Experimental Measurements
Author 3	W.A. Brown (15%) – Draft of Paper
Author 4	S. Taj (30%) – Design and Construction work
Author 5	M.R.S. McCoustra (15%) – Initial Idea, Design work and Draft Paper
Signature:	
Date:	

Citation details	Surface Science Investigations of Icy Mantle Growth on Interstellar Dust Grains in Cooling Environments, *ACS Earth Space Chem*, 2019, https://doi.org/10.1021/acsearthspacechem.9b00052.
Author 1	D. Marchione (55%) – Experimental Work and Draft of Paper
Author 2	A. Rosu-Finsen (10%) – Experimental Work and Draft of Paper
Author 3	S. Taj (5%) – Experimental Work
Author 4	J. Lasne (5%) – Experimental Work
Author 5	Ali G. M. Abdulgalil (5%) – Experimental Work
Author 6	J. D. Thrower (5%) – Experimental Work
Author 7	V. L. Frankland (5%) – Experimental Work
Author 8	M. P. Collings (5%) – Experimental Work
Author 9	M. R. S. McCoustra (5%) – Initial Idea and Draft of Paper
Signature:	
Date:	

Table of Contents

List of Table Captions

4.7 The vibrational assignment of the infrared spectrum of solid MF. A comparison of work carried out in this thesis with that of Palumbo and co-workers [45] and Brown and co-workers [42]: (**a**) amorphous MF films deposited at 16 K [45], 26 K [42] and 18 K [1] in this thesis and (**b**) the spectra of crystalline MF deposited at 110 K [45], 105 K [42] and 108 K in this thesis [1]. The uncertainty in the line positions is dependent of the resolution of the measurement. In this work, 1 cm^{-1} resolution was employed and we are confident that the positions are defined to within ±0.5 cm^{-1}.

4.8 Computed harmonic (H) ν_{CO} vibrational frequency, anharmonic (AH) correction to the 0 - 1 transition, and anharmonic 0 - 1 transition (cm^{-1}) in *cis*- and *trans*-MF and δMP2 (AH) represents the anharmonic correction obtained at the MP2 level [1].

4.9 The increase in LO - TO splitting at higher deposition temperatures and illustrates the trend of increasing vibrational Stark Effect [2].

Chapter 5

5.1 The correlation between $\Delta\tilde{\nu}_{co}$ and E_{des} for the σ-C_{co} bonding configuration, adapted from Collings *et al.* [2].

5.2 Experimental values extracted from the TPD experiments of various coverages CO on $aSiO_2$ [1].

5.3 Experimental values extracted from the TPD and RAIRS experiments of various coverages CO on $aSiO_2$, where δ is the linewidth of the ν_{CO} derived from the FWHM using **Equation 15** [1].

5.4 Compares the best-fit parameters $\bar{\upsilon}_o$, δ and $I_{0,}$ along with the corresponding FWHM for the modelled profiles and the experimental CO vibrational line profiles on $aSiO_2$ and p-ASW substrate [1].

Chapter 6

6.1 An overview of the different names for solid water phases upon deposition in ultrahigh vacuum [5].

6.2 Adsorption behaviour of CO on astrophysically relevant surfaces: (**a**) monolayer coverages and (**b**) multilayer coverages. The deposition temperatures are given in brackets.

6.3 The table shows published values for experimental activation energies and pre-exponential factors for CO desorbing from a range of well-defined crystal surfaces [30].

6.4 Comparison of E_{des} and ν for CO on c-ASW and CSW from this work and from the literature.

6.5 Compares the best-fit parameters $\bar{\upsilon}_o$, δ and I_0, along with the corresponding FWHM for the modelled profiles and the experimental CO vibrational line profiles on $aSiO_2$ and p-ASW [17].

6.6 Summary of the pre-exponential factors, entropy of activation, E_{des} and E_{diff} for CO interactions on $aSiO_2$, c-ASW, CSW, CH_3OH and NH_3. Note the diffusion barrier, E_{diff}, is typically around 10% of the E_{des} [12].

Chapter 7

7.1 Compares the best-fit parameters $\bar{\upsilon}_o$, δ and I_0, along with the corresponding FWHM for the modelled profiles and the experimental CO vibrational line profiles on $aSiO_2$ and p-ASW substrate.

7.2 Summary of the ν, $\Delta^{\ddagger}S$, E_{des} and E_{diff} for CO interactions on $aSiO_2$, c-ASW, CSW, CH_3OH and NH_3. Note the diffusion barrier is typical 10% of the E_{des} [11].

List of Figure Captions

Chapter 1

6.9 Shows the structure of the CO on H_2O, CH_3OH (compact and crystalline) films and NH_3. The experiments are carried out by depositing water at 100 K compact or 140 K crystalline water on the $aSiO_2$ layer. This is then followed by depositing CO.

6.10 The χ^2 between experimental and simulated TPD of CO from $aSiO_2$ for all initial coverages *versus* logarithm of the pre-exponential factor used in the Extended Inversion Analysis. The dashed line in this figure is fourth-order polynomial fit to χ^2 and yields a minimum at a value of 21.24±0.16. A number of different low order polynomial fits were tried. However, the fourth order polynomial proved to give the best fit for the experimental data. Hence, the optimised value of *v* is $1.74^{+0.75}_{-0.53} \times 10^{21}\ s^{-1}$.

6.11 **(a)** E_{des} *versus* coverage for sub-monolayers of CO derived using *v* of $1.74^{+0.75}_{-0.53} \times 10^{21}\ s^{-1}$ and (**b**) E_{des} *versus* coverage for sub-monolayers of CO calculated using ν of $1.00\times10^{12}\ s^{-1}$ as in **Chapter 5** [17]. The inset contains the averaged data.

6.12 TPD traces for CO desorbing from c-ASW for coverages 10 to 25 L, recorded on m/z of 28 m_u. The data has a rising background, labelled A, which is removed in order to use in the data in the Extended Inversion Analysis.

6.13 TPD traces for CO desorbing from c-ASW for coverages 1 to 9 L, recorded on m/z of 28 m_u. The data has a rising background labelled A, which is removed in order to use in the data in the Extended Inversion Analysis.

6.14 Raw TPD spectra for 14 L CO on c-ASW. The regions A and B are used to define the rising background.

6.15 Removing the rising background from the experimental TPD data: (**a**) results of fitting an exponential function to data regions A and B in **Figure 6.14**; (**b**) shows 14 L CO on c-ASW TPD data from which the rising background has now been removed.

6.16 TPD data for CO on c-ASW for coverages of 1 to 25 L after correcting for the rising background: (**a**) multilayer 10 to 25 L coverages and (**a**) sub-monolayer 1 to 9 L coverages.

6.17 The χ^2 between the experimental and simulated TPD CO for c-ASW for all initial coverages *versus* logarithm of the pre-exponential factor used in the Extended Inversion Analysis. The dashed line in this figure is PsdVoigt1 fit to χ^2 and yields a minimum at a value of 2.57±0.28. Hence, the optimised value of ν is $2.57^{+1.04}_{-1.21} \times 10^{15}$ s^{-1}.

6.18 E_{des} *versus* coverage for CO sub-monolayers adsorbed on c-ASW and the inset shows the averaged data. The plots were obtained using the optimised ν of $2.57^{+1.04}_{-1.21} \times 10^{15}$ s^{-1} and the inset contains the averaged data.

6.19 A comparison of the experimental (black) and simulated (red) TPD data for sub-monolayer coverages of 0.9 to 0.5 ML CO on c-ASW. The simulated data were obtained using a pre-exponential factor of $2.57^{+1.04}_{-1.21} \times 10^{15}$ s^{-1} and the $E_{des}(\theta)$ distribution presented in the inset in **Figure 6.18**.

6.20 TPD traces for CO desorbing from CSW for exposures 10 to 25 L recorded on m/z = 28 m_u. The data has a rising background, labelled A, which is removed in order to use the data in the Extended Inversion Analysis.

6.21 TPD traces for CO desorbing from CSW for exposures of 1 to 9 L recorded on m/z = 28 m_u. The plot has a rising background, labelled A, which is removed in order to use the data in the Extended Inversion Analysis.

6.22 TPD data for CO from CSW for CO coverages of 1 to 25 L after correcting for the rising background: **(a)** multilayer 10- 25 L and (**b**) sub-monolayer 1 to 9 L coverages.

6.23 The χ^2 between the experimental and simulated TPD of CO from CSW for all initial coverages *versus* logarithm of the pre-exponential factor used in the Extended Inversion Analysis. The dashed line in this figure is fourth-order polynomial fit to χ^2 and yields a minimum at a value of 17.40±0.20. A number of different low order polynomial fits were tried. However, the fourth order polynomial proved to give the best fit for the experimental data. Hence, the optimised value of ν is $2.51^{+1.47}_{-0.93} \times 10^{17}$ s^{-1}.

6.24 E_{des} *versus* coverage for CO sub-monolayers adsorbed from CSW and the inset shows the averaged data. The plots were obtain using with ν of $2.51^{+1.47}_{-0.93} \times 10^{17}$ s^{-1} and the inset contains the averaged data.

6.25 A comparison of the experimental (black) and simulated (red) TPD spectra for sub-monolayer coverages of CO on CSW. The simulated spectra were obtained using the $E_{des}(\theta)$ curve in **Figure 6.24** obtained using a pre-exponential factor of $2.51^{+1.47}_{-0.93} \times 10^{17}$ s^{-1}.

6.26 TPD traces for CO desorbing from CH_3OH for exposures of 10 to 25 L, recorded on m/z = 28 m_u. The plot has a rising background, labelled A, which is removed in order to carry out Extended Inversion Analysis.

6.27 TPD traces for CO desorbing from CH_3OH for exposures of 1 to 9 L, recorded on m/z = 28 m_u. The plot has a rising background, labelled A, which is removed in order to use the data in the Extended Inversion Analysis.

6.28 TPD data for CO on CH_3OH for coverages of 1 to 25 L after correcting for the rising background: (**a**) multilayer 10 to 25 L coverages and (**b**) sub-monolayer 1 to 9 L coverages.

6.29 The χ^2 between the experimental and simulated TPD of CO from CH_3OH all initial coverages *versus* logarithm of the pre-exponential factor used in the Extended Inversion Analysis. The dashed line in this figure is PsdVoigt1 fit to χ^2 and yields a minimum at a value of 16.41±0.43. Hence, the optimised value of ν is $1.41^{+0.29}_{-0.45} \times 10^{16}$ s^{-1}.

6.30 E_{des} *versus* coverage for sub-monolayer quantities of CO on CH_3OH. The inset shows the averaged data. The plots were obtained using the optimised ν of $1.41^{+0.29}_{-0.45} \times 10^{16}$ s^{-1} and the inset contains the averaged data.

6.31 A comparison of the experimental (black) and simulated (red) TPD data for sub-monolayer coverages of CO on CH_3OH. The simulated and experimental TPD produced using the optimised pre-exponential factor, ν, of $1.41^{+0.29}_{-0.45} \times 10^{16}$ s^{-1}.

6.32 TPD traces for CO desorbing from NH_3, for coverages 10 to 15 L, recorded on m/z = 28 m_u. The plot has a rising background, labelled A, which is removed in order to use in the data in the Extended Inversion Analysis.

6.33 TPD traces for CO desorbing from NH_3, for coverages 1 to 9 L, recorded on m/z = 28 m_u. The plot has a rising background, labelled A, which is removed in order to use in the data in the analysis process.

6.34 TPD data for CO on NH_3 for coverages of 1 to 20 L after correcting for the rising background: (**a**) multilayer 10 - 15 L and (**b**) sub-monolayer 1-9 L coverages.

6.35 The χ^2 between the experimental and simulated TPD CO for NH_3 for all initial coverages *versus* logarithm of the pre-exponential factor used in in the Extended Inversion Analysis. The dashed line in this figure is fourth-order polynomial fit to χ^2 and yields a minimum at a value of 12.18±0.13. A number of different low order polynomial fits were tried. However, the fourth order polynomial proved to give the best fit for the experimental data.Hence, the optimised value of v is $1.51^{+0.46}_{-0.40} \times 10^{12}$ s^{-1}.

6.36 E_{des} versus coverage for CO sub-monolayers adsorbed on NH_3 and inset shows the average data. The plots were obtained using the optimised ν of $1.51^{+0.46}_{-0.40} \times 10^{12}$ s^{-1} and the inset contains the averaged data.

6.37 A comparion of the experimetnal (black) and simulated (red) TPD spectra for sub-monolayer coverages of 044 to 0.67 ML CO on NH_3. The simulated spectra were obtained using the the pre-exponetial factor of $1.51^{+0.46}_{-0.40} \times 10^{12}$ s^{-1}.

6.38 $P(E_{des})$ *versus* E_{des} as derived from the sub-monolayer TPD of CO from $aSiO_2$ substrate (**a**) using pre-exponential factor of 1.00×10^{12} s^{-1} [17] and (**b**) using optimised pre-exponential factor of $1.74^{+0.75}_{-0.53} \times 10^{21}$ s^{-1} .

6.39 Vibrational line profile synthesis for 0.6 ML CO on $aSiO_2$ (**a, d**) assuming ballistic deposition and (**b, e**) adsorb and diffuse deposition at instrument limited linewidth of 0.1 cm^{-1} and (**c, f**) show adsorb and diffuse deposition with optimised linewidth.

6.40 IR spectrum of solid $aSiO_2$ [38] and solid H_2O [39].

Glossary

AA	Arrhenius Analysis
ABG	Asymptotic Giant Branch
AGN	Active Galactic Nuclei
ASW	Amorphous Solid Water
CASW	Compact Amorphous Solid Water
CKS	Chemical Kinetics Simulator
CNM_a	Atomic Cold Neutral Medium
CNM_b	Molecular Cold Neutral Medium
COM	Complex Organic Molecules
CP	Curie Point
CPD	Contact Potential Difference
CRI	Complex Refractive Index
CSW	Crystalline Solid Water
DIB	Diffuse Interstellar Bands
E-R	Eley - Rideal
FTIR	Fourier Transform Infrared
FWHM	Full Width Half Maximum
HIM	Hot Ionised Medium
H-K	Harris - Kasemo
HOPG	Highly Oriented Pyrolytic Graphite
HWHM	Half Width Half Maximum
IR	Infrared
ISM	Interstellar Medium
ISRF	Interstellar Radiation Field
IVR	Intermolecular Energy Redistribution
KP	Kelvin Probe
LEA	Leading Edge Analysis
L-H	Langmuir-Hinshelwood
LO	Longitudinal Optical
MAPE	Mean Absolute Percentage Error
MCT	Mercury Cadmium Telluride
ML	Monolayer

MSSR	Metal Surface Selection Rule
PAH	Polycyclic Aromatic Hydrocarbons
p-ASW	Porous Amorphous Solid Water
QMS	Quadrupole Mass Spectrometer
RAIRS	Reflective-Absorption Infrared Spectroscopy
TO	Transverse Optical
TPD	Temperature Programmed Desorption
UHV	Ultrahigh Vacuum
UIR	Unidentified Infrared
UMIST	University of Manchester Institute of Science and Technology
UV	Ultraviolet
VSE	Vibrational Stark Effect
VUV	Vacuum Ultraviolet
WIM	Warm Ionised medium
WMN	Warm Neutral Medium
YSO	Young Stellar Object

List of Publications and Conference Presentations

Publications:

*"*Surface heterogeneity and inhomogeneous broadening of vibrational line profiles*"*; S. Taj, D. Baird, A. Rosu-Finsen and M. R. S. McCoustra, *Phys. Chem. Chem. Phys*., 2017, **19**, 7990.

"A Fibre-Coupled UHV-Compatible Variable Angle Reflection-Absorption UV/Visible Spectrometer"; J. W. Stubbing, T. L. Salter. W. A. Brown, S.Taj and M. R. S. McCoustra, *Rev. Sci. Inst.*, 2018, **89**, 054102.

"Assigning a Structural Motif using Spontaneous Molecular Dipole Orientation in Thin Films"; M. Roman, A. Dunn, S. Taj, Z. G. Keolopile, A. Rosu-Finsen, M. Gutowski, M. R. S. McCoustra, A. M. Cassidy and D. Field, *Phys. Chem. Chem. Phys*., 2018, **20**, 29038.

"Non-linear and Non-local Behaviour in Spontaneously Electrical Solids";M. Roman, S. Taj, M. Gutowski, M. R. S. McCoustra, A. C. Dunn, Z. G. Keolopile, A. Rosu-Finsen, A. M. Cassidy and D. Field, *Phys. Chem. Chem. Phys*., 2018, **20**, 5112.

*"*Surface Science Investigations of Icy Mantle Growth on Interstellar Dust Grains in Cooling Environments*"*; D. Marchione, A. Rosu-Finsen, S. Taj, J. Lasne, Ali G. M. Abdulgalil, J. D. Thrower, V. L. Frankland, M. P. Collings and M. R. S. McCoustra, *ACS Earth Space Chem*, 2019,https://doi.org/10.1021/acsearthspacechem.9b00052.

"Thermal Desorption of Carbon Monoxide from Model Ice Interstellar Surfaces: Surface Heterogeneity"; S.Taj and M. R. S. McCoustra, *Mon. Not. Roy. Astron. Soc*, In preparation.

"Impact of Surface Heterogeneity on IR Line Profiles of Adsorbed Carbon Monoxide"; S. Taj, A. Rosu-Finsen and M. R. S. McCoustra, *Mon. Not. Roy. Astron. Soc*, In preparation.

Conference Presentations:

Poster presented at Faraday Joint Interest Group Conference 2017: Surface Heterogeneity and Inhomogeneous Broadening of Vibrational Line Profiles, University of Warwick, 3th - 4th of April 2017.

Chapter 1

The Interstellar Medium

1.1 The Interstellar Medium

1.1.1 Introduction

The interstellar medium (ISM) is a turbulent system comprising the matter that exists in the space between the stars in a galaxy. The ISM only represents 10-15% of the galactic mass, but most of its volume. In terms of the mass of the ISM, half of it is contained within discrete interstellar clouds occupying around 1-2% of the interstellar volume; hence it can be thought of as mainly 'empty'. However, it is a largely inhomogeneous system, which is enriched by complex physiochemical processes, and can be divided into types of environment [1] specified according to their physical and chemical properties (**Table 1.1**):

- Hot ionised medium (HIM);
- Warm ionised medium (WIM);
- Warm neutral medium (WMA);
- Atomic cold neutral medium (CNM_a);
- Molecular cold neutral medium (CNM_b).

Table 1.1 shows the typical properties of these different regions within the ISM [1, 2] where temperatures range from 10^6 K in the HIM to just above absolute zero in the CNM; and the number of particles per unit volume varies from extremely low values in the HIM to considerably higher values in molecular clouds. In molecular clouds, the inner parts are shielded from most of the vacuum ultraviolet (VUV) radiation from the interstellar radiation field (ISRF). Thus, allowing atoms to build into more and more complex molecules. The ISM plays a key role in the evolution of the present-day Universe. When a star comes to the end of its life (*e.g.* as a supernova), much of its matter is expelled into the surrounding ISM. Hence the ISM becomes enriched with nucleo-synthesised elements. Stars can also lose mass through stellar outflows, winds and as novae [3-5], which also enrich the ISM.

ISM region	Common designation	Temperature / K	Number[1] density / cm^{-3}	State of hydrogen	Ionisation fraction, χ_e	How it can be observed?
Atomic cold neutral medium (CNM_a)	Diffuse clouds	100	10-100	H and H_2	10^{-3}	Absorption in the UV, microwave radiation (H 21.1 cm line absorption) and IR (3.4 µm)
Molecular cold neutral medium (CNM_b)	Molecular clouds, dense clouds or dark clouds	0-50	10^3-10^5	H_2	10^{-7} -10^{-8}	Absorption and emission in the IR, microwave and radio range
Warm neutral medium (WNM)	Intercloud H_I	$8x10^3$-10^4	0.1	H	0.1	Microwave radiation (H 21.1 cm line mission)
Warm ionised medium (WIM)	Diffuse ionised gas (DIG)	10^4	>10	H^+	1	UV, Vis (H Balmer H_α), IR
Hot ionised medium (HIM)	Coronal gas	10^6	0.03	H^+	1	X-ray emission, UV absorption of highly ionised metals

Table 1.1: The various parts of the interstellar medium and their properties. [I] Note that the number density is referred to molecular hydrogen (H_2) in molecular clouds and to atomic H in other cases [4, 5].

Energy can be injected into the ISM from a variety of sources including supernova explosions [6], VUV photons from large O and B stars and asymptotic giant branch (AGB) stellar winds. Hence a large fraction of the molecules and clusters released from stellar remnants are destroyed as chemical bonds are dissociated by the strong VUV radiation. Thus, only atoms and large stable molecules such as polycyclic aromatic hydrocarbons (PAHs) remain in some regions of the ISM.

This process of enrichment of matter and energy can lead to the formation of diffuse clouds. The neutral ISM occurs in the galaxy in two phases, WNM and CNM. These two phases are in thermal equilibrium, and have similar kinetic behaviour of the atomic and molecular gases from which they are formed. Hence the distinction between the two phases is often not clear [1]. Once formed, the diffuse clouds are assumed to be the precursors of dense molecular clouds. The distinction between CNM_a and CNM_b is driven by gravity and shocks (stellar winds or supernova). Dark clouds are thought of as the cradle of chemistry in the ISM and even the Universe. Dark clouds have greater density when compared with diffuse clouds, up to 10^5 times, which results in a greater shielding from intense VUV radiation. Cosmic rays can penetrate deep inside clouds, producing H_3^+ and He^+ and stimulate considerable gas-phase chemistry. The cold temperatures experienced in the ISM [1] can result in molecules freezing onto dust grains with a sticking efficiency close to unity. Hence, icy ISM dust is formed *in situ,* and is derived from the ice-free dust from diffuse clouds. Where more and more species, both in number and in complexity, accrete on to the grains, their sizes increase to the order of around 1 μm [3, 6-9]. The importance and role of dust is discussed in **Section 1.2.** The physical processes and interstellar chemistry which occur in diffuse and molecular clouds determine the boundary conditions for the composition of the material that would be incorporated into the proto-stellar nebula and cometary matter. Within molecular clouds, regions of high density could have conditions suitable for collapse into a proto-stellar core, which may eventually become a star. Around this core, a protoplanetary disk is formed, in which small grains can collide and stick together, giving birth to planets [10-11]. Once a star is formed, it will stay on the main sequence for a certain period. When all the hydrogen in the core of the star is converted into helium by nuclear fusion, it begins the slow process by which its life will end. This chemically enriches the ISM.

Hence the reservoir of elements from which the Solar System was formed is a result of nucleo-synthetic processes from at least two previous generations of stars.

1.1.2 Molecular Clouds

Molecular clouds (**Figure 1.1)** are important and of considerable interest since the chemical and physical processes occurring in these environments are of fundamental interest. These include:

- The complex chemistry that happens before and during star and planet formation.
- The molecules which are formed within the molecular clouds allow small stars to form.
- These clouds play a key role in the genesis of life.

Figure 1.1: Wide-field view of the Taurus Molecular cloud, which is around 450 light years from the Earth (Reproduced from [12]).

In the HIM, WIM, WNM and in the diffuse clouds, where the density is far too low to guarantee any significant shielding from VUV radiation from the interstellar environment, the destruction rate for even simple molecules is considerably higher than the formation rate. Hence, due to the low density and the presence of energetic photons, ion bombardment, heating shocks and the presence of reactive molecular fragments, only certain stable molecules remain. These include PAHs and simple molecules such as carbon monoxide (CO), cyanide (CN-), methylidyne (CH) and

molecular hydrogen (H_2); all of which have been identified in diffuse clouds [13]. Atomic ions and neutral atoms dominate the gas phase. In dark clouds, the effects of reduced VUV flux coupled with cosmic ray bombardment (radiolysis) and thermal processing encourage a prolific chemistry, both in the gas phase and on dust grain surfaces. Cloud collapse leads to proto-stellar object formation, and, during this process, the temperature increases as a result of the large amount of gravitational energy released. All the chemical species, which were frozen on to the icy mantles, desorb into the gas phase where they are more readily observed and where they might engage in gas-phase chemistry. Some of the energy is used to promote thermally activated reactive pathways. While inelastic scattering converts translational energy into other degrees of freedom, resulting in molecules being excited into higher rotational and vibrational levels. IR, microwave and longer-wavelength radiative emission is then observed when they relax to lower energy states. This provides efficient cooling of the collapsing system and thus allows the process of collapse to continue towards stellar ignition.

Molecular clouds have a bearing on cometary composition [14]. Comets are the agglomeration of residual icy grain material left over from the process of star and planet formation. Comets contain a pristine record of the cold grain chemistry. For example, it has been proposed that ethane (C_2H_6), which is found in comets, may be of interstellar origin. It may have formed from cold H atom addition reactions in ices which contain acetylene (C_2H_2) [14]. Other molecules such as nitriles, which are found in the ISM [15-17], have great importance from a biological point of view. Biogenic molecules, which have been formed in the ISM, may have been delivered by comets during the heavy bombardment which occurred during Earth's early existence.

Diffuse and dense clouds contain a range of simple and complex atoms and molecules. More than 180 molecules have been identified [18]. These include atoms and ions (*e.g.* H, O, C, C^+, N, S, S^+), diatomic molecules (*e.g.* CH, CH^+, CS OH, CO, NH, H_2), PAHs and carbonaceous and silicate grains containing metals (*e.g.* Mg, Fe, Al). Additional examples of atoms and molecules that these clouds contain are listed in **Table 1.2**.

Two atoms	AIF, AlCl, C_2, CH, CH^+, CN, CO, CO^+, CP, CS, HCl, H_2, KCl, NH,.....
Three atoms	C_3, C_2H, C_2O, C_2S, CH_2, HCN, HCO, HCO^+, HCS^+, HOC^+, H_2O, H_2S, HNC, HNO, MgCN,.....
Four atoms	c- C_3H, l- C_3H, C_3N, C_3O, C_3S, C_2H_2, CH_2D^+,.....
Five atoms	C_5, C_4H, C_4Si, c-C_3H_2, CH_2CN, CH_4, HC_3N, HC_2NC,.....
Six atoms	C_5H, C_5O, C_2H_4, CH_3CN, CH_3NC, CH_3OH, ...
Seven atoms	C_6H, CH_2CHCN, CH_3C_2H, HC_5N, $HCOCH_3$, ...
Eight atoms	CH_3C_3N, $HCOOCH_3$, CH_3COOH, C_7H, H_2C_6, ...
Nine atoms	CH_3C_4H, CH_3CH_2CN, CH_3OCH_3, CH_3CH_2OH, ...
Ten atoms	CH_3C_5N, $(CH_2OH)_2$, $(CH_3)_2CO$, NH_2CH_2COOH, ...
≥Eleven atoms	HC_9N, CH_3, C_6H, C_6H_6, CO $(CH_2OH)_2$, $HC_{11}N$, C_{60}, C_{70}, ...

Table 1.2: The table illustrates the range of molecular complexity as observed in molecular clouds in the ISM [18].

The variety and richness of the chemistry in interstellar clouds is surprising given the typical conditions in such interstellar clouds. However, the timescale of chemical evolution of astronomical objects can be measured in tens of thousands or even millions of years. In such conditions, the gas-phase chemistry, mainly driven by cosmic ray ionisation, is dominated by the so-called barrierless reactions. Surface processes on dust grains, along with the processes on and in ices absorbed on interstellar dust, also play a role in favouring the formation of complex organic molecules (COMs).

1.1.3 Astrochemistry

In the ISM, there are two types of chemistry: gas phase and surface. Gas-phase reactivity in the ISM is complex, and increasingly so as the conditions become more extreme in dense molecular clouds. This represents a challenge for astronomers in terms of modelling interstellar molecular abundances. There are chemical networks of thousands of reactions, which take into account the hundreds of atomic and molecular species that have been detected in space. For example, the UMIST

(University of Manchester Institute of Science and Technology) database contains chemistry associated with He, C, N, O, F, Na, Ng, Si, P, S, Cl, Fe and their associated rate parameters [19, 20].

Gas-Phase Chemistry

Gas-phase chemistry is the major pathway for the formation of new molecules in the ISM as gas makes up around 99% of the matter in the ISM [21]. Even though the conditions in the ISM are hostile, as discussed earlier, gas-phase chemistry persists through ion-neutral molecule reactions due to their barrierless character. These types of reactions take place between two bodies. Three-body reactions are rare due to the low density, even in cold, dense molecular cores. However, a recent proposal relating to desorption from solid surfaces suggests that icy mantles coating the dust grains in dense clouds may explode due to the energy released by H_2 formation in the bulk of the ice [22, 23]. Immediately after the ice has exploded, this leads to a high gas-phase concentration, similar to that of solid ice, where three-body reactions might not be as rare as initially thought. These gas-phase reactions are thought to occur through one of three pathways: formation of new molecules, bond rearrangement and destruction of a species [24-26].

The formation pathways are concerned with the creation of larger molecules from smaller precursor molecules. There are different types of reactions for the formation of molecules (A and B may be reactive atoms, radicals or molecules):

- Radiative Association

  $A(g) + B(g) \rightarrow AB(g) + h\nu$ **(R1)**

- Three-Body Reactions (M is the third body)

  $A(g) + B(g) + M(g) \rightarrow AB(g) + M(g)$ **(R2)**

- Negative Ion Association

  $A(g) + A(g)^- \rightarrow A_2(g) + e^-$ **(R3)**

  $A(g) + B(g)^- \rightarrow AB(g) + e^-$ **(R4)**

Bond rearrangement pathways occur between previously formed molecules and atoms:

- Neutral Exchanges

$$AB(g) + C(g) \rightarrow A(g) + BC(g) \quad \textbf{(R5)}$$

- Ion-Molecule Reaction and Charge Transfer

$$AB(g) + C^{+}(g) \rightarrow A(g) + BC^{+}(g) \text{ or } A(g) + B^{+}(g) + C(g) \quad \textbf{(R6)}$$

$$AB(g) + C^{+}(g) \rightarrow AB^{+}(g) + C(g) \quad \textbf{(R7)}$$

The following three pathways are destructive and reduce molecular size:

- Photodissociation

$$AB(g) + h\nu \rightarrow A(g) + B(g) \quad \textbf{(R8)}$$

- Collisional Dissociation

$$AB(g) + M(g) \rightarrow A(g) + B(g) + M(g) \quad \textbf{(R9)}$$

- Dissociative Recombination

$$AB(g) + e^{-} \rightarrow A(g) + B^{-}(g) \quad \textbf{(R10)}$$

$$AB^{+}(g) + e^{-} \rightarrow A(g) + B(g) \quad \textbf{(R11)}$$

Additional reaction pathways also occur which are key to the formation of ions used in the above examples or yielding neutral products and radiation. These reactions typically involve electrons produced from cosmic ray interaction with the gas:

- Radiative Recombination

$$A^{+}(g) + e^{-} \rightarrow A(g) + h\nu \quad \textbf{(R12)}$$

- Radiative Association

$$A(g) + M(g) + e^{-} \rightarrow A^{-}(g) + M(g) + h\nu \quad \textbf{(R13)}$$

$$A(g) + e^{-} \rightarrow A^{-}(g) + h\nu \quad \textbf{(R14)}$$

There is a large potential chemistry involving these 14 general reactions with the atoms and molecules present in dense environments. While there are many molecules in the Universe, the most common is molecular hydrogen (H_2). It plays a role in many reactions yielding more complex molecules. Below are some examples of reactions that can occur with H_2:

- H_2 formation *via* Negative Ion Association

$$H^-(g) + H(g) \rightarrow H_2(g) + e^-(g) \quad \textbf{(R15)}$$

This reaction is one of the main sources of molecular hydrogen in the early Universe. The H^- anion forms through radiative association with an electron (**Reaction 14**) [27, 28]. The key reaction of H_2 is H_3^+ formation:

- H_3^+ Formation *via* Ion Molecule Reaction

$$H_2^+(g) + H_2(g) \rightarrow H_3^+(g) + H(g) \quad \textbf{(R16)}$$

The H_2^+ ion in **Reaction 16** is formed as a result of cosmic ray ionisation of H_2. The resulting H_3^+ cation is important as it reacts with neutral molecules to form hydrogenated molecular cations and molecular hydrogen [28], as shown in **Reaction 17** below:

$$H_3^+(g) + A(g) \rightarrow AH^+(g) + H_2(g) \quad \textbf{(R17)}$$

H_3^+ is also readily destroyed,

- H_3^+ Destruction *via* Dissociative Recombination

$$H_3^+(g) + e^-(g) \rightarrow H_2(g) + H(g) \quad \textbf{(R18)}$$

The electron is again generated from cosmic ray interactions with the gas or grains. Larger molecules can be created in the gas phase from the reactions above, which in turn can take part in further reactions. This eventually results in the observed molecules containing more than ten atoms. Simplified examples of the formation of these chain molecules are shown below [29]:

$$C_2H(g) + C_mH_n(g) \rightarrow C_{m+2}H_n\ (g) + H(g) \quad \textbf{(R19)}$$

$$C_bH_2(g) + C_aN(g) \rightarrow HC_{a+b}N(g) + H(g) \quad \textbf{(R20)}$$

where *m* can have a value up to 8, *n* can have a value up to 2, *a* can have a value up to 9 and *b* a value up to 8. The sum of *a* and *b* can be as large as 11, since the largest species presently observed is $HC_{11}N$. The previous chemistry demonstrates that there are many possible reactions in gas-phase ISM. However, when reviewing the production pathways of small hydrides, H_2, H_2O, NH_3 … *etc.*, one discovers that the calculated abundances do not match with the large values observed in the ISM. In order to explain this discrepancy, other formation mechanisms must be present. This is where heterogeneous chemistry occurring at the surface of dust grains plays a vital role in filling the gap in models.

Surface Chemistry

The number of chemical reactions on surfaces in the ISM is small compared with those in the gas-phase chemistry, but their role is nonetheless essential [30, 31]. The key role of dust has been known for a considerable length of time, but not all the reaction processes were fully understood. General reaction pathways are understood for model systems, as are possible desorption mechanisms of molecular species post-formation. Studying certain heterogeneous reactions allows us to more completely understand chemical processes in molecular clouds, which helps to explain abundances of molecules and clarify the origins of unknown spectroscopic features observed in the ISM.

Surface Reaction Pathways

When looking at grain-surface chemistry, there are three possible pathways to consider. These are [26]:

- Langmuir-Hinshelwood (L-H);
- Eley-Rideal (E-R);
- Harris-Kasemo (H-K), also known as the *hot atom mechanism*.

The L-H mechanism involves molecules (A and B) which initially absorb on to the surface. It is critical that the molecules are physisorbed as this allows diffusion across the surface at a low temperature. When the reagents meet, a bimolecular reaction

occurs and the product (C) desorbs from the surface [26]. This is represented schematically in **Figure 1.2**.

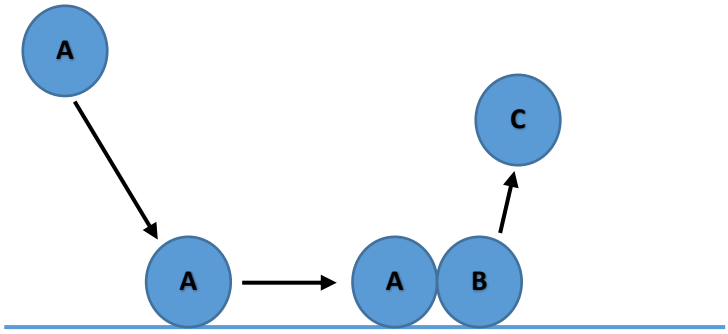

Figure 1.2: The Langmuir-Hinshelwood mechanism in which atoms or molecules adsorb, diffuse, react and desorb [32].

The adsorption process in **Figure 1.2** is reversible and the diffusion process can bring the reactants together, it can also force them apart.

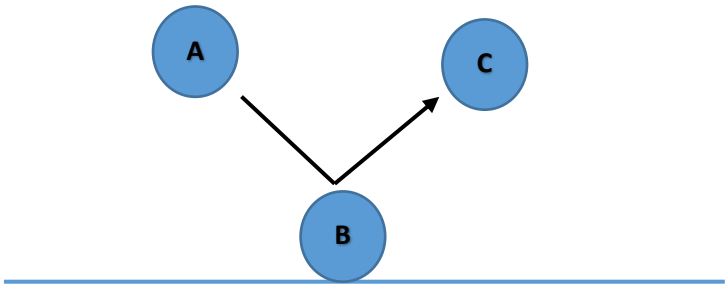

Figure 1.3: The Eley-Rideal mechanism, where one gas phase species never interacts with the surface, but interacts only with adsorbed atom or molecule to produce a new molecule [32].

The E-R mechanism is shown in **Figure 1.3**. This process revolves around a chemisorbed or physisorbed atom or molecule already present on the surface (B) and occurs where a second atom (A) or molecule in the gas phase reacts with B, where A does not interact with the surface [26]. Of course the E-R process is also reversible.

When considering the reverse of the L-H and E-R reactions, a third mechanism is possible. This is the H-K mechanism, which begins with molecular dissociation of an adsorbed reactant induced by a photon or cosmic ray. The fragment produced is a non-thermalised species, and is not released into the general gaseous environment,

but is trapped and can easily translate over the surface [32]. This atom can then participate in a reaction with a second adsorbed reactant. **Figure 1.4** shows the H-K mechanism:

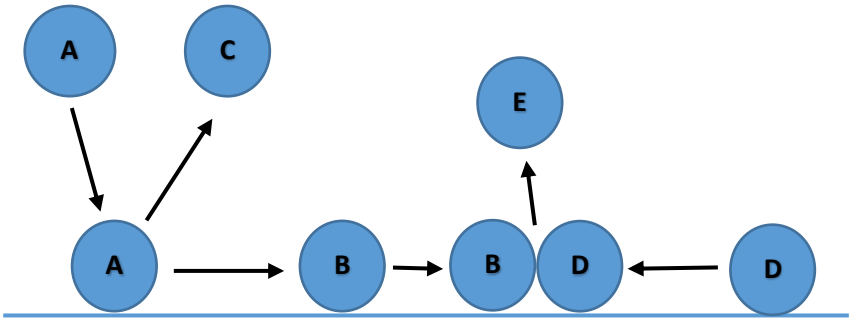

Figure 1.4: The Harris-Kasemo mechanism showing the mixed steps leading to the overall product [32].

Desorption

Not all the molecules created on the surface of dust grains desorb. Some of the species stay on the grain and form ice mantles. If the bond formation energy is not high enough to bring the newly formed molecule to the gas phase, it will require extra energy input to help with desorption process. The various energy sources have been described earlier, and the effect they have on the molecules in interstellar ices is explained below. These energy sources assist in desorption or initiate chemical reactions on icy surfaces or in the bulk ice mantle on dust grains.

Thermal desorption results from the temperature of the substrate rising above a species' sublimation temperature. The protostellar regions found in molecular clouds are in the late stages of cloud evolution. The increased temperature resulting from the heat released from gravitational collapse and then from the protostar itself adds energy to the molecules on the grain surfaces. When enough energy is supplied, the molecules sublime. Desorption occurs continually as the temperature increases.

Cosmic rays are mainly atomic nuclei (H^+, He^{2+}). They comprise only about 1 in 10^9 of interstellar particles [33] but can carry large amounts of energy; often as much as TeV [29]. Sputtering occurs when the nuclei hit the grain and enter the solid, *i.e.* if enough energy is transmitted from the cosmic ray particle to the surface atoms in the collision, the binding energy can be overcome and the species are then injected into

the gas phase [1, 34, 35]. As the nuclei travel through the solid, they break bonds, electrically excite and ionise atoms and molecules. This creates a trail of damage and secondary electrons which represents an extra source of energy. This is *collision-induced desorption*.

Stellar UV radiation does not completely penetrate the depths of dark clouds, but it is responsible for exciting molecules and forming radicals and products in some regions of the ISM. With dark clouds, an internal UV field can be created when molecules excited by cosmic rays relax back to the ground state and release photons [1, 34-36]. This UV radiation, the cosmic rays themselves and the secondary electrons they produce in the icy grain mantles can all induce electronic excitation in molecules in the ices, which in turn can result in desorption. This *desorption induced by electronic excitation*

Work by Cecchi-Pestellini *et al.* [22] and Rawlings *et al.* [18] proposes ice mantle explosions as a desorption mechanism. The reason why ice mantles may explode is linked to the formation of H_2 in the bulk ice. The subsequent exothermic reaction leads to an immense temperature rise that rips apart the weak intermolecular forces holding the solid together, releasing molecules into the gas phase. Enthalpy release from other reactive processes can also desorb the products of the reaction. This is *reaction enthalpy-induced desorption*.

1.2 Dust in the ISM

Microscopic grains (**Figure 1.5)** of matter found in space play an important role in the origins of planetary systems, and maybe even of life itself. Interstellar dust grains comprise only about 1% of the ISM mass, but they catalyse the formation of many crucial molecules, *e.g.* H_2. This allows the cooling and collapse of molecular clouds and ultimately the formation of stars and planets.

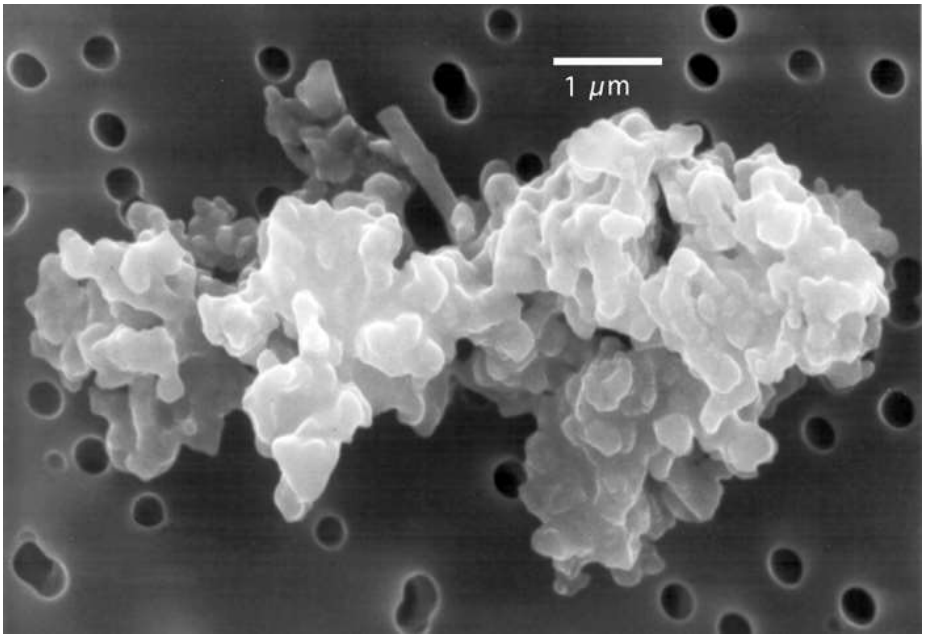

Figure 1.5: Porous chondrite interplanetary dust particle - NASA Johnson Space Centre (Reproduced from [37]).

Dust grains are solid, microscopic particles comprising dielectric and refractory materials. Their size, composition and other properties vary from one location in space to another. For example, grains in dense interstellar clouds are larger than those in the general ISM, while even larger particles are found in circumstellar dust disks. Dust grains injected into the ISM evolve in response to the interstellar radiation and particle fields along with chemical reactions with interstellar atoms and molecules, which changes both their chemical composition and physical structure [38].

1.2.1 Where Does Dust Come From?

Figure 1.6 shows the typical life cycle of stars. Most of the dust found in space comes from Asymptotic Giant Branch (AGB) stars which have moved off the main sequence and entered the red giant phase of their evolution (**Figure 1.7)**.

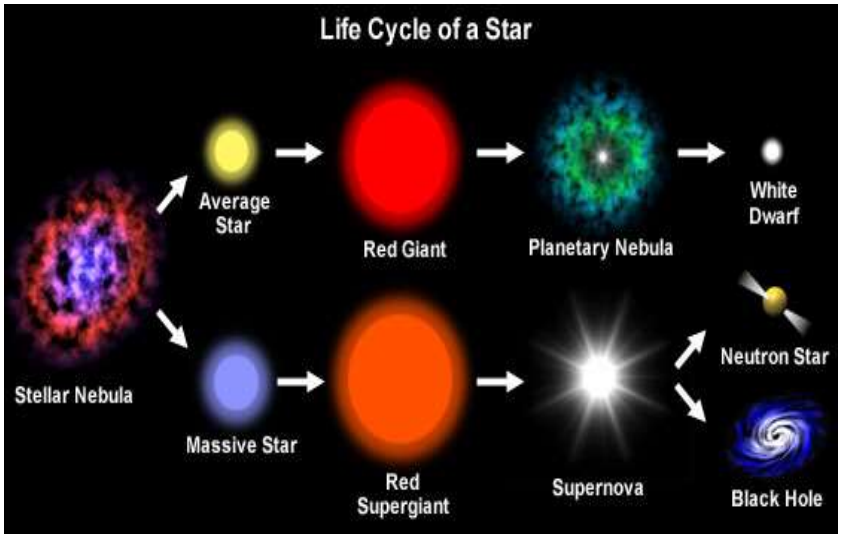

Figure 1.6: The life cycle of a star (Reproduced from [39]).

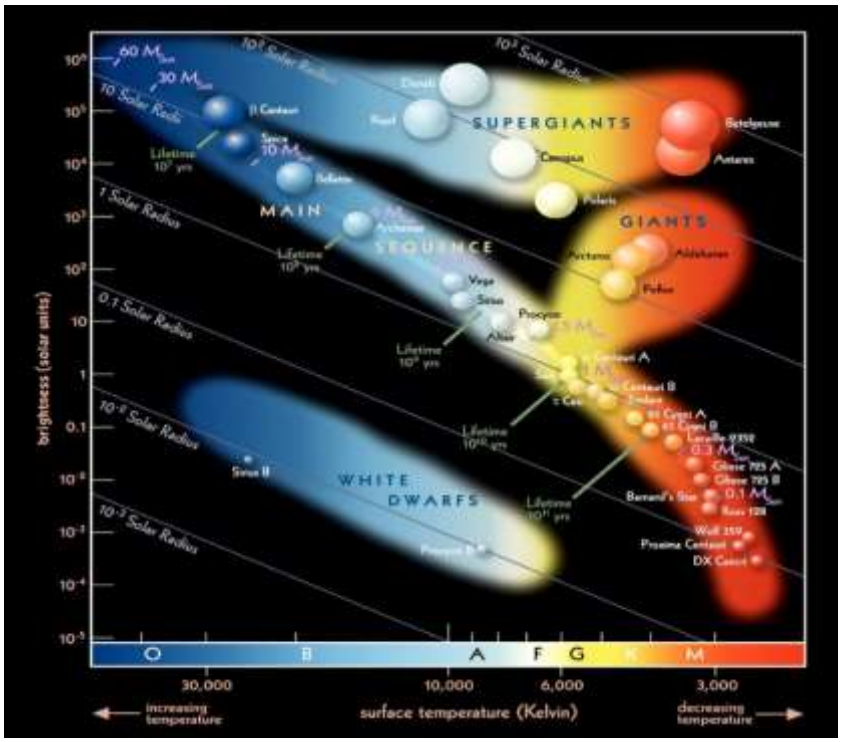

Figure 1.7: The Hertzsprung-Russell diagram shows the stars in the stable phase of hydrogen burning lie along the main sequence according to their mass. After a star uses ~ 10% of its hydrogen in its core, it leaves the main sequence and moves towards the red giant branch (Reproduced from [40]).

These stars have extended atmospheres which are rich in oxygen, silicon and carbon. These are elements manufactured in the stellar core, but which have been dredged up to the surface by convection currents, as shown in **Figure 1.8**.

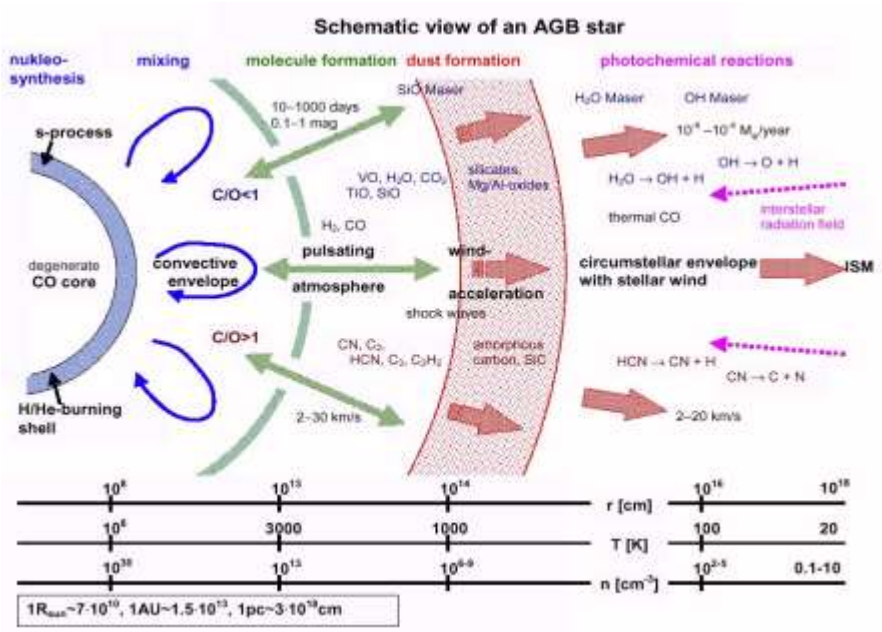

Figure 1.8: Overview of mass-losing AGB stars, showing the important physical and chemical processes (Reproduced from [41]).

In low-mass, oxygen-rich AGB red giants, the O atoms react in the stellar atmosphere with silicon and any other metal atoms to form silicate grains (around 1 μm across) and so these stars lose mass as silicates and metal oxides. Meanwhile, more massive silicon-burning stars probably end with supernovae ejecting precursor molecules (*e.g.* SiO) and silicate dust into the ISM. The diatomic molecule SiO has been observed in the ISM [34]. In contrast, a carbon-rich star gives rise to a dense pall of carbon particles in the form of graphite flakes or amorphous carbon grains which can measure up to 0.01 μm across.

Dust grains are blown away from their parent star by radiation pressure into the general ISM. The grains then find their way into diffuse clouds and, eventually, into dense molecular clouds where their temperature falls and they begin to acquire additional hydrogen, oxygen, carbon, nitrogen and sulfur atoms, which have also escaped from stars. These accreted materials build up into icy mantles of water ice, solid ammonia, methane *etc*. As the temperature drops other substances may be adsorbed on ice mantles, *e.g*. small molecules such as carbon monoxide (CO) and hydrogen sulfide (H_2S). If the grain is bombarded by UV radiation from local hot young stars or the interstellar radiation field (ISFR), this can trigger reactions

between the different chemical species on the grain surface, leading to the formation of more complex organic substances.

1.2.2 The Role of Dust in Astrophysics and Astrochemistry

Simple astronomical observations made using a telescope show the presence of dust in our Galaxy which is more fully revealed in various images of nebulae. Photometric and spectroscopic observations have helped to reveal the nature and composition of this interstellar dust [42], which has two important chemical roles:

1. Passively shielding molecules from the destructive effects of stellar radiation.
2. Actively participating in chemical processing. In the gas phase, colliding atoms such as H may simply bounce apart before they can form a chemical bond. In contrast, atoms adsorbed on the surface of a dust grain may be held together until a reaction occurs and some of the excess energy of the forming bond is dissipated into the grain. It is believed that H_2 is formed in this way, and is ejected from dust grain surfaces into the gas at high speed and in high states of vibration and rotation. Other simple molecules, such as H_2O, methane (CH_4), and ammonia (NH_3), are also likely to form in this way [43].

In our Galaxy, the gas-to-dust ratio is about 100:1, and, since the ISM comprises around 10% of the galaxy's baryonic mass, dust grains make up 0.1% of the Galactic mass. Dust absorbs 30 - 50% of the starlight emitted by the Galaxy and this is re-radiated as the far-infrared continuum emission. This means that only 0.1% of the baryons are ultimately responsible for a third to half of the galaxy's bolometric luminosity. Dust grains help to determine what galaxies look like, the way the ISM in a galaxy behaves and the very process of star formation which creates the visible galaxy. **Figure 1.9** shows the dark cloud Barnard 68 [44], a typical quiescent dense cloud whose opacity is determined by the presence of dust. The lack of colour in **Figure 1.9a** is due to the object obscuring visible light from background stars due to the large concentration of gas and dust. **Figure 1.9b** image shows the same region as observed in the IR. The gas and dust in the molecular cloud does not completely absorb and scatter all wavelengths of radiation as the right hand IR image demonstrates.

(a) (b)

Figure 1.9: Barnard 68 is a large, dense cloud of cold gas and dust. **(a)** The dust scatters and absorbs the light from the stars behind and hence it creates an apparent void in space. The infrared light from those stars penetrates the cloud as the false colour IR image in (**b**) (Reproduced from [44]).

The presence of dust in the ISM is deduced observationally in one of two basic ways [45]:

I. Interaction with starlight

1. The reflection of starlight by dusty clouds located behind bright stars.
2. The polarisation of light by scattering in regions with macroscopically aligned non-spherical dust grains.
3. Total and wavelength-selective extinction of starlight passing through dusty regions due to a combination of absorption and scattering; *e.g.* absorption of starlight by carbonaceous materials in the near-UV, and by silicate materials and various ices in the IR.

II. Emission from dust grains:

1. IR emission bands from heated grains, many of which, are still not clearly identified.

2. Thermal continuum emission from non-equilibrium heating of small grains at near-to mid-IR wavelengths.
3. Thermal continuum emission from dust grains in radiative equilibrium with the local radiation field. This radiation emerges at mid-to-far IR wavelengths.
4. Radio continuum emission from rotating grains (both electric and magnetic dipole radiation).

Where the gas is very cold, the dust grains are also at a very low temperature (as low as 10 K). Gas phase molecules colliding with such grains tend to stick to their surfaces, and, over time, the grains in these regions accumulate mantles of ice, mostly H_2O ice, which is formed by reactive accretion [46]:

$$H(ads) + O(ads) + H(ads) \rightarrow H_2O(s) \qquad \textbf{(R21)}$$

but also ices of other molecules such as CO, CO_2, and CH_3OH. Some of these are formed in the solid state by hydrogenation of CO and photo-processing

$$H_2O(g) + CO(g) + h\nu \rightarrow CO_2\,(g) + H_2(g) \qquad \textbf{(R22)}$$

Astronomers can detect these ices spectroscopically.

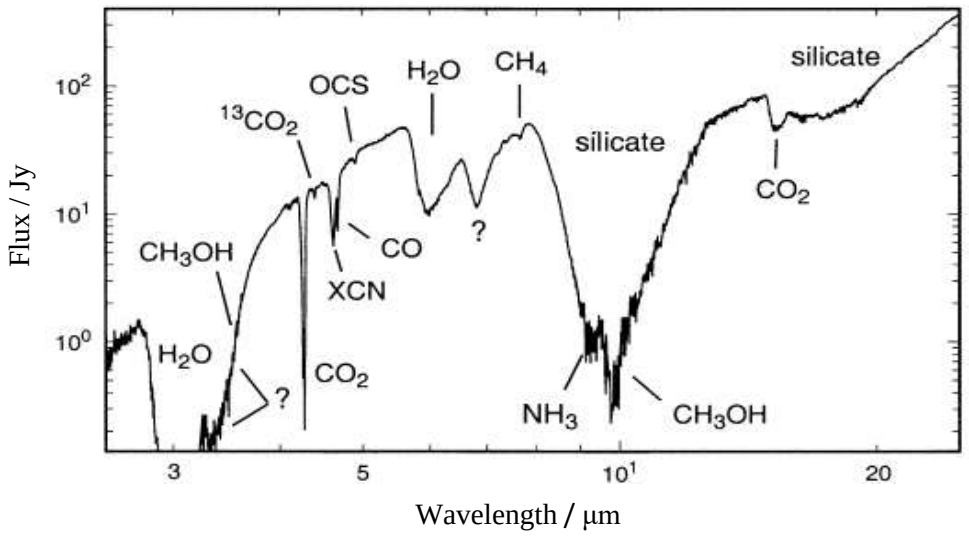

Figure 1.10: W33A, a dust-embedded massive young star (Reproduced from [35]).

For example, H_2O molecules in water ice absorb radiation at a wavelength of about 3.0 μm, associated with the O–H stretching vibration (**Figure 1.10**). In cases where such ice-coated dust grains lie along a line-of-sight towards a star that shines in the infrared, this 3.0 μm absorption will be seen (**Figure 1.10**). The formation of planetary systems is thought to start with dust grains in the protostellar disk, where they coagulate into large grains, leading to planetesimals and eventually to planets and comets. The latter carry their complex organic molecules with them on to the planets as a precursor to life. The dust in our Solar System comes from a range of sources including fragmentation of asteroids, activity of comets and collisions and emission processes in the Kuiper Belt [47, 48]. Additionally, dust particles enter the solar system directly from interstellar space, as shown in **Figure 1.11**.

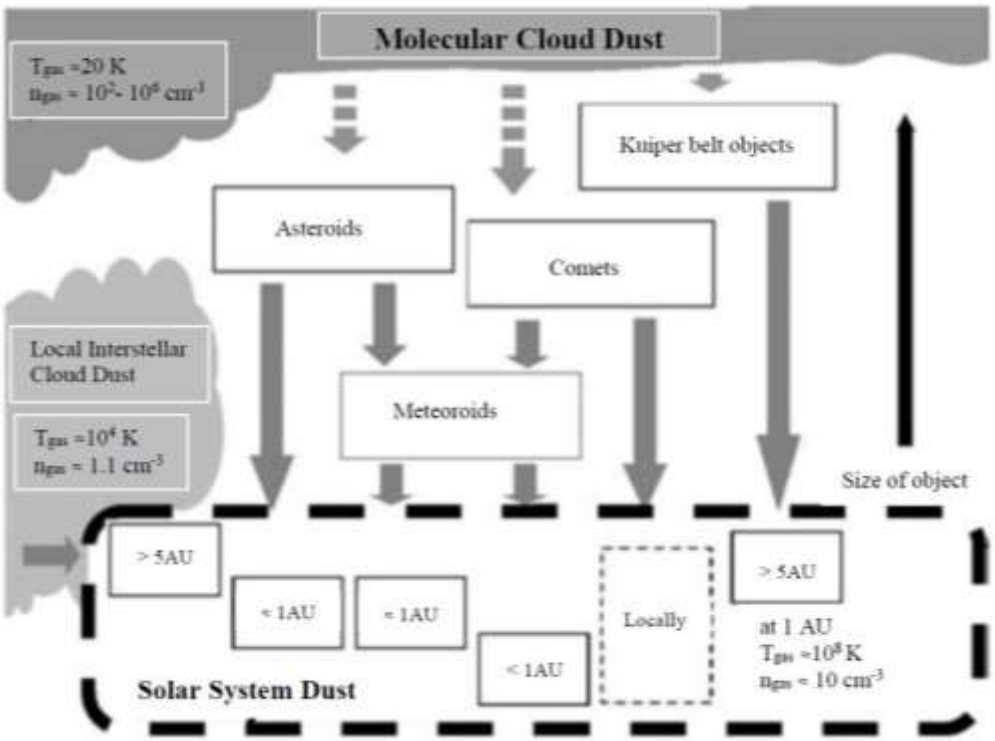

Figure 1.11: Where the dust comes from within the Solar System: The parent bodies of dust in the Solar System are asteroids, comets and Kuiper belt objects, and interstellar dust particles which enter the Solar System directly from the local interstellar medium. Most of the dust outwards from 7.48×10^{11} m is interstellar dust and dust produced in the Kuiper belt. Dust near 1.50×10^{11} m comes from comets and asteroids. Most dust from asteroids and comets is not directly released from the parent bodies, but is produced from collisional fragmentation of meteoroids that come from these sources. The inner Solar System dust cloud is replaced from collisions of asteroidal meteoroids (Reproduced from [47])

1.2.3 Interstellar Dust Grains

The presence of solid particles in interstellar space was noted by Trumpler [49] through the discovery of colour excess between photographic (with an effective wavelength, λ_{eff}, of 430 nm) and visual magnitudes. Grains were estimated to weigh around 10^{-19} g, corresponding to radii of greater than 2 nm [49]. However, by the end of the 1930s, a λ^{-1} extinction law (the interstellar extinction varies approximately inversely with wavelength λ) in the wavelength range 300 to 1000 nm had been well established [50, 51]. In order to explain the λ^{-1} extinction law, it was proposed that metallic grains with a dominant size of around 50 nm [52] or a power law $dn(a)/da \sim a^{-3.6}$, and distribution in the size range 8 nm to 1 cm, were responsible [52], since meteoric particles (mainly metallic) and interstellar grains were then thought to have the same origin. This is much greater than expected from large grains at 15 - 25 K in thermal equilibrium with the ISRF. The presence of a population of ultra-small grains in the diffuse interstellar medium was inferred by the 12 μm and 25 μm 'cirrus' emission detected by the Infrared Astronomical Satellite (IRAS) [53]. Additionally, measurements by the Diffuse Infrared Background Experiment (DIRBE) instrument on the Cosmic Background Explorer (COBE) satellite confirmed this, while also detecting broadband emission at 3.5 μm and 4.9 μm [53]. Spectrometers aboard the Infrared Telescope in Space (IRTS) [54-55] and the Infrared Space Observatory (ISO) have shown that the diffuse interstellar medium radiates strongly in emission with features at 3.3, 6.2, 7.7, 8.6, and 11.3 μm [56].

These emission features were first seen in the spectra of the planetary nebula NGC 7027 and BD+ $30^0$3639, and have been observed in a range of astronomical environments including planetary nebula, protoplanetary nebula, reflection nebula, HII regions, circumstellar envelopes and external galaxies. They are sometimes referred to as 'unidentified infrared' (UIR) bands. These emission features are now attributed to free flying PAH molecules which are vibrationally excited on absorption of a single UV/visible photon and subsequently relax by emitting IR [42, 56-59]. Other carriers have been suggested, including carbonaceous grains with a partially aromatic character [60, 61], quenched carbonaceous composite, fullerenes (C_{60}) [62] and surface-graphitised nanodiamonds [63].

A number of grain models have been developed since the 1970s which generally fall into the following three broad categories:

1. The silicate-graphite model

This model consists of two physically separate components with a power-law size distribution $dn(a)/dn \sim a^{-3.5}$ in the size range 5 nm to 25 μm [64, 65]. Modifications to this model have been made to include new dust components such as amorphous carbon, carbonaceous organic refractory material and PAHs, alongside adjustments to the dust sizes [21, 66-70].

2. The silicate core-carbonaceous mantle model

This model was originally proposed by Greenberg [71] and consists of larger silicate grains coated with a layer of carbonaceous organic refractory material, produced by UV photolysis of ice mixtures. It attempts to simulate the physical and chemical processes occurring in interstellar space. Further development of this model has taken place [72] to take into account the PAH components and population of small grains, which are added to take into account the far–UV extinction rise, plus the 'UIR' emission bands and the 217.5 nm extinction hump. Additionally, modifications to this model have taken into account different coating materials, *e.g.* amorphous carbon, hydrogenated amorphous carbon (HAC) and new dust types, *e.g.* iron, small bare silicates and varying dust size distributions [61, 73-77].

3. The composite grain model

Mathis and Whiffen [77] realised that grain shattering due to grain-grain collisions and subsequent reassembly through agglomeration of grain fragments may be important in the ISM. They modelled grains as composite collections of small silicates, vacuum (≈ 80% in volume) and various types of amorphous carbon, organic refractories and HAC. With power law size distribution $dn(a)/da \sim a^{-3.7}$ in the range 300 to 900 nm. Additionally, a small graphite component was needed to take into account the 217.5 nm extinction hump. However, Wright [78] argued that a fractal structure would be expected for interstellar grains, which are formed through coagulation of small grain fragments and created from grain disruption caused by

supernova shock waves. Taking into account that the relative abundances of refractory elements in the ISM may be as low as 65% of solar [79], Mathis [80] modified the composite model in order to take into account the tighter abundance constraints and the heavy elements, Mathis [80] derived a vacuum fraction of around 45%. The models by Mathis and Whiffen [77] and Mathis [80] did not take into account the UIR emission. However, Zubko [76] took account of UIR emission by including a population of PAH molecules.

Chemical Composition of Dust Grains

Depletion is a measure of the under-abundance of an element in the gas phase of an interstellar region compared with a standard abundance. The amount of depletion observed is to some extent governed by the mean H number density along a line-of-sight. The observed abundances of a number of heavy elements are strongly depleted relative to solar values. It can be concluded that the 'missing' abundance is locked up in the solid phase in dust grains [81]. This removes the elements from the gas phase, making them inaccessible to absorption line studies. Significant amounts of depletion are observed in high-density regions. Additionally, cold diffuse clouds display greater overall depletion than warm diffuse ones. Depletion is often stated in logarithmic form, **Equation 1**:

$$D(\mathrm{X}) = \log A(\mathrm{X})_{\mathrm{gas}} - \log A(\mathrm{X})_{\mathrm{standard}} = \log\left(\frac{N_{\mathrm{H}}(\mathrm{X})}{N_{\mathrm{H}}(\mathrm{H})}\right)_{\mathrm{gas}} - \log\left(\frac{N_{\mathrm{H}}(\mathrm{X})}{N_{\mathrm{H}}(\mathrm{H})}\right)_{\mathrm{standard}} \quad \textbf{(E1)}$$

where $N(\mathrm{X})$ is the number density of species X and N_{H} is the number density of H [82]. As with abundances, depletions are typically determined in respect to one of the proxies for H rather than to H itself. Depletions are useful in terms of giving a general picture of dust formation and composition, and for seeing trends of elemental incorporation into dust, correlating with the physical conditions in the interstellar medium. There is a strong correlation between the amount of depletion and condensation temperature (T_{c}) of the element being depleted. Typically, the higher the condensation temperature of an element, the more it will be depleted from the gas

phase. **Figure 1.12** shows the depletion of elements relative to solar as a function of the condensation temperature.

Elements with T_c above 1200 K are able to form 'refractory' solids possessing large binding energies. Hence, strongly depleted elements tend to be those with high values of T_c. As the observed elemental depletions provide insight into the composition of interstellar dust, it can be seen that the 'electron donor' species in interstellar dust are mostly C, Mg, Si and Fe. The grains typically contain a large amount of O and even H [83].

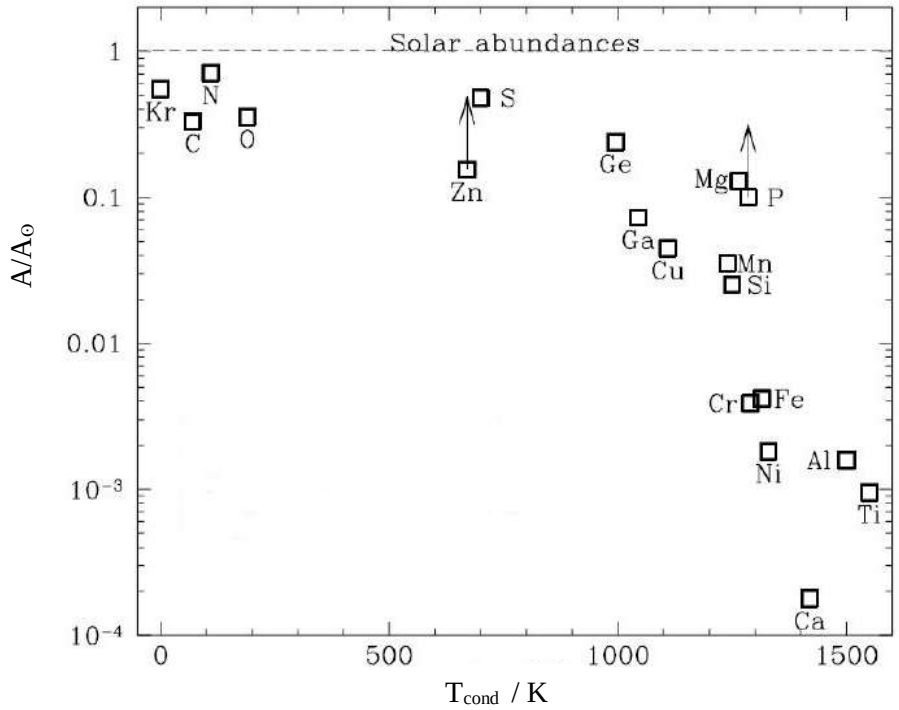

Figure 1.12: The pattern of depletion of the gas phase elements onto dust grains measured towards the ζ Oph (Reproduced from [83]).

A number of authors have observed that relative depletion levels among elements correlate with characteristics of the elements themselves [81]. These types of relationships are helpful in determining how grains form. For example, Snow [84] discovered a correlation between the first ionisation potential of an element and its depletion, suggesting that the accretion of the gas is a key source of grain material. Cardelli [85] discovered that depletions correlate with their location in the periodic table, *i.e*. chemistry, which again points to the accretion process contributing to grain composition. However, none of the relationships between depletion and elemental

characteristics is perfect, since multiple processes are most likely to contribute to dust grains' chemical make-up.

One possible explanation for interstellar depletion is that dust grains themselves promote further depletion. Efforts to quantify this hypothesis, in the case of the most heavily depleted elements in the diffuse gas have run into difficulties [82]. Draine [86] noted that extremely high rates of mass transfer from molecular clouds to the diffuse medium were needed. However, the existence of a population of very small grains may assist this process, where the presence of this population is deduced from observations of 3 to 60 μm IR emission, thought to be generated by small grains at temperatures of 30 - 300 K or greater by the absorption of a single stellar photon [67]. It is thought that small grains are more efficient accretors than larger 'classical' grains for the following reasons:

1. Small grains contribute a greater total surface area.
2. They are more inclined to be negatively charged or neutral, compared with classical grains which tend to be positively charged.

The collision cross-section for small grains is enhanced because the depleted metals in the gas have been singly ionised, whereas it is reduced for bigger grains. There is no single type of grain, rather there is a mixture of different types of grains formed under different physical conditions. The leading materials are silicates and carbonaceous (carbon-bearing) materials, with ice materials of volatile compounds such as H_2O or CO_2 condensed on their surfaces (*i.e.* ice mantles). Pure metallic grains such as iron spheres or needles materials have also been considered [45]. However, silicates along with carbonaceous (carbon-bearing) materials provide a large proportion of the total mass of dust grains in the ISM.

Structure and Composition of Silicate Grains

Silicate materials form a considerable fraction of the total mass of interstellar dust. Interstellar silicate grains are likely to be with Fe and Mg, since both of these elements are astrophysically abundant and strongly depleted. At least ~95% of the silicate material is amorphous [87]. Crystalline silicates are distinguished from

amorphous silicates due to the presence of lattice modes at beyond 25 μm, as in **Figure 1.13** [88].

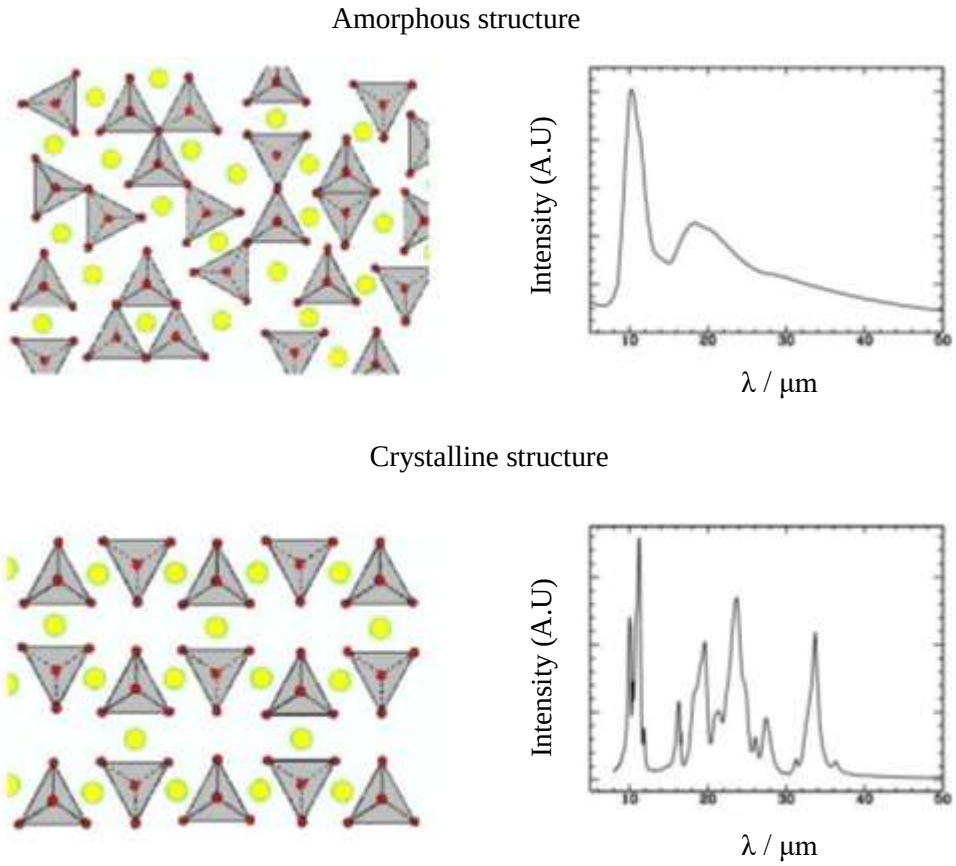

Figure 1.13: A potential atomic structure of an amorphous (or disordered) silicate and crystalline (or ordered) silicate, along with their typical infrared emission spectra. The tetrahedra are four oxygen atoms around a silicon atom. The large circles represent metal atoms. There are a number of sharp features in the crystalline silicate spectrum, compared to two broad bumps in the amorphous silicate spectrum (Reproduced from [88]).

In certain circumstellar disks, the crystalline fraction appears to be higher, however it appears that the bulk of the silicates remain amorphous. Bouwman *et al*. [89] found that 5 - 10% of the olivine mass is crystalline in the dust around Herbig Ae/Be stars. The principal forms expected are Pyroxenes ($Mg_xFe_{1-x}SiO_3$), which includes such minerals as Enstatite ($MgSiO_3$) and Ferrosilite ($FeSiO_3$), and Olivines ($Mg_{2x}Fe_{2-2x}SiO_4$), which includes such minerals as Fayalite (Fe_2SiO_4) and Forsterite (Mg_2SiO_4) [45]. Additionally, there are two different crystalline structures for the pyroxenes: orthopyroxene and clinopyroxene. All of these are common in meteorites, and spectral signatures of enstatite and forsterite have been seen in the dusty shells around AGB stars. Olivine and forsterite have been seen in comets and in dust grains

captured by the Stardust mission [45]. Silicate grains typically dominate dust emission in many astrophysical environments, and are observed in the cold neutral medium, comets and proto-planetary disks and even in the far-distant Universe [90]. The 9.7 μm Si-O stretching feature and the 18 μm O-Si-O bending feature are universally seen in absorption as illustrated by the well-known ISO spectra of W33A (**Figure 1.10**). These features are broad and relatively featureless reflecting the amorphous nature of interstellar silicates. In the diffuse interstellar medium, silicate materials are mainly amorphous, and crystalline silicate is mainly observed towards young stars, suggesting that *in situ* formation by thermal annealing or shocks may have occurred [91,92]. Some circumstellar dust displays emission features. These are characteristic of crystalline silicates, and from the locations and strengths of these features it is possible to infer the Mg:Fe ratio. In all examples known so far, the crystalline silicate material appears to be very Mg-rich and Fe-poor, which is consistent with pure forsterite and enstatite [93-95]. However, Molster *et al*. [96] reported that enstatite ($MgSiO_3$) is more abundant than forsterite (Mg_2SiO_4) around most evolved stars. Silicon is generally, very much depleted in the ISM, however, if Si is mainly in silicates, and Fe is not present in these, then the interstellar silicates would be expected to be enstatite ($MgSiO_3$). Hence, Fe would be present as either metallic Fe or in oxide form (*i.e.* FeO, Fe_2O_3 and Fe_3O_4). While there is some evidence for Mg-rich silicates in circumstellar dust, there is, however, no reliable indication of the composition of interstellar silicates. Hence, a large Fe fraction and olivine-like composition are still possible. Observed gas-phase abundances of Mg, Fe and Si, along with variations from one cloud to another, have been interpreted to possibly indicate that silicate grains may have an Mg-rich mantle and Fe-rich core [97]. The total ratio of Fe + Mg atoms to Si atoms in grains is estimated to be 3:4:1 or about 3.1 in excess of the 2:1 ratio expected for olivines, suggesting that metal oxides or metallic Fe may be present as well as silicates [98, 99].

These conclusions, however, depend on the assumption of total interstellar abundances. Sofia and Meyer [100] conclude that the (Fe + Mg):Si ratio in the ISM dust is actually close to 2:1 for both halo dust and the dust in the well-studied Oph cloud. Hence the composition of interstellar silicates remains uncertain, but the work done by Sofia and Meyer [100] suggests that olivine ($MgFeSiO_4$) appears to be a reasonable approximation. Silicates are composed of linked SiO_4 tetrahedra with

cations in between *e.g*. Mg, Fe, Na and Al. A silicate can have various stoichiometries depending on the number of oxygen atoms shown between the SiO_4 tetrahedra [101]. In the case of silicates with an olivine type stoichiometry, no oxygen atoms are shared and the bonds are formed through the cations. For Mg/Fe olivines, this results in the chemical composition $Mg_{2x}Fe_{2-2x}SiO_4$ (where $0 < x < 1$ determines the Mg to Fe ratio, $x = Mg/(Fe + Mg)$). Silicates with a pyroxene type stoichiometry share one oxygen atom, resulting in linked chains of tetrahedra. This results in a composition $Mg_xFe_{1-x}SiO_3$, of course when all the oxygen atoms are shared between the tetrahedra, we get silica SiO_2 [101].

Structure and Composition of Carbonaceous Grains

Carbonaceous grains are produced by carbon-rich (C/O ratio >1) AGB stars in contrast to oxygen-rich (C/O < 1) AGB stars which produce metal oxides and silicates. In such stars, most of the O in the stellar outflow is tied up in CO, allowing carbonaceous dust to form. Observational estimates suggest that two thirds of the dust we detect in the Milky Way has been produced by carbon-rich AGB stars [102]. However, at sub-solar metallicities, their total dust contribution relative to supernovae, the efficiency of dust condensation and the chemical composition of the dust remains uncertain. Carbonaceous dust grains include pure carbon in both crystalline forms (*i.e*. diamond and graphite) and amorphous or glassy forms (*i.e.* composed of a mixture of graphite and diamonds), alongside hydrocarbons in the form of hydrogenated amorphous carbons, polycyclic aromatic hydrocarbons (PAHs), aliphatic hydrocarbons and fullerenes [103]. Also seen, but rare (probably less than 5% of all forms of carbonaceous grains), are other carbonaceous compounds including Silicon Carbide (SiC) and carbonates such as Calcite ($CaCO_3$) and Dolomite ($CaMg(CO_3)_2$) [103].

Dust Grain Sizes and Shapes

Interstellar grains have a range of sizes from a few Å to a few μm. The presence of nanometre-sized or smaller particles in the interstellar medium is indicated directly by the interstellar far-UV extinction; the ubiquitous 3.3, 6.2, 7.7, 8.6 and 11.3 μm PAH emission features; the near- and mid-IR broadband emission seen in the IRAS 12 and 25 μm bands and the COBE-DIRBE 3.5, 4.9, 12 and 25 μm bands; the 10-100 GHz Galactic foreground microwave emission; and indirectly by interstellar gas

heating [104]. The extinction curve rises from the near-IR to the near-UV with a broad absorption feature at around 217.5 nm, followed by a steep rise into the far-UV at 100 nm.

The interstellar polarisation rises from the IR and it has a maximum somewhere in the optical and then decreases towards UV. Hence, there must be a population of aligned non-spherical grains with a typical size of 0.1 μm, which is responsible for the peak polarisation at 0.55 μm. Micron-sized pre-solar grains such as graphite, silicon carbide (SiC), corundum (Al_2O_3) and silicon nitride (Si_3N_4), and nm-sized pre-solar grains (*e.g.* nano-diamonds and titanium carbide nano-crystals) of interstellar origin as indicated by their anomalous isotropic composition have been identified in primitive meteorites [105]. Pre-solar silica grains have been recently identified in IDPs [106]. Sub-micron-sized GEMS (glass with embedded metals and sulfides) of pre-solar origin have also been identified in IDPs, and their 8-13 μm absorption spectrum is similar to that observed in dense molecular clouds and young stellar objects [107]. Very large grains, with radii of 1 μm, which enter the Solar System from the ISM, have been detected by the interplanetary spacecraft Ulysses and Galileo [108, 109]. Very large grains of radii of around 10 μm, whose interstellar origin has been indicated by their hyperbolic velocities, have been detected by radar methods [110]. However, Frisch [111] and Weingarther and Draine [112] have argued that the volumes of very large grains which have been inferred from the detections were difficult to reconcile with the interstellar extinction and interstellar elemental abundances.

The shape of dust grains is not well known, but it has great importance in interstellar processes. Dust serves as a cooling agent during the clump contraction phase of star formation through emission of far-IR radiation from dust grain surfaces. The larger the surface area of the grain, the more efficient this cooling is. By looking at how dust absorbs, emits and reflects light, it is possible to deduce the geometrical properties of interstellar dust. Models of observed interstellar extinction over the wavelength range between 0.1μm and 1 μm, feature generalised particle size distributions of graphite, enstatite, olivine, silicon carbide, iron and magnetite or combinations of these materials. The size distributions are power laws, which monotonically decrease towards larger sizes between 0.005 μm and 2.5 μm. **Figure**

1.14 shows a grain of interplanetary dust which has been caught by a high-flying U2 aircraft. The grain is around 10 μm across, and it is composed of glass, silicate minerals and carbon. Models involving the shape of dust grains, such as those shown in **Figure 1.14**, are rare.

The shape of dust grains is generally approximated to be spherical or cylindrical in order to more completely solve for electromagnetic field configurations. However, dust grains are not likely to be spherical. It is more likely that grains stick together, collide and shatter, leading to a rather random distribution of shapes. **Figure 1.14** shows a possible way to illustrate the results of such a random conglomeration process. It assumes that dust grains are fractal, created from a coagulation of smaller sub-units called monomers, dimers, tetramers, and so on [64]. The shape of the dust grains has a large influence on the shape of the absorption and extinction spectrum of the grains. Grains come in a range of shapes, since the detection of interstellar polarisation indicates that some fraction must be non-spherical and aligned. Since the wavelength dependence of the interstellar polarisation exhibits a steep decrease towards the UV, this suggests that the ultra-small grain components, which are responsible for the far-UV extinction curve, are either spherical or unaligned [113]. An understanding of grain shapes is important for working out grain dynamics (*e.g.* thermal spin-up of grains) and for the physics and chemistry of molecular formation on grain surfaces (non-spherical grains have larger surface areas for a given volume).

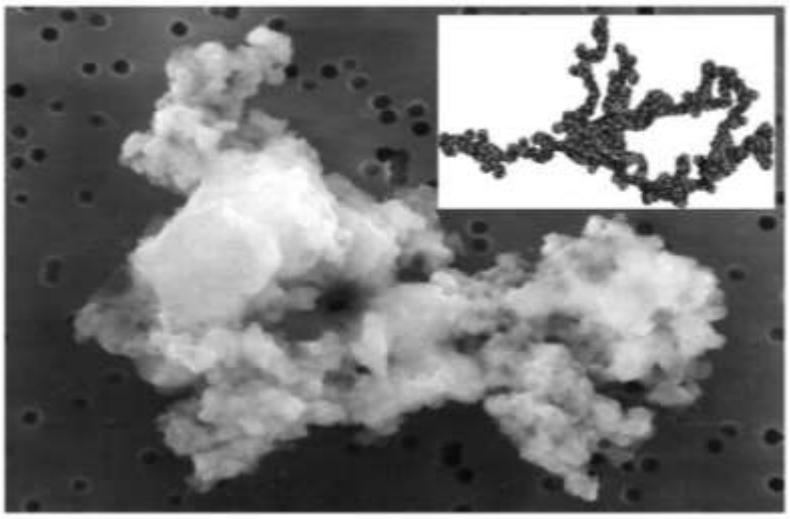

Figure 1.14: A grain of interplanetary dust which is likely to date from the early days of our Solar System. It is 10 μm across and composed of glass, silicate minerals and carbon [Credit: NASA, 2001]. The inset shows how interstellar dust, which is generally much smaller than 10 μm, could appear by means of fractals [Credit: E. L. Wright UCLA, 1999].

Grain Modification by High Energy Radiation

Within the harsh conditions of the interstellar medium, both processing (modification) and destruction of dust grains play a vital role. Most of the grains in the ISM and some in the protoplanetary disks are heavily irradiated. Demyk *et al.* [114, 115] estimates that the majority of ISM silicate grains would be amorphised in a single fast supernova shock. Intense radiation can result in distinctive microstructures while producing chemical changes in the grain that can be looked for. Protoplanetary disks, interstellar clouds and active galactic nuclei (AGNs) contain X-ray-dominated regions, in which the X-rays interact with dust and gas. X-rays from active nuclei are commonplace, and fast shocks from supernovae, such as stellar wind bubbles pushing into dense interstellar media of starburst galaxies, can also emit X-rays [116, 117]. High-energy radiation from hot stars or supernovae can alter dust grains' physical properties and thus affect their role in processes, including being a catalyst for the formation of gas phase molecules. X-rays interact with grains by photoionising the inner (K and L) shells of their constituent atoms. The photoelectrons and Auger electrons produced transfer some of the kinetic energy into thermal energy in the grain and so temporarily raising the grain temperature. These processes can render dust grains amorphous and alter their chemical composition; this is definitely the case for silicates, which have been observed to be partially

crystalline in many circumstellar shells, but are completely amorphous in the interstellar medium [118]. Whichever process is amorphising silicates may have a similar effect on carbonaceous grains species. However, the effect of such processes on carbon grains has not yet been fully investigated.

A number of laboratory experiments have been carried out simulating the different physical processes that grains undergo during their life cycle, to understand the evolution of silicate dust [119]. Experiments have shown that irradiation of silicates with H^+ and He^+ ions in the 4-50 keV range results in modifications of the physico-chemical properties for ion fluences of less than 10^{18} ions cm^{-2} [115]. Within the ISM, such ions and energies are likely to be encountered in diffuse clouds and regions where there are supernovae generated-shock waves. Where high velocity, over 100 km s^{-1}, shock waves propagate, this represents an efficient mechanism for destroying dust grains within the ISM. Among the most obvious changes in silicate due to irradiation are structural modifications. Another effect of the irradiation of dust grains, depending on the ion energy along with grain size, is the implantation of incident iron atoms into the grains. This can result in a change in their compactness, so that they become more porous under irradiation. It is hard to quantify the extent of the porosity which is achievable within the ISM *via* this process. This, however, may partly explain the grain porosity, which is typically proposed to reproduce the silicate bands observed in the ISM [120].

To support this idea, the width of the interstellar silicate bands can be compared with that of the irradiated laboratory silicate bands [115]. Irradiation can also result in chemical changes in silicates *via* sputtering of atoms. Within the ISM, chemical changes are of greater significance for small grains than larger grains, since the surface/volume ratio is higher. Hence, in shocks, the dust grains have a size which is comparable with the penetration depth of the incident ions, and should undergo differential sputtering leading to chemical fractionation. Grain erosion caused by sputtering is responsible for the observed increase in the gas phase abundance of dust-forming elements in regions with increasing cloud velocity and decreasing density [121].

It is challenging to determine the chemical composition of the amorphous silica components in the ISM from IR spectroscopic observations. A number of studies

show that the silicates around evolved stars are well reproduced with olivine silicates [121, 122]. However, in molecular clouds and young protostellar objects, the band position of the stretching mode is around 9.6 μm leans towards a pyroxene-like stoichiometry [123-125]. Spectral characteristics of irradiated silicates reflect changes in the physico-chemical properties. IR spectral signatures are quite different before and after irradiation. The sharp peaks which are characteristic of the crystalline arrangement of atoms disappear, leaving two broad and structureless bands at 9.8 and 18 μm. **Figure 1.15** shows a qualitative comparison of spectra of irradiated silicates, along with the spectrum of the ISM towards the Galactic Centre GC-IRS3. The observed interstellar silica bands are a result of the spectral distribution of various silicate components. The amorphous silica is formed around late-type stars or supernovae, which are the most abundant in terms of mass and amorphized crystalline silicates (around 20% of the total silicate mass). The spectral bands of the irradiated minerals are similar to silicate bands observed in the ISM, where the spectra of amorphized minerals display a lack of structure and their bands are as broad as observed in the ISM. The comparison of observed spectra in the ISM with laboratory data highlights the challenge of characterising amorphous silicate from IR data where amorphous silicates possess different stoichiometries display similar infrared characteristics depending on their microstructure and compactness.

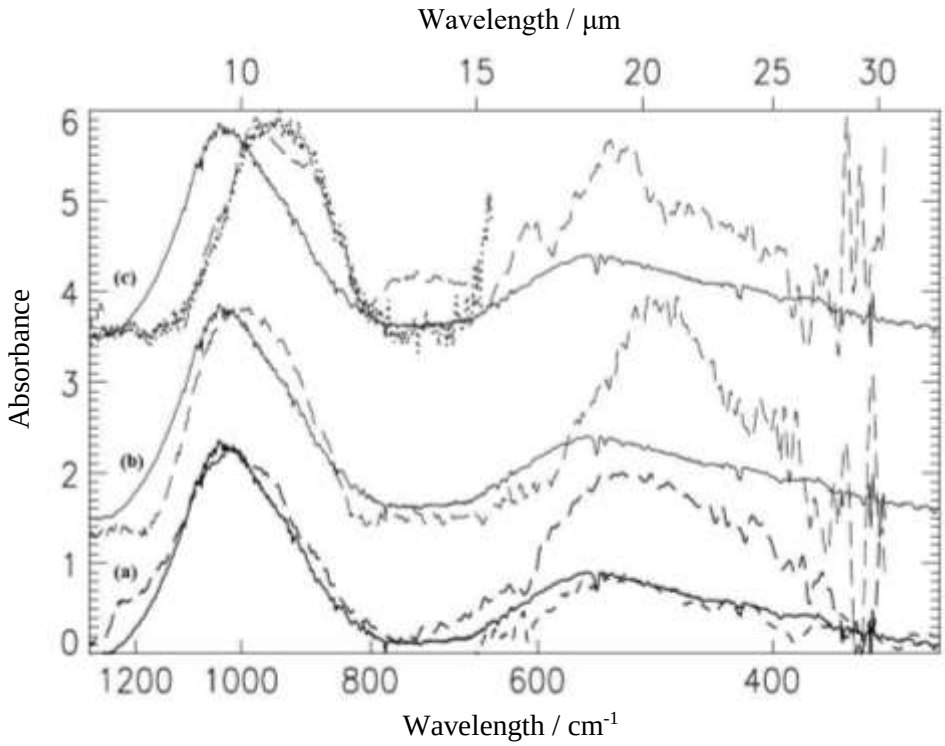

Figure 1.15: Comparing the continuum ISO-SWS spectrum of the Galactic Centre (GC–IRS3) continuous line with the spectra of the irradiated samples: (**a**) enstatite, (**b**) diopside and (**c**) olivine (the dotted line) (Reproduced from [115]).

1.2.4 Outstanding Questions about Dust

The composition of interstellar dust remains controversial, since meteorites provide us with specimen grains, which can be examined. Because these samples are subject to severe selection effects, they cannot be considered to be representative of interstellar grains. The main sources of information on the composition of interstellar dust come from spectral features in extinction, scattering or emission. However, the NASA Stardust mission shed some further light on the composition and origins of the grains [126]. However, there are a number of unsolved or partially solved problems in relation to interstellar dust, as listed below:

1. What is the source and nature of the Diffuse Interstellar Bands?
2. Which carrier is responsible for the 217.5 nm extinction hump?
3. How did dust first form in the galaxy? And what is the composition and size of dust in extragalactic environments?
4. What size are the larger dust grains that appear to be larger than 0.25 μm?

5. How does the dust evolve in protostellar regions?
6. What information will be revealed by analysing comet nuclei and dust material?
7. What are the sources and sinks of interstellar dust? What is the exact composition of interstellar grains? Are they made in the cold ISM or are the silicate cores just stardust (acting as condensation seeds)?

A number of new observational facilities are becoming available [113], including the Atacama Large Millimeter Array (ALMA), the Far Infrared and Sub-millimetre Telescope (FIRST), the James Web Space Telescope (JWST), the Space Infrared Telescope Facility (SIRTF) and the Sub-millimetre Wave Astronomy Satellite (SWAS). These will help to answer some of the outstanding questions relating to dust.

1.3 Ices in the ISM

1.3.1 Origin and Composition of Ices

In order to understand the formation and evolution of interstellar ices, it is important to consider the environment in which the ices are formed, dense molecular clouds. The ISM is an inhomogeneous distribution of gas and dust. The densest regions of the ISM are its cores, where the density is large enough to lead to gravitational collapse, resulting in the formation of new stars and planets [127, 128]. These collapsing regions are fed from vast molecular clouds which provide shielding from the interstellar UV field, creating the conditions allowing for the formation of interstellar ices on cold dust grains. These low temperatures allow atoms to accrete, move around on the surface and form new molecules [129]. The shielding provided to the dust grains by molecular clouds allows molecules to accumulate on the grains and hence form mantles of interstellar ice, **Figure 1.16**.

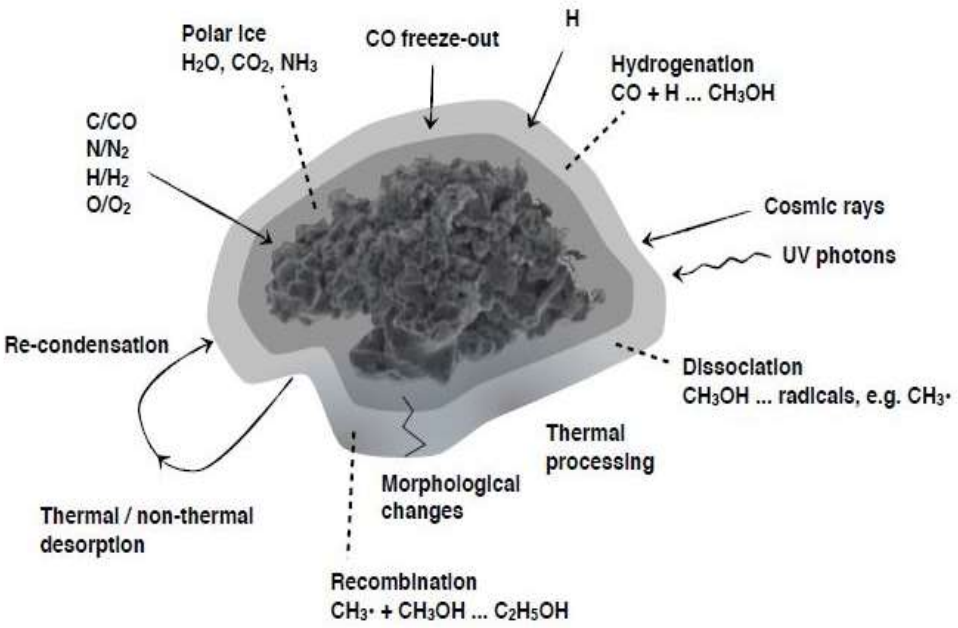

Figure 1.16: Processes in and on interstellar ices (Reproduced from [129]).

The physical conditions in the ambient gas determine the composition of interstellar ice. For example, carbon arrives on dust grains in the form of CO. Other elements can either arrive in atomic or molecular form. At low temperatures, typically around 10 K, the atoms move on to the dust grain surface and find other atoms and molecules with which to react. In the case of H, it can do so by quantum mechanical tunnelling [130]. While heavier atoms such as O, N and C do so *via* the process of thermal mechanical hopping. The subsequent ice layer forms as a result of simple atom addition reactions *via* the L-H mechanism. The molecular composition of pristine interstellar ices is dominated by H_2O, with considerable amounts of CO, NH_3, hydrogen peroxide (H_2O_2), CO_2, nitrogen (N_2) and methanol (CH_3OH) [131].

Many observations of ices in the ISM have been reported [132-137]. **Figure 1.10** shows the ice composition towards a dust-embedded high massive young stellar object (YSO) W33A, which was obtained using the infrared space observatory (ISO). The spectrum shown in **Figure 1.10** is typical of interstellar ice and shows silicate features from the dust as well as from small molecules frozen as the interstellar ice [138]. CH_3OH is one of the more common ice components with abundances varying from 2 to 15% relative to H_2O [134, 137]. CH_3OH forms on the cold dust grains through successive hydrogenation of CO [131, 139-142], and is considered an

important intermediate in the production of complex organic molecules in star-forming regions [143-146].

The ice mantles covering interstellar dust grains are inhomogeneous in their composition. Species with relatively low volatility accumulate more readily on the grain surface than those with high volatility. As the cloud collapses and the density and shielding gradually increase, the dust will first gain a polar layer dominated by H_2O, followed by CO freeze-out into a separate apolar layer [147, 148]. Most of the CO_2 forms simultaneously with H_2O on the grain [149]; this process is considered responsible for the presence of pure CO_2 in interstellar ices [135, 149, 150].

Various ideas have been put forward to explain how ice molecules are returned to the gas phase. This includes grain heating by cosmic rays, mantle explosions, injection upon chemical reactions, sputtering through low velocity shockwaves and grain-grain collisions [151-156]. While most of the features observed in ices can be explained by non-energetic surface reactions, there is some evidence that interstellar ices are subject to energetic processing. In the case of XCN, the features around 4.2 μm [150] can be attributed to OCN^- formed by UV photolysis, ion bombardment and or thermal reactions [157-161].

Interstellar ices are not shielded from cosmic rays, which can penetrate deep into molecular clouds. Cosmic rays can directly interact with ice, and they can generate an internal UV field in the cloud through secondary electron excitation of H_2 [162, 163]. The resulting flux of photons (around 10^3 photons cm^{-2} s^{-1}), though smaller than in the unshielded regions outside the cloud, is still strong enough to promote photochemistry in the ice. Cosmic rays and UV photons can both break bonds in the molecules forming the ice. This leads to the production of highly reactive radicals. These can recombine directly to reform the parent species, or are left with enough energy to relocate and react with another molecule. Radicals can also become trapped in the ice, and are therefore immobilised, until further changes in conditions occur. In the early phase of cloud collapse, molecules and atoms radiatively cool the cloud [164]. As the cloud increases in density, the energy can no longer escape, leading to the heating of the ices in the surrounding envelope. As a consequence of the rising temperatures for the ice, these trapped radicals can become mobile and subsequent recombination into larger, complex organic molecules can occur [145].

1.3.2 Morphology of Interstellar Ices – Amorphous *versus* Crystalline Phases of Ices

The importance of ice in the interstellar medium is indisputable. Interstellar processes influence the structure, composition and evaporation of ices. Observations of ices, and gas which is evaporated from them, are direct probes of the physical conditions in the interstellar medium. Hence ices can trace the evolution of material, and can also shed light on essential processes, including the formation of solar systems like our own. Due to strong hydrogen bonding in H_2O-rich ISM ices, the sticking of small icy dust grains may be enhanced. Porous ice structures can dissipate collisional energy, hence they facilitate aggregation at high velocities. This can help promote coagulation and the formation of larger planetary system bodies and planetesimals.

Interstellar ices are also vital stores of complex, potentially prebiotic, organic molecules and so have a bearing on the origins of life. Indeed, it is possible that icy comets may have delivered volatile organic material for the prebiotic soup from which life arose on the early Earth while also generating the oceans [129]. Thus, the composition and physical structure in interstellar ice is key to our understanding of the formation of stars, planets and the origins of life.

H_2O dominates ices in the ISM [132,134,165,166], while in the gas phase H_2O has abundances varying from 10^{-8} (with respect to H_2) in cold dense regions, where most of it resides in ices on dust grains, to 10^{-4} in warm gas in shocked regions where ices evaporate or are sputtered [167-169]. The H_2O abundances observed in the ISM cannot be reproduced by the gas-phase chemistry. Rather the formation of H_2O though several different grain-surface routes has been proposed by Tielens and Hagen [131]. These routes have been the subject of a number of studies, both theoretical and experimental, in recent times [129]. The hydrogen-bonding character governs the morphology of H_2O. Thus, depending on the pressure and temperature conditions H_2O can exist in 15 different forms, with each form differentiated by the degree of crystalline structure, ordering and density. In astronomical environments, the majority of H_2O observed is in an amorphous form as deduced from the shape of the broad absorption feature at around 3.7 μm, corresponding to the bulk asymmetric O-H stretching (ν_3) mode. This amorphous solid water (ASW) exhibits a tetrahedral

H-bonding network, but lacks long-range crystalline order. This disordered structure provides a broad range of trapping sites, making the absorption features broad. The ASW can be divided into three distinct structures, defined by the number and location of adjacent O atoms [129]:

1. Low density ASW with density of 0.94 g cm^{-3}.
2. High density ASW with density of 1.17 g cm^{-3}.
3. Very high density ASW with density of 1.26 g cm^{-3}.

In the ISM, where particles land on the dust grains in random trajectories and on cold surfaces (<130K), diffusion is limited. Newly deposited particles become incorporated into the ice near their landing site. As a result, for H_2O, this hit-and-stick (ballistic) film growth results in a porous ice structure [170, 171]. Porous ASW (p-ASW) when compared with compact ASW (c-ASW) (**Figure 1.17**) has nm-sized cavities with an internal surface area from hundreds to thousands of m^2/g^{-1} [172-176]. The level of porosity of ASW depends on the growth conditions, including temperature, growth rate and directionality of H_2O molecules landing on the ice surface [151, 177-180].

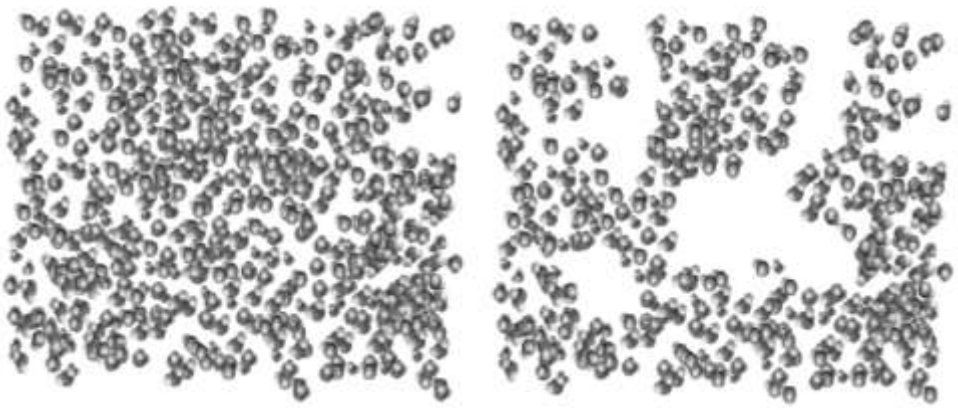

Figure 1.17: Illustration of compact (left) and porous (right) amorphous solid water (Reproduced form [129]).

The compaction of porous ASW has been experimentally demonstrated to be driven by cosmic rays and UV photons [181-183]; and thermal processing [184, 185]. In the ISM, porosity can have a major impact on the chemical processes relying on surface accessibility. Porous ices provide large effective areas for adsorption of atoms and

molecules, catalysis of chemical reactions, and further retention of these species. The pores store large quantities of molecules, and they are later thermally released [184, 185]. The structural changes in the interstellar ices can have some interesting consequences for the chemistry. Pore collapse at low temperature could drive diffusion-limited recombination of radicals trapped in interstellar ices [186, 187]. The band profiles of molecules trapped in interstellar ices can provide an abundance of information about the composition of the ice. The strength of the molecular bonds is influenced by the lattice environment and the vibrational frequencies become shifted from the corresponding gas phase values. The existence of multiple trapping sites is seen by the overall broadening of absorption features. Therefore the composition of interstellar ice can be inferred from the shape of the observed absorption features. Certain ice features can also be influenced by the shape of grain. However, this may complicate the interpretation of the ice composition, but it can be used as an indication of how the ice layer has been formed [131]. Laboratory studies have focused on the characterisation of the band profiles of abundant ices species, and in particular those of CO_2 and CO [188, 189]. Combining laboratory spectra and observations of these features towards icy sources has revealed the presence of CO in numerous solid environments, namely pure CO-CO_2-containing or crystalline CO and CO in polar, possibly H_2O-rich, environments [190]. In the case of CO_2, comparisons with laboratory spectra and with observations imply the co-existence of both H_2O-rich and H_2O-poor, along with pure H_2O [150, 191]. The molecular environment has a restraining effect on the chemical correlations between different molecules, along with formation processes of the ices.

The existence of abundant pure CO components supports its freeze-out separate from other components. Where CO is closely mixed with CO_2, it supports the chemical correlation between the two. In the case of CO_2, the existence of a pure component is taken as evidence of thermal processing, which isolates it from its native H_2O-rich environment [192, 193]. The lattice structure of a particular ice composition changes with ice morphology, which can provide further information into the thermal history of the ice. The absorption features in a crystalline (*e.g.* ordered) structure are typically narrower than those in an amorphous (*e.g.* disordered) structure [194,195]. The difficulty in understanding the astronomical ice features is complicated by a combination of the above, along with the fact that an observational spectrum along a

given line of sight typically contains several ice compositions at different evolutionary stages. Additionally, not all the band profiles have been assigned to a specific molecule in a specific molecular and morphological environment. Hence the interpretation of the observed features which vary in ice composition and morphology present a challenge in trying to reproduce interstellar ices in the laboratory.

1.4 Small Molecules on Grains and in Ices

Dust plays a key role in astrochemistry in aiding molecule formation, so the surface physics and chemistry of dust grains must also play a vital role. The interaction of molecular species with surfaces is of vital importance in astrophysical environments. A great deal of interstellar chemistry takes place within or on the ice layers, where the ice layers cover the dust grains in molecular clouds, within which stars and planets are created. However, the surface physics and chemistry of these dust grains is not well understood, hence there is a need to build grain models and probe their surfaces for comparison against observations using small molecules. Temperature programmed desorption (TPD) can be used to investigate the interaction of small molecules including ammonia (NH_3) and methanol (CH_3OH) with amorphous solid water (ASW), crystalline solid water (CSW) and carbon monoxide (CO) films, as an example of the characteristic ice surfaces present in the interstellar medium. Small, abundant molecules such as CO, O_2, N_2 and H_2O can be used to investigate the nature of the surfaces of grain mimics at sub-monolayer coverages where the interactions between the adsorbates and the surface dominate [26, 196]. Gas-grain interactions are becoming increasingly recognised as key to the physics and chemistry of the ISM [197-199]. These heterogeneous interactions rely on key parts of the gas-solid interaction, including the nature of the binding sites, binding energies in those sites, along with the rates of the surface diffusion. The composition of interstellar grains is described in **Section 1.2.3**. However, the nature of grain surfaces is not fully understood [200].

1.4.1 Water

The existence of water (H_2O) ice in the interstellar medium has been hypothesised over a number of decades before its detection *via* the solid state on the 3.07 μm O-H stretching absorption band. Water is the main component of interstellar ices [199], while CO_2, CO and CH_3OH are the other main building blocks [134,136,201,202]. H_2O ice is a vital solid constituent of many astrophysical environments. In order to fully understand the role of H_2O ice in the chemistry and evolution of dense molecular clouds along with comets, it is vital to understand freeze-out, potential surface reactivity and desorption mechanisms of these molecular systems. There is a need within the astronomical modelling community for accurate empirical data regarding these processes, and so there have been a number of studies regarding H_2O ices [187, 198, 203-205]. Atomic hydrogen-related chemistry studying interstellar dust grain surfaces plays a vital role in the chemical evolution of the ISM. Since H is by far the most abundant atomic species in the universe, it is involved in reactions producing numerous molecules which play a key role in physical and chemical processes [206]. The majority of grain surface reactions within the ISM rely on hydrogen in a direct or indirect way. H_2O formation is an example of such a vital reaction. H_2O is a coolant and tracer in gravitation cloud collapses [207, 208], and is the main component of ices coating dust grains which are a source of chemical enrichment to many space environments, including dense clouds and protoplanetary disks [209, 210]. Gas-phase reactions by themselves cannot account for the abundance of water in the ISM [211, 212]. H_2O is thought to be mainly formed on the surface of interstellar grains. Tielens and Hagen [131] suggested there are three routes to forming H_2O, by the hydrogenation of O atoms, O_2 and ozone (O_3) on grain surfaces. The first and simplest pathway which leads towards the formation of solid H_2O is *via* the sequential hydrogenation of O atoms:

$$O(ads) + H(ads) \rightarrow OH(ads) \qquad \textbf{(R23)}$$

$$OH(ads) + H(ads) \rightarrow H_2O(ads) \qquad \textbf{(R24)}$$

Reaction 23 has been suggested as the foremost route for the formation of H_2O in diffuse and translucent clouds, in which H atoms are more widespread than H_2O

molecules [213]. The second simple pathway involves the sequential hydrogenation of O_2 *via* the formation of hydrogen peroxide (H_2O_2):

$$O_2(ads) + H(ads) \rightarrow HO_2(ads) \quad \textbf{(R25)}$$

$$HO_2(ads) + H(ads) \rightarrow H_2O_2(ads) \quad \textbf{(R26)}$$

$$H_2O_2\ (ads) + H(ads) \rightarrow H_2O(ads) + OH(ads) \quad \textbf{(R27)}$$

It has been demonstrated experimentally that **Reactions 25-27** above occur at 10 K [214]. The final route for the formation of H_2O is *via* sequential hydrogenation of O_3 and this is likely to occur in molecular clouds:

$$O_3(ads) + H(ads) \rightarrow O_2(ads) + OH(ads) \quad \textbf{(R28)}$$

where the products O_2 and OH are likely to be used further for H_2O formation [215]. In each of the pathways discussed, OH is always produced before the formation of H_2O. Besides the H-related reactions shown above, **Reaction 29** results in the formation of H_2O:

$$OH(ads) + H_2(ads) \rightarrow H_2O(ads) + H(ads) \quad \textbf{(R29)}$$

where the activation barrier is around 2100 K in the gas phase [216]. Even with such a large activation barrier, **Reaction 29** may produce H_2O on grain surfaces in dense molecular clouds. Here temperatures are above 10 K, with a very low UV flux, and H_2 is the main H-bearing species in the gas phase [27, 131, 217]. At low temperatures, below 10 K, reactions with an activation barrier of around 200 K occur only rarely, thus **Reaction 29** needs quantum mechanical tunnelling in order to proceed on grain surfaces. This has been observed in gas phase reactions at low temperatures [218].

1.4.2. Carbon Monoxide

Carbon monoxide (CO) and H_2O are two of the most frequently detected molecules in the solid phase in molecular clouds in the ISM [219]. H_2O is the most abundant molecule in interstellar ices, followed by CO, which is readily accessible with ground-based telescopes [220]. CO spectroscopy is sensitive to its environment and is widely used in probing both the gas phase and solid state in astrophysical

environments. This makes CO a highly popular species for observations of interstellar ices [190]. In addition to these observations, CO has been widely studied in laboratory astrophysics experiments. Indeed, the mid-infrared spectrum of CO has been measured for a range of astrophysically relevant mixtures along with solid CO over a range of temperatures in films with varied thermal histories [221]. It accretes on dust grains around 20 K and plays a vital role in solid-state astrochemical processes, where it can be the starting point in hydrogenation reactions resulting in the formation of formaldehyde and methanol [222]. Solid interstellar CO was originally observed by Soifer *et al.* [223**]** with an absorption band around 2139 cm^{-1}. Laboratory experiments have demonstrated that CO molecules can be mixed with molecules able to form hydrogen bonds, including H_2O, NH_3 and CH_3OH, and which are sometimes referred to as 'polar' ices. Alternatively, CO can be mixed with molecules which participate in van der Waals-type interactions, including CO itself, along with CO_2 and possibly N_2 and O_2, which are referred to as 'non-polar' ices [197, 206]. CO has been detected in dense molecular clouds in the gas phase, along with icy mantles [200, 224, 225] coating interstellar dust grains, with abundances of about 10^{-4}, and has also been detected in diffuse clouds [226]. CO is detected at 4.67 µm *via* the C-O stretch, and along with H_2O typically comprises more than 90% of the icy mantles which accrete on grains in dense clouds [227]. Thus understanding the physics and chemistry of H_2O along with CO is vital in developing a greater understanding of the part these icy grains play in the physical and chemical evolution of their host clouds. Laboratory experiments can contribute to this and other discussions regarding ices, as long as they can mimic the conditions observed astronomically, along with appropriate simplifications.

1.4.3 Methanol

Methanol (CH_3OH) is a key interstellar molecule and a vital precursor to the formation of larger species. Along with its precursor formaldehyde (H_2CO), CH_3OH is one of the most widely studied organic molecules in the ISM. CH_3OH has been observed abundantly in both the gas phase and solid state [46,228-234]. CH_3OH is typically found in water-rich interstellar ices frozen out on the surface of dust grains [235-237]. Since CH_3OH has a lower gas phase abundance in molecular clouds, it is thus more likely to be formed on the surface of dust grains rather than freezing out

after formation in the gas phase. Oberg *et al*. [146] demonstrated that UV irradiation of CH_3OH results in the molecule breaking apart into fragments, which can recombine to form complex organic molecules (COM). Hence in UV-rich environments in the ISM, the formation of CH_3OH is vital in the formation of larger COMs.

The most efficient method of CH_3OH formation is *via* solid-state interactions with icy grain mantles. A number of models which have been supported by experimental data show that gas-phase synthesis of methanol results in abundances greatly below those of the observed fractional abundance of CH_3OH [196, 238]. Thus, CH_3OH synthesis in the gas phase and subsequent accretion on the grain mantle is regarded as miniscule. CH_3OH has a greatly reduced gas-phase abundance in molecular clouds and in solid state [238]. Equally, studies show that methanol is formed in CO-rich ices *via* sequential hydrogenation of CO *via* a four-step process [142, 239-241] in which the reactions involving CO and H_2O have a small action energy barriers.

$$CO(ads) + H(ads) \rightarrow HCO(ads) \quad \textbf{(R30)}$$

$$HCO(ads) + H(ads) \rightarrow H_2CO(ads) \quad \textbf{(R31)}$$

$$H_2CO(ads) \rightarrow H_2COH(ads) \quad \textbf{(R32)}$$

$$H_2COH(ads) \rightarrow CH_3OH(ads) \quad \textbf{(R33)}$$

This mechanism is supported by various computational models showing that hydrogenation of CO ices results in the production of CH_3OH [199, 242].

1.4.4 Ammonia

NH_3 is a vital building block of biologically important molecules including amino acids and proteins, as well as being a valued condensable species in the Solar System [243]. NH_3 has become a vital spectroscopic tool in the study of the ISM. Due to a considerable number of transitions sensitive to a wide range of excitation conditions, and since NH_3 can be detected in a wide range of regions, it is regarded as second only to CO in terms of importance. As a gas phase probe molecule, NH_3 has a number of advantages including [244]:

1. It exists in considerable abundance and this makes it readily detectable in surveys of various regions [245, 246].
2. It possesses a number of transitions lying within a narrow frequency range. Thus direct comparisons of different lines with the same antenna can be used to infer rotational temperatures between different *K*-ladders (states with the same value of *K*, the principal rotational quantum number).
3. Inversion lines are split by hyperfine interactions, allowing for comparisons of lines of known but different relative optical depths where the main hyper-fine splitting is that of the electronic quadrupole moment of the N nucleus interacting with the electric field resulting from the electrons.

There are a number of properties making NH_3 of particular interest in terms of astrophysical conditions, including the existence of metastable and non-metastable states, ortho-and para-species, inversion motion of the molecule and hyperfine structures. The rotational energy of NH_3 is a function of the two principal quantum numbers (*J*, *K*); *J* is the total angular momentum and *K* is the projection along molecular axis. Due to the possible orientation of hydrogen spins, there are two distinct forms of NH_3, ortho-NH_3 ($K = 3n$, in which *n* is an integer and H spins parallel) and para-NH_3 ($K \neq 3n$, all H spins not parallel) [247]. Ammonia (NH_3) is a widely observed interstellar molecule and was initially detected by Cheung *et al*. [248] in 1968. It has since been observed in a range of astronomical environments including circumstellar shells [243], galaxies [249] and giant molecular clouds where observations can assist in determining the physical conditions and structure of dark clouds. However, NH_3 is a poor probe of ice environments as its solid state spectra are hard to distinguish from those of solid H_2O. A summary is given below of the characteristics of the different regions containing ammonia:

1. Molecular clouds: NH_3 is widespread and with an abundance relative to hydrogen 10^{-8} to 10^{-7}. A number of surveys have looked at supporting the correlation between high-density molecular concentrations present in NH_3 and the presence of extremely young, newly formed stars ($< 10^6$ years old) [250, 251]. NH_3 observations demonstrate that it is a cold gas

with temperatures of 10 - 20 K. Additionally, the observations identify cold dense clumps (10^4 cm^{-3}) typically associated with young stars which are in the contraction phase and progressing towards becoming a Solar-type star. Thus NH_3 cores are thought of as the sites for the future generation of young stars.

2. Masers: NH_3 masers are rare within the ISM and ammonia is a useful temperature probe since its population distribution between the levels is generally well behaved. A number of maser emissions have been observed and population inversion has occurred in which the most dominant ammonia maser is NH_3 [252].
3. Circumstellar envelopes: NH_3 has been found in a small number of theses envelopes [253-255]. All the observed envelopes in which ammonia was detected are losing mass rapidly and are in the final stages of their evolution before becoming planetary nebulae. Estimated abundances for NH_3 are between 10^{-5} and 10^{-8} relative to H. NH_3 has been observed in both C and O-rich circumstellar envelopes.

1.5 Thesis Overview

The main focus of this thesis is looking at desorption of CO from a range of astrophysically relevant environments. Emphasis is given to investigating adsorbate-surface interactions by temperature programmed desorption through the pre-exponential factor (ν_{des}) and activation energy (E_{des}) for desorption. An overview and content for the remaining chapters is set out below:

- **Chapter 2** will focus on the experimental equipment, theory and methods used to obtain the results presented in each chapter.

- **Chapter 3** will focus on the design, construction and initial results from a UV/visible reflection-absorption spectrometer which is used to determine the complex refractive index, $\hat{n}$, and the thickness, d, of ice films. Preliminary results are presented for benzene (C_6H_6) ices on a highly-orientated pyrolytic graphite (HOPG) surface.

- **Chapter 4** presents the adsorption of Methyl Formate ($HCOOCH_3$) on an amorphous silica ($aSiO_2$) substrate. This includes the use of reflection–absorption infrared spectroscopy (RAIRS) to investigate the Spontelectric Effect in $HCOOCH_3$.

- **Chapter 5** reports on the results of probing the surface heterogeneity of $aSiO_2$ using coverage dependent temperature programmed desorption (TPD) using CO as probe molecule. First, there is discussion of how the interaction energies are used in an environmentally broadened vibrational line profile synthesis. This is followed by simulations of line profiles, which are compared against measured lines profiles obtained RAIRS, for CO on $aSiO_2$ and on porous amorphous solid water (p-ASW).

- **Chapter 6** reports on the experimental results for adsorption of CO on CH_3OH, c-ASW (compact amorphous solid water), CSW (crystalline solid water) and NH_3 (ammonia), deposited on an $aSiO_2$ substrate. Firstly, there is a discussion of the different methods which can be used to calculate the pre-exponential factor in TPD. This is followed by details of how the Extended Inversion Analysis is carried out, allowing the calculation of the pre-exponential factor and activation energy for desorption (E_{des}).

- **Chapter 7** will summarise the conclusions from **Chapter 3, 4, 5** and **6** discussing various possible future directions for work.

1.6 References

[1] D. H. Wooden, S. B. Charnley and P. Ehrenfreund, *From the interstellar medium to comet particles and molecules*, (University of Arizona Press, Tucson, 2004).

[2] B. E. Turner, *Astrophys. J.*, 2000, **542**, 837.

[3] A. P. Jones, *Phil. Trans. R. Soc.*, 2001, **A359**, 1961.

[4] C. Chiappini, D. Romano and F. Matteucc, *Annu. Rev. Astron. Astrophys*., 2003, **339**, 68.

[5] C. J. Wheeler, C. Sneden and J. W. J. Truran, *Annu. Rev. Astron. Astrophys.*, 1989, **27**, 279.

[6] C. F. McKee and J. P. Ostriker, *Astrophys. J*., 1977, **218**, 148.

[7] P. F. Goldsmith and W. D. Langer, *Astrophys. J*., 1978, **222**, 881.

[8] A. P. Jones, A. G. G. M. Tielens, D. J. Hollenbach and C. F. McKee, *Astrophys. J*., 1994, **433**, 797.

[9] A. P. Jones, A. G. G. M. Tielens and D. J. Hollenbach, *Astrophys. J*., 1996, **469**, 740.

[10] A. P. Jones, *J. Geophys. Res.*, 2000, **105**, 10257.

[11] A. G. G. M. Tielens, *Astrophys. J*., 1998, **499**, 267.

[12] https://www.eso.org/public/images/eso1209d/ (last accessed 8/11/18).

[13] R. Lucas and H. S. Liszt, *Astrophys. J.*, 2000, **358**, 1069.

[14] W. D. Langer, E. F. van Dishoeck, E. A. Bergin, G. A. Blake and A. G. G. M. Tielens., *Chemical evolution of protostellar matter*. In *Protostars and Planets IV*, (University of Arizona, Tucson, 2000).

[15] P. M. Solomon, K. B. Jeerts, A. A. Penzias and R. W. Wilson, *Astrophys. J.*, 1971, **168**, L107.

[16] B. L. Ulich and E. K. Conkling, *Nature*, 1974, **248**, 121.

[17] L. E. Snyder and D. Buhl, *Astrophys. J.*, 1971, **163**, 147.

[18] J. M. C. Rawlings, D. A. Williams, S. Viti and C. Ceechi-Pestellini, *Mon. Not. R. Astron. Soc.*, 2013, **430**, 264.

[19] University of Manchester Institute of Science and Technology (UMIST), (http://www.udfa.net/ last accessed 8/11/18).

[20] J. Woodall, M. Agundez, A. J. Markwick-Kemper and T. J. Millar, *Astron. Astrophys.*, 2007, **466**, 1197.

[21] G. C. Clayton, M. J. Wolf, U. J. Sofia, K. D. Gordon and K. A. Misselt, *Astrophys. J.*, 2003, **588**, 871.

[22] C. Ceechi-Pestellini, J. M.C. Rawlings, S. Viti and D. Williams, *Astrophys. J.*, 2010, **725**, 1581.

[23] R. Carbo and A. Ginebreda, *J. Chem. Edu.*, 1985, **62**, 832.

[24] N. Murray and M. Rahman, *Astrophys. J.*, 2010, **709**, 424.

[25] I. Cherchneff and A. Glassgold, *Astrophys. J.*, 1993, **419**, L41.

[26] D. A. Williams and S. D. Taylor, *Q. J. R. Astron. Soc.*, 1996, **37**, 565.

[27] A. G. G. M. Tielens, *The Physics and Chemistry of the Interstellar Medium*, (University Press Cambridge, Cambridge, 2005).

[28] N. Murray and M. Rahman, *Astrophys. J.*, 2010, **709**, 424.

[29] J. C. Evertt and E. G. Zweibel, *Astrophys. J.*, 2011, **739,** 60.

[30] D. Hollenbach and E. E. Salpeter, *J. Phys. Chem.*, 1970, **53**, 79.

[31] F. Palla, E.E. Salpeter and S. W. Stahler, *Astrophys. J.*., 1983, 271, 632.

[32] Y. M. San, *J. Chem. Phys.*, 1998, **108**, 10231.

[33] E. G. Zweibel, *Phys. Plasma.*, 2013, **20**, 055501.

[34] A. M. Shaw, *Astrochemistry; From Astronomy to Astrobiology*, (Wiley, Chichester, 2006).

[35] G. E. Morfill, *Astrophys. J.*, 1982, **262**, 749.

[36] D. Flower, *Molecular Collisions in the Interstellar Medium, 2nd Edition* (Cambridge University Press, Cambridge, 1997).

[37] https://curator.jsc.nasa.gov/stardust/interstellardust.cfm (last accessed 9/11/18).

[38] E. M. Bringa, S. O. Kucheyev, M. J. Loeffler, R. A. Baragiola, A. G. G. M. Tielens, Z. R. Dai, G. Graham, S. Bajt, J. P. Bradley, C. A. Dukes, T. E. Felter, D. F. Torres and W. van Breuge, *Astrophys. J.*, 2007, **662**, 1.

[39] https://www.schoolsobservatory.org/learn/astro/stars/cycle (last accessed 13/1/19).

[40] http://www.astro.cornell.edu/academics/courses/astro201/hrdiagram.htm (last accessed 9/11/18).

[41] http://www.univie.ac.at/agb/agbdetail.html (last accessed 9/11/18).

[42] L. J. Allamandola, D. M. Hudgins and S. A. Sandford, *Astrophys. J.*, 1999, **511**, L115.

[43] R. A. Bernstein, W. L. Freedman and B. F. Madore, *Astrophys. J.*, 2002, **571**, 107.

[44] (a) https://apod.nasa.gov/apod/ap141214.html (last accessed 1/11/19); (b) https://www.eso.org/public/images/eso9934a/ (last accessed 2/1/19).

[45] http://www.astronomy.ohio-state.edu/~pogge/Ast871/Notes/Dust.pdf (last accessed 9/11/18).

[46] B. Turner, *Astrophys. J.*, 1998, **501**, 731.

[47] C. D. Ferandes, D. Johnson, J. C. Bridges and M. Grady, *Int. J. Astrobiol.*, 2006, **5**, 287.

[48] I. Mann., *Asteroids, Comets, and Meteors, Proceedings of the 229th Symposium of the International Astronomical Union*, (Cambridge University Press, Cambridge, 2005) pp.41.

[49] R. J. Trumpler, *Publ. Astron. Soc. Pacif.*, 1930, **42**, 214.

[50] J. S. Hall, *Astrophys. J.*, 1937, **85**, 145.

[51] J. Stebbins, C. M. Huffer and A. E. Whitford, *Astrophys. J.*, 1939, **90**, 209.

[52] J. L. Greenstein, *Harvard Obs. Circ.*, 1938, No.422.

[53] F. Boulanger and M. Perault, *Astrophys. J.*, 1988, **330**, 96.

[54] T. Onaka, I. Yamamura, T. Tanabe, T. L. Roellig and L. Yuen, *Pubi. Astron. Soc. Japan.*, 1996, **48**, L59.

[55] M. Tanaka, *Pubi. Astron. Soc. Japan.*, 1996, **48**, L53.

[56] A. Leger and J. L. Puget, *Astron. Astrophys.*, 1984, **137**, L5.

[57] L. J. Allamandola, A. G. G. M. Tielens and J. R. Barker, *Astrophys. J*, 1985, **290**, L25.

[58] B. T. Draine and A. Li, *Astrophys. J.*, 2001, **551**, 807.

[59] A. P. Jones and L. B. d'Hendecourt, *Astron. Astrophys.*, 2000, **355**, 1191.

[60] W. W. Duley and D. A. Williams, *Mon. Not. R. Astron. Soc.*, 1981, **196**, 269.

[61] W. W. Duley, A. P. Jones and D. A. Williams, *Mon. Not. R. Astron. Soc.*, 1989, **236**, 709.

[62] A. Webster, *Mon. Not. R. Astron. Soc.*, 1993, **264**, 121.

[63] S. Schulz, *The Formation and Early Evolution of Stars: From Dust to Stars and Planets* (Springer-Verlag, Berlin, 2012).

[64] J. S. Mathis, W. Rumpl and K. H. Nordsieck, *Astrophys. J.*, 1977, **217**, 425.

[65] B. T. Draine and H. M. Lee, *Astrophys. J.*, 1984, **285**, 89.

[66] B. T. Draine and N. Anderson, *Astrophys. J.*, 1985, **292**, 494.

[67] J. L. Weiland, *Astrophys. J.*, 1986, **306**, L101.

[68] W. H. Sorrell, *Mon. Not. R. Astron. Soc.*, 1990, **243**, 570.

[69] R. Siebenmorgen and E. Krügel, *Astron. Astrophys.*, 1992, **259**, 614.

[70] M. Rowan-Robinson, *Mon. Not. R. Astron. Soc.*, 1992, **258**, 787.

[71] J. M. Greenberg, in *Cosmic Dust*, Edited by *J.A.M. McDonnell* (Wiley, New York, 1978) pp187.

[72] A. Li and J. M. Greenberg, *Astron. Astrophys.*, 1997, **323**, 566.

[73] G. Chlewicki and R. J. Laureijs, *Astron. Astrophys.*, 1988, **207**, L11.

[74] F. X. Desert, F. Boulanger and J. L. Puget, *Astron. Astrophys.*, 1990, **237**, 215.

[75] A. Li and J. M. Greenberg, *Astron. Astrophys.*, 1998, **339**, 591.

[76] V. G. Zubko, *in Formation and Evolution of Solids in Space*, Edited by. J. M. Greenberg and A. Li (Kluwer, Dordrecht, 1999) pp85.

[77] J. S. Mathis and G. Whiffen, *Astrophys. J.*, 1989, **341**, 808.

[78] E. L. Wright, *Astrophys. J.*, 1987, **320**, 818.

[79] T. P. Snow and A. N. Witt, *Astrophys. J.*, 1996, **468**, L65.

[80] J. S. Mathis, *Astrophys. J.*, 1996, **472**, 643.

[81] U. J. Sofia and D. M. Meyer, *Astrophys. J.*, 2001, **554**, 2.

[82] J. C. Weingartner and B. T. Draine, *Astrophys. J.*, 1999, **517**, 292.

[83] B. T. Draine, *Interstellar Dust, Origin and Evolution of the Elements*, Edited by A. McWilliam and M. Rauch (Cambridge University Press, Cambridge, 2004) pp3317.

[84] T. P. Snow, *Astrophys. J.*, 1975, **202**, L87.

[85] J. A. Cardelli, *Science*, 1994, **265**, 209.

[86] B. T. Draine, *Evolution of Interstellar Dust, in ASP Conf. Ser. 12*, Edited by L. Blitz (ASP, San Francisco,1990) pp193.

[87] A. Li and B. T. Draine, *Astrophys. J.*, 2002, **564**, 803.

[88] F. Molster and C. Kemper, *Crystalline Silicates*, Edited by C. Cesarsky and A. Salama (Springer, Dordrecht, 2004).

[89] J. Bouwman, G. Meeus, A. deKoter, S. Hony, C. Dominik and L. B. F. M. Waters, *Astron. Astrophys.*, 2001, **375**, 950.

[90] E. Dwek, J. Staghun, R. G. Arendt A. Kovacs, T. Su and D. J. Benford, *Astrophys. J.*, 2014, **788**, L30.

[91] P. Abraham, A. Juhasz, C. P. Dullemond, A. Kospal, R. Van Boekel, J. Bouwman, T. Henning, T. Csengeri, C. Grady, M. Goto, Z. Regaly, M. van den Ancker, J. Brown and A. Carmona, *Nature*, 2009, **459**, 224.

[92] B. T. Draine, *Annu. Rev. Astron. Astrophys.*, 2003, **41**, 241.

[93] A. G. G. M. Tielens, L. B. F. M. Waters, F. J. Molster and K. Justtanont, *Astrophys. Space Sci.*, 1998, **255**, 41.

[94] F. J. Molster, L. B. F. Waters and A. G. G. M. Tielens, *Astron. Astrophys.*, 2002, **382**, 222.

[95] F. J. Molster, L. B. F. M. Waters, A. G. G. M. Tielens, C. Koike and H. Chihara, *Astron. Astrophys.*, 2002, **382**, 241.

[96] F. J. Molster, L. B. F. Waters, A. G. G. M. Tielens and M. J. Barlow, *Astron. Astrophys.*, 2002. **382**, 184.

[97] L. S. Spitzer and E. L. Fitzpatrick, *Astrophys. J.*, 1993, **409,** 299.

[98] E. L. Fitzpatrick, *Astrophys. J. Lett.*, 1997, **482**, L199.

[99] J. C. Howk, B. D. Savage and D. Fabian, *Astrophys. J.*, 1999, **525**, 253.

[100] U. J. Sofia and D. M. Meyer, *Astrophys. J. Lett*., 2001, **554,** L221; **558**, L147.

[101] M. Min, L. B. F. M. Waters, A. de Koter, J. W. Hovenier, L. P. Keller and F. Markwick-Kemper, *Astron. Astrophys*., 2008, **486,** 779.

[102] R. D. Gehrz, *Interstellar Dust, In IAU Symposium 135,* edited by L. J. Allamandola and A. G. G. M. Tielens, (Kluwer, Dordrecht, 1989) pp431.

[103] E. Grün, H. A. Zook, M. Baguhl, A. Balogh, S. J. Bame, H. Fechtig, R. Forsyth, M. S. Manner, M. Horanyi, J. Kissel, B.-A. Lindblad, D. Linkert, G. Linkert, I. Mann, J. A. M. McDonnell, G. E. Morfill, J. L. Phillips, C. Polanskey, G. Schwehm, N. Siddique, P. Staubach and J. Svestka and A. Taylor, *Nature,* 1993, **362**, 428.

[104] A. Li, In *Astrophysics of Dust* Edited by A. N. Witt, G. C. Clayton, and B. T. Draine (ASP Conference Series, Paris, 2004) Vol.309, pp417.

[105] D. D. Clayton and L. R. Nittler, *Mon. Not. R. Astron. Soc.*, 2004, **42**, 39.

[106] S. Messenger, L. P. Keller, F. J. Stadermann, R. M. Walker and E. Zinner, *Science.*, 2003, **300**, 105.

[107] J. P. Bradley, *Astromineralogy,* Edited by Th. Henning (Springer, Berlin, 2003) pp217.

[108] E. Grün, B. Å. S. Gustafson, I. Mann, M. Baguhl, G. E. Morfill, P. Staubach, A. Taylor and H. A. Zook, *Astron. Astrophys.*, 1994, **286**, 915.

[109] E. Grün, *Nature,* 1993, **362**, 428.

[110] A. Taylor, W. J. Baggaley and D. I. Steel, *Nature*, 1996**, 380**, 32.

[111] P. C. Frisch, *Astrophys. J.*, 1999, **525**, 492.

[112] J. C. Weingartner and B. T. Draine, *Astrophys. J.*, 2001, **548**, 296.

[113] A. Li, *Interstellar Grains- The 75th Anniversary*: *Light, Dust and Chemical Evolution*, Edited by F. Borghese and R. Saija (Journal of Physics: Conference Series, Italy, 2005).

[114] K. Demyk, Ph. Carrez, H. Leroux, P. Cordier, A. P. Jones, J. Borg, E. Quirico, P. I. Raynal and L. d'Hendecourt, *Astron. Astrophys.*, 2001, **368**, 38.

[115] K. Demyk, L. d'Hendecourt, A. Jones, H. Leroux, Ph. Carrex and P. Cordier, in *Astrophysics of Dust,* Edited by A. N. Witt, G. C. Clayton and B. T. Draine (ASP Conference Series, Paris, 2004) Vol. 309, pp239.

[116] J. M. Shull and D. York, *Astrophys. J.*, 1977, **211**, 803.

[117] J. C. Wheeler, T. J. Mazurek and A. Sivaramakrishnan, *Astrophys. J.*, 1980, **237**, 781.

[118] J. S. Mathis, *Ann. Rev. Astron. Astrophys.*, 1990, **28**, 37.

[119] L. Colangeli, Th. Henning, J. R. Brucato, D. Clement, D. Fabian, O. Guillois, F. Huisken, C. Jager, E. K. Jessberger, A. Jones, G. Ledoux, G. Manico, V. Mennella, F. J. Molster, H. Mutschke, V. Pirronello, C. Reynaud, J. Roser, G. Vidali and L. B. F. M. Waters, *Astron. Astrophys. Rev.*, 2003, **11**, 97.

[120] J. S. Mathis, *Astrophys. J.*, 1998, **497**, 824.

[121] K. Demyk, E. Dartois, H. Wiesemeyer, A. P. Jones and L. d'Hendecourt, *Astron. Astrophys.*, 2002, **364**, 170.

[122] F. Kemper, A. de Koter, L. B. F. M. Waters, J. Bouwman and A. G. G. M. Tielens, *Astron. Astrophys.*, 2002, **384**, 585.

[123] J. E. Bowey, A. J. Adamson and D. C. B. Whittet, *Mon. Not. R. Astron. Soc.*, 1998, **298**, 131.

[124] J. Dorschner, C. Friedemann, J. Gürtler and T. Henning, *Astron. Astrophys.*, 1988, **198**, 223.

[125] K. Demyk, A. P. Jones, E. Dartois, P. Cox and L. D'Hendecourt, *Astron. Astrophys.*, 1999, **329**, 267.

[126] https://stardust.jpl.nasa.gov/news/news110.html (last accessed 1/2/19).

[127] F. H .Shu, F. C. Adams and S. Lizano, *Mon. Not. R. Astron. Soc.*, 1987, **25**, 23.

[128] C. F. McKee and E. C. Ostriker, *Annu. Rev. Astron. Astrophys.*, 2007, **45**, 565.

[129] T. Van. Verkrigging, *Ph.D. Thesis* (University of Leiden, Leiden, 2013).

[130] G. Manicò, V. Ragunì, J.Pirronello, E. Roser and G. Vidali, *Astrophys. J.*, 2001, **548**, 235.

[131] A. G. G. M Tielens and W. Hagen, *Astron. Astrophys.*, 1982, **114**, 245.

[132] E. L Gibb, D. C. B. Whittet, A. C. A. Boogert and A. G. G. M Tielens, *Astrophys. J.*, 2004, **151**, 35.

[133] C. Knez, A. C. A. Boogert and K. M. Pontoppidan, *Astrophys. J.*, 2005, **635**, L145.

[134] A. C. A. Boogert, K. M. Pontoppidan, C. Knez, F. Lahuis, J. Kessler-Silacci, E. F. van Dishoeck, G. A. Blake, S. E. Augereau, J. C. Bisschop and S. Bottinelli, *Astrophys. J.*, 2008, **678**, 985.

[135] K. M. Pontoppidan, A .C .A. Boogert and H. J. Fraser, *Astrophys. J.*, 2008, **678**, 1005.

[136] K. I. Oberg, A. C. A. Boogert and K. M. Pontoppidan, B. Saskia, E. F. van Dishoeck, B. Sandrine, A. B. Georey and N. J. Evans II, *Astrophys. J.*, 2011, **740**, 109.

[137] S. Bottinelli, A. C. A. Boogert and J. Bouwman, *Astrophys. J.*, 2010, **718**, 1100.

[138] E. F. van Dishoeck, *Annu. Rev. Astron. Astrophys.*, 2004, **42**, 119.

[139] A. G. G. M. Tielens and L. J. Allamandola, *Processes in Interstellar Clouds, NATO Science Series C,* Edited by. G. E. Morfill and M. Scholer, (Springer, Dordrecht, 1987) pp161.

[140] K. Hiraoka, T. Sato and S. Sato, *Astrophys. J.*, 2002, **577**, 265.

[141] N. Watanabe and A. Kouchi, *Astrophys. J.*, 2002, **567**, 651.

[142] G. W. Fuchs, H. M. Cuppen and S. Ioppolo, *Astron. Astrophys.*, 2009, **505**, 629.

[143] S. B. Charnley, *Astrophys. J.*, 1997, **481**, 396.

[144] R. T. Garrod and E. Herbst, *Astron. Astrophys.*, 2006, **457**, 927.

[145] R. T. Garrod, S. L. W. Weaver and E. Herbst, *Astrophys. J.*, 2008, **682**, 283.

[146] K. I. Öberg, R. T. Garrod, E. F. van Dishoeck and H. Linnartz, *Astron. Astrophys.*, 2009, **504**, 891.

[147] E. A. Bergin, G. J. Melnick, P. A. Gerakines, D. A. Neufeld and D. C. B. Whittet, *Astrophys. J.*, 2005, **627**, L33.

[148] C. Knez, J. H. Lacy, N. J. Evans, E. F. van Dishoeck and M. J. Richter, *Astrophys. J.*, 2009, **696**, 471.

[149] K. M. Pontoppidan, *Astron. Astrophys.*, 2006, **453**, L47.

[150] P. A. Gerakines, D. C. B. Whittet and P. Ehrenfreund, *Astrophys. J.*, 1999, **522**, 357.

[151] M. S. Westley, G. A. Baratta and R. A. Baragiola, *J. Chem. Phys.*, 1998, **108**, 3321.

[152] E. A. Bergin, D. A. Neufeld and G. J. Melnick, *Astrophys. J.*, 1998, **499**, 777.

[153] S. B. Charnley, S. D. Rodgers and P. Ehrenfreund, *Astron. Astrophys.*, 2001, **378**, 1024.

[154] J. E. Dickens, W. D. Langer and T. Velusamy, *Astrophys. J.*, 2001, **558**, 693.

[155] A. J. Markwick, T. J. Millar and S. B. Charnley, *Astrophys. J.*, 2000, **535**, 256.

[156] R. J. A. Grim and J. M. Greenberg, *Astrophys. J.*, 1987, **321**, L91.

[157] M. P. Bernstein, S. A. Sandford, L. J. Allamandola, S. Chang and M. A. Scharberg, *Astrophys. J.*, 1995, **454**, 327.

[158] P. Schilke, T. D. Groesbeck, G. A. Blake and T. G. Phillips, *Astrophys. J.*, 1997, **108**, 301.

[159] K. Demyk, E. Dartois and L. D'Hendecourt, *Astron. Astrophys.*, 1998, **339**, 553.

[160] M. P. Bernstein, S. A. Sandford and L. J. Allamandola, *Astrophys. J.*, 2000, **542**, 894.

[161] M. E. Palumbo, Y. J. Pendleton and G. Strazzulla, *Astrophys. J.*, 2000, **542**, 890.

[162] S. S. Prasad and S. P. Tarafdar, *Astrophys. J.*, 1993, **267**, 603.

[163] R. Gredel, S. Lepp, A. Dalgarno and E. Herbst, *Astrophys. J.*, 1989, **347**, 289.

[164] E. A. Bergin and M. Tafalla, *Annu. Rev. Astron. Astrophys.*, 2007, **45**, 339.

[165] D. C. B. Whittet, P. A. Gerakines and A. G. G. M. Tielens, *Astrophys. J.*, 1998, **498**, 159.

[166] K. M. Pontoppidan, E. F. van Dishoeck and E. Dartois, *Astron. Astrophys.*, 2004, **426**, 925.

[167] E. F. van Dishoeck and F. P. Helmich, *Astron. Astrophys.*, 1996, **315**, L177.

[168] G. J. Melnick and E. A. Bergin, *Adv. Space. Res.*, 2005, **36**, 1027.

[169] P. Bjerkeli, R. Liseau and M. Olberg, *Astron. Astrophys.*, 2009, **507,** 1455.

[170] V. Buch, *J. Chem. Phys.*, 1992, **96**, 3814.

[171] A. L. Barabási and H. E. Stanley, *Fractal Concepts in Surface Growth,* (Cambridge University Press, Cambridge, 1995).

[172] E. Mayer and R. Pletzer, *Nature*, 1986, **319**, 298.

[173] A. Bar-Nun, J. Dror, E. Kochavi and D. Laufer, *Phys. Rev. B.*, 1987, **35**, 2427.

[174] C. Manca, *Chem. Phys. Lett.*, 2000, **330**, 21.

[175] C. Martin, *Surf. Sci.*, 2002, **502**, 280.

[176] P. Ayotte, R. S. Smith and K. P. Stevenson, J. *Geophys. Res.*, 2001, **106**, 33387.

[177] B. S. Berland, D. E. Brown, M. A. Tolbert and S. M. George, *Geophys. Res. Lett.*, 1995, **22**, 3493.

[178] K. P. Stevenson, G. A. Kimmel, Z. Dohnalek, R. S. Smith and B. D. Kay, *Science*, 1999, **283**, 1505.

[179] G. A. Kimme, Z. Dohnálek, K. P. Stevenson, R. S. Smith and B. D. Kay, *J. Chem. Phys.*, 2001, **114**, 5295.

[180] Z. Dohnálek, G. A. Kimmel, P. Ayotte, R. S. Smith and B. D. Kay, *J. Chem. Phys.*, 2003, **118**, 364.

[181] M. E. Palumbo, *Astron. Astrophys.*, 2006, **453**, 903.

[182] M. E. Palumbo, G. A. Baratta, G. Leto and G. Strazzulla, *J. Mol. Struct.*, 2010, **972**, 64.

[183] U. Raut, M. Famá, M. J. Loeer and R. A. Baragiola, *Astrophys. J.*, 2008, **687**, 1070.

[184] A. Bar-Nun and T. Owen, In *Astrophysics and Space Science Library, Vol. 227*: *Solar System Ices*, Edited by B. Schmitt, C. de Bergh and M. Festou, (Springer, Netherlands, 1998).

[185] K. J.-B. Bossa, M. S. de Valois. Isokoski and H. Linnartz, *Astron. Astrophys.*, 2012, **545**, A82.

[186] M. P. Collings, J. W. Dever, H. J. Fraser, M. R. S. McCoustra and D. A. Williams, *Astrophys. J.*, 2003, **583**, 1058.

[187] U. Raut, M. Famá , B. D. Teolis and R. A. Baragiola, *J. Chem. Phys*, 2007, **127**, 204713.

[188] S. A. Sandford, L. J. Allamandola, A. G. G. M. Tielens and G. J. Valero, *Astrophys. J.*, 1988, **329**, 498.

[189] D. W. White, P. A. Gerakines, A. M. Cook and D. C. Whittet, *Astrophys. J*., 2009, **180**, 182.

[190] K. M. Pontoppidan, H. J. Fraser, E. Dartois, W. F. Thi, E. F. van Dishoeck, A. C. A. Boogert, L. d'Hendecourt, A. G. G. M. Tielens and S. E. Bisschop, *Astron. Astrophys.*, 2003, **408**, 981.

[191] J. V. Keane, A. C. A. Boogert, A. G. G. M. Tielens, P. Ehrenfreund and W. A. Schutte, *Astron. Astrophys.*, 2001, **375**, L43.

[192] P. Ehrenfreund, E. Dartois, K. Demyk and L. D'Hendecourt, *Astron. Astrophys.*, 1998, **339**, L17.

[193] K. I. Öberg, E. C. Fayolle, H. M. Cuppen, E. F. van Dishoeck and H. Linnartz, *Astron. Astrophys.*, 2009, **505**,183.

[194] W. Hagen, *Chem. Phys.*, 1981, **56**, 367.

[195] Z. Dohnále, G. A. Kimmel, S. A. Joyce, P. Y. Ayotte, R. S. Smith, and B. D. Kay, *J. Phys.Chem. B.*, 2001, **105**, 3747.

[196] R. Garrod, I. H. Park, P. Caselli and E. Herbst, *Faraday Discuss*., 2006, **133**, 51.

[197] F. Dulieu, E. Congiu, J. Noble, S. Baouche , H. Chaabouni, A. Moudens, M. Minisalle and S. Cazaux, *Sci. Rep*., 2013, **3**, 1338.

[198] A. G. G. M. Tielens, *Rev. Mod. Phys*., 2013, **85**, 1021.

[199] E. A. Bergin, G. J. Melnick, J. R. Stauer, M. L. N. Ashby, G. Chin, N. R. Erickson, P. F. Goldsmith, M. Harwit, J. E. Howe, S. C. Kleiner, N. D. A. Koch, D. G., B. M. Patten, R. Plume, R. Schieder, R. L. Snell, V. Tolls, Z. Wang, G. Winnewisser and Y. F. Zhang, *Astrophys. J*., 2000, **539**, L129.

[200] E. L. Gibb, D. C. B. Whittet, W. A. Schutte, A. C. A. Boogert, P. Chiar, J. E. Ehrenfreund, P. A. Gerakines, J. V. Keane, A. Tielens, E. F. van Dishoeck and O. Kerkhof, *Astrophys. J.*, 2000, **536**, 347.

[201] F. C. Gillett and W. J. Forrest, *Astrophys. J.*, 1973, **179**, 483.

[202] E. Dartois, K. Demyk, L. d'Hendecourt and P. Ehrenfreund, *Astron. Astrophys.,* 1999, **351**, 1066.

[203] A. Bar-Nun, G. Herman, D. Laufer and M. L. Rappaport, *Icarus*, 1985, **63**, 317.

[204] P. T. O'Neill and D. A. Williams, *Astrophys. Space Sci.*, 1999, **266**, 539.

[205] M. P. Collings, J. W. Dever, H. J. Fraser and M. R. S. McCoustra, *Astrophys. Space Sci.*, 2003, **285**, 633.

[206] G. Vidali, *J. Low. Temp. Physics.*, 2013, **170**, 1.

[207] D. A. Neufeld, S. Lepp and G. J. Melnick, *Astrophys. J.*, 1995, **100**, 132.

[208] J. C. Mottram, E. F. van Dishoeck, M. Schmalzl, L. E. Kristensen, R. Visser, M. R. Hogerheijde and S. Bruderer, *Astron. Astrophys.*, 2013, **558**, A126.

[209] L. E. Kristensen and E. F. van Dishoeck, *Astronomische Nachrichte*, 2011, **332**, 475.

[210] M. R. Hogerheijde, E. A. Bergin, C. Brinch, L. I. Cleeves, K. J. Fogel, A. G. Blake , C. Dominik, C. D. Lis, G. Melnick, D. Neufeld, O. Panić, C. J. Pearson, L. Kristensen, A. U. Yıldız and E. F. van Dishoeck, *Science*, 2011, **334**, 6054, 338.

[211] T. Hasegawa, E. Herbst and C. Leung, *Astrophys. J.*, 1992, **82**, 167.

[212] H. Roberts, and E. Herbst, *Astron. Astrophys.*, 2002, **395**, 233.

[213] Y. Oba, N. Watanabe, T. Hama, K. Kuwahata, H. Hidaka and A. Kouchi, *Astrophys. J.*, 2012, **749**, 12.

[214] N. Miyauchi, H. Hidaka, T. Chigai, A. Nagaoka, N. Watanabe and A. Kouchi, *Chem. Phys. Lett.*, 2008**, 456**, 27.

[215] H. Mokrane, H. Chaabouni, M. Accolla, E. Congiu, F.Dulieu, M. Chehrouri and J. L. Lemaire, *Astrophys. J.*, 2009, **705,** L195.

[216] R. Atkinson, D. L. Baulch, R. A. Cox, J. N. Crowley, R. F. Hampson, R. G. Hynes, M. E. Jenkin, M. J. Rossi and J. Troe, *Atmos. Chem. Phys.*, 2004, **4**, 1461.

[217] H. M. Cuppen and E. Herbst, *Astrophys. J.*, 2007, **668**, 294.

[218] T. L. Nguyen, J. F. Stanton and J. R. Barker, J. *Phys. Chem. A.*, 2011, **115,** 5118.

[219] L. J. Allamandola, M. P. Bernstein, S. A. Sandford and R. L. Walker, *Space Sci. Rev.*, 1999, **90**, 219.

[220] J. E. Chiar, A. J. Adamson, T. H. Kerr and D. C. B. Whittet, *Astrophys. J.*, 1995, **455**, 234.

[221] P. Ehrenfreund, A. C. A. Boogert, P. A. Gerakines, D. J. Jansen, W. A. Schutte, A. G. G. M. Tielens and E. F. van Dishoeck, *Astron. Astrophys.*, 1996, **315**, L341.

[222] J. Bouwman, W. Ludwig, Z. Awad, K. I. Öberg, G. W. Fuchs, E. F. van Dishoeck and H. Linnartz , *Astron. Astrophys*., 2007, **476**, 995.

[223] B. T. Soifer, R. C. Puetter, R.W. Russell, S. P. Willner, P. M. Harvey and F. C. Gillett, *Astrophys. J.*, 1979, **232**, L53.

[224] J. E. Chiar, P. A. Gerakines, D. C. B. Whittet, Y. J. Pendleton, A. G. G. M. Tielens, A. J. Adamson and A. C. A. Boogert, *Astrophys. J.*, 1998, **498**, 716.

[225] W. F.Thi , F. E. van Dishoeck, K. M. Pontoppidan and E. Dartois, 2010, *Mon. Not. R. Astron. Soc*., 2010, **406**, 1409.

[226] H. S. Liszt, *Astron. Astrophys*., 2007, **476**, 291.

[227] H. J. Fraser, M. R. S. McCoustra and D. A. Williams, *Astron. Geophys., 2002,* **43**, 2.10.

[228] P. Friberg, A. Hjalmarson, S. C. Madden and W. M. Irvine, *Astron. Astrophys*., 1988, **195**, 281.

[229] B. Parise, C. Ceccarelli, A. Tielens, E. Herbst, B. Lefloch, E. Caux, A. Castets, I. Mukhopadhyay, L. Pagani and L. Loinard, *Astron. Astrophys*., 2002, **393**, L49.

[230] P. Bergman, B. Parise, R. Liseau and B. Larsson, *Astron. Astrophys.*, 2011, **527**, A39.

[231] E. Wirström, W. D. Geppert, A. Hjalmarson, C. M. Persson, J. H. Black, P. Bergman, T. J. Millar, M. Hamberg and E. Vigren, *Astron. Astrophys.*, 2011, **533**, A24.

[232] V. Guzmán, J. Goicoechea, J. Pety, P. Gratier, M. Gerin, E. Roueff, F. Le Petit, J. Le Bourlot and A. Faure, *Astron. Astrophys*., 2013, **560**, A73

[233] K. I. Öberg, E. C. Fayolle, J. B. Reiter and C. Cyganowski, *Faraday Discuss.*, 2014, **168**, 81.

[234] V. Taquet, A. López-Sepulcre, C. Ceccarelli, R. Neri, C. Kahane and S. B. Charnley, *Astrophys. J.*, 2015, **804**, 81.

[235] T. P. M. Goumans, A. Wander, C. Richard, A. Catlow and W. A. Brown, *Mon. Not. R. Astron. Soc.*, 2007, **382**, 1829.

[236] T. J. Millar and D. A. Williams, *Dust and Chemistry in Astronomy* (IOP Publishing, Bristol, 1993.

[237] K. M. Pontoppidan, E. Dartois, E. F. Van Dishoeck. W. F. Thi and L. D'Hendecourt, *Astron. Astrophys.*, 2003, **404**, L17.

[238] W. D. Geppert, M. Hamberg and R.D. Thomas, F. Österdahl, F. Hellberg, V. Zhaunerchyk, A. Ehlerding, T. J. Millar, H. Roberts, J. Semaniak, M. Ugglas, A. Källberg, A. Simonsson, M. Kaminskad and M. Larssona, *Faraday Discuss.*, 2006, **133**, 177.

[239] K. Hiraoka, N. Ohashi, Y. Kihara, K. Yamamoto, T. Sato and A. Yamashita, *Chem. Phys. Lett.*, 1994, **229.**

[240] N. Watanabe and A. Kouchi, *Astrophys. J.*, 2002, **571**, L173.

[241] S. B. Charnley, A. G. G. M. Tielens and S. D. Rodgers, *Astrophys. J.*, 1997, **482**, L203.

[242] H. Cuppen, E. van Dishoeck, E. Herbst and A. G. G. M .Tielens, *Astron. Astrophys*., 2009, **508**, 275.

[243] A. L. Betz, R. A. McClaren and D. L. Spears, *Astrophys. J.*, 1979, **229**, L97.

[244] P. T. P. Ho, A. H. Barret, C. P. Mayers, N. D. Matsakis, C. A. Cheung, F. M. Chui, H. C. Townes and S. K. Yngvesson, *Astrophys. J.*, 1979, **234**, 912.

[245] P. R. Schwartz, A. C. Cheung, J. M. Bologna, M. F. Chui, J. A. Wauk and D. Matsakis, *Astrophys. J.*, 1977, **218**, 671.

[246] P. T. P. Ho, R. N. Martin, P. C. Myers and A. H. Barrett, *Astrophys. J.*, 1977, **215**, L29.

[247] P. T. P. Ho and C. H. Townes, *Ann. Rev. Astron. Astrophys.*, 1983, **21**, 239.

[248] A. C. Cheung, D. M. Rank, C. H. Townes, D. D. Thornton and W. J. Welch, *Phys. Rev. Lett.*, 1968, **21**, 1701.

[249] R. N. Martin and P. T. P. Ho, *Astrophys. J.*, 1986, **308**, L7.

[250] P. J. Benson and P. C. Myers, *Astrophys. J. Suppl.*, 1989, **71**, 89.

[251] J. Harju, C. M. Walmsley and J. Wouterloot, *Astron. Astrophys. Suppl.*, 1993, **98**, 51.

[252] S. Madden, W. M. Irvine, H. E. Matthews, R. D. Brown and P. D. Godfrey, *Astrophys. J.*, 1986, **300**, L79.

[253] J. Maxtin-Pintado and R. Bachiller, *Astrophys. J.*, 1992, **391**, L93.

[254] R. Mauersberger, C. Henkel and T. L. Wilson, *Astron. Astrophys.*, 1988, **205**, 235.

[255] M. Morris, S. Guilloteau, R. Lucas and A. Omont, *Astrophys. J.*, 1987, **321**, 88.

Chapter 2

Experimental Methods and Their Implementation

2.1 Introduction

There are a number of routes to investigating the role of dust grains in the ISM, especially those surface reactions leading to the production of a range of molecules:

- Observations;
- Experiments;
- Modelling and simulation.

Observations are a direct way of gaining information on the abundances of molecules in the gas phase and in the solid state. The main sources of this information are spectroscopic features at a range of wavelengths and along various lines-of-sight. The observations have enabled various models to be constructed which allow observed abundances of atoms and molecules to be interpreted and reproduced. Experiments carried out in the laboratory are crucial to building an understanding of the physics and chemistry occurring on ISM dust grains. Laboratory gas phase spectra help to identify observed spectroscopic features. While the chemical reactions forming molecules can be investigated in the laboratory to determine mechanism and routes of formation and hence explain observed abundances. The numerous rate equations describing the chemistry occurring across the Universe, such as those in the University of Manchester Institute of Science (UMIST) database [1, 2], are only as accurate as the kinetic information which they contain. Some of this information comes from laboratory experiments and other from sophisticated computer modelling. This thesis takes an experimental approach to investigating dust; and this chapter describes the experimental techniques used in the studies in this thesis.

2.2 Surface Science

Surface science is a vital tool in astrochemistry, as it can be used to investigate processes occurring on dust grain surfaces within the ISM. The Propst diagram shown below in **Figure 2.1** is one way of looking at surface science experiments.

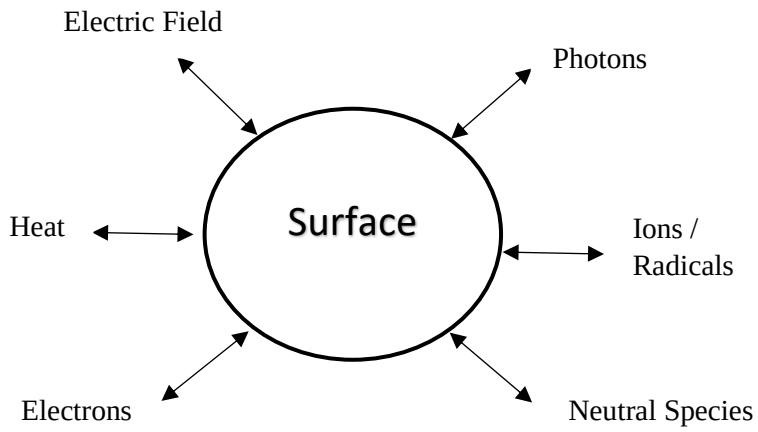

Figure 2.1: The Propst diagram showing surface science processes which are possible and studied in various fields of physical science. In this work, the areas of interest include electric fields, heat and neutral species [3].

Figure 2.1 shows that a wide variety of probes can be successfully used to interrogate surface processes. Surface science experiments are generally aimed at determining how species adsorb on surfaces, what structures they adopt, what physical and chemical changes happen on the surface, and how species desorb. Adsorbed molecules can be studied using a range of techniques giving complementary information.

A molecule is adsorbed to a surface through one of two processes: physisorption or chemisorption. Both can be considered extreme forms of adsorption. Physisorption is long range, involves weak van der Waals interactions and so is a balancing act between repulsive and attractive forces with energies of the order of tens of kJ mol^{-1} [4]. The work carried out in this thesis involves physisorbed species. There is no electron sharing in this process. Chemisorption, on the other hand, is generally associated with strong, short-range interactions in which electrons are shared between the adsorbate and surface and a strong chemical bond is formed between the surface and the adsorbate, with typical energies of hundreds of kJ mol^{-1} [4]. The interaction of atoms and molecules with a solid surface can be described through a potential energy diagram [5], as seen in **Figure 2.2**, which highlights the two limiting adsorption behaviours.

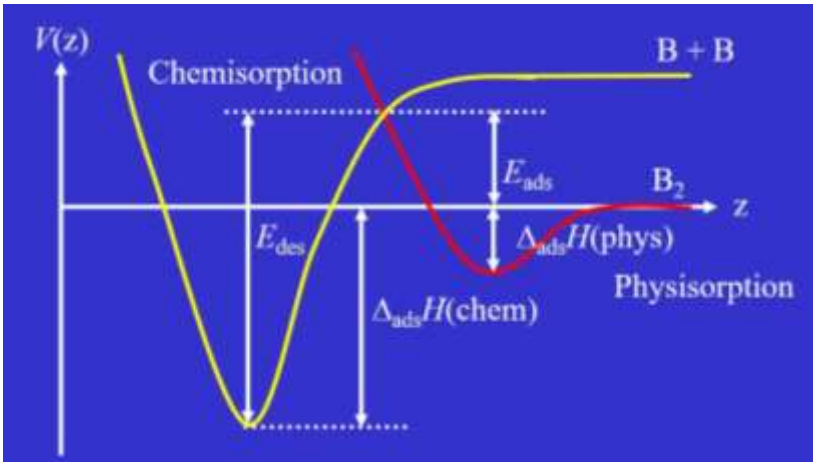

Figure 2.2: The interaction of atoms and molecules with a solid surface. Although physisorption and chemisorption are energetically different, the stronger chemisorption process must be preceded by physisorption (Reproduced from [6]).

In this work, the focus is on the deposition of neutral molecules. The interaction of the deposited molecules with the substrate is analysed *via* infrared spectroscopy and heating of the system is monitored by a quadrupole mass spectrometer which will detect the molecules in the gas phase above the surface as they desorb.

Initially, a gas phase species hits a surface, and can either be reflected or accommodated. The rate at which gas phase species collide with the surface, the wall collision rate, Z_w is given by **Equation 1**:

$$Z_w = \frac{P}{\sqrt{2\pi m k_B T}} \qquad \textbf{(E1)}$$

where P is the partial pressure of the gas, m is the molecular mass of the chemical species, k_B is the Boltzmann constant and T is the absolute temperature of the gas**.** **Table 2.1** shows the approximate times it takes to completely adsorb a monolayer at a given pressure for nitrogen (N_2). These calculations are only valid if N_2 sticks to the surface, which only occurs if the temperature is low enough [7].

Pressure / mbar	Approximate Time / s
10^{-3}	3.5×10^{-3}
10^{-7}	35
10^{-10} (Experimental Conditions)	3.5×10^{4} (~10 hours)
10^{-12}	3.5×10^{6} (~1000 hours)

Table 2.1: Shows the approximate times taken to adsorb a monolayer of N_2 at the indicated pressures, assuming all incident molecules stick to the surface. The gas temperature is assumed to be 300 K. These times vary depending on the molecule of interest [7].

In this thesis, experiments are typically carried out in ultrahigh vacuum (UHV) *i.e*. pressures in the region of $1\text{-}5\times10^{-10}$ mbar. From **Table 2.1**, it can take approximately 10 hours for a monolayer of N_2 to accumulate on the surface in this pressure range. Thus, it is vital to maintain UHV pressures to keep the surface clean during experiments. A major contaminant in UHV systems is H_2, molecular hydrogen, as it is the most abundant molecule in an UHV system due to outgassing from the stainless steel surfaces. The temperature of the surfaces is generally high enough to prevent H_2 from sticking to them. However, H_2 will stick to UHV surfaces at temperatures below 10 K. Additionally, H_2 does not react with the surfaces used or molecules which are introduced *via* the dosing lines. Hence, H_2 contamination can be ignored.

The values calculated and shown in **Table 2.1** assume a sticking coefficient of unity, *i.e*. every molecule which strikes the surface will stick to it. However, this is not always the case. The sticking coefficient, *S*, is the probability that a species from the gas phase stays on the grain long enough for it to be bound at a site on the surface. The sticking process is mainly influenced by the ability of a gas species to lose its kinetic energy and hence become trapped on the surface. Thus, a high adsorption energy or good momentum transfer will further increase the sticking efficiency [8, 9]. The sticking coefficient, is defined in terms of the rates of adsorption, ν_{ads} , and collision, Z_{w}. This is described by **Equations 2** and **3**:

$$S = \frac{\nu_{\mathrm{ads}}}{Z_{\mathrm{w}}} \qquad \textbf{(E2)}$$

$$\upsilon_{\mathrm{ads}} = \frac{k_{\mathrm{t}}}{1 + \frac{k_{\mathrm{d}}}{k_{\mathrm{a}}}} \quad \textbf{(E3)}$$

where k_t, k_d and k_a are the rate constants for trapping, desorption and adsorption, respectively. In this case, trapping refers to the intermediate state of a molecule between the gas phase and being adsorbed to the surface.

S is found to vary with the amount of material already on the surface as defined by the coverage θ. The simplest form of variation assumes random sticking and formation only of a monolayer, **Equation 4,**

$$S = S_{\mathrm{o}}\,(1 - \theta) \quad \textbf{(E4)}$$

where S_o is the initial sticking coefficient. More complex relationships exist describing more complex but realistic adsorption scenarios. Additionally, when discussing molecules adsorbing to a surface, it is necessary to consider the accommodation coefficient, α, which describes the ability of atoms and molecules to effectively transfer their thermal energy to the surface. If this transfer is efficient, the species will not possess enough thermal energy to be reflected from the surface, and it will be adsorbed. The thermal accommodation coefficient is defined in **Equation 5:**

$$\alpha = \frac{T_{\mathrm{f}} - T_{\mathrm{i}}}{T_{\mathrm{s}} - T_{\mathrm{i}}} \quad \textbf{(E5)}$$

where T_i is the initial temperature of the molecule before a collision with the surface, and T_f is the temperature of the molecule after a surface collision. T_s is the temperature of the molecule of surface on which the gas-phase molecules collide. In the case when $\alpha = 1$, then all the species are accommodated on to the surface and are adsorbed, and when $\alpha = 0$ no species are accommodated.

There are many methods for determining *S*. Typically for *S* larger than 0.1, we use the method outlined by King and Wells [10]. In this experiment, a beam of gas-phase species is directed towards a surface, where a flag is used to obstruct the path of the

beam, resulting in a background pressure which can be measured using a mass spectrometer. By moving the flag, the molecules will hit the surface, and stick to it which results in a drop in the mass spectrometer count rate *i.e*. partial pressure. A simple ratio of partial pressure changes then gives *S*. However, for *S* values of less than 0.1, it is more common to use methods which are based on calibrated surface spectroscopy, where the surface concentration of species may be directly determined [9,11,12,13].

2.3 UHV Experimental Equipment

The ice rig (**Figure 2.3**) is designed for astrochemical surface science experiments, as work by a number of authors demonstrates [7]. It has been used to study a range of astrophysical surfaces, ices and molecules found in the ISM [14,15]. A brief description of the UHV main chamber and equipment is presented below. There is extensive literature discussing the use and operation of the UHV system [7, 16].

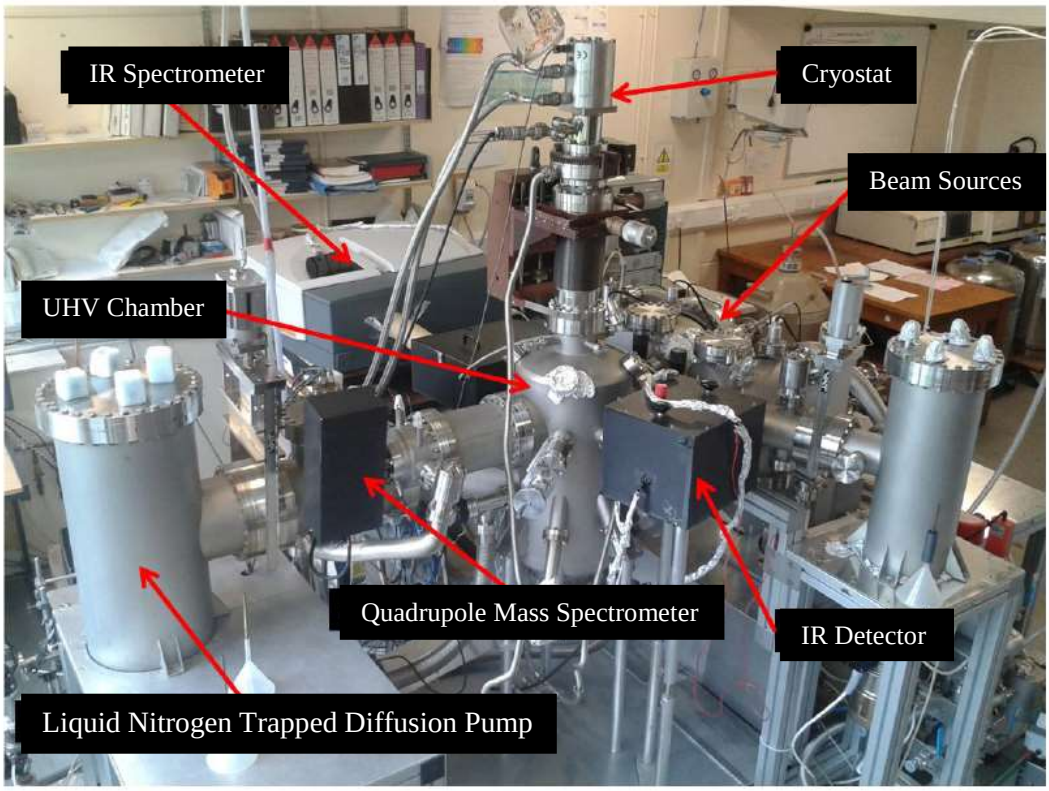

Figure 2.3: A picture showing the experimental set-up used for this thesis. The main aspects of the equipment are labelled with red arrows [7].

2.3.1 Instrumentation

The details below explain how to simulate the environment in a molecular cloud along with the surface which is used simulate an interstellar dust grain.

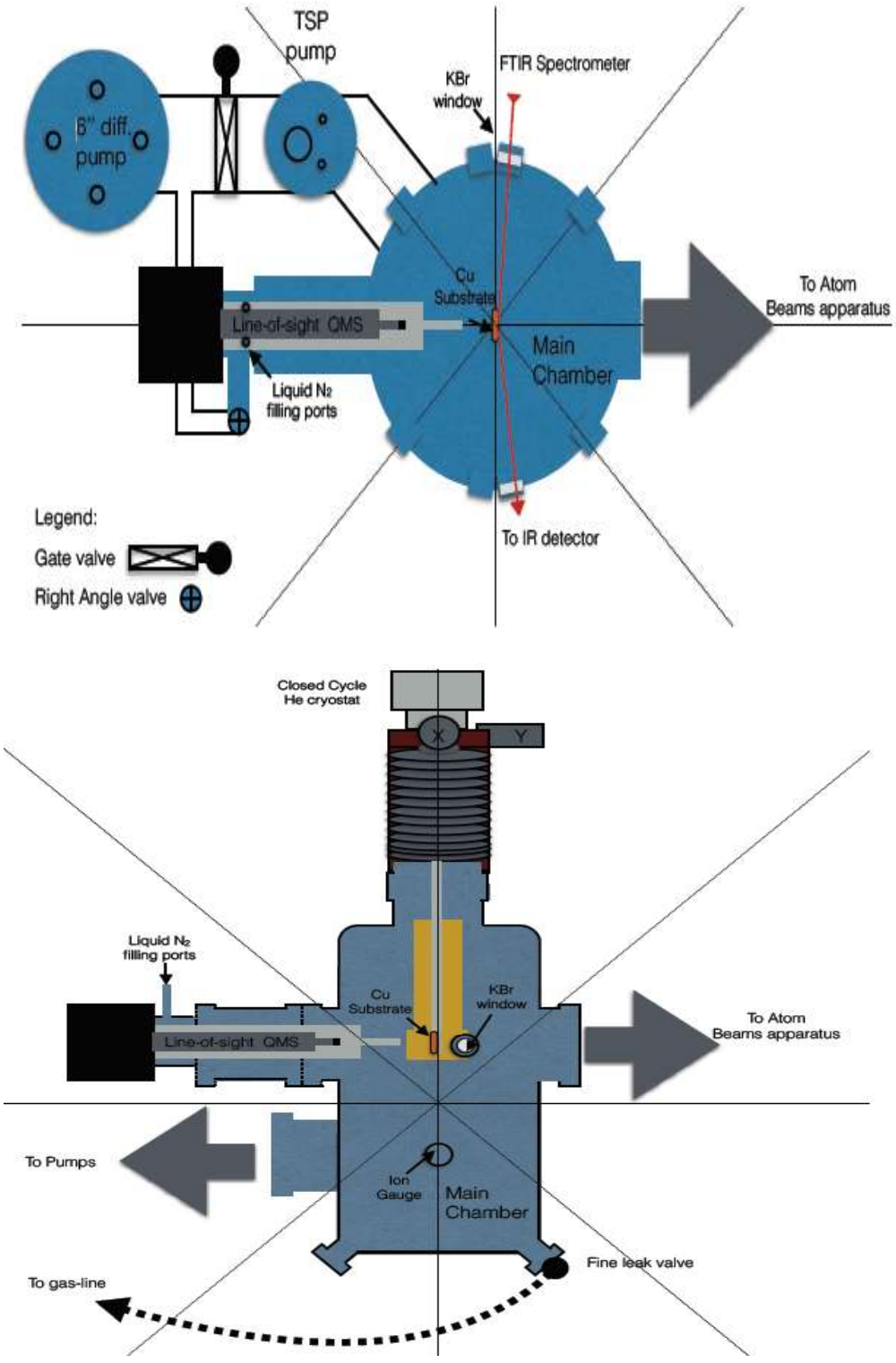

Figure 2.4: Schematic of the experimental chambers and pumping group of the ice rig (Reproduced from [16]).

The requirements for a UHV system include: a chamber with pumps to create and hold the vacuum; a sample on which the surface processes take place; equally, reagents need to be introduced and products need to be analysed. **Figure 2.4** shows the cross-section of the UHV apparatus. The central part of the UHV system is a 30 cm diameter stainless steel chamber (Instrument technology Ltd), which can reach UHV conditions after baking for 72 hours at 120 ^{o}C. The chamber is equipped with two infrared (IR) transparent KBr windows for IR spectroscopy. Three pumps are used to pump the chamber down. The first pump is a mechanical rotary pump (Edwards, E2M18), which backs a liquid nitrogen - trapped 6" diffusion pump (Edwards, E06). Additionally, a liquid nitrogen-trapped titanium sublimation pump (AML, TSP2) is used to help reduce residual oxygen-containing gaseous contamination. A gate valve is placed between the diffusion and sublimation pumps. To measure the pressure of the chamber, a nude hot cathode ionisation gauge (Instrument technology Ltd) with thoria filaments is used. The typical operational range of this ion engage is 10^{-4} - 10^{-11} mbar. There are three active Pirani gauges (Edwards High Vacuum, APG-L) located between the diffusion and rotary pumps. All gauges are interfaced to an active gauge controller (Edwards). There are two fine-control leak valves (Vacgen, ZLVM940) connected to the metal gas lines and the UHV system as shown in **Figure 2.4**.

2.3.2 Cryostat and Sample

The sample used is an oxygen-free, high-conductivity copper (OFHC) block, coated with a layer of amorphous silica (aSiO_2) to about 300 nm thick. This mimics the silicate grain materials in the ISM. The sample is fixed at the end of a refrigerated cold finger mounted on an XYZ manipulator providing three-axis translation and rotation of 360^0 about the Z axis, as shown in **Figure 2.5**. The cold finger itself is a 1 m closed copper tube connected to a closed-cycle helium cryostat (APD Cryogenics, HC–2). The cold finger is enclosed in a 1 m gold-coated, OFHC copper tube acting as a cryoshield, which is only cooled *via* the first stage of the cryostat. The cryostat creates a cryogenic microenvironment around the cold finger and the sample mount [16]. This helps to reduce the radiative thermal gain from the surrounding environment. **Figure 2.6** shows the sample which is regularly cooled to below 20 K. In order to heat the sample surface of the copper block, a cartridge heater (Heatwave Labs Inc., TB–175)

is placed inside the block. The heater is insulated by ceramic beads, and its connections are insulated by peribraid sleeves, which pass through the cavity in the support block and are tied around the cold finger and up to appropriate feedthroughs leading to an external power supply.

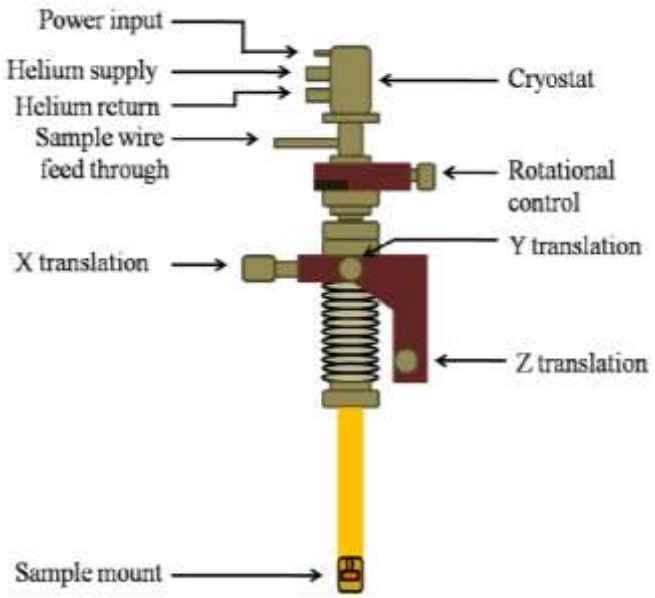

Figure 2.5: Schematic of the complete manipulator, with the closed-cycle He cryostat, which cools the sample to the base temperature of 15 K used in this work. Additionally, the sample has XYZ translation along with a virtual 360° rotation (Reproduced from [7]).

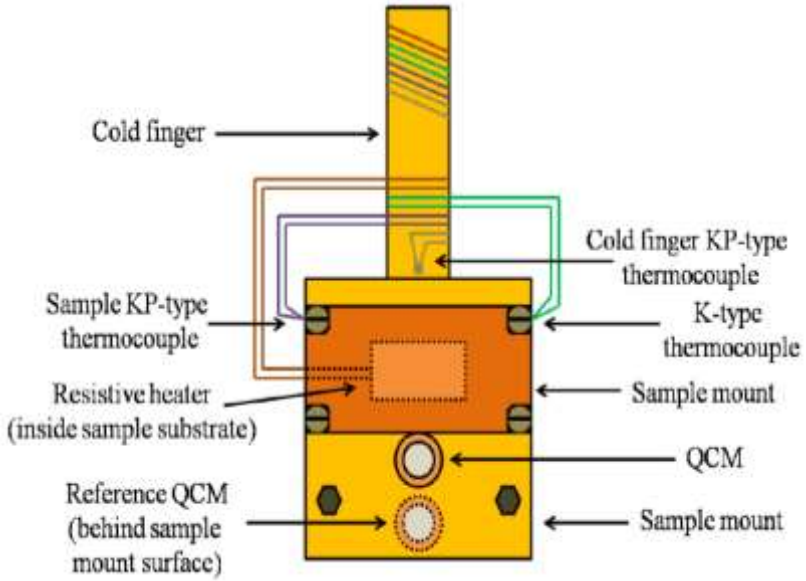

Figure 2.6: Schematic of sample, located at the end of closed cycle Helium cryostat (Reproduced from [7]).

Two KP-type thermocouples are used to measure temperature. These are made from two wires, one gold and one chromel (90% Ni and 10% Cr). One thermocouple is at the sample and other is at the base of the cold finger. Both thermocouples follow a similar way out of the UHV system to the cartridge heating circuit, and are insulated by peribraid and wrapped around the cold finger. The thermocouples are interfaced airside with controllers (IJ instruments Ltd., J-06-BZ9MC-02YI for the cold finger and IJ instruments Ltd., 06-BZ9MC-02YJ for the sample). When the closed-cycle helium cryostat is turned on, the sample gradually cools down to base temperature; reaching a steady state in which the heat removal due to the cryostat matches heat supplied from the chamber, *i.e.* from the ion gauge and chamber walls. Applying a constant voltage to the heater cartridge will result in additional heating. Therefore, the sample temperature will rise until it levels to a plateau that stays constant over time. This new steady state is established at higher temperatures rather than base conditions. By adjusting the controlling voltage, it is possible to adjust the temperature of the sample to a certain value.

2.3.3 Dosing and Sample Preparation

The gases used in dosing are held in gas cylinders, while the reagents are held in the glass bulbs (as gases or liquids) on a metal dosing line under a high vacuum, which is linked to fine-control leak valves, allowing chemical species to be introduced into the UHV chamber, as shown in **Figure 2.7**. The process of background dosing fills the entire chamber with a vapour which adsorbs on to the cold surfaces. Before each experiment, the gas lines are cleaned using the species to be used in the experiments. This process is repeated three times before the experiment is started. To evacuate the dosing lines, all of the valves are opened and the lines see the diffusion pump at **A** in **Figure 2.7**. Samples are attached to the manifolds **B** and **C** using valves (Swagelok, SS-4BK) and special glass connectors. This allows separate dosing of two substances *via* the dosing lines on the UHV chamber. Valves **D** and **E** isolate the manifolds and dosing lines from the diffusion pump at **A**.

Gas samples are introduced to the manifolds directly after evacuation. Liquids, in glass phials, are subject to freeze-pump-thaw cycles before expanding into the manifold. The exposure of a surface to an adsorbent is measured in Langmuir L, and

this is defined with 1L being exposure to a pressure of 1.33×10^{-6} mbar (10^{-6} Torr) for a period of 1 second. This represents the uncorrected exposure. To correct the exposure, the ionisation coefficient, γ_i, of the adsorbate is required. In this work, the ionisation coefficients from Bartmess and Georgiadis [17] are used. Subsequently, *via* experimental measurements, the exposure in L can be referenced in terms of monolayers, or ML. Assuming all molecules stick and we know the density of the layers involved, it is possible to assign monolayer exposure by observation.

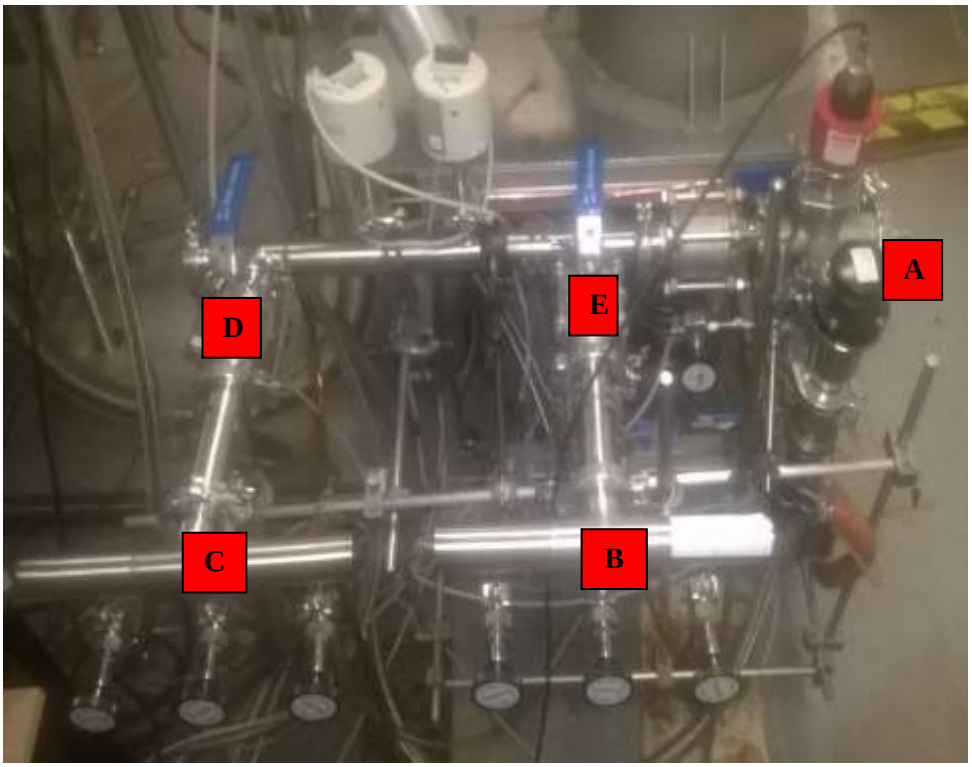

Figure 2.7: The arrangement of the metal dosing lines connected to the leak valves.

2.4 Experimental Techniques

2.4.1 Reflection-Absorption Infrared Spectroscopy (RAIRS)

Infrared spectroscopy is a non-destructive tool which provides information about the various molecular vibrational modes present on the surface of the sample and their local environment. Various surface-specific IR sampling methods are available, allowing a wide variety of sample surfaces and adsorbate systems to be studied in the monolayer and sub-monolayer regimes. These are classified into reflection and non-reflection techniques, depending on the light path through the sample. The main

reflection techniques are Reflection-Absorption Infrared Spectroscopy (RAIRS), Internal Reflection or Attenuated Total Reflectance (ATR) spectroscopy and Diffuse Reflectance Infrared Fourier Transform (DRIFT) spectroscopy. Transmission measurements (TIR) and emission spectroscopy (EMS) are some of the key non-reflective surface techniques available [18].

The experimental work carried out in this thesis makes use of RAIRS. This technique was initially proposed by Greenler [19] for studying thin layers of adsorbates on metal substrates. It has the benefit of being a very sensitive surface tool. This technique requires the IR beam to be reflected by the substrate, which acts as a mirror. The reflected beam is subsequently directed on to the detector. The addition of an adsorbate to the substrate will change the reflectivity (ΔR) of the substrate. This results in a spectrum of $\Delta R/R$, where R is the total reflected IR beam from a clean surface.

When carrying out a RAIRS experiment in the UHV chamber, the IR beam is directed into the chamber initially by flat and paraboloidal mirrors housed in the optics box (**Figure 2.4)**. This beam passes through the KBr window and subsequently is incident on the sample at a grazing angle of 75°, after which it is directed towards another KBr window. The KBr windows are used since they are IR-transparent in the detection range of the Mercury Cadmium Telluride (MCT) detector. After the IR beam has passed through the second KBr window, it is subsequently re-collimated and re-focused by an ellipsoidal mirror before it arrives at the detector located in the second optics box. The MCT detector is liquid nitrogen-cooled and has a detection range of 4000 - 800 cm^{-1}. The optics boxes are purged with dry, carbon dioxide-free air, to reduce interference.

The presence of a surface imposes a certain symmetry on the electromagnetic fields associated with IR radiation. As shown in **Figure 2.8**, the electric field of the radiation can be polarised either parallel (a) or perpendicular (b) to the surface. On reflection at the metal surface, the electric field undergoes a phase change (**Figure 2.9**). This depends on the polarisation. Hence, the net electric field at the point of reflection depends on the polarisation [20].

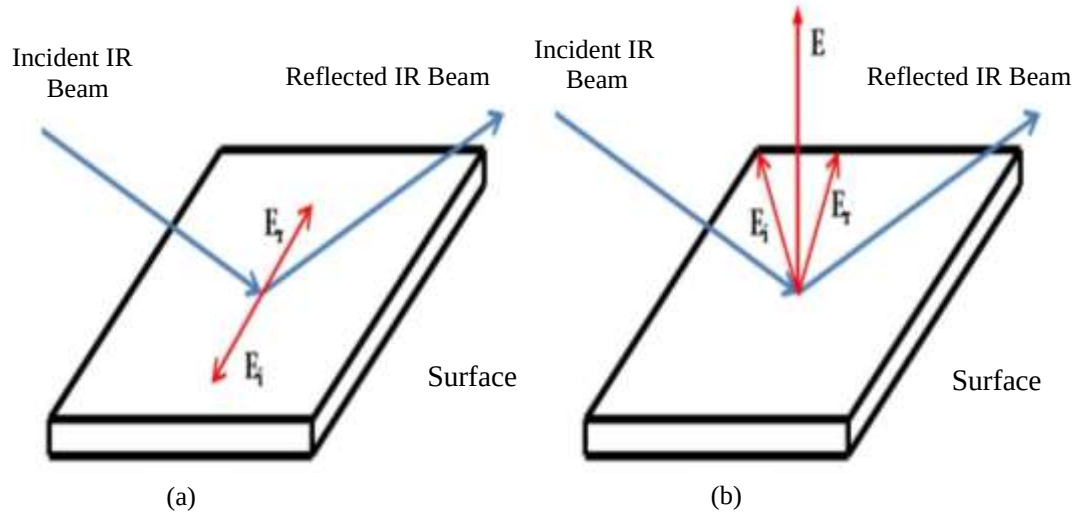

Figure 2.8: The electric field vectors on a surface from (**a**) parallel polarised light, where the electric field vectors cancel and (**b**) light which is perpendicular to the surface, where the vectors are enhanced (Reproduced from [7]).

In the case of parallel polarised light, there is zero field and thus no possibility of absorption of energy from the IR radiation field. However, for radiation polarised perpendicular to the surface, an enhanced net field is observed at the point of reflection and so absorption from the electromagnetic field is possible. When molecular thin films are being studied, incidence angles of light polarised perpendicular to the surface of approximately 72° have been used in the past [3]. The sensitivity of RAIRS comes from the fact that the intensity of the p-polarised component of the reflected IR radiation (the electric field being perpendicular to the plane of the metal surface) is enhanced at a metal surface at such a high angle of incidence. This high angle of incidence is known as the ‘grazing angle’ [21].

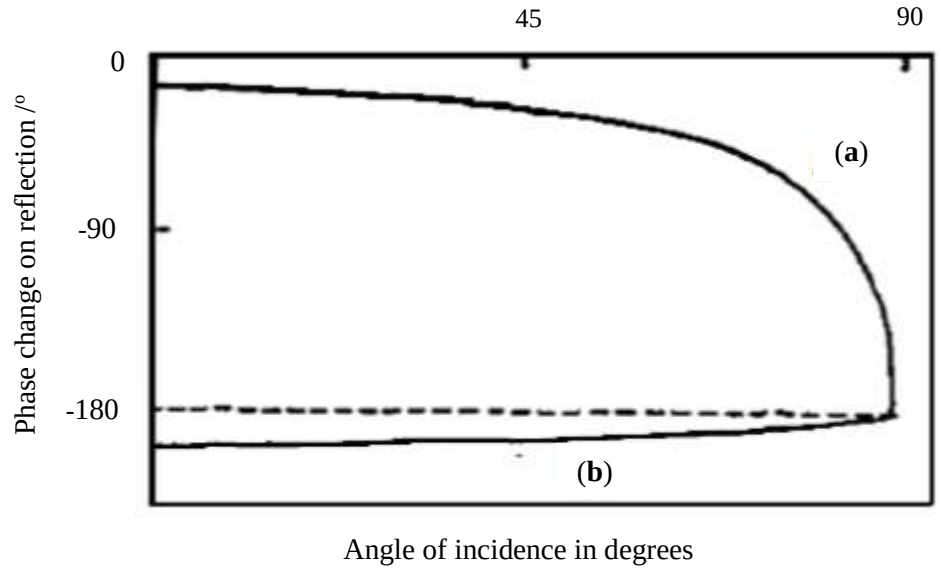

Figure 2.9: A graph showing the variation of the phase shift upon reflection for (**a**) perpendicular and (**b**) parallel polarised IR radiation incident upon a metal surface with the angle of incidence (Reproduced from [3]).

In the case of normal incidence, the IR beam would create a circular spot. However, an additional advantage in having a beam which is at grazing incidence is an elliptical spot of greater area is created on the surface of the sample. This results in a greater number of molecular oscillators being probed and interacting with the radiation. This defines the surface intensity function, the product of the enhanced electric field and the increased number of oscillators, which gives an enhancement of 50 to 60 times compared to transmission IR spectroscopy. Hence, for weak absorbers such as hydrocarbons, high quality spectra can be obtained at the monolayer level on a metal single crystal surface, while for strong absorbers it is possible to obtain resolved spectra of the small fractions of a monolayer.

The grazing incidence geometry also allows us to look at adsorbates on thin (typically less than 500 nm) insulator films such as oxides deposited on the metal. This is the Buried Interface Method (**Figure 2.10**) developed by Goodman [22]. In this approach, thin oxide films ranging from less than a monolayer to a few tens of monolayer thick (*e.g.* less than 10 nm) are deposited on a metal substrate and can be used to assist a range of surface investigate techniques, many of which are excluded when applied to the corresponding bulk oxide. The electronic, structural and chemical properties of these thin very thin oxide films can be investigated using a range of techniques including, electron energy loss spectroscopy loss spectroscopy

(HREELS), temperature programmed desorption (TPD) and RAIRS. Of course, the RAIRS enhancement still applies hence the utility of the method.

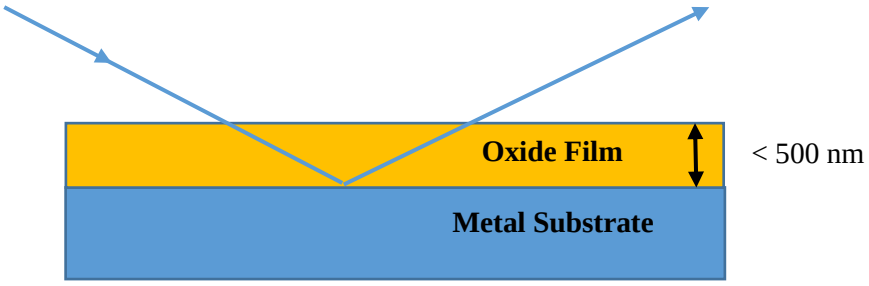

Figure 2.10: Adsorbate on an oxide surface can be detected in RAIRS using the buried interface method [22].

When looking at IR spectroscopy on a metal surface, the metal surface selection rule (MSSR) [20] has to be considered. **Figure 2.11** demonstrates the origin of this rule.

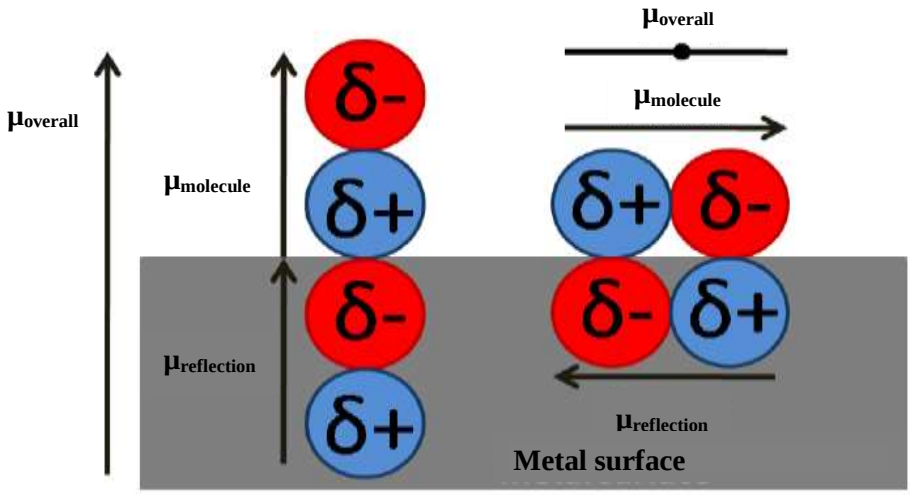

Figure 2.11: The metal surface selection rule. The molecules which are orientated perpendicular to the surface will possess a dynamic dipole moment resulting from the image dipole arising in the metal surface. However, this effect can be nullified when the molecules are aligned parallel to the surface (Reproduced from [7]).

The metal surface selection rule controls which vibrational modes are seen when an IR-active molecule is absorbed on to a surface. The dynamic dipole of a vibrational mode creates an image of itself in the free electrons in the metal. The dynamic dipole and its image can then enhance each other or cancel each other. In the latter case, no

IR absorption will be observed. This selection rule is vital when a molecule is absorbed directly on to a flat metal substrate. However, where irregular and rough layers of silica cover the metal substrates, this results in molecules being absorbed with random orientations with respect to the metallic mirror plate. Consequently, the metal surface selection rule is circumvented, allowing modes which would otherwise be inactive in an orientated sample directly absorbed on the metal surface to be observed.

From a practical perspective, RAIRS experiments are relatively easy to carry out: they need a standard FTIR spectrometer, IR optics and a detector as described above. The main advantages of RAIRS include [16]:

1. It is a highly versatile technique which can operate in a variety of conditions from UHV to elevated pressures.
2. It can achieve high resolution (≤ 1 cm^{-1}) and a sensitivity of ($\frac{\Delta R}{R} < 0.001$).

Like most experimental techniques, however, RAIRS does have some issues, including a complex dependence of the change in reflectivity, $\Delta R/R$, **Equation 6,**

$$\frac{\Delta R}{R} = \frac{R^0 - R}{R^0} \qquad \textbf{(E6)}$$

on the thickness of the adsorbed layer, and on the angle of incidence, along with the optical constants of the substrate and the adlayer [3, 23]. So in some cases, RAIRS is not as sensitive as it could be under optimal conditions, especially if the adsorbates sit on the substrate preferentially with a geometry that aligns the dynamic dipoles parallel to the surface [24-27].

The RAIR spectra in this thesis have been collected using a Fourier transform infrared spectrometer (Varian 670). The theory of FTIR is discussed in greater detail elsewhere [28]. However, below is a brief overview of the principles of how the FTIR works. Essentially, FTIR is based on two elements: the Michelson interferometer and the Fourier transform. A schematic is shown below in **Figure 2.12.**

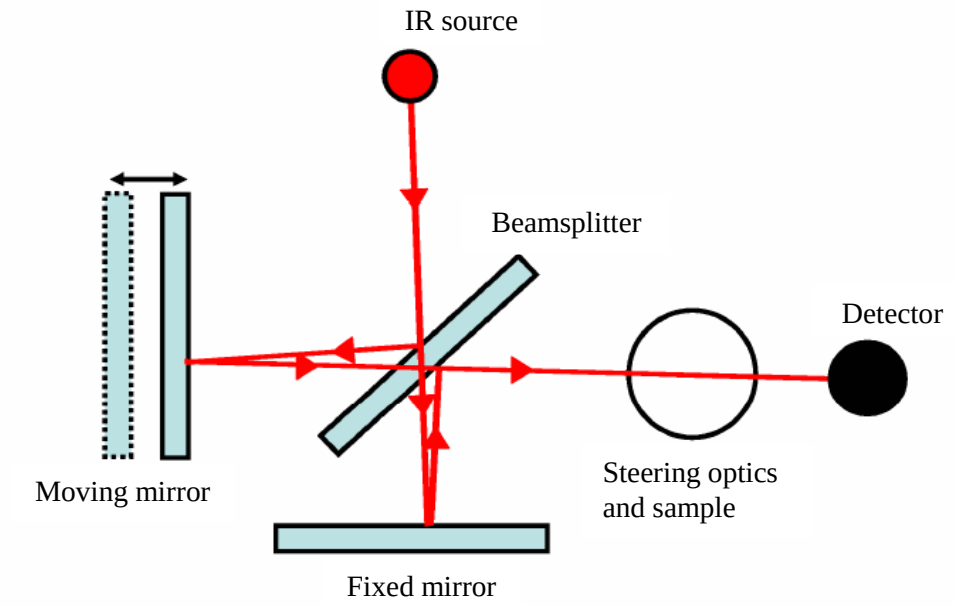

Figure 2.12: The Michelson interferometer as used in the FTIR (Reproduced from [2]).

The interferometer consists of a source, beamsplitter, two mirrors, a laser and detector. The radiation which comes from the source is directed towards a beam splitter that reflects only 50% of the radiation and lets through the other 50%. The transmitted part of the incoming beam is incident on a stationary mirror, while the reflected part propagates towards a moving mirror. This moves back and forth, constantly changing the length of the optical path. The two beams are combined at the beamsplitter, and then sent to the detector where it acquires the signal $I(t_o)$ at the instant t_o, with no optical delay. Afterwards, at t_i, the moving mirror has changed the optical path by a certain distance, resulting in a phase difference and hence change in the intensity $I(t_i)$, seen by the detector at t_i. The intensity is increased or decreased due to interference effects at the beamsplitter. The final dataset consists of the detected intensity as a function of the optical delay; this is known as the interferogram [2, 16]:

$$I(t) = \int_0^\infty I(w)\, cos(wt)\, \mathrm{d}w \qquad \textbf{(E7)}$$

The interferogram is converted by using Fourier transformation (**Figure 2.13**) to yield the single beam spectrum, **Equation 8**:

$$I(w) = \int_0^{\infty} I(t)\, cos(wt)\, \mathrm{dt} \qquad \textbf{(E8)}$$

Since only a single-beam spectrum can be extracted, it is necessary to record background spectra of the clean substrate before carrying out experiments. The background scans are carried out with the sample under the same conditions (*e.g.* position and temperature) as the spectra recorded when carrying out the experiments. The final spectrum is determined by the following relationship, **Equation 9:**

$$I_{\mathrm{corr}} = -\log_{10}\left(\frac{I_{\mathrm{sam}}}{I_{\mathrm{bg}}}\right) = \log_{10}\left(\frac{\Delta R}{R}\right) \qquad \textbf{(E9)}$$

where I_{corr} is the background corrected spectrum, I_{sam} is the sample spectrum and I_{bg} is the background spectrum. The subsequent spectrum is on a scale of fractional absorbance, defined by $\log_{10}(\Delta R/R)$. In the case of a curved baseline, a background correction is applied. The curved baseline occurs due to small variations in the IR source intensity and other experimental conditions from one scan to another. The x-axis of the FTIR is usually displayed in wavenumbers or cm^{-1}.

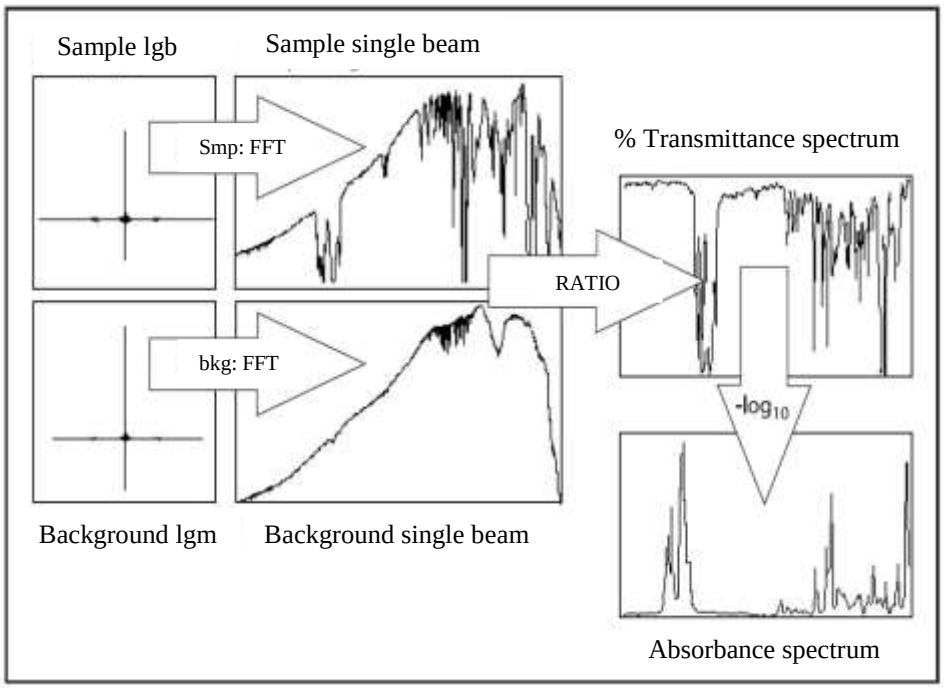

Figure 2.13: The process of collecting an infrared spectrum in FTIR (Reproduced from [29]).

FTIR spectroscopy has a number of advantages when compared with dispersive spectroscopy [29]:

1. FTIR can achieve a greater signal-to-noise ratio (since the detector receives all wavelengths at once, *i.e.* multiplexing) in a shorter time than a dispersive spectrometer.
2. The FTIR spectrometer does not have optical slits, which reduces the beam intensity in dispersive spectrometers, thus FTIR spectrometers have a greater optical throughput, which in turn also increases the signal-to-noise ratio.
3. Signal improvements can be achieved by the co-addition of scans. This is achieved thanks to the accuracy of the frequency scale, which is due to the use of a fixed frequency reference laser along with the Fourier transform technique.
4. The use of dynamic alignment of the IR beam inside the FTIR spectrometer results in an increased degree of stability over longer periods of time.

2.4.2 Temperature Programmed Desorption (TPD)

Temperature programmed desorption (TPD) is an analytical method which allows the determination of the binding energy between adsorbates and a surface. TPD is key tool in describing surface kinetics [30, 31]. The basic concept of TPD involves heating a surface which is coated with molecules and observing what desorbs using a mass spectrometer, while monitoring the temperature of the surface. TPD is, however, a destructive analytical method, since the original solid sample is analysed after desorption to the gas phase. In order to obtain information from TPD experiments, various criteria must be met to allow the data to be interpreted easily. The sample or surface, along with the chemicals which are adsorbed, must be heated in a controlled fashion. This can be achieved by heating the sample using a linear heating ramp. This allows the determination of temperature at various instances, as shown in **Equation 10**:

$$T(t) = T_{\mathrm{o}} + \beta t \qquad \textbf{(E10)}$$

where *T(t)* is the temperature of the sample as a function of the time (*t*), T_o is the initial temperature and β is the heating ramp, which are both known experimentally. During TPD, the sample heats up along with the sample mount and the cold finger. Analysing the resulting experimental data allows the investigation of desorption of molecules from the sample *versus* non-sample surfaces when recording the temperature of the sample and the cold finger against the quadrupole mass spectrometer signal as done in the instrument used here.

In order for desorption to take place from the surface, the temperature must be high enough for the chemical species to break the interaction which is holding it to the surface, **Reaction 1**:

$$\mathrm{A(ads)} \rightarrow \mathrm{A(des)} \qquad \textbf{(R1)}$$

The rate at which desorption occurs, r_{des}, is a function of the surface coverage is defined by **Equation 11:**

$$r_{\mathrm{des}} = k_{\mathrm{des}}\theta_{\mathrm{s}}^{m} \qquad (\textbf{E11})$$

where k_{des}, is the desorption rate constant, θ_{s} is the coverage and *m* is the order of process. The temperature dependence of the rate constant k_{des} follows an Arrhenius law. Thus, k_{des} increases exponentially as the temperatures rises:

$$k_{\mathrm{des}} = \nu_{\mathrm{des}}\exp\left({}^{-E_{\mathrm{des}}}/_{\mathrm{RT}}\right) \qquad (\textbf{E12})$$

where ν_{des} is the pre-exponential factor, E_{des} is the activation energy for desorption, *R* is the ideal gas constant and *T* is the absolute temperature of the surface. If the pumping speed is high, the rate of desorption can be found from the change in partial pressure of desorbate in the vacuum chamber. The surface coverage will start to decrease as the temperature is raised. From the exponential increase of the rate constant along with a decline of the surface coverage, a plot (**Figure 2.14**) can be constructed to show a prototypical TPD trace.

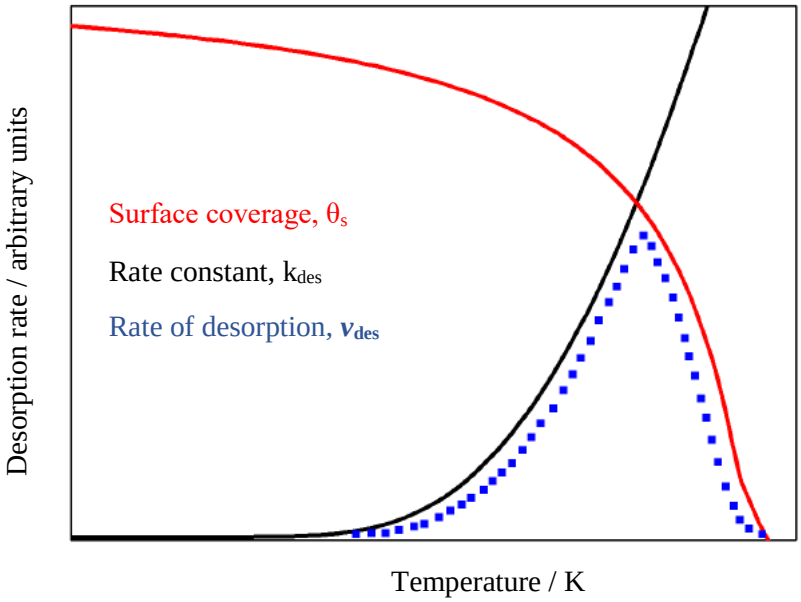

Figure 2.14: The plot shows the formation of a TPD trace. Molecules are deposited on to a surface (red curve) to a certain coverage, θ_s, before the sample is heated. As this happens, the coverage reduces and the rate constant, $k_{des,}$ increases (black curve). The point where the two curves intersect representing the maximum rate of desorption and area under the newly made curve, v_{des}, is proportional to the amount of the species deposited (blue curve) (Reproduced from [7]).

The area under the desorption trace indicates the surface coverage. However, there may be contributions from other sources, including other surfaces or species, which can prevent this [32].

The orders of desorption processes range from zero to first and second order (n = 0, 1 and 2 respectively), as shown in **Figure 2.15**. Fractional orders can also be observed. In order to determine the order of desorption, a number of experiments on the same species with different initial surface coverages must be carried out. When enough measurements have been taken, it is then possible to see a trend with coverage. Zero order (**Figure 2.15** top) desorption would normally be expected for desorption of a thick, multilayer film. The coincident leading edges and movement of the peak desorption temperature, T_{max}, to high temperatures with increasing coverage data is typical of zero order desorption kinetics. The first order (**Figure 2.15** middle) desorption process is consistent with desorption of non-weakly interacting species from sub-monolayer to monolayer coverages. The growth with increasing

coverage around a common T_{max} is typical of this kind of desorption. Second order desorption (**Figure 2.15** bottom) has coincident trailing edges and a T_{max} which moves to lower temperatures with increasing coverage. There are a number of ways this behaviour can be interpreted. The simplest is associated with adsorbates recombining before desorption. Where this does not happen, strong adsorbate-adsorbate interactions or a distribution of adsorbate-substrate binding energies could be attributed to this type of profile. Additional experiments would, of course, clarify the situation.

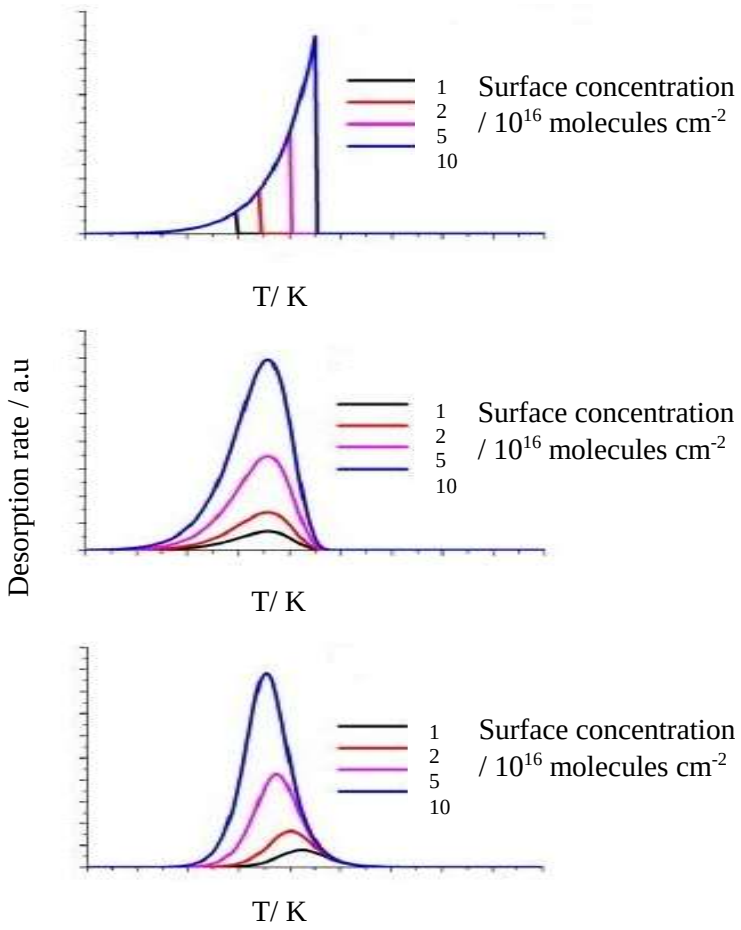

Figure 2.15: Kinetic order effects of the desorption process on the TPD curves. Zero order kinetics (**top**), where the leading edges align and most of the bulk material desorbs and the maximum temperatures move to higher ones as coverage increases (**top**), first order (**middle**) where all the peaks line up to the same peak temperature of desoprtion, which is likely for sub-monolayer desorption, with weak adsorbate-adsorbate interaction and second order (**bottom**) common trailing edge and T_{max} moving to lower temperatures can be interpreted as second order kinetics from a recombinative desorption system or reflecting a decrease in E_{des} with increasing coverage (Reproduced from [32]).

Figure 2.16 displays the TPD profiles for O_2, CO, N_2 and H_2O on amorphous silica; the left-hand panel displays high coverages, the right-hand one low coverages [33].

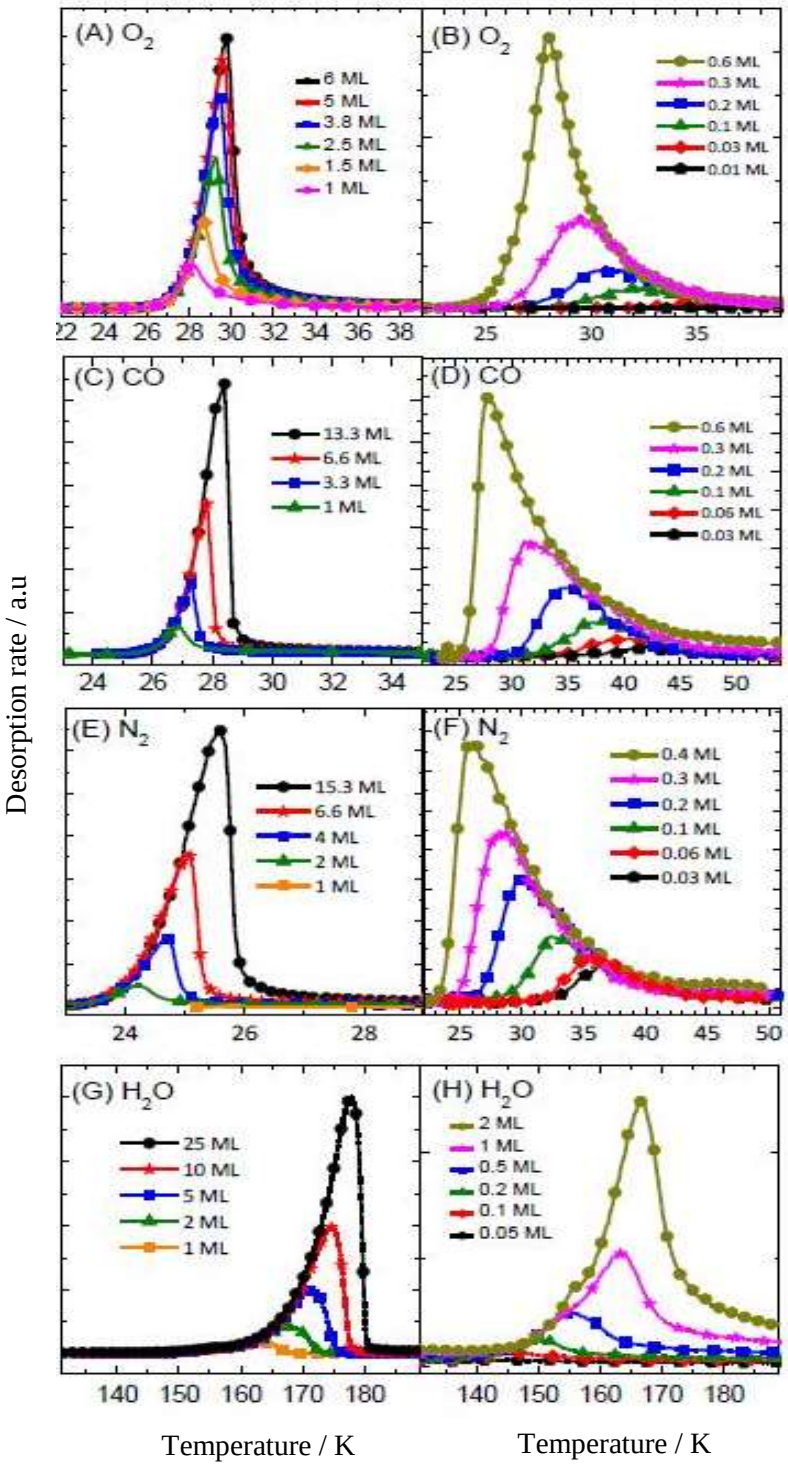

Figure 2.16: TPD profiles of O_2 (A-B), CO (C-D), N_2 (E-F) and H_2O (G-H) on amorphous silica (Reproduced from [33]).

The H_2O TPD profiles in **Figure 2.16** (G-H) for both low and high coverages demonstrate zero-order desorption, since the leading edges align and the maximum temperatures move to higher temperature as coverage increases. **Figure 2.16** also shows TPD profiles at high coverage (A, C and E) of O_2, CO, N_2 and H_2O on $aSiO_2$. For each of these molecules, the TPD profiles display coincident leading edges, as is typical of zero-order desorption, suggesting that molecules are desorbing from multilayer, where the lateral adsorbate-adsorbate interactions dominate. However at low coverage, the TPD traces of O_2, CO and N_2 show coincident trailing edges. This is typical of second order recombinative desorption but these molecules do not dissociate on silica at low temperature. The $aSiO_2$ surface presents a range of binding sites, with varied binding energies for adsorption [34]. The alignment of the trailing edges thus indicates that molecules which are located in the weaker binding sites desorb first, resulting in desorption peak broadening.

The kinetic parameters for multilayer desorption can be determined by a combination of Leading-Edge Analysis (LEA) [35], Arrhenius Analysis (AA) and kinetic modelling using the Chemical Kinetic Simulator (CKS) [32]. The starting point for all kinetic treatment of TPD is the desorption rate equation or Polanyi-Wigner Equation, **Equation 13**, which expresses the desorption rate r_{des} as a function of the surface concentration, N, of the adsorbed species at time t:

$$r_{\mathrm{des}} = -\frac{\mathrm{d}N}{\mathrm{d}t} = \nu_{\mathrm{des}} N^m \, \mathrm{e}^{-E_{\mathrm{des}}/RT} \qquad \textbf{(E13)}$$

The order of desorption, m, can be calculated using leading-edge analysis or by comparison of TPD profiles with **Figure 2.15**. By taking the natural logarithms of **Equation 13**, **Equation 14** is obtained:

$$\ln(r_{\mathrm{des}}) = \ln(\upsilon_{\mathrm{des}}) + m \ln(N) - \frac{E_{\mathrm{des}}}{RT} \qquad \textbf{(E14)}$$

Under isothermal conditions, there is a linear relationship between $\ln(r_{\mathbf{des}})$ and $\ln(N)$, from which the order is derived from the gradient. It is also clear that under constant coverage conditions, Arrhenius analysis using the linear relationship between $\ln(r_{\mathrm{des}})$ and $1/T$ yields the activation energy for desorption, E_{des}, from the

corresponding gradient (= -E_{des}/R). Alternatively, we can use Redhead analysis to estimate E_{des}. This is built around knowledge of T_{max}, *i.e.* the temperature at which the peak in the desorption trace occurs. However, orders of desorption are vital when determining the desorption energy, as in **Equation 15:**

$$\frac{E_{\mathrm{des}}}{RT_{max}^2} = \frac{\upsilon_{\mathrm{des}}}{\beta} mN^{m-1} \exp^{\left(-E_{\mathrm{des}}/RT_{max}\right)} \qquad \textbf{(E15)}$$

which is the general Redhead equation [2, 16]. This of course can be simplified given the desorption order and is based on the assumption that kinetic parameters are independent of surface coverage. However, this method does rely on an accurate determination of the pre-exponential factor (v_{des}). Hence, it is best to determine E_{des} when the pre-exponential factor is accurately known

The above represent ideal behaviour of desorbing moelculear layers. However, more complex interactions often occur, including fractional desorption orders and desorption pseudo-orders. In the case of fractional desoprtion orders, these have been noted in TPD experiments of CH_3OH in various cases [36,37] and is believed to be due to H-bonding in such molecules. Pseudo-order desorption arises from the nature of the surface. For example, taking an amorphous $aSiO_2$ surface which is rough and offers a range of binding sites for the sub-monolayer coverages of molecules, will see adsorbates on $aSiO_2$ diffusing and acquiring their most energetically favoured binding site before forming the monolayer. This results in a set of TPD plots which appear closer to second order, in comparision to first order, hence the designation pseudo-first order. Nevertheless, the molecules seen to be experiencing pseudo-first order desorption do not recombine on $aSiO_2$, hence second order desorption kinetics can be ruled out.

2.5 References

[1] J. Woodall, M. Agundez, A. J. Markwick–Kemper and T. J. Millar, *Astron. Astrophys.*, 2007, **466**, 1197.

[2] J. D. Thrower, *Ph.D. Thesis* (Heriot–Watt University, Edinburgh, 2009).

[3] R. L. Park, *Experimental Methods in Catalytic Research, Vol. 3*, Edited by R. B. Anderson and P. T. Dawson (Academic Press, New York, 1976).

[4] P. Atkins and J. de Paula, *The Elements of Physical Chemistry, 4th Edition* (Oxford University Press, Oxford, 1992).

[5] J. E. Lennard-Jones, *Trans. Faraday Soc.*, 1932, **28**, 333.

[6] M. R. S. McCoustra, *Advanced Physical Chemistry, Lecture 3*, (Heriot–Watt University, Edinburgh, 2018).

[7] A. Rosu-Finsen, *Ph.D. Thesis* (Heriot–Watt University, Edinburgh, 2016).

[8] R. I. Masel, *Principles of Adsorption and Reaction on Solid Surfaces* (Widely New York, 1996).

[9] *The Chemical Physics of Solid Surfaces Volume 11*, Edited by D. P. Woodruff (Elsevier, Amsterdam, 2003) pp225.

[10] D. King and M. G. Wells, *Surf. Sci.*, 1972, **29**, 454.

[11] https://hal.archives-ouvertes.fr/hal-00004273/document (last accessed 6/3/19).

[12] H. Chadwick and R. D. Beck, *Chem. Soc. Rev*., 2016, **45**, 3576.

[13] H. Chaabouni, H. Bergeron, S. Baouche, F. Dulieu, E. Matar, E. Congiu, L. Gavilan and J. L. Lemaire, *Astron. Astrophys.*, 2012, **538**, 128.

[14] M. P. Collings, J. W. Dever, H. J. Fraser and M. R. S. McCoustra, *Astrophys. Space Sci*., 2003, **285**, 633.

[15] M. P. Collings, J. W. Dever, H. J. Fraser, M. R. S. McCoustra and D. A. Williams, *Astrophys. J*., 2003, **583**, 1058.

[16] D. Marchione, *Ph.D. Thesis* (Heriot–Watt University, Edinburgh, 2015).

[17] J. E. Bartmess and R. M. Georgiadis, *Vacuum*, 1983, **33,** 149.

[18] R. W. Bittner and H. Hoffmann, in *Reference Module in Chemistry, Molecular Sciences and Chemical Engineering* (Wiley Online Library, 2018).

[19] R. G. Greenler, *J.Chem. Phys*., 1966, **44**, 310.

[20] R. Aroca, *Surface–Enhanced Vibrational Spectroscopy* (Wiley, Chichester, 2006).

[21] *Applied Polymer Science: 21st Century, 1st edition*, Edited by C. D. Craver and C. E. Carraher (Elsevier, Oxford, 2000) pp709.

[22] S. C. Street and D. W. Goodman, *Annu.Rev. Phys. Chem*., 1997, **48**, 43.

[23] O. S. Heavens, *Optical Properties of Thin Solid Films*, (Academic Press Inc, New York, 1955).

[24] K. I. Oberg, G. W. Fuchs, Z. Awad, H. J. Fraser, S. Schlemmer, E. F. van Dishoeck and H. Linnartz, *Astrophys. J*., 2007, **662**, L23.

[25] M. J. Loeer, G. A. Baratta, M. E. Palumbo, G. Strazzulla and R. A. Baragiola, *Astron. Astrophys*., 2005, **435**, 587.

[26] G. M. Munoz Caro, A. Jimenez-Escobar, J. A. Martın-Gago, C. Rogero, C. Atienza, S. Puertas, J. M. Sobrado and J. Torres-Redondo, *Astron. Astrophys*., 2010, **522**, A108.

[27] www.thermo.com.cn/Resources/200802/productPDF_21615.pdf (last accessed 21/11/18).

[28] W. G. Golden, D. D. Saperstein, M. W. Severson, and J. Overend, *J. Phys. Chem*., 1984, **88**, 574.

[29] www.thermo.com.cn/Resources/200802/productPDF_21615.pdf (last accessed 21/11/18).

[30] J. T. Yates, Jr., *Experimental Innovations in Surface Science* (Springer, New York, 1998).

[31] G. Attard and C. Barnes, *Surfaces* (Oxford University Press, Oxford, 1993).

[32] V. L. Frankland, *Ph.D. Thesis* (Heriot–Watt University, Edinburgh, 2011).

[33] M. P. Collings, V. L. Frankland, J. Lasne, D. Marchione, A. Rosu-Finsen and M. R. S. McCoustra, *Mon. Not. R. Astron.*, 2015, **449**, 182.

[34] J. D. Thrower, M. P. Collings, F. J. M. Rutten and M. R. S. McCoustra, *J. Chem. Phys*., 2009, **131**, 244711.

[35] D. A. King, *Surf. Sci*., 1975, **47**, 384.

[36] K. Christmann and J. E. Demuth, *J. Chem. Phys.*, 1982, **76**, 6308.

[37] M. Wu, C. M. Truong and D. W. Goodman, *J. Phys. Chem.*, 1993, **97**, 9425.

Chapter 3

UV/Visible Reflection – Absorption Spectrometer

3.1 Introduction

This chapter outlines the design and construction of a UV/visible reflection-absorption spectrometer and the initial results obtained from application of the instrument. Firstly, the design of the spectrometer will be discussed, followed by details of how the spectrometer was constructed. Finally, initial results demonstrating the use of the spectrometer are presented through collaboration with colleagues at the University of Sussex. The work presented in this chapter is a result of a number of contributions and they include:

1. The design, build and initial testing were carried out at Heriot-Watt University by S.Taj and M. R. S. McCoustra.
2. Initial experimental results for C_6H_6 were obtained at the University of Sussex by J. W. Stubbing, T. L. Salter and W. A. Brown.

The work in this chapter is reported in reference [1].

3.2 Light and Dust

Dust is widespread within the Universe, and directly or indirectly impacts most areas of modern astronomy. This is discussed in **Chapter 1**. In particular, dust is an absorber, scatterer, polariser and emitter of electromagnetic radiation [2], as summarised in **Figure 3.1**. This conceptual illustration shows the fundamental optical processes occurring in any icy grain illuminated by light; reflection, refraction, absorption and emission. Absorption can occur in both phases of the grain (the icy mantle and the core). Emission will follow absorption but at longer wavelengths due to relaxation of excited states in the solids.

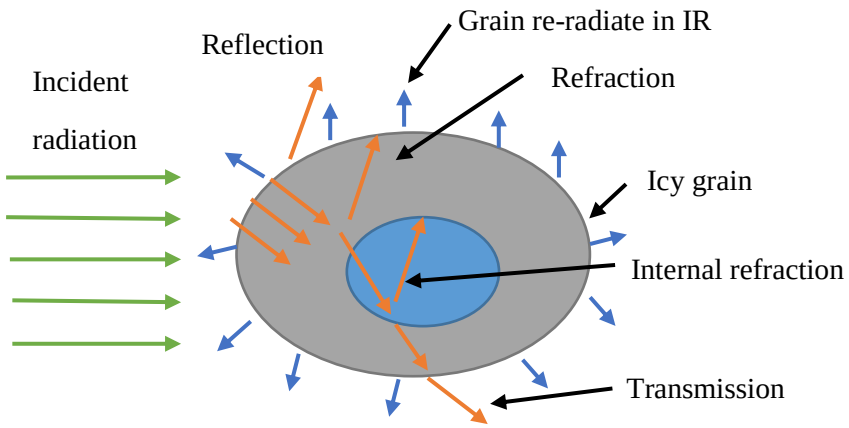

Figure 3.1: A conceptual illustration of the scattering of light by a dust grain [2].

All of these processes are dependent on the size, shape and chemical composition of the grains [2]. The fundamental optical processes of reflection and refraction are governed by simple rules, Snell's law for angles of refraction [3] and the Fresnel Equations for the intensities of reflection and refraction [4]. These depend on the refractive index $\hat{n}(= n + ik)$ of the substances involved. From knowledge of the relevant refractive indices, we can then determine how much light will be scattered (simply reflected) and how much will be absorbed (or transmitted).

For simple scattering processes, the spatial distributions observed in Rayleigh and Mie scattering are illustrated in **Figure 3.2** [5]. In Rayleigh scattering, there is no transfer of energy, linear or angular momentum between the optical field and the icy grains. The intensity of the scattered radiation for Rayleigh scattering is given by **Equation 1**:

$$I = I_o \frac{(1+\cos^2\theta)}{2R^2}\left(\frac{2\pi}{\lambda}\right)^4\left(\frac{n^2-1}{n^2+2}\right)^2\left(\frac{D}{2}\right)^6 \qquad \textbf{(E1)}$$

where n is the refractive index of the material, D is the grain diameter, λ is the wavelength and θ is the scattering angle. In Rayleigh scattering, we have essentially a point scattering centre (D << λ).

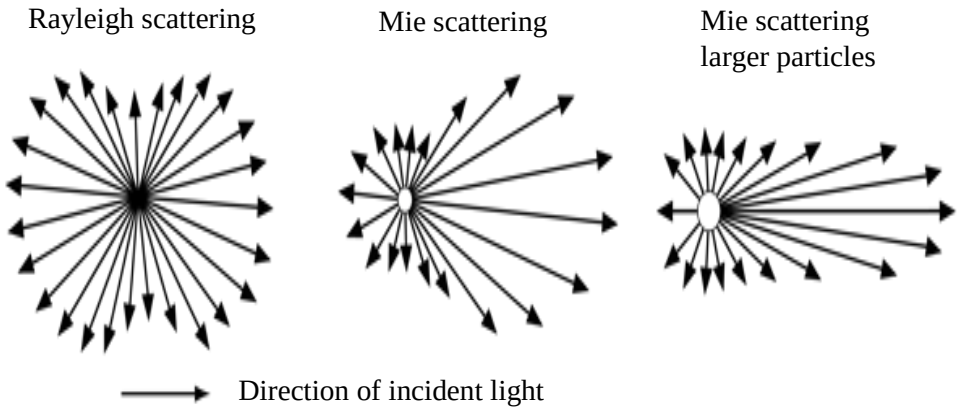

Figure 3.2: Rayleigh and Mie scattering. In the former, forward and backward scattering are balanced. In the latter forward dominates (Reproduced from [5]).

Integrating over a sphere surrounding the particle, the Rayleigh scattering cross-section, σ, is (**Equation 2**)

$$\sigma = \frac{2\pi^5}{3}\frac{D^6}{\lambda^4}\left(\frac{n^2-1}{n^2+2}\right)^2 \qquad \textbf{(E2)}$$

where λ is the wavelength of the light, D is the grain diameter and n is the refractive index. Mie Theory provides a more general approach to scattering for uniform particles. Mie Theory calculates coefficients for absorption (Q_a), scattering (Q_s) and extinction (Q_e) as efficiencies relative to the geometric cross-section of the scatterer [6];

$$Q_i = \frac{\sigma_i}{\pi a^2} \qquad \textbf{(E3)}$$

where the Q_i are the efficiencies for the interaction of radiation derived from cross sections, σ_i, normalised to the particle cross section, πa^2. The *i* represents extinction (ext), absorption (abs), scattering (sca), back-scattering (bsca), and radiation pressure (pr). Energy conservation requires that

$$Q_{ext} = Q_{sca} + Q_{abs} \text{ or } \sigma_{ext} = \sigma_{abs} + \sigma_{sca} \qquad \textbf{(E4)}$$

The relations for scattering and extinction are of the following form:

$$Q_e = \frac{2}{x^2}\sum_{n=1}^{\infty}(2n+1)\,Re(a_n + b_n) \quad \textbf{(E5)}$$

$$Q_s = \frac{2}{x^2}\sum_{n=1}^{\infty}(2n+1)(|a_n|^2 + |b_n|^2) \quad \textbf{(E6)}$$

where *a* and *b* are Mie scattering coefficients [6]. Mie scattering occurs when the dimensions of the scattering centre are much greater than the wavelength of the incident EM radiation as shown in **Figure 3.2.** Scattering is greater in the forward direction than in the backward. The combination of absorption and scattering is referred to as extinction, and represents the total loss of energy from the incident radiation field.

The radiative transfer problem describes the interaction between radiation and matter. It is a problem with applications in all sciences, and is generically described using the following equation [7]:

$$a.\nabla I(x,a,l) = -k(x,\lambda)\rho(x)I(x,a,\lambda) + j(x,a,\lambda) \quad \textbf{(E7)}$$

where the left hand side of the equation represents the change in intensity over an infinitesimal distance along a path determined by the position *x* and propagation direction a. $I(x,a,\lambda)$ describes the stationary radiation field by the specific intensity, *I*, at a location, *x*, in space, where *a* is the unit vector indicating the direction of the radiation and λ is its wavelength [7, 8]. The first term on right hand is a sink term representing mass extinction, $k(x,\lambda)$ where there is loss of radiation when radiation passes through matter of mass density $\rho(x)$. The second term, $j(x,a,\lambda)$, on the right hand represents the source term; the new luminosity released into the medium at *x* in direction *n*. The complexity of the radiative transfer equation depends on the nature of the source and sink terms (*e.g*. different physical processes that are responsible for the extinction and emission) [7]. Alternatively **Equation 7** can be expressed in the following form:

$$\frac{dI}{ds}(s,\lambda) = -k(s,\lambda)\rho(s)I(s,\lambda) + j(s,\lambda) \quad \textbf{(E8)}$$

which uses the distance *s* along the path defined by a position *x* and propagation direction *a* as a variable. Primary emission and absorption in a dusty medium are two key process, which need to be taken into account. Primary emission takes into account radiative energy, which is added to the radiation field and is mainly stellar emission. This can be characterised by a function $j_*(x, a, \lambda)$. Absorption is the processes in which EM radiation is taken up by dust grains and is converted into the internal energy. This is characterized by the absorption coefficient k_{abs} (for certain chemical composition, size and shape of a dust grain). Taking only primary emission and absorption by dust into consideration, **Equation 7** can be written as [7]:

$$\frac{dI}{ds}(x, a, \lambda) = -k_{abs}(x, \lambda)\rho(x)I(x, a, \lambda) + j_*(x, a, \lambda)_{\mathrm{x}} \qquad \textbf{(E9)}$$

Equation 9 is a first-order differential equation which can solved by integrating along the line-of-sight. However, in the case of interstellar dust, radiative transfer becomes far more complex when scattering is taken into account, which removes radiation from a beam and thus introduces a second sink term into the radiative transfer equation. This is quantified by the scattering coefficient, k_{sca}. Thus, **Equation 10** is obtained [7].

$$\frac{dI}{ds}(x, a, \lambda) = -k_{ext}(x, \lambda)\rho(\mathrm{x})I(x, a, \lambda) + j_*(x, a, \lambda) + j_d(x, \lambda) + k_{sca}\big((x, \lambda)\big)\rho(x)\int_{4\pi}\Phi(a, a'x, \lambda)\mathrm{I}(x, a', \lambda)\mathrm{d}\Omega' \qquad \textbf{(E10)}$$

k_{ext} (= k_{abs} + k_{sca}) is the extinction coefficient (*i.e.* the sum of the absorption and scattering coefficient respectively); and $\Phi(a, a'x, \lambda)$, describes the probability that a photon originally propagating in direction *a'* and scattered at position *x* will have *a* as its new propagation direction after the scattering event. The difficulties with **Equation 10** include [7]:

- This is a partial integro-differential equation in six dimensions;
- Dust emissivity is a complex non-linear function of the mean non-local intensity;

- Simulation requires significant computing power and complex algorithms;
- Geometry is often complicated (3D, inhomogeneous);
- Optical properties of the dust are relatively poorly known.

Hence, there is a need to experimentally determine the optical properties of astronomically relevant materials, *i.e.* dust and ices.

3.3 Optical Properties of Solid Films

3.3.1 Introduction

In astronomy, there are many challenges in understanding how electromagnetic radiation interacts with samples in both the gas and solid phases. Of relevance in this thesis are solids and in order to interpret astronomical observations of materials it is vital to know how they interact with electromagnetic radiation. The optical properties of a homogeneous material can be described by the complex refractive index (CRI), $\hat{n}$, and the thickness, *d*. Deposited on a substrate, the film optics (reflectance, transmittance and phase shifts) are described by generalised Fresnel Equations. However, determining the $\hat{n}$ and *d* of the film is a challenging task and a number of methods have been proposed [9]. One simple method is to infer the $\hat{n}$ value by measuring optical transmittance, *t*, and reflectance, *r*, of a film, provided the thickness, *d*, is known. A number of papers discuss methods ranging from manual graphic solutions to computer-based approaches [9]. The main problem arising from these is that, for certain values of *t* and *r*, small errors in the experimental data can result in big deviations of the resulting $\hat{n}$ value.

The optical constants of gases, liquids and room temperature solids have been studied extensively, but the optical properties of ices within the ISM are poorly understood due to difficulties in making these measurements [9]. Some of the studies have produced in contradictory results [10-14]. Accurate optical constants are, however vital. Furthermore valves for pure materials may not truly represent the complex solids produced by photochemistry and radiation chemistry in the ISM. Ideally we need to know how $\hat{n}\ (= n + ik)$ evolves for icy grains with time. For example Rocha

et al. [15] calculated $\hat{n}$ for a number of astrophysical water-containing ices bombarded by model cosmic rays. Laboratory spectral data provides band positions, shapes and intensities, while optical constants have been used in the interpretation of observational data. This includes vibrational bands which have been interpreted using laboratory data, and have led to the identification of icy species:

- The identification of H_2O at 3 μm has been identified in several sources [16] and the optical constants for H_2O in the amorphous phase ice at 10, 23 and 77 K along with crystalline phase at 150 K are known. These optical constants, along with the models for the radii of the underlying interstellar grains were used to generate fits to the observations;
- The laboratory absorption spectra of CH_3OH at 10 K are a good fit for the distinctive absorption feature found on the low-frequency wing of the H_2O band for several sources [17].

Dust grains within the ISM present a surface on to which molecules can accrete to form icy mantles [17], which are composed of various chemical species, *e.g.* water (H_2O), carbon monoxide (CO), ammonia (NH_3) and methane (CH_4). Reactions promoted by light, cosmic rays and heat take place in and on these icy grains' surfaces, increasing their chemical complexity, which also alters the way radiative transfer of energy take place within various regions of the ISM. This in turn changes the optical properties of the icy grains as described by the CRI [18]. Understanding the complex refractive index is vital for modelling this process [11, 15].

3.3.2 Thin Film Optics

In this work, thin films are used to represent icy dust grains. The analysis of the results is this chapter is based on using the Fresnel Equations [15, 18] and the method developed by Harrick [19] which is discussed further in **Section 3.3.4**. The Fresnel Equations describe the reflection and transmission of electromagnetic waves at an interface, when light moves between media of different refractive indices. The Fresnel Equations give the reflection and transmission coefficients for waves parallel and perpendicular to the plane of incidence; and the phase shift of the reflected light. **Figure 3.3** shows light moving from the medium of refractive index, n_i, into a second medium with refractive index n_{i+1} and the relevant

reflectance, r_{pq}, and transmittance, t_{pq}, which can be parallel (**Equations 11 - 12**) or perpendicular (**Equations 13 - 14**) to the surface.

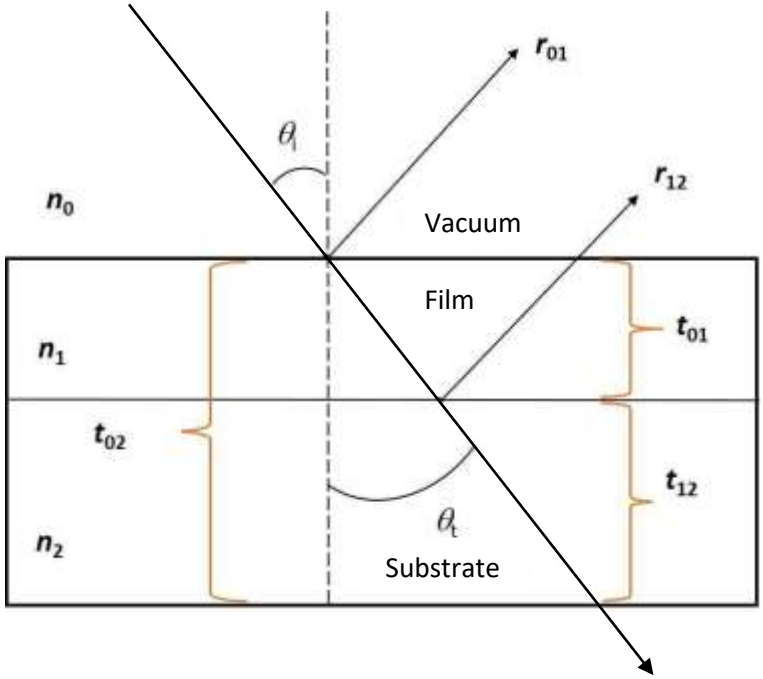

Figure 3.3: Schematic representation of an incoming ray interacting with a thin film (Reproduced from [20]).

$$t_{\parallel pq} = \frac{2\hat{n}_p \cos(\theta_i)}{\hat{n}_p cos(\theta_t) + \hat{n}_q cos(\theta_i)} \quad \textbf{(E11)}$$

$$r_{\parallel pq} = \frac{\hat{n}_q \cos(\theta_t) - \hat{n}_p \cos(\theta_i)}{\hat{n}_p \cos(\theta_t) + \hat{n}_q \cos(\theta_i)} \quad \textbf{(E12)}$$

$$t_{\perp pq} = \frac{2\hat{n}_p \cos(\theta_i)}{\hat{n}_p \cos(\theta_i) + \hat{n}_q \cos(\theta_t)} \quad \textbf{(E13)}$$

$$r_{\perp pq} = \frac{\hat{n}_q \cos(\theta_i) - \hat{n}_p \cos(\theta_t)}{\hat{n}_p \cos(\theta_i) + \hat{n}_q \cos(\theta_t)} \quad \textbf{(E14)}$$

where $r_{\parallel pq}$ is the reflection amplitude coefficient at the generic interface pq, $t_{\parallel pq}$ transmission amplitude coefficient, $\hat{n}_q$ is the refractive index of a generic phase q,

$\hat{n}_p$ refractive index generic phase *p*, θ_i is the angle of incidence and θ_t is the angle of transmittance. In a system that exhibits absorption as well as simple reflection, the refractive index of the material is complex linking the refractive index, *n*, to the absorption coefficient, *k*, in the manner *n* + *ik*. Analysis of angle-dependent reflection-absorption spectroscopic data can be used to determine *n* and *k* as a function of wavelength. The process of finding optical constants is an iterative one, where the simulated spectra are compared with the experimental data until a good agreement is reached, as summarised below **(Figure 3.4)**:

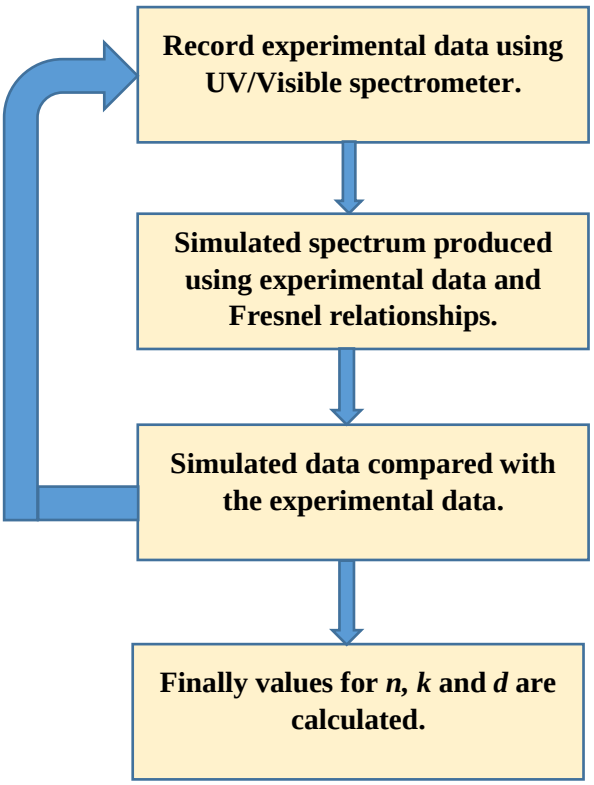

Figure 3.4: The iterative process used to find the optical constants, *n*, *k* and *d* [1].

3.3.3 Methods for Calculating the Complex Refractive Index (CRI) and Film Thickness

All the methods for calculating CRI and film thickness fundamentally rely on Snell's Law and the Fresnel Equations. However, the majority of methods in the literature make use of the Kramers-Kronig relationship as a simplification and this is illustrated by the work of Rocha *et al*. [15, 18]. There are a number of methods which can be used to calculate the CRI but they need an accurate value for the thickness in order to calculate the optical constants. Illustrative of this is the work by Rocha *et al*. [15] and Rocha and Pilling [18] who calculated complex refractive indices using the NKABS code, a Python-based code of which full details are given in [10, 16]. The optical constants are calculated in the infrared range, directly from the absorbance data of thin films which have been acquired in the laboratory but this could be extended to UV. Additionally, the code can be used to calculate the optical constants of materials that have been processed by radiation. The code uses the Lambert-Beer Law and Kramers-Kronig relationship to calculate *n* and *k*. The code can be split into four components and they are briefly described below:

1. The imaginary part *k* is calculated using the Lambert–Beer Law:

$$\alpha\ (\mathrm{cm}^{-1}) = \frac{1}{d}\left(2.3\ \times Abs_{\nu}\ + \ln\left|\frac{\hat{t}_{01}\hat{t}_{12}/\hat{t}_{02}}{1+\hat{r}_{01}\hat{r}_{12}\mathrm{e}^{2\mathrm{i}\dot{x}}}\right|^{2}\right) \qquad \textbf{(E15)}$$

$$\alpha\ (\mathrm{cm}^{-1}) = 4\pi\nu k \qquad \textbf{(E16)}$$

where α is the absorption coefficient, *d* is the thickness (cm) of the ice, Abs_{ν} is the absorbance in the infrared, $\hat{t}_{12}$, $\hat{t}_{02}$, $\hat{t}_{01}$ and, $\hat{r}_{12}$ are the Fresnel coefficients of transmission and reflection, $\dot{x} = 2\pi\nu d\hat{n}$, in which ν is the wavenumber and $\hat{n}$ is the complex refractive index. In this first step the code evaluates **Equation 15** and then calculates *k* using **Equation 16**.

2. The second part of code calculates the real part of the refractive index by using the Kramers- Kronig relationship, **Equation 17**,

$$n(v) = n_o + \frac{2}{\pi} \wp \int_{\nu_1}^{\nu_2} \frac{\nu' k(\nu')}{\upsilon'^2 - \nu^2} \mathrm{d}\nu' \quad \textbf{(E17)}$$

where n_o is the refractive index and the $\wp$ is the Cauchy principal value.

3. This step calculates the theoretical infrared spectrum and is compared to the one calculated in the laboratory.
4. Final step is where the best values of *n* and *k* are obtained *via* analysis of the error, in comparing the theoretical and laboratory spectra.

In this method, the major source of error in the values of *n* and *k* comes from the measurements of the integrated absorbance of specific bands in the infrared spectra and the sample thickness. Using this method, the error is found to be around 12% for *n* and *k* [3]. **Figure 3.5** illustrates the computational procedure of the NKABS code where the input parameters are sample thickness *d*, standard refractive index in the visible range n_o, refractive index of the substrate n_2, the absorbance data in the IR and calculation error, which is expressed in terms of the Mean Absolute Percentage Error (MAPE) along with the given chi-square function χ^2 [18].

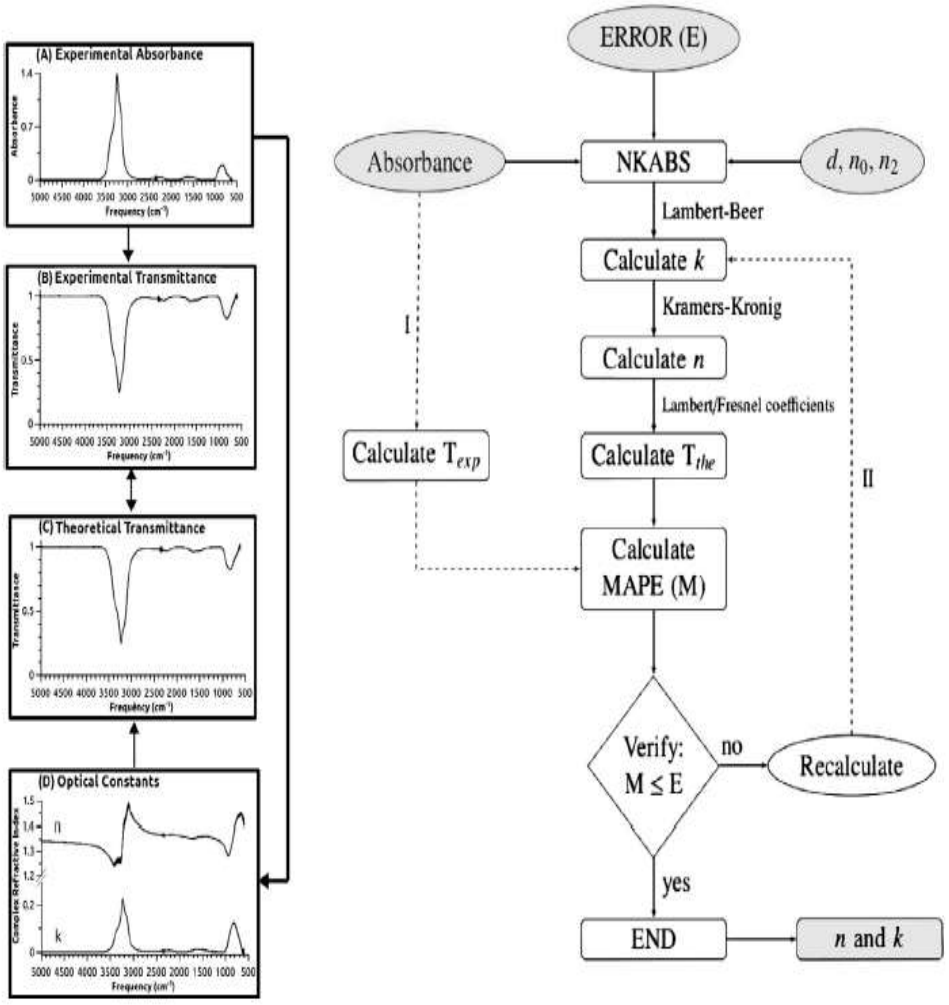

Figure 3.5: Implementation of the NKABS code. (**A**) Shows the absorbance data for crystalline water at 195 K, while (**B**) and (**C**) display the experimental and theoretical transmittance. (**D**) Optical constants for crystalline water, where the arrows indicate the path executed by the code in calculating the optical constants. The right-hand side shows a flow chart indicating how the code executes (Reproduced from [18]).

This code has the advantage of allowing the optical constants to be calculated directly from the absorbance data more accurately than other available codes [4, 21]. Rocha and Pilling [18] calculated the optical constants in the infrared spectral region for 28 different samples, which are of astrophysical interest at different temperatures (10-300 K) using the NKBAS code. **Figure 3.6** and **3.7** shows some of the values for *n* and *k,* which have been calculated using the NKABS code and those which are available in literature. The residuals are the difference between the literature and NKABS code values of *n* and *k,* where the difference between the literature and NKABS values is 0.8% for *n* and 0.9% for *k* [18].

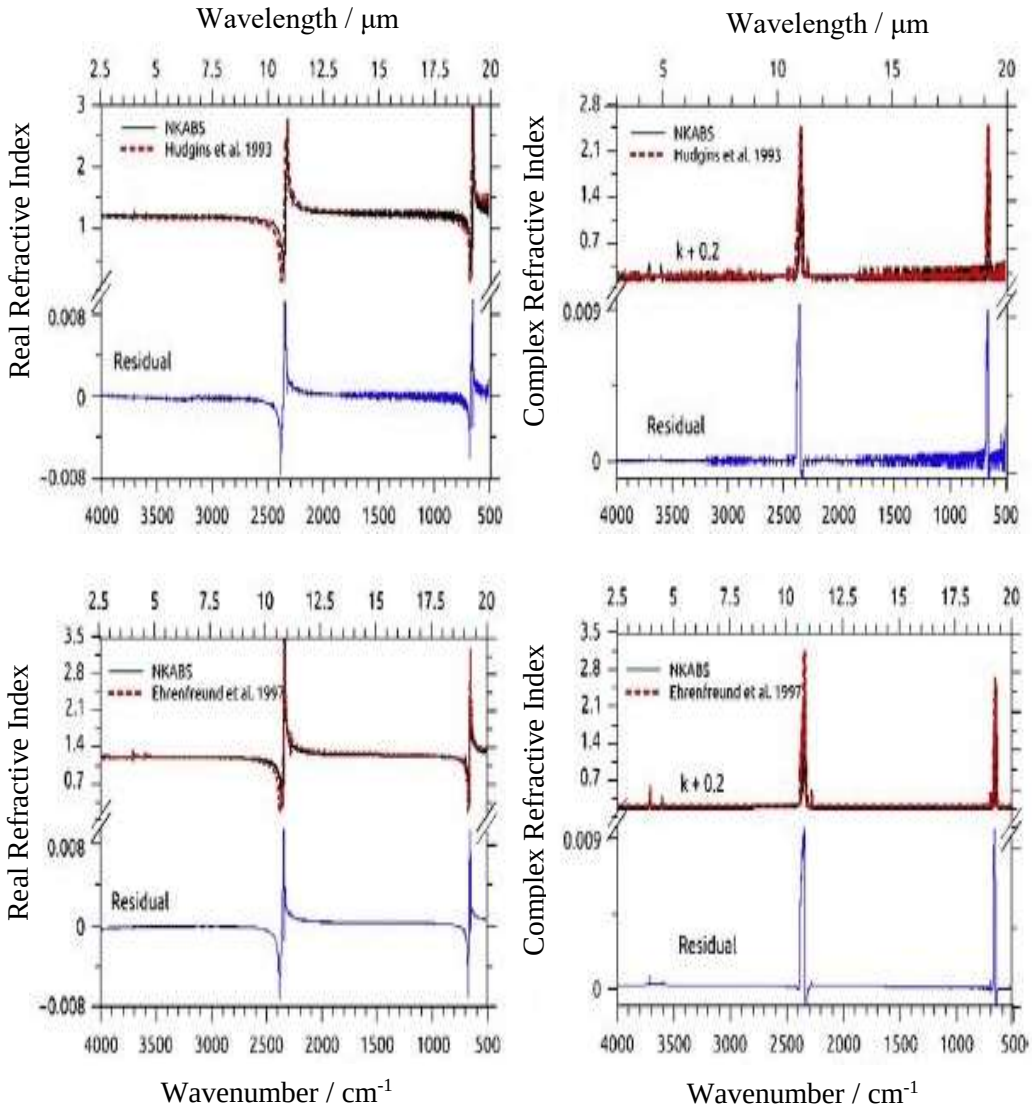

Figure 3.6: The optical constants calculated (left hand side CO_2 and CO right hand side) using the NKBAS (continuous black) code and those available in the literature (dashed red line) Hudgins *et al.* [11] and Ehrenfreund *et al.* [13] .The residual is shown as a continuous blue line (Reproduced from [18]).

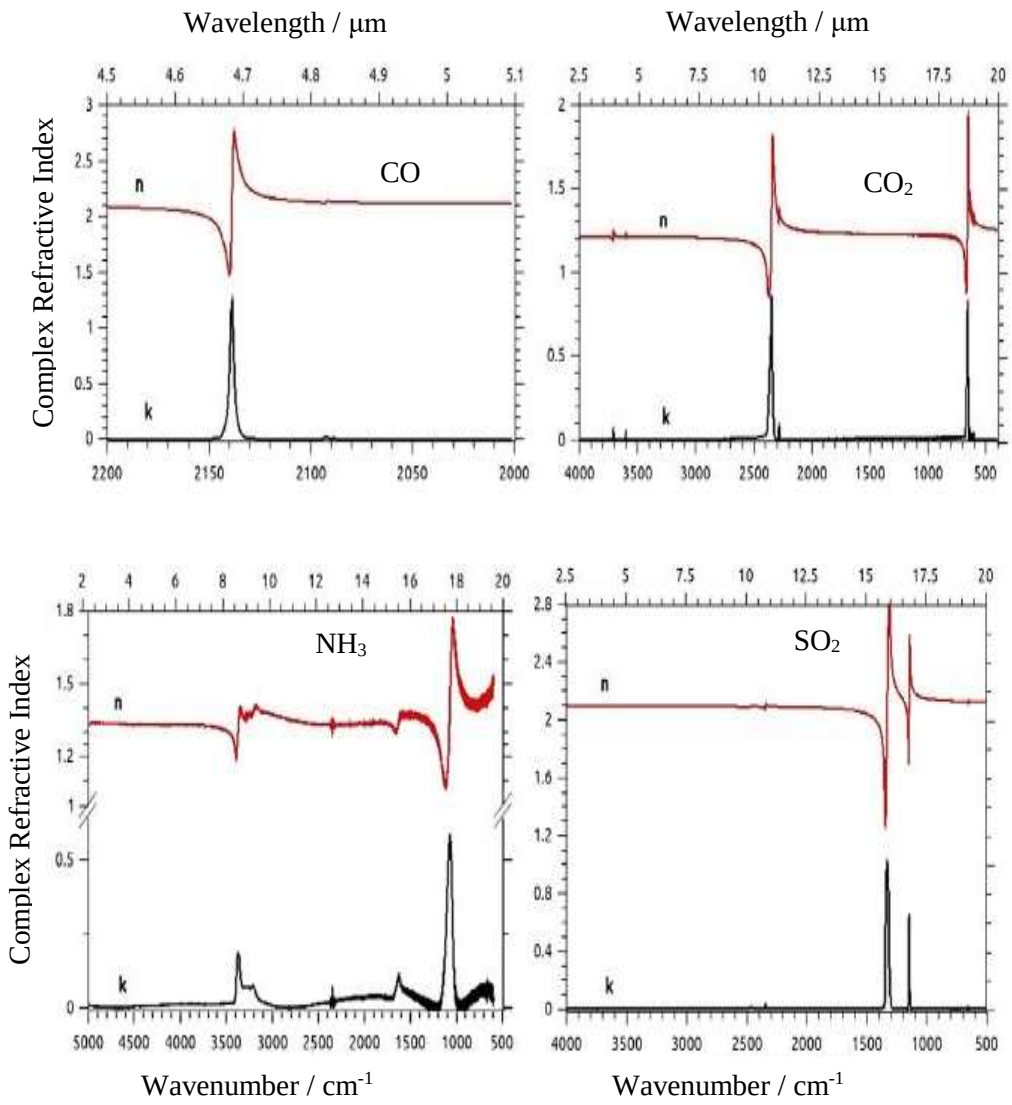

Figure 3.7: The optical constants which have been calculated using the NKBAS code from the absorbance spectra of thin films (CO, CO_2, NH_3 and SO_2) (Reproduced from [18]).

The results shown in **Figure 3.7** and **3.8** are important in the astrophysical context where the conditions for condensation of molecules onto dust grains forming ice mantles is favourable. In some cases, ices are formed by pure molecules, *e.g*. CO, CO_2 and NH_3 (**Figure 3.7**). In other situations, the interstellar ices or Solar System ices are composed of mixtures of frozen molecules and the typical optical constant for such ices is shown in **Figure 3.8**.

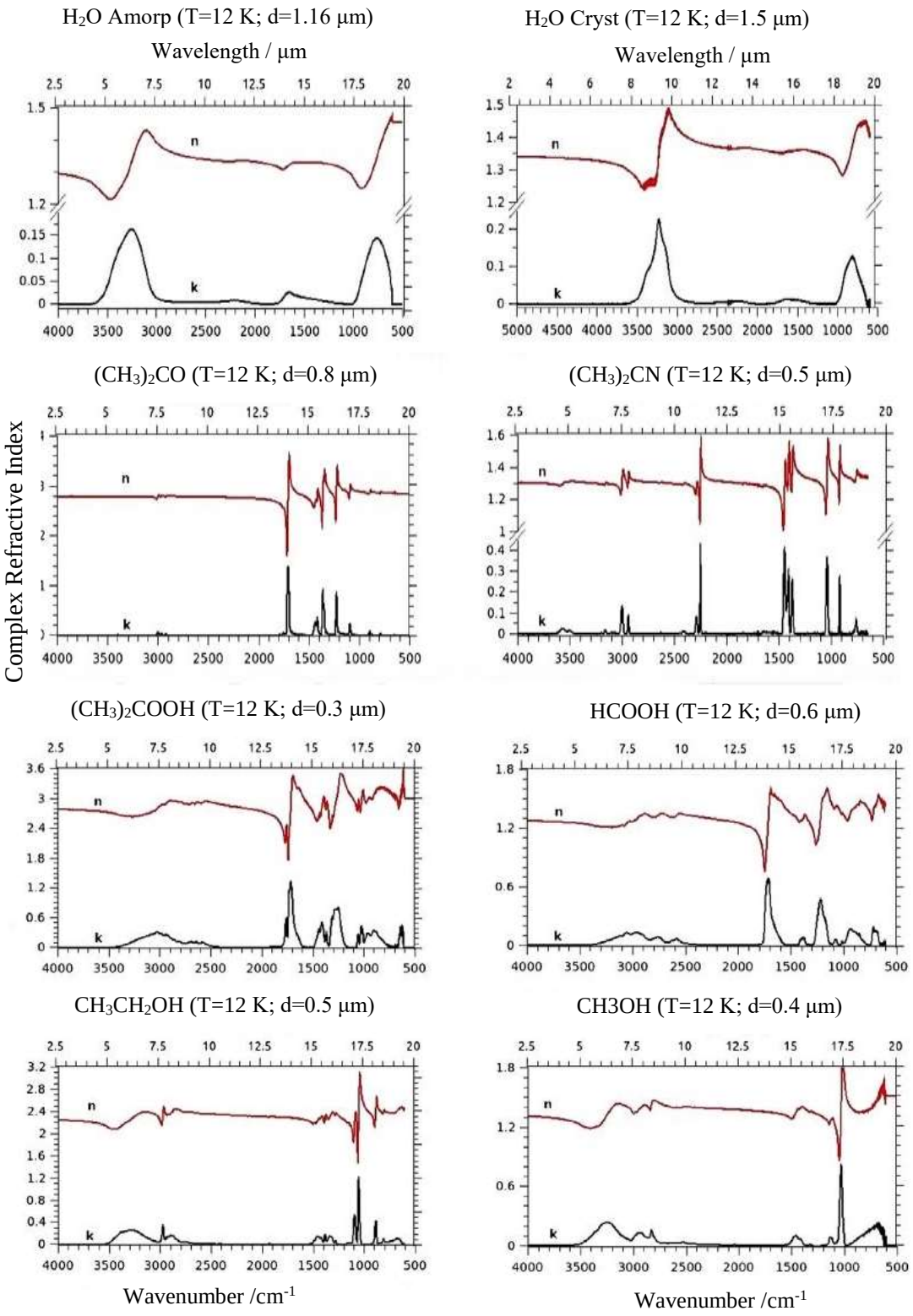

Figure 3.8: The optical constants of thin films produced *via* vapour condensation over cold surfaces of sublimated pure liquids, H_2O amorphous, H_2O crystalline, $(CH_3)_2CO$, CH_3CN, CH_3COOH, HCOOH, CH_3CH_2OH, CH_3OH and c-C_6H_{12} (Reproduced from [18]).

However, depending on the temperature of the grains, the water can be in different crystalline phases *e.g.* amorphous around 20 K and crystalline at around 160 K,

Figure 3.9. Values of *n* and k which have been calculated at low temperature should be used with caution at high temperature, and *vice versa*. Rocha *et al.* [15] also calculated the complex refractive indices using the NKABS code in the infrared from 5000 to 600 cm^{-1} (2.0 - 16.6 μm) for 13 water-bearing ices processed by model cosmic rays which are indispensable in astronomical scenarios. **Figure 3.9** shows some the results from running the code and full results are shown in Rocha *et al.* [15]. The panels display the real and imaginary parts at different wavenumbers in the infrared. The results shows that CRI changes with the projectile fluence during irradiation.

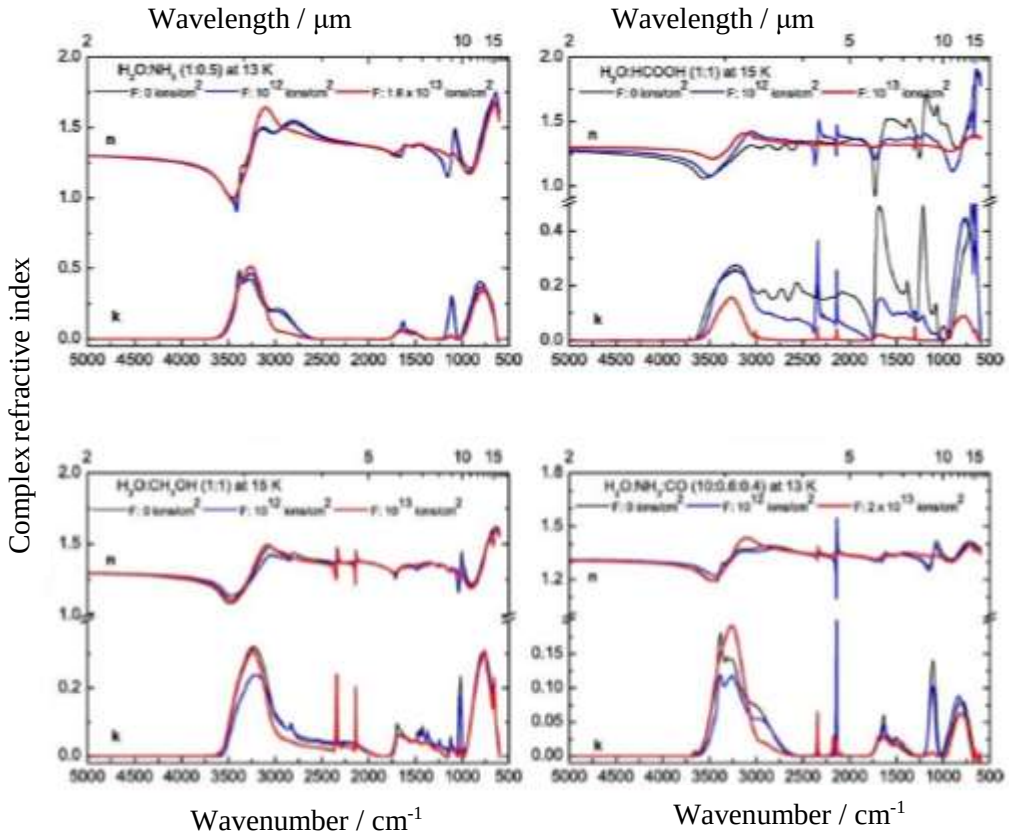

Figure 3.9: The complex refractive index of H_2O:CO_2 (1:1) at 13 K, H_2O:CH_4 (1:1) at 16 K and H_2O:CH_4 (1:1) at 16 K, and H_2O:CH_4 (10:1) at 16 K at different ion fluences. The black line indicates the unprocessed ice spectrum, and blue line denotes an ice spectrum at intermediary fluence, and the red line ice spectrum at the final fluence (Reproduced from [15]).

The changes observed depend on the initial ice composition and radiation fluence; and they point to the appearance of new species in the sample as the parent species

are destroyed and morphological changes occur in the sample. The data presented in **Figures 3.7 - 3.9** can be used for example in radiative transfer codes, determining more realistic simulations of the chemical evolution in astrophysical environments.

3.3.4 Determining Film Thickness

In the work discussed above, film thickness, *d*, is a vital parameter when calculating *n* and *k* values. However, film thickness is not easily determined. Laser interference measurements are the most common approach to such measurements [22-24]. Typically, thickness can be independently determined by using a He-Ne laser reflected off a surface, resulting in interference fringes during the deposition. The interference fringes are used to calculate the thickness, *d*, from in **Equation 18** [22, 26-32]**:**

$$d = m(\lambda) / \left(2\sqrt{n^2 - sin\theta}\right) \qquad \textbf{(E18)}$$

where $m(\lambda)$ is the number of complete fringes observed and θ is the reflection angle with respect to the surface normal. The issue with this method is that, when calculating thickness, if the substrate is rotated for deposition, irradiation and spectra collection and the sample is not returned to the identical position then, errors in thickness calculations can result. This in turn leads to errors in evaluation of the complex refractive index values [5]. Some studies of molecular ices have used an assumed value for *n* where experimental values are unavailable [10, 13]. A number of studies have been carried out and have determined the film thickness for a range astrophysically relevant ices using interference fringes [26-32], including CO frozen in non-polar ices containing N_2, CO_2, O_2 and in H_2O [14], and amorphous and crystalline HNO_3 / H_2O [29].

A further issue with this approach is that thickness is measured during deposition (*e.g.* unprocessed ice), and any processing affecting the thickness after it has been deposited cannot be measured. In this instance, ice thickness can be determined using the integrated band strength, *A*, along with the density, ρ [33-36]. Other experiments, however, have [18] demonstrated that it is possible to calculate the thickness of unprocessed ices from absorbance spectra using **Equations 19** and **20**:

$$d(\mu\text{m}) = \left(\frac{N}{\rho}\ \frac{M}{N_A}\right) \times 10^3 \qquad \textbf{(E19)}$$

$$N = \frac{2.3}{A} \int_{\nu_2}^{\nu_1} Abs_\nu \, \text{dv} \qquad \textbf{(E20)}$$

where N is the column density (mol/cm^2), ρ is the specific density (g/cm^3) of the film, M is molar mass (g/mol) of the film, N_A is the Avogadro number, A is band strength of the molecular vibration and Abs_ν is the absorbance measured in the laboratory. The errors are due to uncertainties from the band strength and density values used [22]. A number of authors have used band strengths obtained from the literature [34], where those values have been estimated for pure ices *e.g*. H_2O, CO, CH_3OH. This has the advantage of allowing the measurement to be taken at any time during the experiment, rather than just during the deposition process. This also allows decoupling of the thickness from the assumed value of the refractive index. However, this can be an issue if the experimental conditions are not the same as those outlined in the literature. For example, values are taken from the spectrum of pure ices when mixed with those being investigated [15]. Ice densities are either assumed to be equal to those of water [11, 33, 34] or a weighted average of individual ice constituents. Real densities do not follow this behaviour [28], and depend on the molecule and growth conditions for the ice [29]. A more reliable method is needed for measuring the film thickness under conditions which aim to reproduce those of the ISM. The work of Romanescu *et al.* [37] is illustrative and involves a He-Ne laser split into three beams, which reflect from an ice sample deposited on a gold substrate at different angles of incidence (**Figure 3.10**):

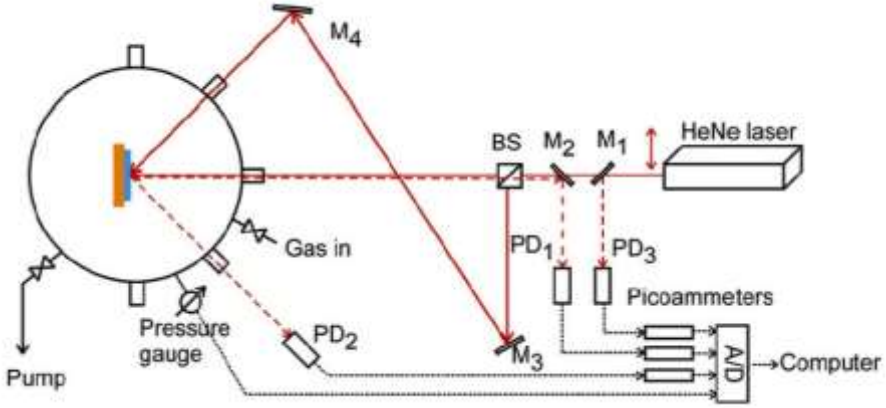

Figure 3.10: Schematic of the experimental apparatus (M: mirror, BS: beamsplitter, PD: photodiode, A/D: analogue-to-digital converter) (Reproduced from [37]).

The period of the interference patterns is recorded as a function deposition time, as shown in **Figure 3.11**. Ishikawa *et al*. [38] have demonstrated a method which uses multi-wavelength laser interference at numerous incident angles to calculate *d*. Other similar studies have been carried out using double-laser interference to look at pure ices and binary mixtures of CO, molecular N_2 and CH_4, all of which are relevant to the ISM [28-29]. The approach taken by Romanescu *et al*. [37] and Ishikawa *et al.* [38] has the disadvantage of not recovering the refractive index.

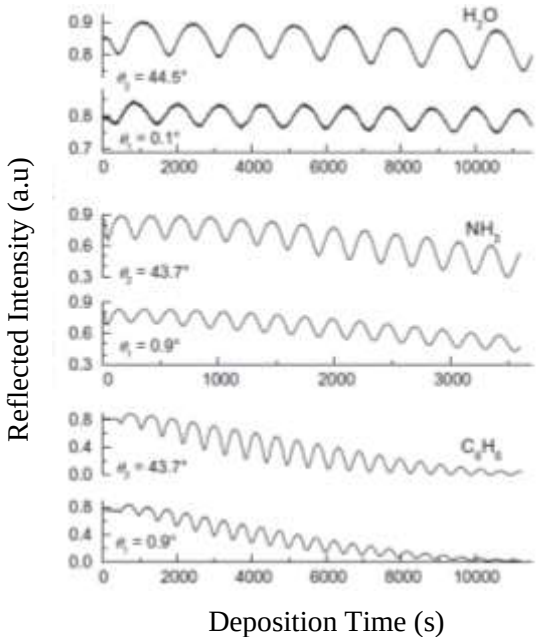

Figure 3.11: Reflected intensity data for water ice at 80 K (top), ammonia ice (middle) and benzene ice at 100 K (bottom) (Reproduced from [37]).

The methods discussed above use independent experimental procedures to calculate *n* and *d*. To start with, *n* is calculated using a reference film along with two reflection angles, and *d* is then determined during a second deposition, using the method demonstrated by Ishikawa *et al*. [38]. These limitations can be overcome by using the reflection-absorption UV/visible spectrometer designed at Heriot-Watt University, which records spectra over a wide range of reflection geometries. This allows *n* and *d* to be calculated for ice films using a dataset from a single set of measurements, and the analysis method based on the work by Harrick [19]. This was developed to analyse reflection–absorption spectra in the infrared. The method uses interference fringe patterns recorded at different angles of incidence. Basically, we have:

$$\sin\theta = n\sin\phi \qquad \textbf{(E21)}$$

$$2nd\cos\phi = m\lambda = m/\nu \qquad \textbf{(E22)}$$

$$2nd\cos\phi = \left(m + \frac{1}{2}\right)\lambda = (m + \frac{1}{2})/\nu \qquad \textbf{(E23)}$$

Equation 21 is Snell's Law, in which θ is the angle of incidence and ϕ is the angle of refraction for light propagating from vacuum to a film with refractive index *n* and thickness *d*. Where the reflection is at a fixed angle, **Equations 22** and **23** give the locations of the fringe minima and maxima for perpendicular or parallel polarisation for the free-standing film. Here, *m* is the order of the fringe, λ is wavelength of the light and *v* is the wavenumber. The refractive index can be calculated (**Equation 24**) by measuring the spacing between the adjacent fringes $\Delta\nu_1$ and $\Delta\nu_2$ for two sets of interference patterns recorded at two different angles of incidence [19].

$$n = \left[\left(\sin^2\theta_1\Delta{\nu_1}^2 - \sin^2\theta_2\Delta{\nu_2}^2\right)/\Delta{\nu_1}^2 - \Delta{\nu_2}^2\right]^{1/2} \qquad \textbf{(E24)}$$

$$d = \Delta m/2(n^2 - \sin^2\theta)^{1/2}\,\Delta\nu_{if} \qquad \textbf{(E25)}$$

where $\Delta m = m_i - m_f$ is the number of fringes between the initial and final fringe counted and $\Delta\nu_{if} = \nu_i - \nu_f$ is the wavenumber difference between the initial and final fringe. If the refractive index is known, the film thickness, *d*, can be calculated from

a single-fringe pattern recorded at any angle of incidence (**Equation 25)**. Here, the accuracy of d depends on the accuracy of measuring the fringe spacing $\Delta\nu$, which can be increased by using more fringes.

3.4 Instrument Design and Assembly

The main requirement for the spectrometer is to measure for astrophysically relevant ices, reflection-absorption spectra in the UV/ Visible at various angles and hence allow film thickness and optical constants to be estimated for conditions mimicking the cold, dense environments of the ISM. It has been shown that to measure the film thickness and optical constants, transmission and/or reflection spectra need to be measured across the wavelength range at variable angles ranging from the near-normal to grazing. A summary of the key requirements for the spectrometer are:

1. UHV operation and UHV-compatible materials;
2. Optical fibre coupling of the light source to the detector;
3. Wide wavelength range (200 - 800 nm);
4. Good spectral resolution (1 nm);
5. Variable angle of incidence (20 - 80°).

The instrument had to be designed and built from UHV-compatible materials, since it will be operating in a UHV environment mimicking the ISM. The requirement to operate in a variable angle mode was solved by considering compressing or extending a square along one of its diagonals, *i.e*. rhombic distortion. This provides a method for coupling a linear motion to an angular change over the range of angles of interest. **Figure 3.12** shows the fundamental design sketch for the rhombic assembly.

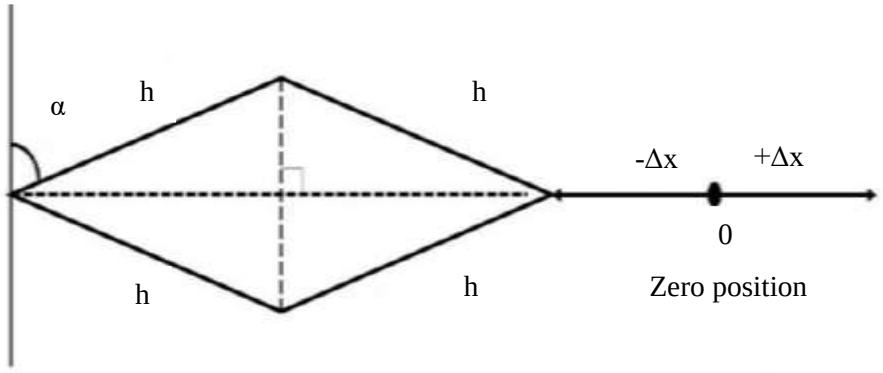

Figure 3.12: A drawing of the rhombic element used to construct the variable angle UV/visible spectrometer.

In **Figure 3.12,** the angle of incidence and of reflection of the optical beam, α, is represented by **Equation 26**:

$$\alpha = 90 - \frac{180}{\pi}\cos^{-1}\left(\frac{h\sqrt{2} \pm \Delta x}{2h}\right) \qquad \textbf{(E26)}$$

where *h* is the length of the square edge (30 mm) and Δ*x* is the linear shift which can be positive or negative from the zero position, as shown in **Figure 3.12**. The fibre-optic components were supplied by Ocean Optics (fibre-optic assemblies for UHV, collimating lenses, UHV feed-through) and Fibredesign (the right-angled fibre mounts). The assembly, along with the fibre optics, is mounted on a Vacgen linear drive (LMD925) with an attached millimetre scale, henceforth referred to as a z-shift, to which a CF70 - CF250 zero length adapter is fitted. The initial testing was carried out at Heriot-Watt University before the instrument was shipped to the University of Sussex. **Figure 3.13** shows the constructed rhombus being bench tested before integration into the UHV system at the University of Sussex. **Figures 3.13a** and **b** show how the variable angle rhombic assembly allows for angular variation by linear adjustment external to the UHV system.

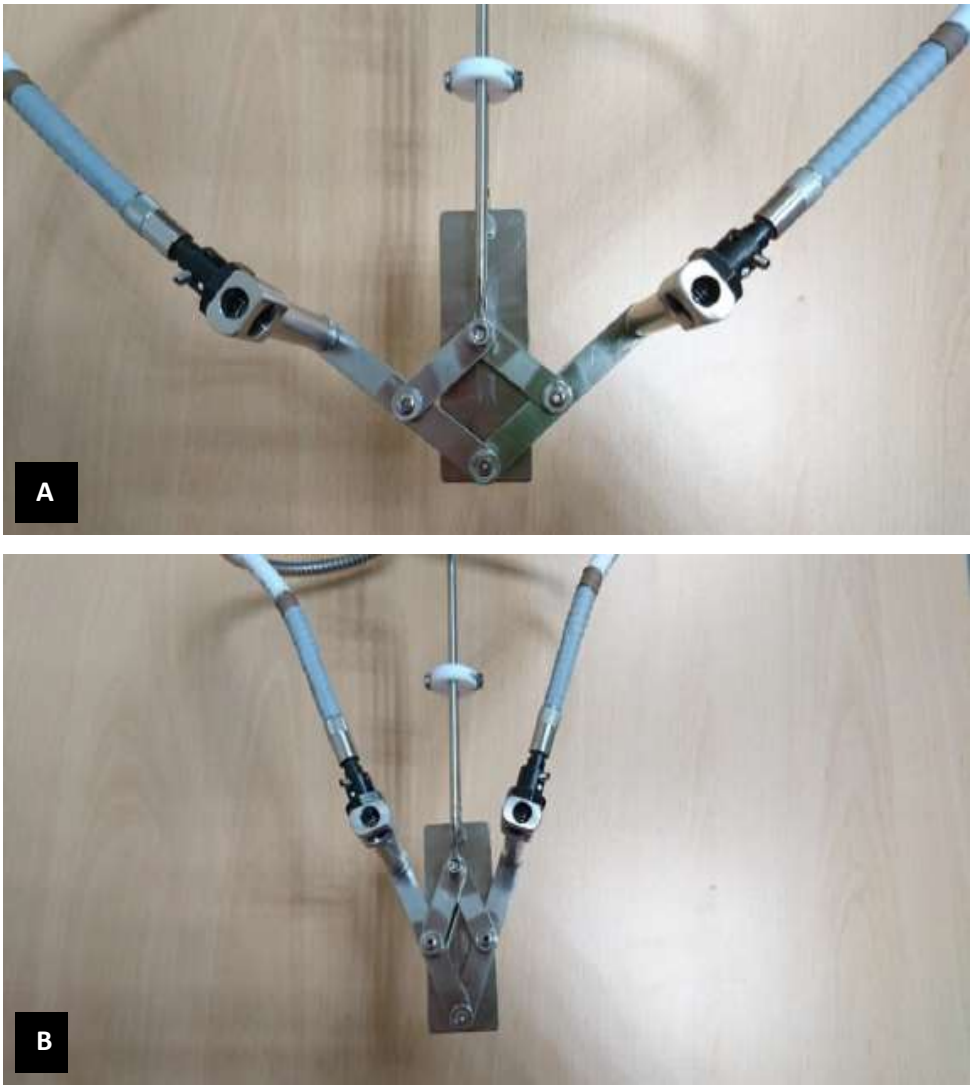

Figure 3.13: Shows the completed rhombic assembly which is part of the complete UV/visible spectrometer. (**A**) and (**B**) show how the variable rhombic assembly allows angular variation. This is achieved by external linear adjustment from outside the UHV chamber (Reproduced from [1]).

The next step after assembling the spectrometer was to test the validity of **Equation 26** by measuring α as a function of Δx, the change in position of the linear motion drive from its rest position. The zero position is defined as $\Delta x = 0$, and at this position α is 45°. **Table 3.1** shows the measured angles as Δx is incremented in steps of ±5 mm.

Δx / mm	α / º
+15	30
+10	35
+5	40
0	45
-5	50
-10	56
-15	70
-20	75

Table 3.1. Shows the change in the angle of incidence and reflection, α, with compression (+) or extension (-) of the external linear drive on the spectrometer, where angle α is calculated using **Equation 26** [1].

Figure 3.14 gives a comparison of the measured angle variation with the position on the z-shift scale with data derived from **Equation 26**. The experimental data is consistent with the model where the edge length h is 30 mm. The consistency of the experimental data with model data in **Figure 3.14** validates design of the instrument and **Equation 26**. Taking into consideration the dimensions of the real materials used to manufacture the rhombus, a small deviation from this calculated angle is expected.

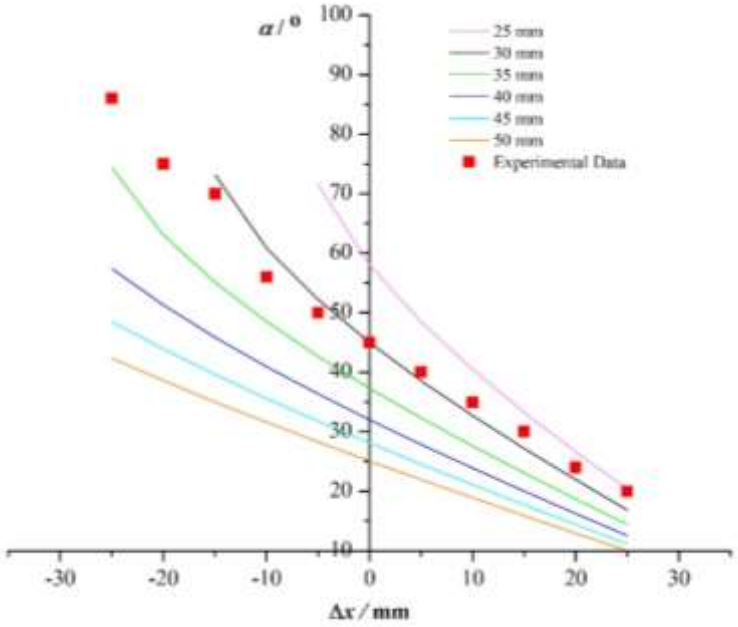

Figure 3.14: The z-shift position *versus* α (as given by **Equation 26**) showing both the data in **Table 3.1** and model calculations for h = 25-50 mm in 5 mm steps.

The completed assembly is connected to a fibre-coupled light source (Ocean Optics DH-2000-S-DUV-TTL) and spectrometer (Ocean optics QE Pro) for additional testing, as is discussed below.

3.5 Why Investigate Benzene (C_6H_6)?

3.5.1 Introduction

Polycyclic aromatic hydrocarbons (PAH), and related species, are thought to play a key role in the chemical evolution of the ISM. PAH-like species are thought to account for up to 30% of galactic interstellar carbon [42], and have been associated with the astrobiological evolution of the ISM [43]. They are thought to provide nucleation sites for the formation of carbonaceous dust particles [44]. PAH's are believed to be the source of diffuse interstellar bands (DIBs), and are associated with the unidentified infrared (UIR) emission bands observed in the 3-4 μm range. UIR bands have been observed towards the Cigar Galaxy M82 and DIBs are widespread in the ISM [45]. Benzene (C_6H_6) is one of the smallest cyclic aromatic molecules, and is abundant on the Earth in petrol, plastics *etc*., and within the Solar System, in particular in the atmospheres of Jupiter and Saturn. It is a difficult molecule to detect, since its emission lies in the infrared region and is not directly observable from ground-based instruments. However, the Infrared Space Observatory (ISO) detected C_6H_6 in the protoplanetary nebula (PPNe) CRL 618 [46, 47] and C_6H_6 has also been detected in Large Magellanic Clouds object SMP LMC 11 [56, 57].

The detection of C_6H_6 in CRL 618 is important, since it marks the beginning of an astrochemistry that is not mainly based on linear carbon chains and small molecules. Having an understanding of chemistry in which rings such as C_6H_6 form will help to understand the formation processes behind prebiotic molecules [48]. C_6H_6 is thought of as a prototypical PAH, and has been the subject of a number of computational and experimental studies in order to better understand its electronic structure [34]. A considerable amount of laboratory work in astrochemistry has focused on IR spectroscopy and TPD studies in order to better understand the physical and chemical properties of condensed molecules on cold surfaces [45]. More recent studies have shown that vacuum ultraviolet (VUV) spectroscopy can

be an additional tool in helping to understand the properties of condensed films [48]. The highly vibrational excited states of these aromatic compounds are consistent with observed spectroscopic features in the IR [49], along with UV-Visible [50] in numerous interstellar lines-of-sight. Thus, from an astrophysical point of view, C_6H_6 is a highly interesting PAH. This is partly why it was used in the experiments carried out at the University of Sussex.

3.5.2 Formation of C_6H_6

The formation mechanism for this simplest building block of the PAH family has remained elusive for a considerable period of time. C_6H_6 and small condensed-phase PAHs are likely to be widespread in cold and dense molecular clouds, and are either incorporated into icy mantles or act as nucleation sites for the condensation of the species [44, 51]. C_6H_6 is most likely formed in the ISM *via* the gas phase reaction of ethanol radicals with 1, 3-butadiene [45]. C_6H_6 is also the starting point for the creation of PAHs according to a number of proposed mechanisms [45, 48, 52]. The process by which C_6H_6 forms depends on the environment, with different pathways dominating in ISM in protoplanetary nebulae (PPNe), planetary atmospheres and proto-stellar disks [53]. However, one of the fundamental conditions for high abundances of C_6H_6 is that of high density ($\geq 10^9$ cm^{-3}). A number of reaction pathways have been suggested and in the ISM, one possible reaction scheme which has been put forward is that of McEwan *et al*. [54].

$$C_4H_2^+(g) + H(g) \rightarrow C_4H_3^+(g) + h\upsilon \quad \textbf{(R1)}$$

$$C_4H_3^+(g) + C_2H_2(g) \rightarrow c\text{-}C_6H_5^+(g) + h\upsilon \quad \textbf{(R2)}$$

$$c\text{-}C_6H_5^+(g) + H_2(g) \rightarrow c\text{-}C_6H_7^+(g) + h\upsilon \quad \textbf{(R3)}$$

$$c\text{-}C_6H_7^+(g) + e^- \rightarrow c\text{-}C_6H_6(g) + H(g) \quad \textbf{(R4)}$$

The variations of the mechanism established in **Reactions 1-4** for example C_2H_3, could replace C_2H_2 in **Reaction 2**. In the highly ionising environment around CRL 168, $C_4H_3^+$ is easily formed *via* reactions of various ions and acetylene:

$$HCO^+(g) + C_2H_2(g) \rightarrow C_2H_3^+(g) + CO(g) \quad \textbf{(R5)}$$

$$C_2H_3^+(g) + C_2H_2(g) \rightarrow C_4H_3^+(g) + H_2(g) \quad \textbf{(R6)}$$

$$C_2H_2^+(g) + C_2H_2(g) \rightarrow C_4H_3^+(g) + H(g) \quad \textbf{(R7)}$$

this is followed by **Reactions 2-4**, the models by Woods *et al*. [46, 47] and results in a fractional abundance of C_6H_6 of ~ 10^{-6}, which is in reasonable agreement with observations. C_6H_6 may also be formed in the condensed phase (liquid and solid) by trimerisation:

$$2C_2H_2(g) \rightarrow C_4H_4(g) \quad (\textbf{R8})$$

$$C_4H_4(g) + C_2H_2(g) \rightarrow C_6H_6(g) \quad (\textbf{R9})$$

3.6 Experimental Technique

All the experiments were carried out at the University of Sussex, where the UV/visible spectrometer is attached to the side of a UHV chamber, full details of which are described elsewhere [39]. An outline of the system is as follows. The UHV chamber (**Figure 3.15**) is a stainless vessel which has a translatable and rotatable cold finger mounted sample. A base pressure of below $2x10^{-10}$ mbar is achieved by using a multiple-pump system coupled with baking of the chamber.

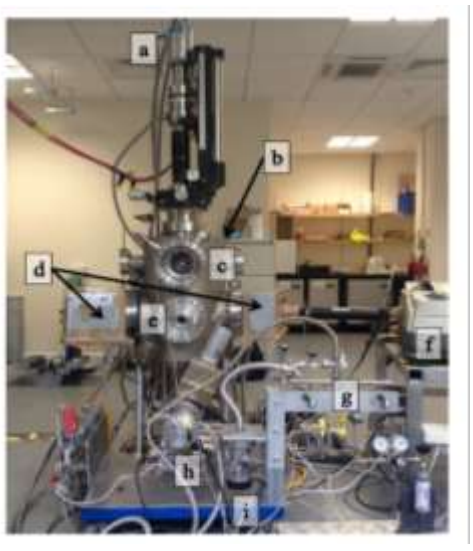

Figure 3.15: UHV chamber at the University of Sussex. (**a**) closed helium refrigerator, (**b**) UHV chamber, (**c**) low energy electron diffraction optics, (**d**) infrared detector and optics, (**e**) ultraviolet window, (**f**) infrared detector, (**g**) dosing manifold and (**h**) main turbomolecular pump and gas line turbomolecular pump (Reproduced from [39]).

A rough vacuum is reached using a rotary pump (Erlikon Leybold, Trivac D8B) and high vacuum is acquired with a turbomolecular pump (Leybold, Turbovac 151). The backing pressure of the turbomolecular pump is monitored *via* a Pirani gauge (Edwards, APG-100-XM) and reaches ~ 7×10^{-4} mbar. Lower pressures are reached after using an ion pump (Physical Electronics, Captorr Ion pump) and a titanium sublimation pump (Physical Electronics, Boostivac TSP) [40]. The surface used in the experiments is a highly orientated pyrolytic graphite (HOPG) sample (Goodfellow Ltd), which is used as an analogue of a carbonaceous interstellar dust grain [39]. HOPG is composed of sheets of graphene held together by weak intermolecular forces, and has a highly ordered crystal structure. The surface is mounted on a copper gold finger and is cooled *via* a closed cycle helium refrigerator, to a base temperature of around 25 K, measured *via* an N-type thermocouple spot welded to the sample mount. The temperature is monitored and controlled *via* a Eurotherm 2048 controller coupled to an E-type thermocouple, as shown in **Figure 3.16**.

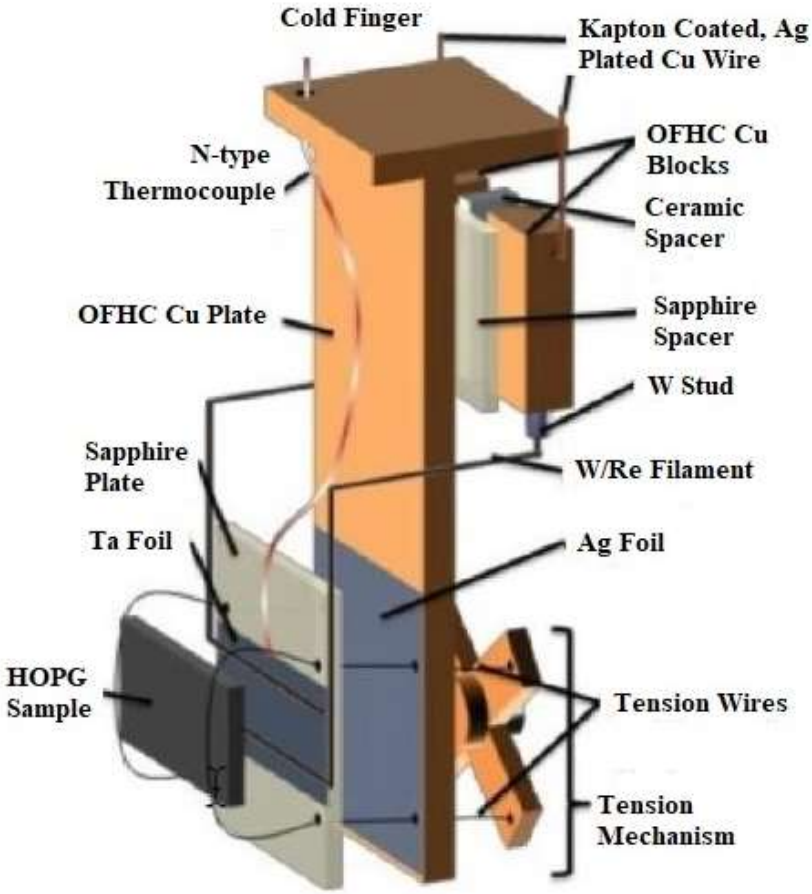

Figure 3.16: Schematic of the sample mount (Reproduced from [39]).

The sample is cleaned by heating to 250 K and maintaining this temperature for one minute. To confirm the cleanness of the sample, TPD experiments are performed without dosing, and the lack of desorption during the TPD experiments confirms the cleanness of the sample. C_6H_6 (Sigma-Aldrich, ≥99.9%) was used in the experiments, and was purified by repeated freeze-pump thaw cycles. It was introduced into the UHV chamber *via* a high-precision leak valve. Analysing the data required interference fringes, and thus the thickness of the ice had to be of the same order as the wavelength of the impinging light. This was achieved by angling the surface towards the leak valve outlet. All the exposures were measured in Langmuir, where 1 Langmuir is equivalent to 10^{-6} mbar s. In all experiments, C_6H_6 was dosed at the base temperature to achieve an amorphous solid film. To acquire the UV/visible spectra, an average of 128 scans was made, with an integration time of 500 ms per scan. This set of parameters was selected by a series of tests to achieve the highest signal without saturating the UV/VIS spectrometer [1].

3.7 Results and Discussion

3.7.1 Results

To acquire a set of reflection-absorption spectra, a background spectrum of the clean HOPG surface was recorded for each reflection angle. This was then followed by dosing the sample and subsequently recording a sample spectrum at each angle when the dosing was completed. For each reflection angle, the sample spectrum was subtracted from the background spectrum. Thus a ratio of the subtracted value to the background was taken, and the spectrum were plotted as $\Delta R/R$ as a function of wavelength, as shown in **Equation 27,** where R_0 is the background spectrum and R_1 is the sample spectrum:

$$\frac{\Delta R}{R} = \frac{R_1 - R_0}{R_0} \qquad \textbf{(E27)}$$

The advantage of fitting the data in this fashion is that it corrects for the output of the light source and thus the uncertainty of reflectance over the spectral range can be examined [1]. **Figure 3.17** shows the unprocessed UV/visible reflection spectra recorded at a reflection angle of 39°, where the blue spectrum is that of the clean

HOPG (background) surface and the red is a dose of 400 L of C_6H_6. There are features currently due to unidentified features present in the data at 486 nm, 581 and 656 nm. **Figure 3.18** shows the light source spectrum from the manufacturer for comparison. These emission features are clearly also visible in these spectra. To ensure reproducibility, the measurements at each coverage were repeated.

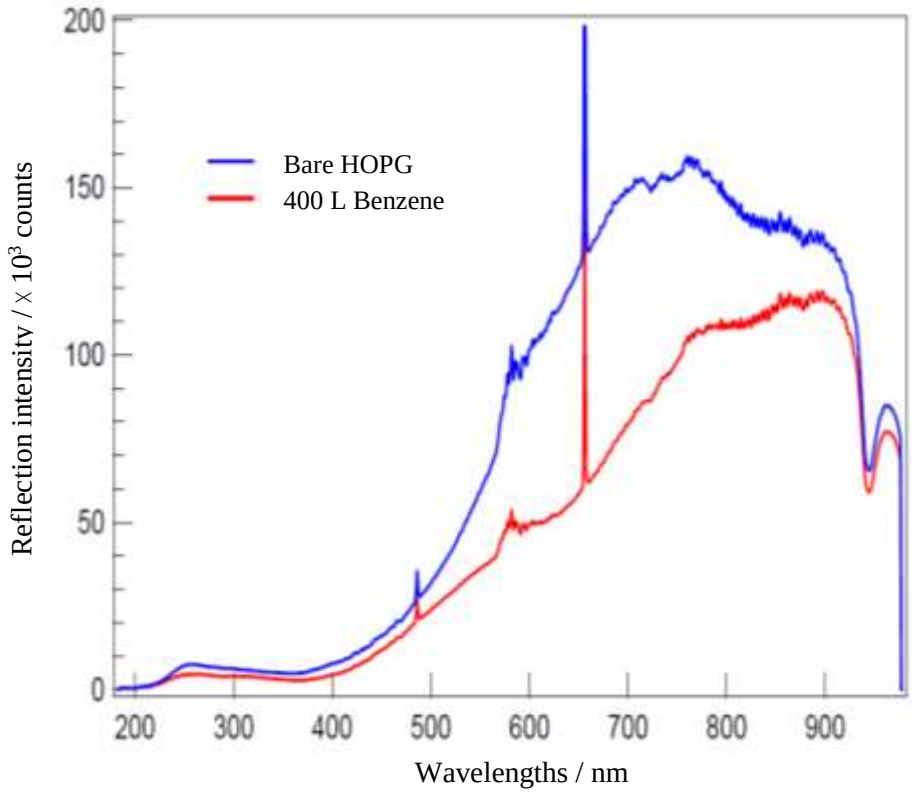

Figure 3.17: $\Delta R/R$ unprocessed UV/visible reflection atomic spectra recorded at a reflection angle of 39°. The features at 486 nm, 581 nm and 656 nm are currently widespread atomic emission lines present in the source output (Reproduced from [41]).

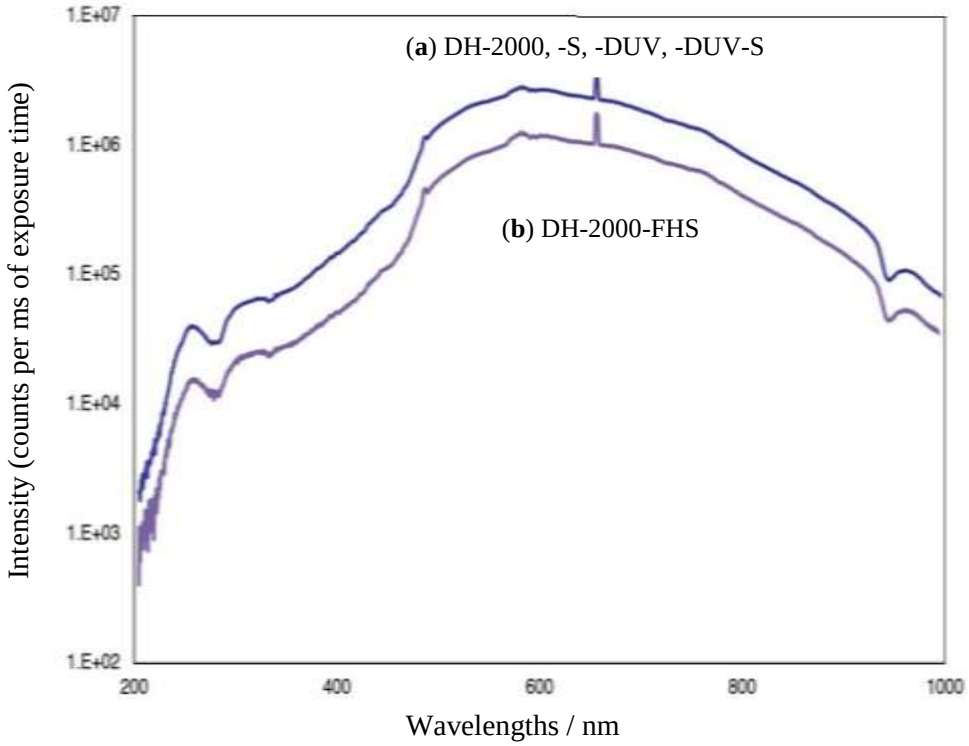

Figure 3.18: The output from the DH-2000 deuterium tungsten halogen light source (Reproduced from [41]).

3.7.2. Determination of Refractive Index and Thickness

Full preliminary analysis of the results is presented in Stubbing *et al*. [1], so only a brief overview is given here. **Figure 3.19 (A)** shows the reflectance spectra of 400 L of C_6H_6 taken at two reflection angles, 31° and 46° and **Figure 3.19 (B)** shows the transmission spectra of C_6H_6 diluted in ethanol (Shimadzu, UV-2550 Spectrophotometer A10844) recorded at Heriot-Watt University. There are sharp absorption features between 210 nm and 270 nm, which can be assigned to $^1B_{1u} \leftarrow {}^1A_{1g}$ transition of C_6H_6 at 214 nm and the $^1B_{1u} \leftarrow {}^1A_{1g}$ transition of C_6H_6 centred at 255 nm [29] and broad interference fringes across the entire wavelength range in **Figure 3.19 (A)**.

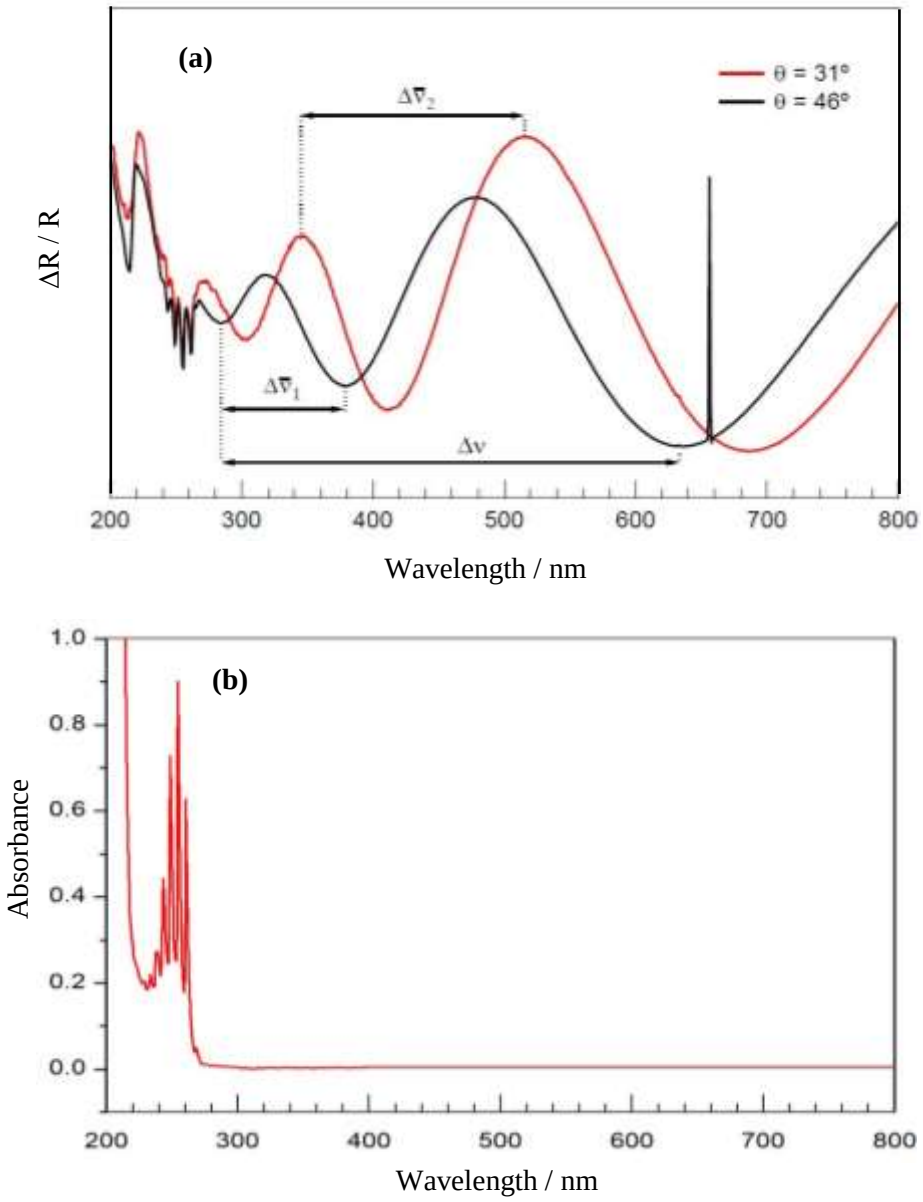

Figure 3.19: (**a**) The reflection-absorption UV/Visible spectra for 400 L of amorphous C_6H_6 on an HOPG surface. From 31^0 (red) and 46^0 (blue) angles of reflection (Reproduced from [1]) and (**b**) UV-VIS transmission spectra of an arbitrary dilute solution of C_6H_6 in ethanol.

Using the method employed by Harrick [19], values for the refractive index, *n*, and the thickness, *d*, of amorphous C_6H_6 ices which have been grown on the HOPG surface at 25 K have been determined. The first step involves calculating *n* using **Equation 24**. After calculating *n*, *d* is calculated for each individual reflectance spectrum, using **Equation 25**. **Figure 3.20** shows the results for refractive index *n* as calculated using **Equation 24** for amorphous C_6H_6 ices which have been grown on the HOPG surface at 25 K.

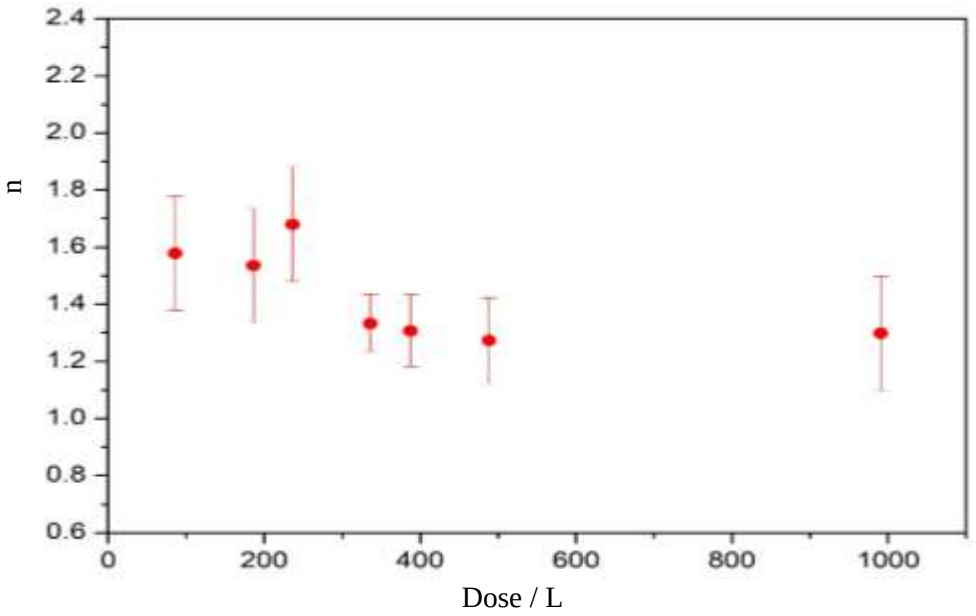

Figure 3.20: The refractive index *n* as a function of coverage at 25 K for amorphous C_6H_6 ice (Reproduced from [1]).

The average value for the refractive index across the wavelength range for C_6H_6 of 1.43 ± 0.07 is within reasonable agreement with the published data. A study by Dawes *et al*. [32] for example found the refractive index ranged from 1.38 to 1.47 (±0.06) at 632.8 nm using He-Ne laser interferometry. To confirm the uniformity of the fringe spacing, a coverage of 1000 L was dosed to produce as many fringes as possible. Hence the gap in the data in **Figure 3.20** between 500 and 1000 L. These results show that using the method developed by Harrick to analyse data acquired in the UV/visible region is valid. However, the calculated value of *n* is lower than that of the liquid C_6H_6 at 293 K, which is 1.501 [55]. Hence, the assumption of taking the value of *n* to be equal to that of the liquid C_6H_6 is not appropriate for application in astrochemistry. The C_6H_6 ice thickness as a function of coverage at a fixed angle is determined using **Equation 25**. **Figure 3.21** shows the thickness of doses from 100 L - 1000 L using the most acute reflection angle of 31°. A linear relationship is noted as the surface concentration, is proportional to the dose, *i.e.* demonstrating compliance with the Beer-Lambert Law.

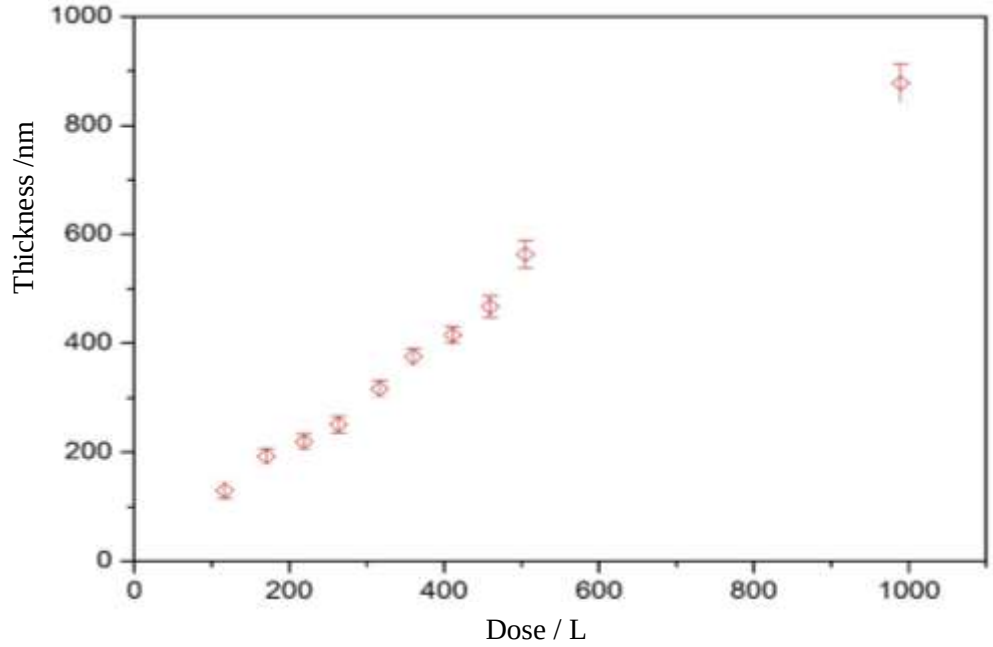

Figure 3.21: The amorphous C_6H_6 ices thickness as a function of exposure on a HOPG surface at 25 K (Reproduced from [1]).

If the coverage is fixed and the angle of reflection is varied, the resulting thickness should be constant. This is the case, as **Figure 3.22** shows for an exposure of 250 L of C_6H_6 on the HOPG surface. The mean thickness is 261±5 nm.

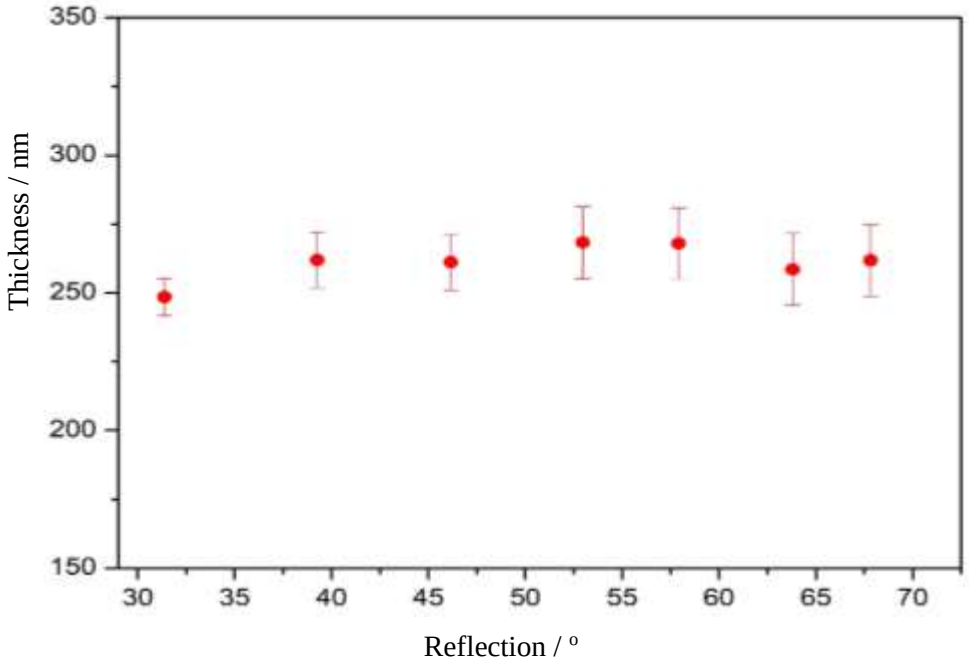

Figure 3.22: Amorphous C_6H_6 ice thickness as a function of reflection angle for a fixed coverage of 250 L (Reproduced from [1]).

The UV/visible reflection absorption spectrometer has been successfully tested and the preliminary results for n and d for C_6H_6 ices are in good agreement with published data. This demonstrates the proof of concept of the instrument and the method employed by Harrick [19] to calculate n and d.

3.8 Conclusions

This chapter has discussed the design, testing and demonstration of a UHV-compatible UV/Visible spectrometer. The preliminary results for n (1.43±0.07) and d (261±5nm) for C_6H_6 ice are in good agreement with published data. This demonstrates the proof of concept of the instrument and of the method employed by Harrick [37] to calculate n and d. The next stage in the analysis is to determine the imaginary part k of the complex refractive index, which will in turn allow the determination of $\hat{n}$, the complex refractive index. This work is currently being undertaken at the University of Sussex. These parameters can then be incorporated into various astronomical models, as discussed in **Section 3.3.1**. Further work will involve other molecules and mixed ices relevant to astrophysical environments. This will include layered and mixed ices of C_6H_6 and water.

3.9 References

[1] J. W. Stubbing, T. L. Salter. W. A. Brown, S.Taj and M. R. S. McCoustra, *Rev. Sci. Inst.*, 2018, **89**, 054102.

[2] https://ned.ipac.caltech.edu/level5/Sept07/Li1/paper.pdf (last accessed 25/11/18).

[3] J. Hawranek, P. Neelakantan, R. Young and R. Jones, *Spectrochim. Acta A: Mol. Spectrosc*., 1976, **32**, 85.

[4] O. S. Heavens, *Rep. Prog. Phys*., 1960, **23,** 1.

[5] http://hyperphysics.phyastr.gsu.edu/hbase/phyopt/freseq.html (last accessed 25/11/18).

[6] http://www.thermopedia.com/content/956/ (last accessed 14/2/19).

[7] J. Steinacker, M. Baes and K. D. Gordon, *Annu. Rev. Astron. Astrophys*., 2013, **51**, 63.

[8] https://www.ast.cam.ac.uk/sites/default/files/talk_archive/Baes.pdf (last accessed 25/11/18).

[9] G. Leveque and Y. Villachon-Renard, *Appl. Opt*., 1990, **29**, 3207.

[10] B. E. Wood and J. A. Roux, *J. Opt. Soc. Am.*, 1982, **72**, 720.

[11] D. M. Hudgins, S. A. Sandford, L. J. Allamandola and A. G. G. M. Tielens, *Astrophys. J. Suppl. Ser.*, 1993, **86**, 713.

[12] F. Trotta, *Ph.D. Thesis* (University Joseph Fourier, Grenoble, France, 1996).

[13] P. Ehrenfreund, A. C. A. Boogert, P. A. Gerakines, A. G. G. M. Tielens and E. F. van Dishoeck, *Astron. Astrophys*., 1997, **328**, 649.

[14] J. Elsila, L. J. Allamandola and S. A. Sandford, *Astrophys. J.*, 1997, **479**, 818.

[15] W. R. M. Rocha, S. Pilling, A. L. F. de Barros, D. P. P. Andrade, H. Rothard and P. Boduch, *Mon. Not. R. Astron. Soc.*, 2017, **464**, 754.

[16] R. G. Smith, K. Sellgren and A. T. Tokunage, *Astrophys. J.*, 1989, **344**, 473.

[17] L. J. Allamandola, S. A. Sandford, A. G. G. M. Tielens and T. M. Herbst, *Astrophys. J.*, 1992, **399**, L34.

[18] W. R. M. Rocha and S. Pilling, *Spectrochim. Acta A.*, 2014, **123**, 436.

[19] N. J. Harrick, *Appl. Opt.*, 1971, **10**, 2344.

[20] https://www.researchgate.net/publication/312180291_The_Application_of_UltravioletVisible_Spectroscopy_to_the_Study_of_Surface_Astrochemistry (last accessed 19/2/19).

[21] T. G. Goplen, D. G. Cameron and R. N. Jones, *Appl. Spectrosc.*, 1980, **34**, 652.

[22] G. A. Baratta and M. E. Palumbo, *J. Opt. Soc. Am.*, 1998, **15**, 12.

[23] M. E. Palumbo, G. A. Baratta, M. P. Collings and M. R. S. McCoustra, *Phy. Chem. Chem. Phys.*, 2006, **8**, 279.

[24] R. L. Hudson, R. F. Ferrante and M. H. Moore, *Icarus*, 2014, **228**, 276.

[25] L. J. Allamandola, A. G. G. M. Tielens, J. R. Barker: *In Interstellar Processes*, Edited by D. J. Hollenbach, and H. A. Thronson, Jr. (Reidel, Dordrecht, 1987) pp471.

[26] B. S. Berland, D. R. Haynes, K. L. Foster, M. A. Tolbert, S. M. George and O. B. Toon, *J. Phys. Chem.*, 1994, **98**, 4358.

[27] M. H. Moore, R. F. Ferrante, W. J. Moore and R. Hudson, *Astrophys. J. Suppl. Ser.*, 2010, **191**, 96.

[28] R. Luna, M. Á. Satorre, M. Domingo, C. Millán and C. Santonja., *Icarus*, 2012, **221**, 186.

[29] M. Á. Satorre, M. Domingo, C. Millán, R. Luna, R. Vilaplana and C. Santonja, *Planet. Space Sci*., 2008, **56**, 1748.

[30] M. S. Westley, G. A. Baratta and R. A. Baragiola, *J. Chem. Phys*., 1998, **108**, 3321.

[31] D. M. Paardekooper, G. Fedoseev, A. Riedo and H. Linnartz, *Astron. Astrophys*., 2016, **596**, A72.

[32] A. Dawes, N. Pascual, S. V. Hoffmann, N. C. Jones and N. J. Mason, *Phys. Chem. Chem. Phys*., 2017, **19**, 27544.

[33] S. Pilling, E. Seperuelo Duarte, A. Domaracka, H. Rothard, P. Boduch and E.F. da Silveira, *Astron. Astrophys.*, 2010, **523**, A77.

[34] S. Pilling, E. Seperuelo Duarte, E. F. da Silveira, E. Balanzat, H. Rothard, A. Domaracka and P. Boduch, *Astron. Astrophys.*, 2010, **509**, A87.

[35] A. Bergantini, S. Pilling, H. Rothard, P. Boduch and D. P. P. Andrade, *Mon. Not. R. Astron. Soc.*, 2014, **437**, 2720.

[36] E. Dartois, J. J. Ding, A. L. F. de Barros, P. Boduch, R. Brunetto, M. Chabot, A. Domaracka, M. Godard, C. F. Mejía Guamán, T. Pino, H. Rothard, E. F. da Silveira and J. C. Thomas, *Astron. Astrophys.*, 2013, **557**, 10.

[37] C. Romanescu, J. Marschall, D. Kim, A. Khatiwada and K. S. Kalogerakis, *Icarus.*, 2010, **205**, 695.

[38] K. Ishikawa, H. Yamano, K. Kagawa, K. Asada, K. Iwata and M. Ueda, *Opt. Lasers Eng.*, 2004, **41**, 19.

[39] M. Whelan, *Ph.D. Thesis* (University of Sussex, Brighton, 2017).

[40] A. S. Bolina, A. J. Wolff and W. A. Brown, *J. Phys. Chem. B*, 2005, **109**, 16836.

[41] https://oceanoptics.com/product/dh-2000-family/ (last accessed 1/1/19).

[42] C. Joblin and G. Mulas, *Interstellar Polycylic Aromatic Hydrocarbons: From Space To The Laboratory, EAS Publ Ser.*, 2009, **35**, 133.

[43] P. Ehrenfreund and S. B. Charnley, *Ann. Rev. Astron. Astrophys.*, 2000, **38**, 427.

[44] M. P. Bernstein, S. A. Sandford, L. J. Allamandola, J. S. Gillette, S. J. Clemett and R. N. Zare, *Science*, 1999, **283**,1135.

[45] B. M. Jones, F. Zhang, R. I. Kaiser, A. Jamal, A. M. Mebel, M. A. Cordiner and S. B. Charnley, *Proc. Natl. Acad. Sci. U. S. A.*, 2010, **108**, 452.

[46] P. M. Woods, T. J. Millar, A. A. Zijlstra and E. Herbst, *Astrophys. J.*, 2002, **574**, L167.

[47] P. M. Woods, T. J. Millar, E. Herbst and A. A. Zijlstra, *Astron. Astrophys.*, 2003, **402,** 189**.**

[48] M. Frenklach, D. W. Clary, W. C. Gardiner and S. E. Stein, *Proc. Combust. Inst.*, 1984, **20**, 887.

[49] W. W. Duley and D. A. Williams, *Mon. Not. R. Astron. Soc*., 1981, **196**, 269.

[50] G. H. Herbig, *Ann. Rev. Astron. Astrophys*., 1995, **33**, 19.

[51] V. Geers, E. Van Dishoeck, K. Pontoppidan, F. Lahuis, A. Crapsi, C. Dullemond and G. Blake, *Astron. Astrophys.*, 2009, **495**, 837.

[52] H. Bockhorn, F. Fitting and H. W. Wenz, *Ber. Bunsenges, Phys. Chem*., 1984, **20**, 1067.

[53] P. M. Woods and K. Willacy, *Astrophys. J*., 2007, **655**, L49.

[54] M. J. McEwan, G. B. I. Scott, N. G. Adams, L. M. Babcock, R. Terzieva and E. Herbst, *Astrophys. J.*, 1999, **513**, 287.

[55] E. Hecht, *Optics, 5th Edition.* (Addison Wesley, San Francisco, 2017).

[56] S. E. Malek, J. Cami and J. Bernard-Salas, *Astrophys. J*., 2012, **744**, 16.

[57] J. Bernard-Salas, E. Peeters, G. C. Sloan, J. Cami, S. Guiles and J. R. Houck, *Astrophys. J*., 2006, **652**, L29.

Chapter 4

The Spontelectric Effect

4.1 Introduction

This chapter reports on investigations of solid methyl formate ($HCOOCH_3$, MF) thin films deposited at temperatures from 15 to 115 K. Firstly, TPD data will be presented. RAIRS will then be used to explore the interaction of MF with an $aSiO_2$ surface. Finally, the results of *ab initio* studies are presented which enable the predication of the structural motif within the unit cell of the crystalline phase of solid *cis*-methyl formate (*cis*-MF). This structural motif is used to explain the observed collapse of the spontelectric field at temperatures greater than 90 K. The work presented in this chapter is result of a number of contributions and they include:

1. The experimental TPD and RAIRS measurements and their initial interpretation were by A. Dunn (Undergraduate Project Student), S. Taj, and M. R. S. McCoustra at Heriot-Watt University.
2. Interpreting the *cis*-MF RAIRS data, fitting of RAIRS line profiles and numerical calculations on the spontelectric effect were carried out by M. Roman (Undergraduate Project Student) and M. R. S. McCoustra at Heriot-Watt University.
3. The computational work supporting the project was carried out by Z. G. Keolopile and M. Gutowski at Heriot-Watt University.
4. All the direct measurements of the spontelectric effect in MF were made by A. Cassidy and D. Field at Aarhus University in Denmark.

The work in this chapter is reported in references [1, 2]. The isomers of MF, glycolaldehyde and acetic acid are key group of complex organic molecules which have been detected in a wide range of astrophysical environments. These molecules are important in interstellar chemistry and may also play a role as pre-biotic species. Hence, this makes them a rich area for study.

4.1.1 What is the Spontelectric Effect?

When a dipolar gas is condensed onto a substrate, a solid film may be formed which can spontaneously exhibit a static electric field without any external stimulus such as an applied electric field [3]. The size of this field can exceeded 10^8 V m^{-1}. This effect is called the 'spontelectric effect' and materials that exhibit this behaviour are known as 'spontelectrics'. These spontelectrics represent a new electrical phase of the solid state. Some species that exhibit this effect include simple hydrocarbons, halocarbons, alcohols, organic formates, benzene derivatives and simple inorganics such as nitrous oxide (**Figure 4.1**).

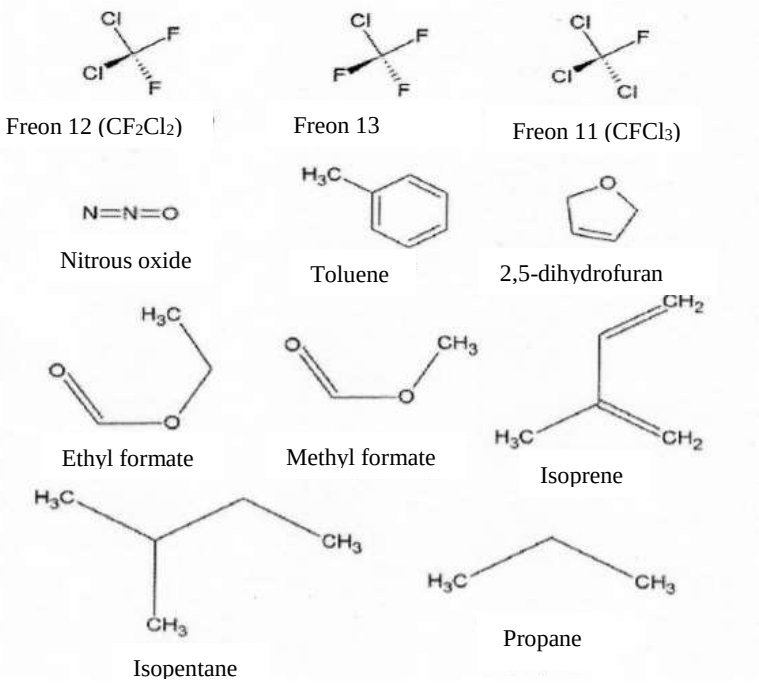

Figure 4.1: Spontelectric materials identified to date, with their chemical structures (Reproduced from [3]).

Dipole orientation is the most likely source of the spontaneous polarization that leads to spontaneous electric fields [2-4]. **Figure 4.2** illustrates the dipole orientation in (a) a non-spontelectric material where the dipoles are oriented to minimise energies with δ+ close to δ- and (b) a typical spontelectric material where dipoles orient in an energetically unfavourable way.

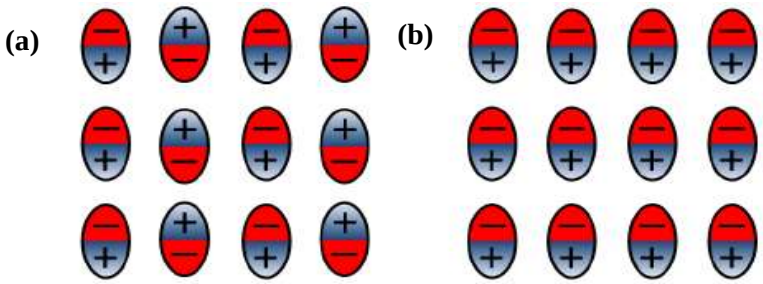

Figure 4.2: Dipole orientation and the spontelectric effect: (**a**) this is an example normal low energy dipole orientation in a typical solid, and (**b**) shows how the dipoles orient in a spontelectric material in a high-energy configuration [3-4].

Spontelectric behaviour is intrinsic to the dipolar nature of the constituent molecules. Dipole-dipole interactions play a key role in this, and infinite range order is spontaneously generated by the relationship between dipole orientation, the electric field and the thermal motion associated with the temperature at which the solid is deposited [3-6]. The dependence of the electric field and the related degree of dipole orientation on the deposition temperature departs greatly from the linear, with a powerful feedback mechanism in play. Dipole orientation induces a polarisation in the solid, which in turn induces further dipole alignment. The polarization gives rise to the measured electric field. The fields are macroscopic and penetrate the entire film, providing a constant presence throughout [3]. Spontelectric materials have been shown to form stable and metastable structures whose properties are governed to a significant extent by the bulk of the material rather than by the interfaces [5]. The feedback between electric fields and dipole orientation in the bulk helps to create an ordered structure; but this is moderated by thermal disorder, which is determined by temperature of the film deposition. The amount of dipole orientation achieved is dictated by the competition between order and disorder, and experimental data has shown that, at higher deposition temperatures, more disordered structures are seen.

4.1.2 Characteristics of Spontelectric Materials

Currently, the notable properties of the spontelectrics are [3]:

1. The strength of the spontelectric field depends on the nature of the material deposited, but not on the substrate on which it is grown.

2. The strength of the spontelectric field is dependent on the thickness of the film and on the temperature at which the film is deposited. It is generally reduced at higher temperatures. However, MF is unique in that the spontelectric field in solid MF initially decreases but then increases.
3. The spontelectric field can either be positive or negative.
4. The spontelectric potential is stable over time, at least over a period of hours for which measurements have been made to date.
5. Initially, small increases in temperature have little effect on the spontaneous potential at the film surface. However, at a certain temperature, the spontelectric effect decays abruptly to zero and the film depolarises, by analogy with ferromagnetism. This is known as the Curie Point (CP). Cooling below the CP does not result in a reintroduction of the spontelectric field.

These properties can be illustrated by considering the data published so far on spontelectric materials. **Figure 4.3** reproduces the work on N_2O and shows the linearly increasing surface potential (and hence spontelectric field) with film thickness and a monotonic decrease in surface potential with increasing deposition temperature [5].

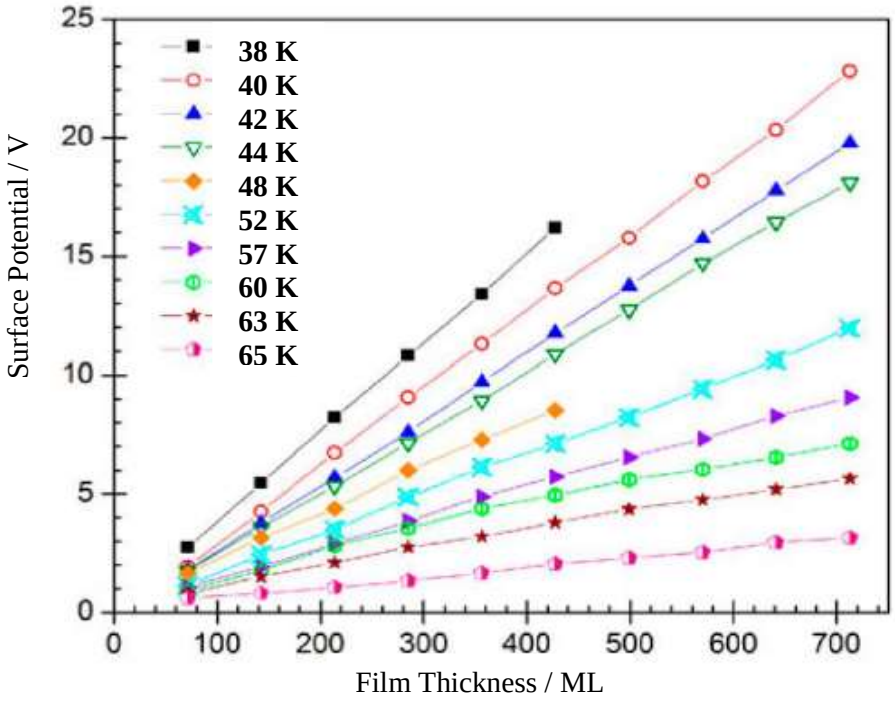

Figure 4.3: Surface potentials (V) of films of N_2O as a function of film thickness in monolayers (ML), and deposition temperature (K) (Reproduced from [3]).

What takes place when a spontelectric film is deposited at a low temperature and is subsequently heated? Consider a 360 ML N_2O film which is deposited at 38 K and is then heated and the value of the potential noted every 3 – 4 K until just below the evaporation point at 75 K. The measurements show that the potential only dropped by 510 meV at 75 K compared with the value at 38 K [3]. This data can be compared with that shown in **Figure 4.3**, where the results for the relaxed state show a drop of 11.95 V between deposition temperatures of 38 and 65 K. Clearly, dipole orientation induces a powerful rigidity that remains in place despite the substantial electromechanical stress induced by heating. If the heating is continued, a critical temperature is reached at which the spontelectric effect decays with varying degrees of abruptness depending on the material. This is the Curie Point (CP) and **Figure 4.4** shows the CP behaviour for CF_2Cl_2.

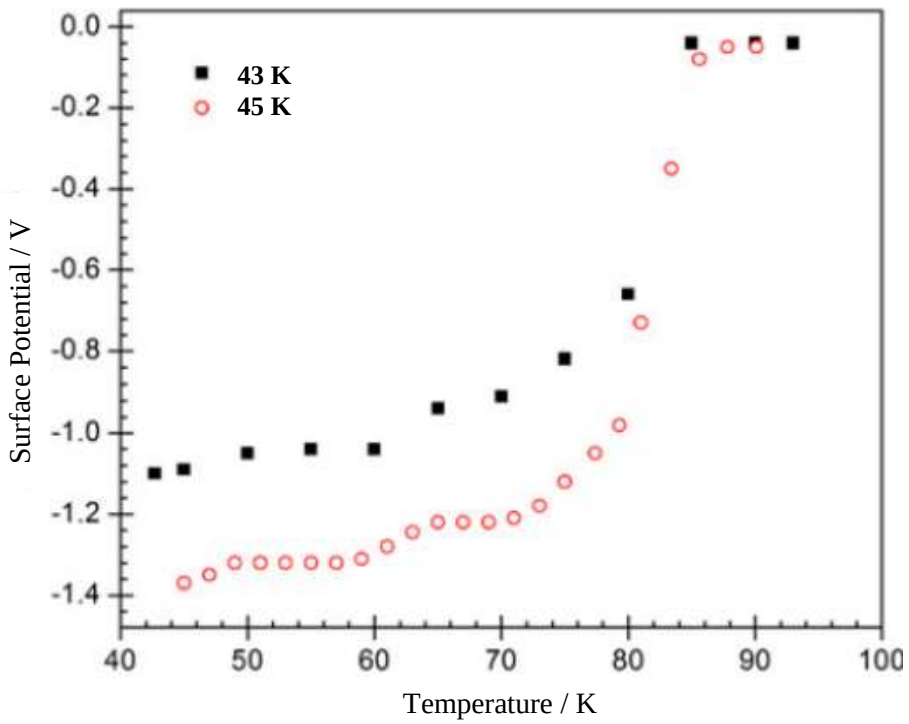

Figure 4.4: The variation of the surface potential (V) of a 90 ML film of CF_2Cl_2 deposited at 43 K and heated to 95 K showing the CP (black points). Red points show the variation of the surface potential of a 120 ML film deposited at 45 K and heated to 95 K (Reproduced from [3]).

There is a drop in spontelectric potential around 60-65 K in upper curve for film deposited at 43 K and this drop in potential is also seen in film deposited at 45 K. This suggests that solid CF_2Cl_2 may form two spontelectric configurations, which

change one into the other at temperatures above 60 K or there may coexist configurations which convert one into the other above 60 K [3].

Most of the spontelectric films show temporal stability over a period of several hours. In the case of a N_2O film deposited at 40 K, after standing for 24 hours, the measured surface potential was virtually unchanged [7]. Issues of contamination make tests over longer periods of time difficult. However, non-linear film-thickness effects and/or reversal of the normal surface potential behaviour can be interpreted as a decay of the spontelectric structure over time. This is observed for some ranges of deposition temperature in methyl formate, ethyl formate, propane, dihydrofuran and trichlorofluoromethane ($CFCl_3$). **Figure 4.5** shows an abrupt change in behaviour between deposition temperatures of 46 K and 50 K for $CFCl_3$.

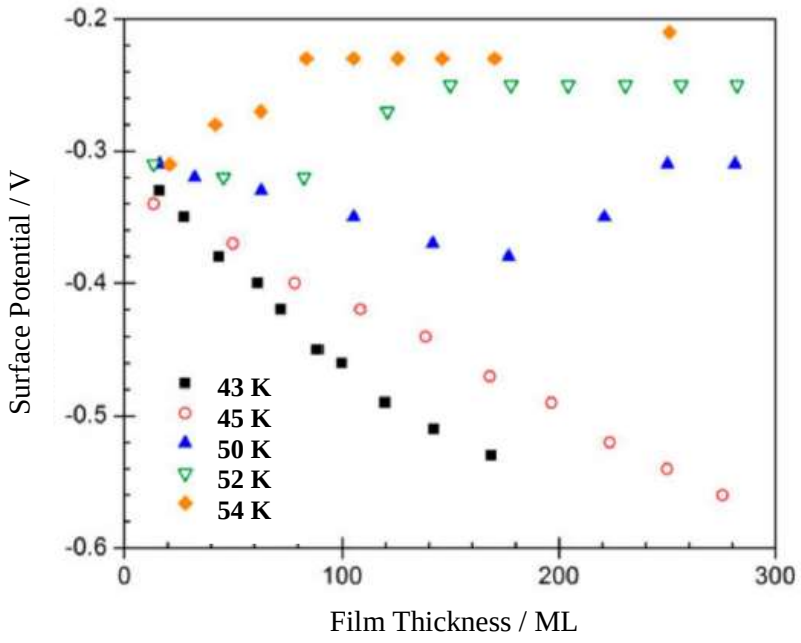

Figure 4.5: The surface potentials (V) measured for films of $CFCl_3$ as a function of thickness in ML and deposition temperature (K). This data illustrates the typical decay of spontelectric effects for deposition temperatures greater than 50 K (Reproduced from [3]).

A considerable amount of experimental work has been done to study ferroelectrics, while the study of spontelectric effects is still very much in its infancy. In general, the spontelectric phase is similar to various other electrical phases of the solid state and in particular ferroelectrics and films of tris (8-hydroxyquinolinato) aluminium

(Alq_3) [3]. A key characteristic of ferroelectrics is the switchable polarisation between two or more discrete states *via* the application of an external field, along with the related hysteresis under applied fields [3, 5]. However, the various properties of spontelectrics make them a unique form of solid [5]. There are a number similarities and differences between organic ferroelectrics and spontelectrics and they include [5, 8]:

1. Spontelectrics and organic ferroelectrics display a CP.
2. Spontelectrics and organic ferroelectrics show macroscopic spontaneous polarisation which is created by ordering of the dipoles in the film.
3. The properties of spontelectrics are generated by dipole-dipole interactions, whereas in organic ferroelectrics the behaviour occurs *via* interactions which are extrinsic to the dipole-dipole interactions.
4. Models of the properties of spontelectrics films can be constructed which do not require domains. However, in ferroelectrics the existence of domains is a general property and may be the decisive factor in their properties [7].
5. A cycle of thermal hysteresis is characteristic of ferroelectrics and is easily observable but has not been experimentally detected in spontelectrics [9-12].
6. The spontelectric behaviour in MF has not been observed in any ferroelectric material, particularly where the temperature increases beyond a critical point and an increase in the spontelectric effect is observed.

So spontelectrics are clearly not a subgroup of ferroelectrics. Hence, it can be concluded that spontelectrics represent a new phenomenon in solid state physics [3].

4.1.3 The Spontelectric Effect in Astronomy

A key question is whether the existence of spontelectric effect has any bearing on the natural Universe. The answer to this question is that it may. It all depends on whether icy dust grains in the dense ISM could acquire a large polarisation charge on the grain surface. It is established that interstellar grains in cold pre-stellar cloud cores are coated with an outer layer of pure CO. The extent of this layer may be 50 to 60 ML in the core in L1544 in Taurus [13]. The low rate of accumulation of CO in the ISM

probably has no influence on the spontelectric nature of the film formed. The spontelectric effect in CO at 20 K would produce a polarisation potential of 0.7 V on such a grain surface [13]. This potential is equivalent to a polarisation charge of 50 electronic charges (a grain is typically considered to have one negative charge on its surface). Collings *et al.* [14] suggests that the positive O-end of the CO would protrude from the surface, hence the polarisation charge would be +50. This would attract electrons to the surface, hence altering the gas phase abundance of electrons [13]. Taking a density of grain material of 2 g cm^{-3} and a grain abundance by mass of 1.3%, the proportion of electrons removed to the grain surface can be given as $1.06 \times 10^{-25}\ n_{\mathrm{ML}} / (\alpha a^2)$, where n_{ML} is the number of monolayers of CO, α (which can range over a few 10^{-9} to over 10^{-8}) is the degree of ionisation and a is the grain radius. If a is 0.025 μm and α is 10^{-8}, the resulting degree of depletion of gas phase electrons would be greater than 80% [13].

Magnetic shocks also exhibit characteristics which depend heavily on the gas phase abundance of electrons [13, 15, 16]. These shocks form in star-forming regions close to the surface of nascent proto-stellar objects. The above suggests that spontelectric icy grains may have an influence on the chemistry and physics of the gravitational collapse of proto-stellar cores, as the polarisation charge could assist in the expulsion of the magnetic field [17, 18]. This could allow a more rapid progression from a dense core to protostar and on to an incipient planetary system [19].

4.1.4 A Model for the Spontelectric Effect

A model of the spontelectric effect has been developed by Field *et al*. [3] and an overview is given here. This mean field model works on the principle that the electric field within the bulk of the film is composed of components in the *x*, *y* and *z* directions. The components in E_x and E_y average out as zero across the whole of the plane. However, there is an electric field in the *z* direction which is at right angles to the surface of the film. This is a result of the net orientation of the molecular dipoles [2]. This field, E_z, has two components: 'symmetrical' and 'asymmetrical'. The symmetrical, $\langle E_{sym} \rangle$, part defines the interactions binding the separate layers of molecules together, while also dictating the molecular force fields. This part of field can be expressed as a constant along with a dipole term, which is proportional to $(\langle\mu\rangle/\mu)^2$, that represents the average intermolecular dipole-dipole interaction [20-

22] and is the degree of dipole orientation. The degree of dipole orientation, $\langle \mu_2 \rangle / \mu$ is the ratio of the average *z*-component of the dipole moment and the total dipole moment of the molecular species in the solid state and the *z*-axis is perpendicular to the plane of the film. Finding a suitable value for $\langle \mu_2 \rangle / \mu$ is vital since it correlates directly to the value of the spontelectric field. Using the mean field theory, the degree of dipole orientation can be expressed as follows [2, 3]:

$$\frac{\langle \mu_z \rangle}{\mu} = \coth\left(\frac{E_z \mu}{T}\right) - \left(\frac{E_z \mu}{T}\right)^{-1} \qquad \textbf{(E1)}$$

where *T* is the deposition temperature of the material [3]. The asymmetrical part, $<E_{asym}>$, corresponds to the spontelectric field within the bulk of the solid. It can be thought of as the long-range interaction between the average dipoles and the electric field they exert, acting in opposition to the symmetrical part and representing the field permeating in the film as a result of the averaged dipoles and experienced by an average dipole [2]. The dipole-field interaction is non-local and non-linear, as the field results from the orientation of the dipoles. Additionally, the dipoles align with the field until they reach a steady state. The electric field in the *z*-direction is defined as [2, 3]:

$$E_z = \langle E_{sym} \rangle \left[1 + \zeta \left(\frac{\langle \mu_z \rangle}{\mu}\right)^2\right] - \langle E_{asym} \rangle \frac{\langle \mu_z \rangle}{\mu} \qquad \textbf{(E2)}$$

where $\langle E_{sym} \rangle, \langle E_{asym} \rangle$ and ζ are parameters that are taken to be independent of the deposition temperature over any temperature range for which there are no sudden structural changes [23]. In **Equation 2**, the dipole term $\langle E_{sym} \rangle \zeta (\langle \mu_z \rangle / \mu)^2$ can be thought of as a measure of the tendency of one dipole species to restrict the angular motion of another dipole species. This is referred to as 'frustration' term [2]. The mean field theory provides an implicit expression for $\langle \mu_z \rangle / \mu$, resulting in the familiar Langevin function **Equation 1** [2, 13, 24]. A detailed analysis is given in work by Field *et al*. [3] while **Equations 1** and **2** can be combined, resulting in an explicit expression for $\langle \mu_z \rangle / \mu$, leading to a total derivative of $\langle \mu_z \rangle / \mu$ *versus T*, as shown in **Equation 3:**

$$\frac{\mathrm{d}\langle \mu_z/\mu \rangle}{\mathrm{d}T} = \frac{1/\mu E_z - (\mu E_z/T^2)\mathrm{cosech}^2(\mu E_z/T)}{(\mu E'/T)\mathrm{cosech}^2(\mu E_z/T) - E'\,T/\mu {E_z}^2 - 1} \quad \textbf{(E3)}$$

$$E' = \langle E_{asym} \rangle - 2\zeta \langle E_{sym} \rangle \langle \mu_z \rangle / \mu \quad \textbf{(E4)}$$

This complete derivative has the property such that in the continuous variable *T*, it retains a set of discontinuities for a certain range of key parameters, $\langle E_{sym} \rangle$, $\langle E_{asym} \rangle$ and ζ, typified by way of a single cut in the (T, $\langle \mu_z \rangle / \mu$) space. In this context, *cis*-MF is currently the only material which displays a singular cut [2, 3]. A feature of **Equation 3** is the reversal of the sign of $\mathrm{d}(\langle \mu_z \rangle / \mu)/\mathrm{d}T$ on each side of the cut, where it is negative at low temperature and positive at high temperature, and where the positive sign signifies increasing degree of orientation with increasing deposition temperature [2]. This is inferred by the increasing field at temperatures above 77 K in **Figure 4.6**.

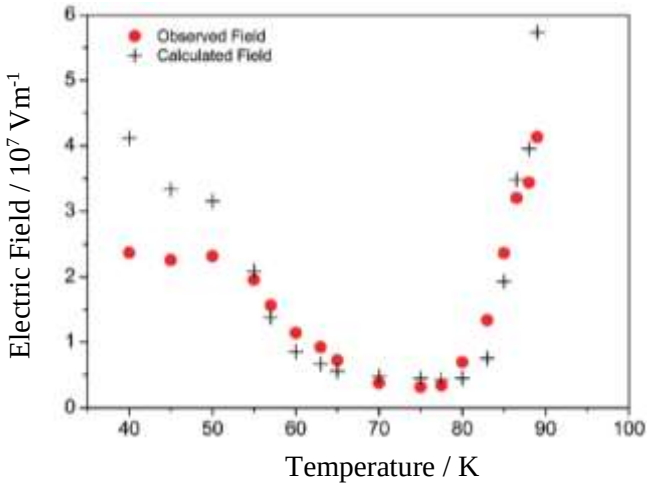

Figure 4.6: The spontelectric field *versus* deposition temperature for *cis*-MF (Reproduced from [3]).

4.1.5 Surface Potentials and the Spontelectric Effect

Low-energy Electron Scattering

The potential on a film surface can be measured using the principle that an electron beam formed at some point at a certain potential can reach another point at another potential [3]. If electrons are formed at a known potential, the potential of their destination can be measured by the bias that must be applied either at the point of

formation or at their destination such that a current begins to flow. The accuracy with which the bias can be measured depends on the energy resolution in the electron beam and the sensitivity of the detection system. The potential which appears on the surface of a spontelectric film can be measured by applying a bias potential to the system and by adjusting that bias until a zero current is detected from an incident electron beam. Since electrons are formed nominally at 0 V with an energy around 5 meV, the beam should be able to reach the target when the target itself is at the same nominal zero, less than 5 mV [3]. **Figure 4.7** below shows the apparatus and further details of this can be found in reference [3].

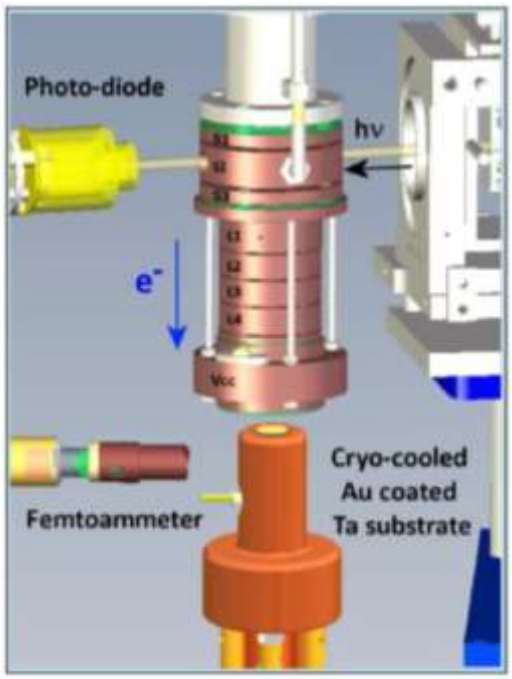

Figure 4.7: Synchrotron radiation with a resolution of 1.5 meV enters a photoionisation source S1, S2 and S3, which contains argon at a pressure around 10^{-4} mbar. The current is detected by femtoammeter and L1-L4 constitute four electron lenses (Reproduced from [3]).

Kelvin Probe Measurements

The Kelvin Probe (KP) is a tool for measuring surface contact potential difference (CPD, assigned as V_c), and potentially both the spatial and temporal variation of the surface potential. It has a vibrating metal capacitance plate (tip), which is placed near the conducting surface of interest [25]. **Figure 4.8a** shows the two metals in close proximity, but without electrical contact between them. Their Fermi levels align at the vacuum level at energies corresponding to the respective work functions Φ. As

the two metal pieces are connected by wire, as shown in the centre of **Figure 4.8b**, electrons flow from the metal with the smaller work function to the one with the larger work function. This results in an electric potential between the two metals, which in turn results in their electronic states shifting relative to one another [25].

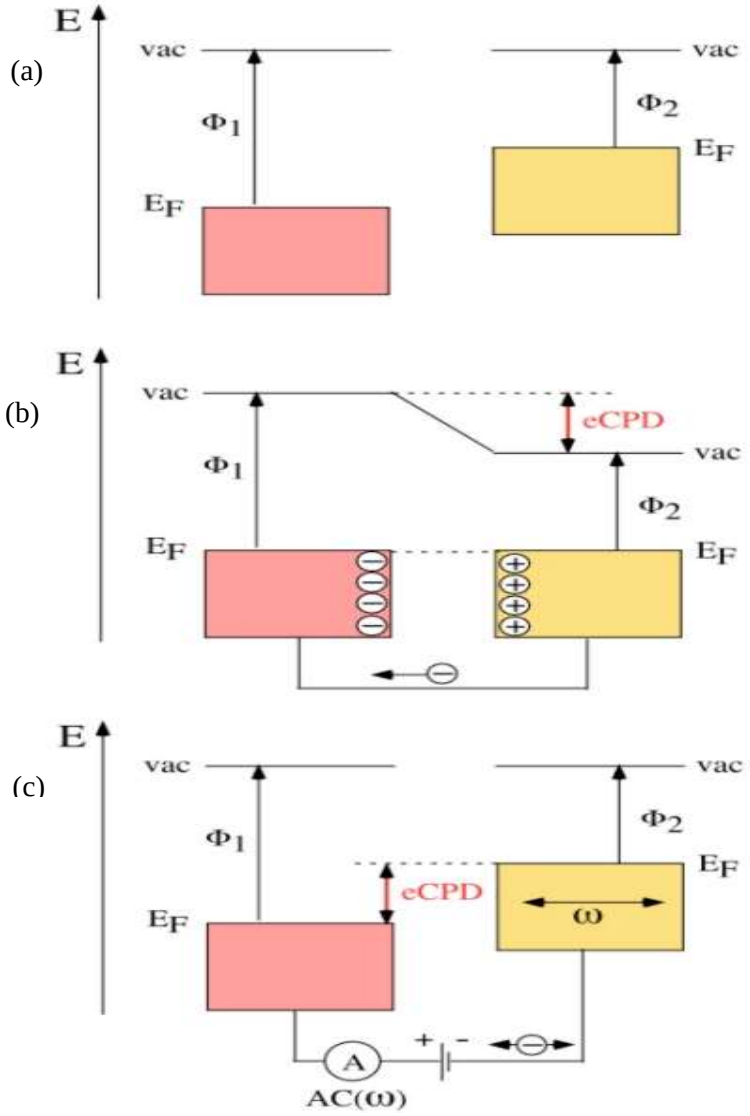

Figure 4.8: Kelvin probe measurements process and the electronic energy levels of the sample and level KP tip. (**a**) tip and sample are separated, with no electrical contact, (**b**) tip and sample are in electrical contact; and (**c**) external bias is applied between tip and sample to nullify V_c (Reproduced from [25]).

The electron transfer process stops once the electric field between them compensates for the work function difference. In this equilibrated state, the potential associated with the electric field exactly equals the work function difference, *i.e.* the contact

potential difference, V_{CPD} between the metals. Gradual application of a counter potential to the V_{CPD} while monitoring the change in potential of one of the metals allows determination of the charge-free point. The counter potential V_b, which achieves this, is exactly $-V_{CPD}$. In the experimental set-up, the Kelvin probe itself is vibrated at the frequency ω (**Figure 4.8c**). Due to the varying distance, the amount of charge needed to maintain the electric field in the capacitor also varies. Hence, using phase-sensitive detection, the AC current generated by the oscillation, $I(\omega)$, can be monitored. Slowly increasing the counter potential and finding the zero of AC current yields the V_{CPD}, **Equation 5** [26]:

$$V_{CPD} = -\frac{(\varphi_{tip} - \varphi_{sample})}{e} \qquad \textbf{(E5)}$$

where φ_{sample} and φ_{tip} are the work functions of the sample and tip and e is the electronic charge.

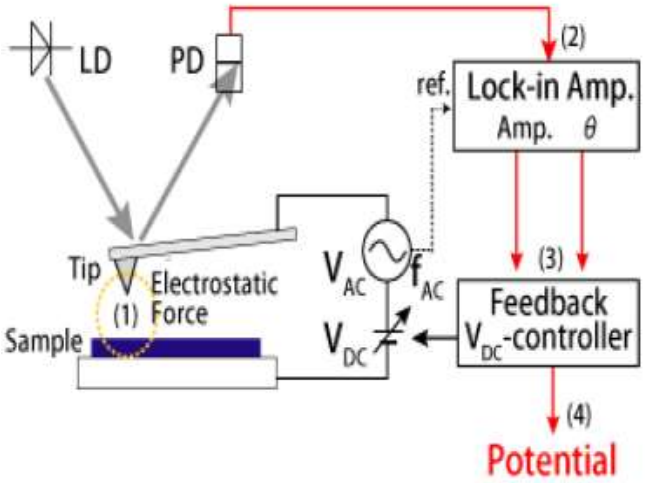

Figure 4.9: KP force microscopy, where a conducting cantilever is scanned over a surface at a constant height (Reproduced from [26]).

This technique can be integrated into a scanning probe microscopy (**Figure 4.9**) to yield images of the variation of surface potential over the surface. In this case, the application of a modulated *AC* bias, V_{AC}, at a frequency f_{AC}, with a *DC* offset bias V_{DC} between the tip and sample generates a electrostatic force between the tip and sample (**1**). The cantilever deflection which is a result of the electrostatic force is detected by a photodetector and the resulting component signal of frequency f_{AC} is

derived by the lock-in amplifier (**2**). The signal is then transferred back as feedback to the controller (**3**). Finally the intended V_{CPD} is obtained by adjusting the *DC* offset bias V_{DC} so that the component signal of frequency f_{AC} becomes zero (**4**) [26].

Amorphous solid water (ASW) grown by condensation of water vapour onto cold surfaces, below 130 K, is the most common form of water in the Universe. Studies of ASW are driven by the need to understand its properties in a range of astrophysical environments [27]. ASW films grown by vapour deposition below 110 K develop a negative surface voltage (ΔV_s) with respect to the substrate [28]. The polarisation is due to a partial alignment of the water molecules during condensation. H_2O molecules possess a balance of up and down dipole. In regular high temperature hexagonal ice this provides no net polarisation [28]. ASW formed by vapour deposition below temperatures of 110 K becomes spontaneously polarised and shows a negative voltage at the vacuum ice interface with respect to the substrate. However, the molecular alignment mechanisms which result in the appearance and growth of the polarisation are not fully understood [28], but a number ideas have been put forward including the favoured attraction of protons to the substrate due to an asymmetric distribution of the electric field around the H_2O molecule [29, 30]. A major study of the spontaneous polarisation of ASW was carried out by Iedema *et al*. [31] which used a KP to investigate surface potentials in films and inferred ferroelectricity behaviour.

Bu *et al*. [28] investigated the effects of microstructure on the spontaneous polarisation in ASW films using a KP. These measurements revealed that the size of the surface potential increases linearly with film thickness and decreases with rising deposition temperature. In **Figure 4.10**, ΔV_s changes sharply by -0.25 V with the 5 ML of deposition and continues to increase linearly in size at a smaller rate with film thickness.

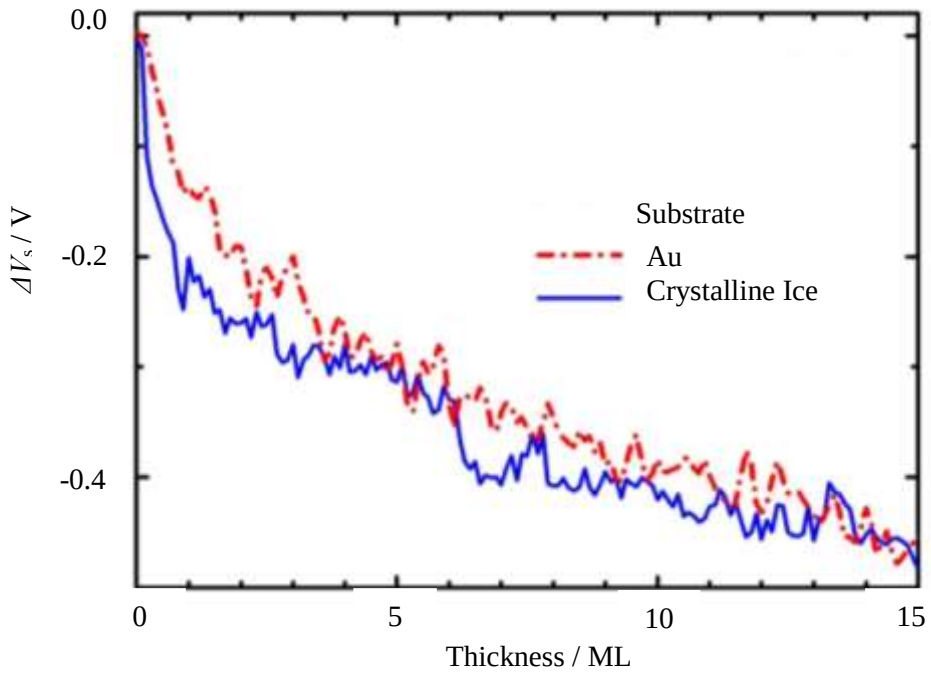

Figure 4.10: Shows the changing surface potential during the deposition of the first 15 ML of ASW deposited at 30 K. The sudden changes in the surface potential for coverages less than 5 ML occur when the ASW is deposited onto Au or crystalline ice (Reproduced from [28]).

In **Figure 4.11**, the change of the surface potential displays no large dependence on the substrate material and the voltage drop indicates the formation of a dipole layer with the negative charge at the film-vacuum interface. **Figure 4.11a** shows the change of the surface potential with varying thicknesses of ASW film at varying deposition temperatures [28].

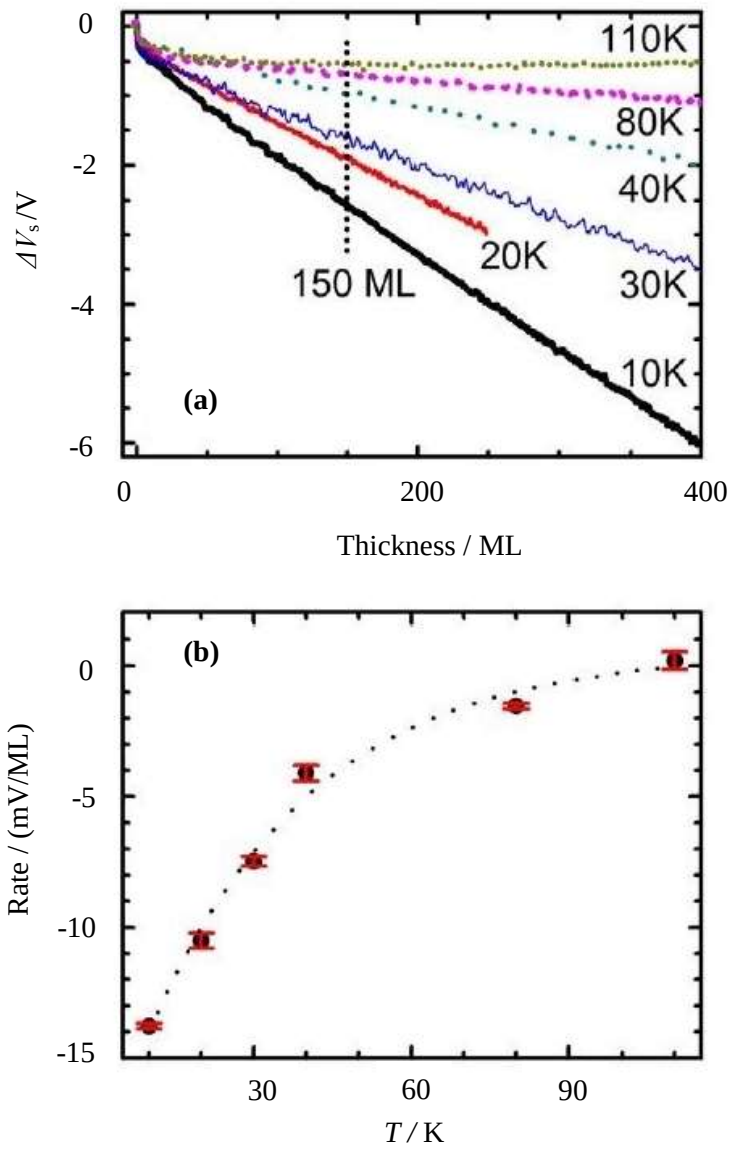

Figure 4.11: (**a**) The change of the surface potential of ASW film thickness at various deposition temperatures and (**b**) Shows the rate of change of the surface potential $\Delta V_s / \Delta_L$ as function of the deposition temperature using the data in (**a**) when film thickness is greater than 150 ML (Reproduced from [28]).

From the initial change, the size of the surface potentials increases linearly with thickness at rates $\Delta V_s / \Delta_L$ and decreases with increasing deposition temperature. **Figure 4.11b** shows the rate of change of the surface potential as a function of deposition temperature. **Figure 4.12** shows the temperature dependence evolution of the negative surface potentials for ASW films of 1100 ML deposited on to Au substrate at various deposition temperatures. The surface potential decreases with

increasing deposition temperature and is irreversibly reduced by 80% when the film is annealed to a temperature of 30 K [28].

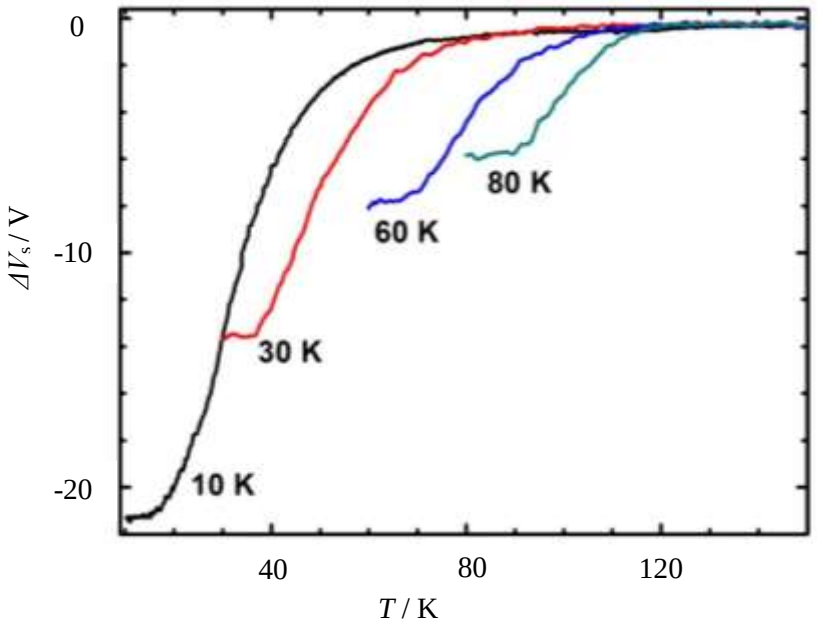

Figure 4.12: The decrease of polarization with annealing temperature for 1100 ML ASW films deposited temperatures from 10 K to 80 K (Reproduced from [28]).

The results from Bu *et al.* [28] support the idea that the spontaneous polarisation of ASW films is a result of the porosity of the ice films, as first reported in 1969 by Elliott *et al.* [33]. Given these observations, we might tentatively conclude that ASW is spontelectric in the low temperature range.

The work of Gavra *et al.* [32] illustrates the use of the KP in measuring the surface potentials of 1-butanol ($CH_3(CH_2)_2CH_2OH$) thin films. 1-Butanol is a small organic molecule bearing a hydroxyl group and hence that partially resembles H_2O. The results for 1-butanol show large surface potentials, which corresponds to significant numbers of deposited molecules that have their dipoles oriented parallel to the substrate normal. **Figure 4.13** shows the film potential, recorded as function of time during film deposition. **Figure 4.13a** shows the raw signal and its calculated error. The steps are a result of the adjustments made to the probe bias in 25 V increments. **Figure 4.13b** shows the signal from **Figure 4.13a** after corrections have been applied [32].

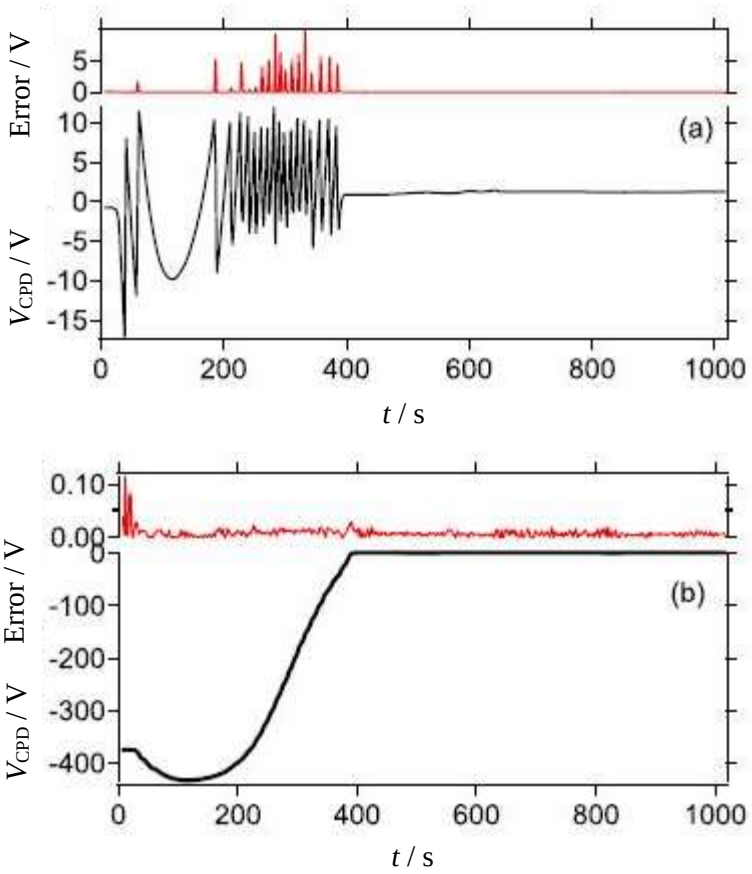

Figure 4.13: Potentials in 1-butanol thin films during film deposition (**a**) the contact potential difference (CPD) determined using the KP along with its associated standard deviation. The steps are associated with large CPD errors, which are due to adjustments of an additional Kelvin probe bias, needed to maintain the voltage difference between the Pt foil and the KP. (**b)** Incorporating an additional bias and removing points which are affected by the bias switching, results in a film voltage which is a smooth curve (Reproduced from [32]).

Figure 4.14 shows the scaled voltage for 1-butanol as a function of deposition temperature. Clearly the properties of 1-butanol are consistent with the material being spontelectric in thin solid films.

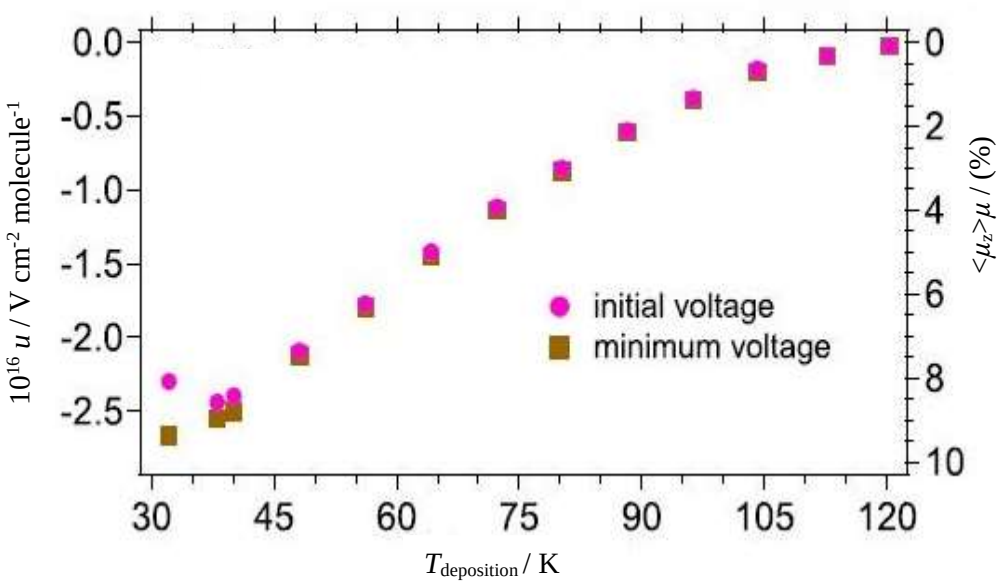

Figure 4.14: Scaled potential of 1-butanol films at the dosing temperature (circles) and at the lowermost points (squares) as function of deposition temperature. The right axis represents the degree of polarization for each sample (Reproduced from [32]).

LO-TO Splitting and the Vibrational Stark Effect

RAIRS is key tool in studying the spontelectric effect, as it can be used to measure the response of molecular vibrations to any electric field in the solid, *i.e*. the impact of the Vibrational Stark Effect (VSE). This technique has been demonstrated by Lasne *et al.* [13] using thin N_2O films. Relative to the incident beam wavelength, the film is considered infinite in the plane of the film and only the transverse optical (TO) phonons can be excited in this plane. If the film thickness is similar to the wavelength of the incident beam, boundary conditions allow for the excitation of longitudinal optical (LO) phonons along the normal axis. This is known as the Berreman effect [34, 35]. The longitudinal phonons resonate at higher frequencies due to the induced electric field associated with longitudinal waves passing through a medium composed of dipolar species. Hence, LO-TO splitting occurs in vibrational modes when an incident beam interrogates a thin film at a suitably oblique angle [2, 4, 13]. If ν_{L} and ν_{T} represent the frequencies for the LO and TO phonons, then

$$\Delta\nu_{LO-TO} = \nu_{LO} - \nu_{TO} \qquad \textbf{(E6)}$$

represents the value of the LO-TO splitting. The presence of the spontelectric field, through the vibrational Stark Effect, modifies the force fields which give rise to ν_{L}

and ν_T and hence $\Delta\nu_{LO-TO}$. Since the spontelectric field strength depends on film deposition temperature, the LO-TO splitting itself becomes dependent on this temperature. **Figure 4.15** illustrates this in the case of N_2O. Here, increasing the deposition temperature red shifts the LO mode, while the TO mode is blue shifted, leading to a contraction in $\Delta\nu_{LO-TO}$ consistent with the behaviour of the spontelectric field with deposition temperature [13].

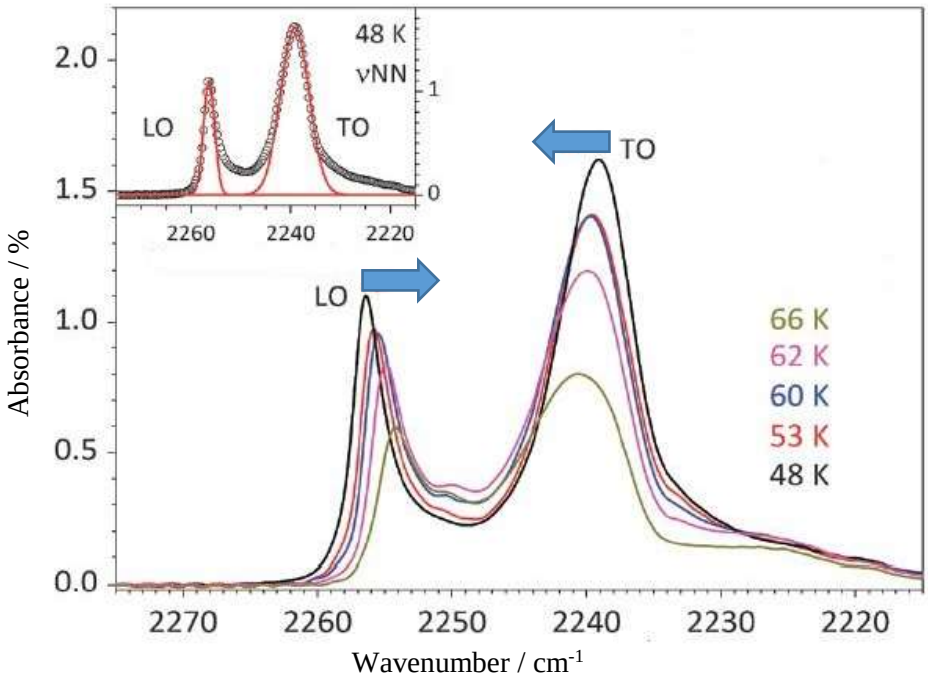

Figure 4.15: RAIR spectra showing the νNN band of 14 ML N_2O films deposited at 48, 53, 60, 62 and 66 K on $aSiO_2$. The blue arrows indicate the shift of the LO and TO modes with increasing temperature deposition temperature of the films. The inset shows the RAIR spectrum of N_2O film deposited at 48 K (circles) and the Gaussian fits (full lines) (Reproduced from [13]).

As stated above, the TO modes are polarised parallel to the surface and hence would be invisible in a RAIR experiment due to the MSSR. This is shown in **Figure 4.16**. The presence of the 300 nm $aSiO_2$ film circumvents this.

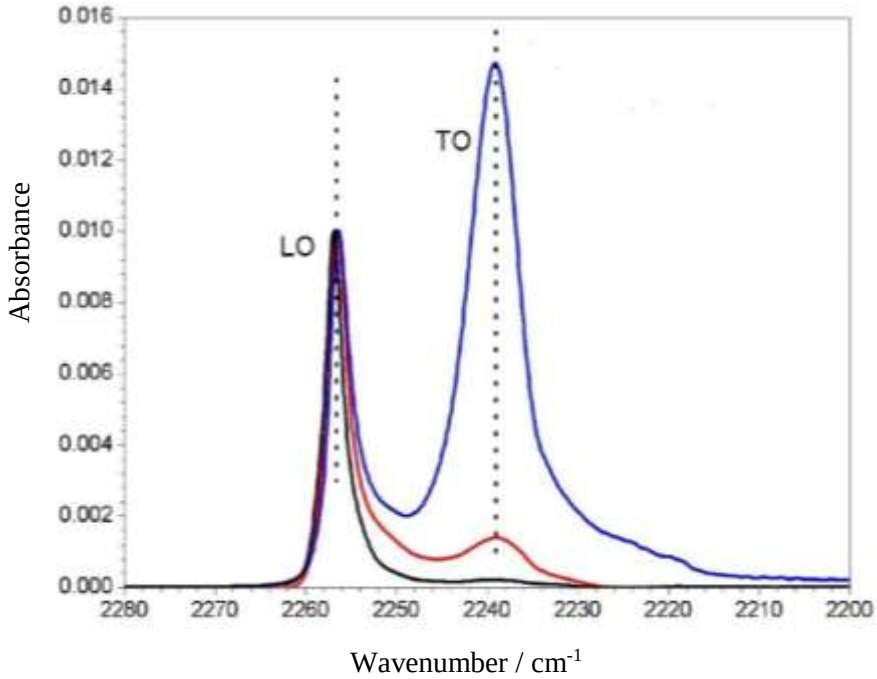

Figure 4.16: RAIR spectra of the vNN mode of 14 ML N_2O on Cu (blue), 200 nm $aSiO_2$, (red), and 300 nm $aSiO_2$ (black). The TO mode of N_2O is silent when deposited directly on Cu. The TO mode becomes visible when the N_2O is deposited on the $aSiO_2$ surface (Reproduced from [35]).

The roughness of the $aSiO_2$ spacing layer gives the molecules additional possible orientations with respect to the underlying metallic substrate which get around the MSSR (**Figure 4.17a**). **Figure 4.17b** then shows what happens as the IR beam investigates a N_2O film [35] on a rough $aSiO_2$ film.

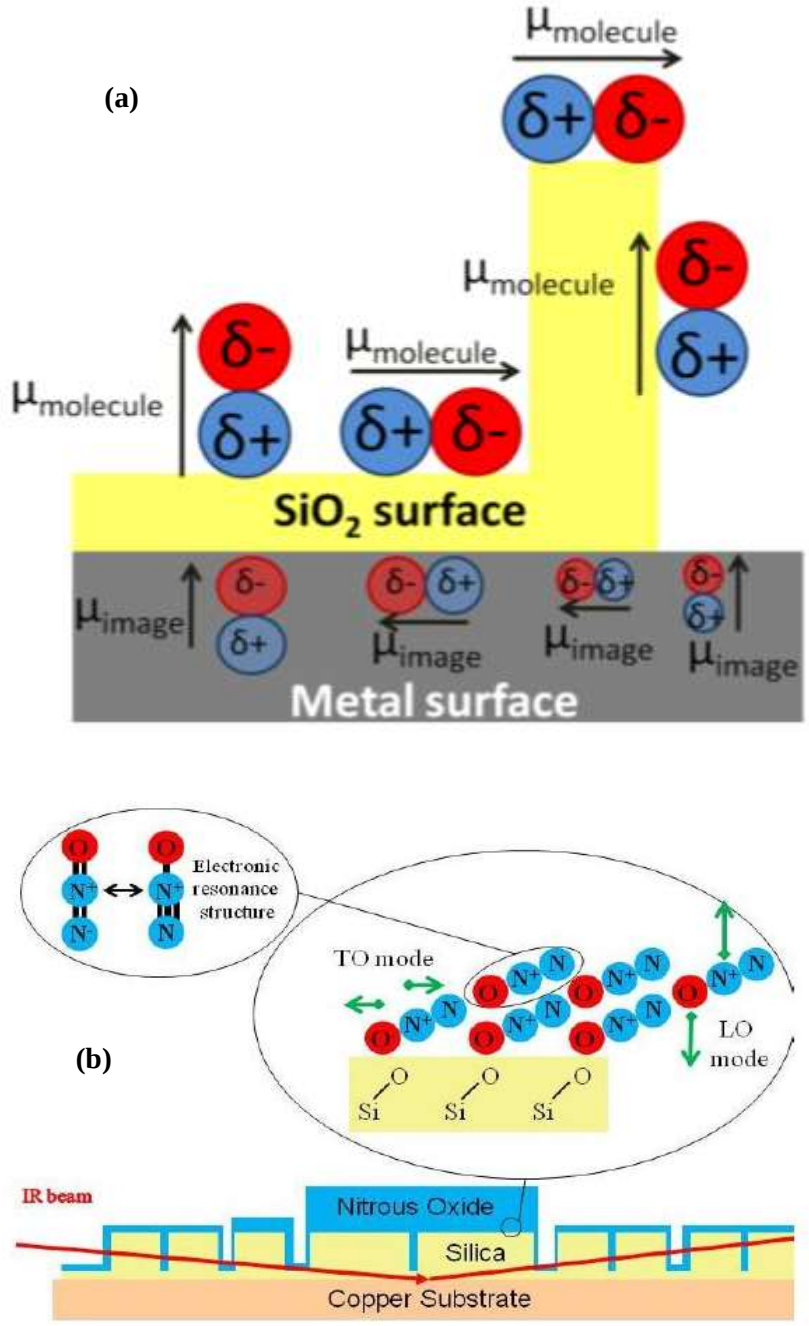

Figure 4.17: (a) An $aSiO_2$ layer has been placed between the metal and the absorbed dipole molecule film, and this shows how the roughness can circumvent the MSSR (Reproduced from [31]) and (**b**) How the LO and TO modes behave in solid N_2O. The TO mode acts oppositely to the LO mode and interacts transversely with the electric field. However, the LO mode is a result of phonons in the solid interacting longitudinally to the electric field when the infrared beam strikes the surface of the copper substrate (Reproduced from [13,35]).

4.1.6 The Exceptional Case of Methyl Formate

The simple ester, Methyl Formate (MF, **Figure 4.18**), is unique among the currently identified spontelectric materials.

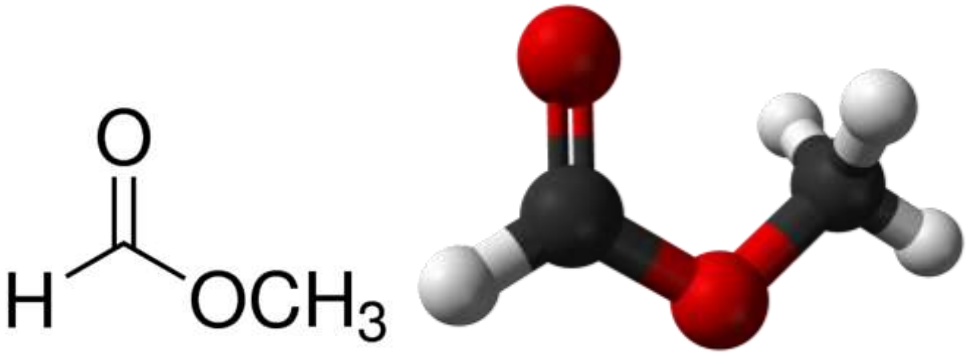

Figure 4.18: Methyl Formate structure (Reproduced from [36]).

MF shows two planar minimum energy conformations, *cis* and *trans* (**Figure 4.19**) of which the computed structure parameters are shown **Table 4.1**. The terms *cis* and *trans* refer to the relative positions of the carbonyl and methyl groups**.** The *cis* → *trans* transformation is hindered by a barrier, which is calculated to be 57.78 kJ mol^{-1} high, and occurs with only minor variation of the internuclear distances [37].

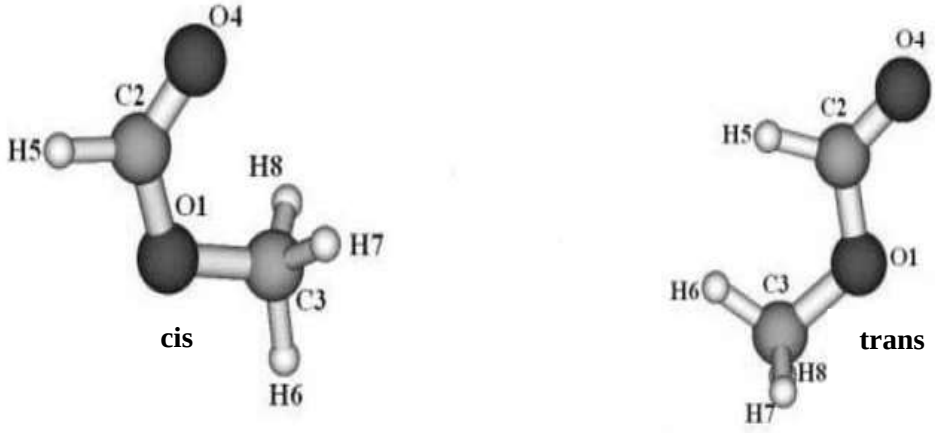

Figure 4.19: Structure of *cis*- and *trans*-MF (Reproduced from [38]).

Parameter/º	*cis* / Å	*trans* / Å
C2O1	1.3370	1.3442
C3O1	1.4344	1.4255
O4C2	1.2035	1.1963
H5C2	1.0922	1.0100
H6C3	1.0817	1.0833
H7C3	1.0851	1.0845
H8C3	1.0851	1.0845
C3O1C2	114.0	117.1
O4C2O1	125.6	122.9
H5C2O1	109.2	112.9
H6C3O1	105.5	111.3
H7C3O1	110.3	108.5
H8C3O1	110.3	108.5
O4C2O1C3	0.0	180.0
H5C2O1O4	180.0	180.0
H6C3O12	180.0	0.0
H7C3O1H5	119.7	120.4
H8C3O1H5	-119.7	-120.4

Table 4.1: MF shows two planar confirmations, *cis* and *trans*, of minimum energy. The structural parameters of the MF conformers are listed in this table [37].

There are two large-amplitude vibrations which cause the non-rigid properties of MF; methyl group torsion and OC-OC central bond torsion. The central bond torsion results in the secondary minimum and the relative energy has been calculated to be 22.19 kJ mol^{-1} [37]. Electronic structure calculations carried out by the Gutowski group at Heriot-Watt University show that the gas phase *cis*-MF is 19.7 kJ mol^{-1} more stable than the *trans*-MF [1]. The value 19.7 kJ mol^{-1} is likely to be highly modified *via* polarisation in the solid, but indicates a firm preference for the *cis*-MF between 55 K and 90 K; *i.e.* the temperature range considered in this work. This can be easily seen from the Boltzmann behaviour in **Figure 4.20** below 100 K where less than 1 part per million of the *trans*-isomer is seen to be present.

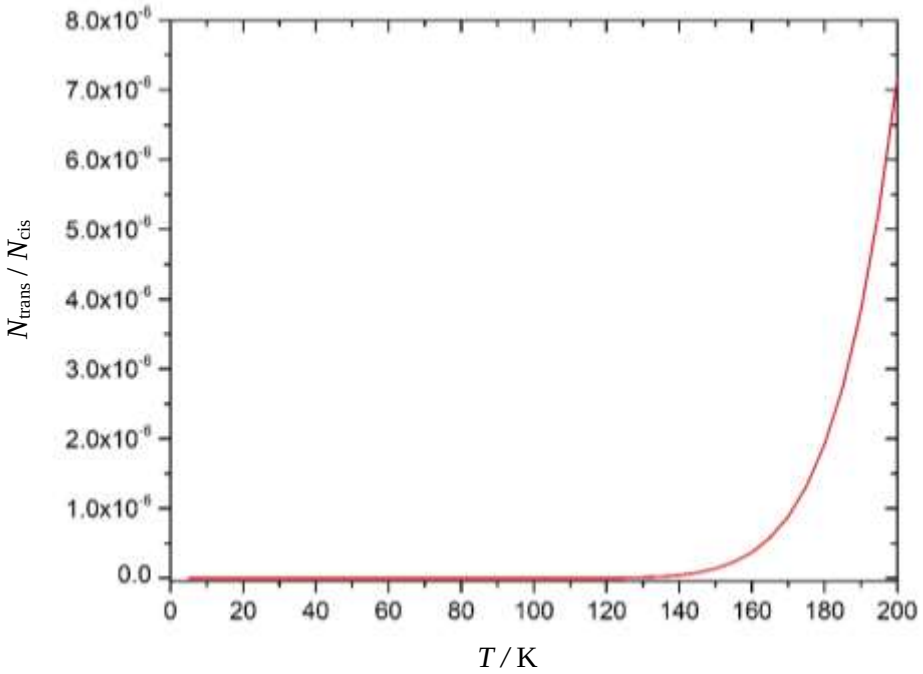

Figure 4.20: Boltzmann population of MF isomers. Below 170 K, less than 1 part in a million of the *trans*-isomer is seen to be present in MF.

Cis-MF shows a totally different dependence of the spontelectric field on deposition temperature to other species. The spontelectric field in *cis*-MF is seen to increase with temperature while it decreases in other spontelectric materials. This can be clearly seen in **Figures 4.21** to **4.23,** which show the surface potential on *cis*-MF films for a range of temperatures between 40 and 89 K. It is clear from these figures that the surface potential and spontelectric field in *cis*-MF films decrease at first with temperature of deposition, as exhibited by other spontelectrics. However, at temperatures of around 78 to 80 K, the surface potential and hence spontelectric field begin to rise steeply, as shown in **Figure 4.21** [3].

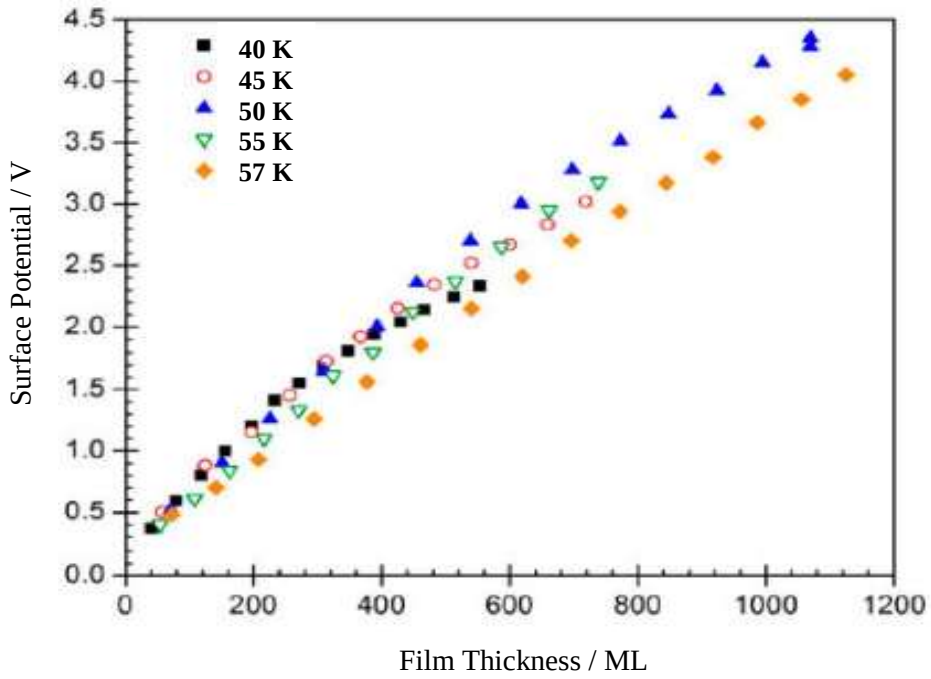

Figure 4.21: The surface potentials for *cis*-MF films as a function of thickness in monolayers for the deposition temperature range 45 to 57 K (Reproduced from [3]).

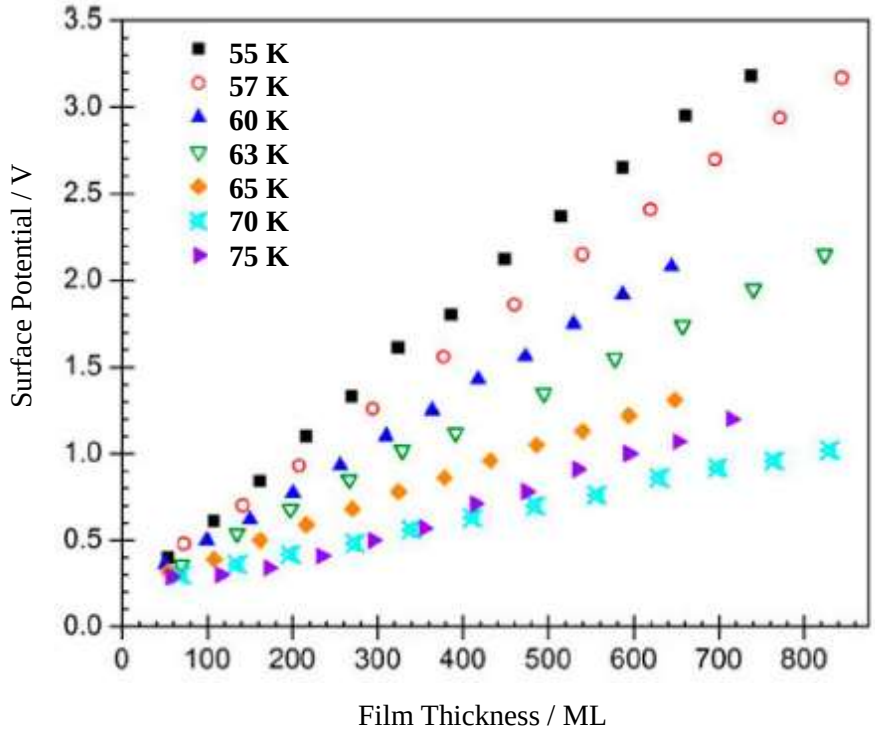

Figure 4.22: The surface potentials of *cis*-MF films as a function of thickness in monolayers for the deposition temperature range 55 to 75 K (Reproduced from [3]).

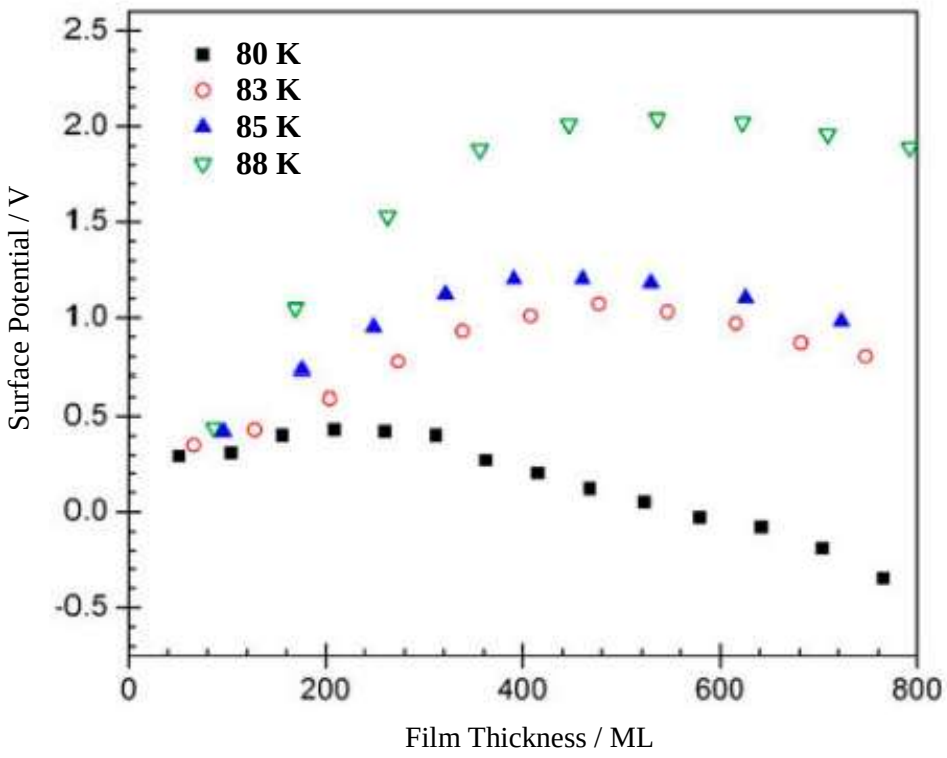

Figure 4.23: The surface potentials, measured for *cis*-MF films, as a function of thickness in monolayers for deposition temperatures ranging from 80 to 88 K. The decay, which is seen in the spontelectric effect at high coverages, may result from instability, or the effects of time, and is not due to the effects of thicker layers of *cis*-MF (Reproduced from [3]).

The decay of the spontelectric behaviour in *cis*-MF is greatest at temperatures higher than 80 K, as seen in **Figure 4.23**. Additionally, there is also a low temperature range, 40 to 55 K, for which curvature of the observed spontelectric field *versus* layer thickness is found. At this point, there exists a temporal instability, which tends to decrease as deposition temperature is increased. The stability of *cis*-MF films above 55 K, along with the instability below, suggests a structural change in *cis*-MF at around this temperature. This interpretation is supported by the Curie Point data, which is best illustrated by the data reproduced in **Figure 4.24**, where the deposition temperature is above 90 K and the spontelectric effect is completely lost [3].

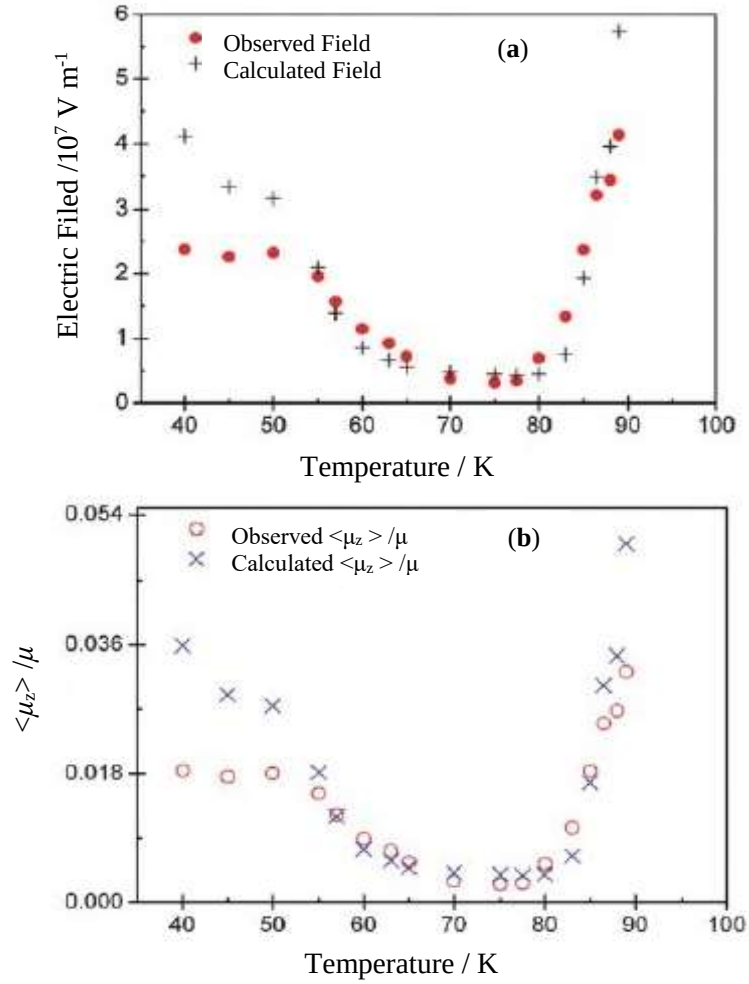

Figure 4.24: (**a)** The variation of the observed electric field as a function of deposition temperature and (**b**) The variation of the degree of dipole orientation, $<\mu_z>/\mu$, as a function of deposition temperature (Reproduced from [3]).

4.2 Experimental and Computational Methods

The experiments were carried out in an ultrahigh vacuum (UHV) chamber, full details of which are given in **Chapter 2** while an overview is given here. The MF (Sigma Aldrich, anhydrous, 99%) was deposited on the cold surface by background-filling the chamber *via* a leak valve. The leak valve was connected to the gas handling line, on which the sample MF was held in a valved glass phial. The MF was prepared by several freeze-pump-thaw cycles. MF dosing times and pressures were varied according to the film coverages required. In general, to ensure enough molecules were in the chamber, dosing was done at high pressure and over a long time period.

Additionally, this permitted the purity of the MF in the gas phase to be assessed by QMS.

TPD was used to investigate the interaction of MF with the surface of $aSiO_2$. Coverages in the range from 10 L to 10,000 L were deposited on the $aSiO_2$ substrate at base temperature using a forward facing leak valve. Particular emphasis was placed on low coverages of MF, since this is the most indicative of the interaction with the underlying substrate. After each coverage TPD experiments were carried out using a temperature ramp with an average heating rate of 0.09 K s^{-1} and monitored using line-of-sight quadrupole mass spectrometer.

Simple kinetic models of TPD can be constructed which allow simulation of the experimental data and hence determination of keynote parameters. The software used is Chemical Kinetics Simulator (CKS) developed by IBM Almaden Research Centre [39]. The software makes use of probability theory. The CKS code performs Monte Carlo integration in order to solve the differential equations given as input. The code can be used to model TPD traces by using a system of differential equations which represent the kinetics steps of each of the key physical processes. The input for the code consists of TPD data, associated rate law [40] and initial concentration of the species involved. The temperature can be fixed for each simulation or varied as required. For the TPD simulation, the inputs to the code include the E_{des} and ν_{des}, which can be extracted from the experimental results as an initial estimate of the values. These can then be optimised to fit the experimental data. The parameters are adjusted until there is good agreement with simulated and experimental TPD results [35, 41].

The reflection–absorption spectra of MF in the spectral range 700 to 4000 cm^{-1} were obtained using a Fourier-transform infrared spectrometer (Varian 670-IR), configured for RAIR spectroscopy, at a grazing angle incidence of 75° with respect to the normal to the substrate. This is the same method as used for N_2O [13, 35]. The spectra were recorded using a resolution of 0.1 cm^{-1}. To investigate the spontelectric effect, thick 10,000 L films of MF were prepared by depositing them on an $aSiO_2$ substrate at the temperatures noted ±0.5 K. The MF was dosed at a range of temperatures starting from the base temperature of 14.5 K and going to 110 K in steps

of 5 K and then the sample was then cooled to base temperature. RAIR spectra, where recorded using 512 scans at a resolution of 0.1 cm^{-1}. Typically two background scans and a sample scan (before dosing) were taken. When the IR detector was filled with liquid nitrogen, roughly every two hours, the instrument was allowed to stand for around 15 minutes before further measurements were taken. In the time-dependent studies of the spontelectric effect, the IR detector was set as above, but the RAIR spectra recorded at 95 K, rather than at base temperature. Over a period of 4.5 hours, four sets of scans were made, one after the other, with a break only for IR detector refilling. The IR spectra were analysed using the Gaussian fit function within the OriginPro software.

Computational chemistry was used in combination with IR sepectrscopy to investigate the *cis*-MF monomers and dimer. This allows the prediction of the structural motif in the solid state. Details of the computational work are discussed in references [1, 2] and a brief overview is given here. The complex calculations were carried out by the Gutowski group (Heriot-Watt University) and consisted of geometry optimisation at two different levels (MP2 and CCSD/ATZ) with the aug-cc-pVTZ (ATZ) basis set of MF structures were found by rotating around the C-O-C-O dihedral angle [1]. For the dimer, initially 43 orientations of the monomers which included *cis-cis*, *cis-trans* and *trans-trans* complexes were investigated. The geometry optimisation for these initial 43 structures converged into 16 structures [1], where *cis-cis* were the most stable, and *trans-trans* the least stable. Hence, *cis-cis* complexes were investigated more thoroughly [1].

4.3 Results and Discussion

Firstly, TPD of MF will be presented and discussed. This is followed by the assignment of the RAIR spectra and identification of the predominant conformational isomer (*cis versus trans*) in the solid state. Then RAIR spectra of MF are used to investigate the spontelectric field in the solid state. This is followed by details of how IR spectroscopy and computational chemistry is used to predicate the structural motif within the unit cell of the crystalline phase of *cis*-MF. Finally, details of non-linear and non-local behaviour in spontaneously electrical *cis*-MF solid will be discussed.

4.3.1 TPD of Methyl Formate from $aSiO_2$

Coverages in the range from 10 L to 10,000 L were deposited on the $aSiO_2$ substrate at base temperature**. Figure 4.25** shows the TPD data for coverages from 20 - 90 L; **Figure 4.26** from 100 – 1,000 L; and **Figure 4.27** from 1,000 to 5,000 L. In **Figure 4.25,** Peak **A** grows to a saturation point and appears to have a common maximum temperature and same commonality of trailing edges. This would be consistent with first-order desorption of the first layer, which suggests that MF wets the $aSiO_2$ surface.

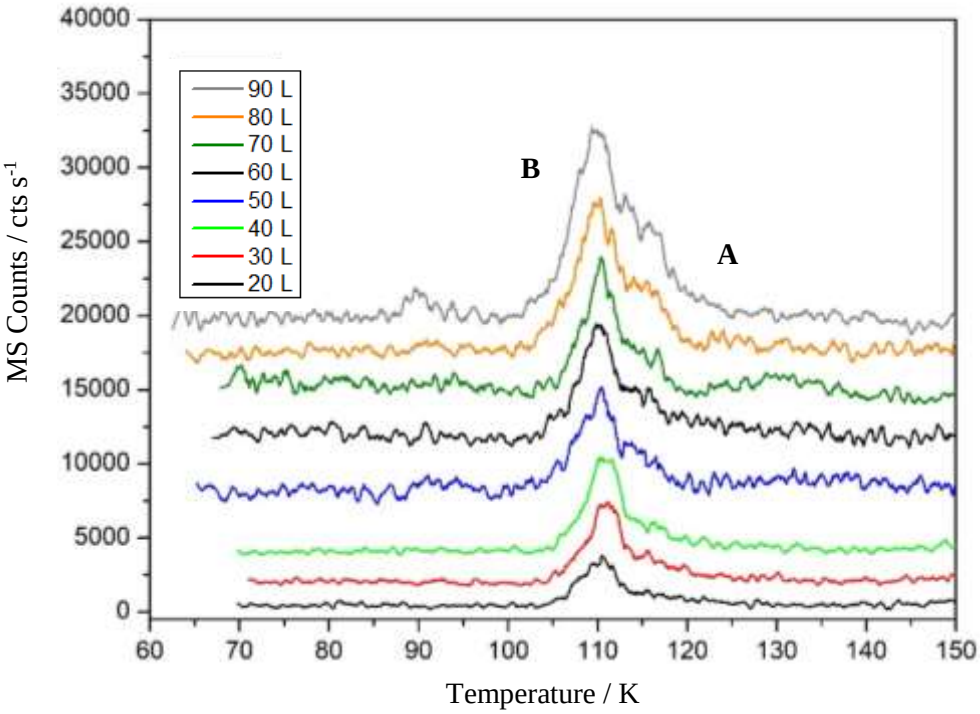

Figure 4.25: TPD of MF 20 – 90 L deposited on the $aSiO_2$ copper substrate at base temperature (14.5 K). Two features are observed, labelled Peak **A** and Peak **B**. The TPD plots have been offset vertically for clarity.

Peak **B,** on the other hand, shows some commonality of leading edge that is consistent with zero-order desorption of a multilayer ice. In **Figure 4.26**, Peak **D** follows the behaviour established by Peak **B** in **Figure 4.25** for zero order desorption of the multilayer ice. **Peak C** and **Peak E**, on the other hand (**Figure 4.26** and **Figure 4.27)**, appears to coincident with the crystallisation of the MF as reported in the RAIRS spectra below which would suggest that latent heat release during crystallisation may promote this desorption process.

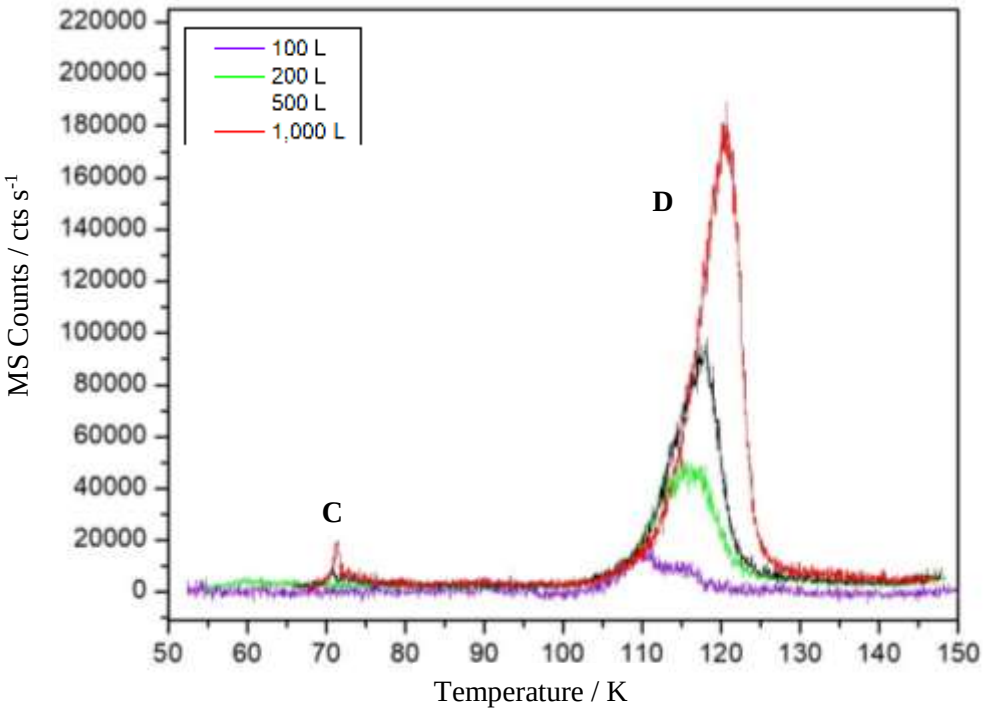

Figure 4.26: TPD of MF (100 – 1,000 L) deposited on the $aSiO_2$ coated copper substrate at base temperature (14.5 K). Two features were observed which are labelled Peak **C** and **D**.

In order to determine the monolayer and multilayer, the TPD plots are inspected. At low coverage the TPD traces exhibit coincident trailing edges, which is consistent with monolayer behaviour and at higher coverages they have coincident leading edges; this is multilayer behaviour. This behaviour has been seen in a number of studies, see **Chapter 2** and the work of Brown and co-workers [42]. At this stage we confirm the TPD behaviour and identify the monolayer exposure as 100 L. Hence, 1 ML is equivalent to 100 L. This allows us to convert exposures into coverage.

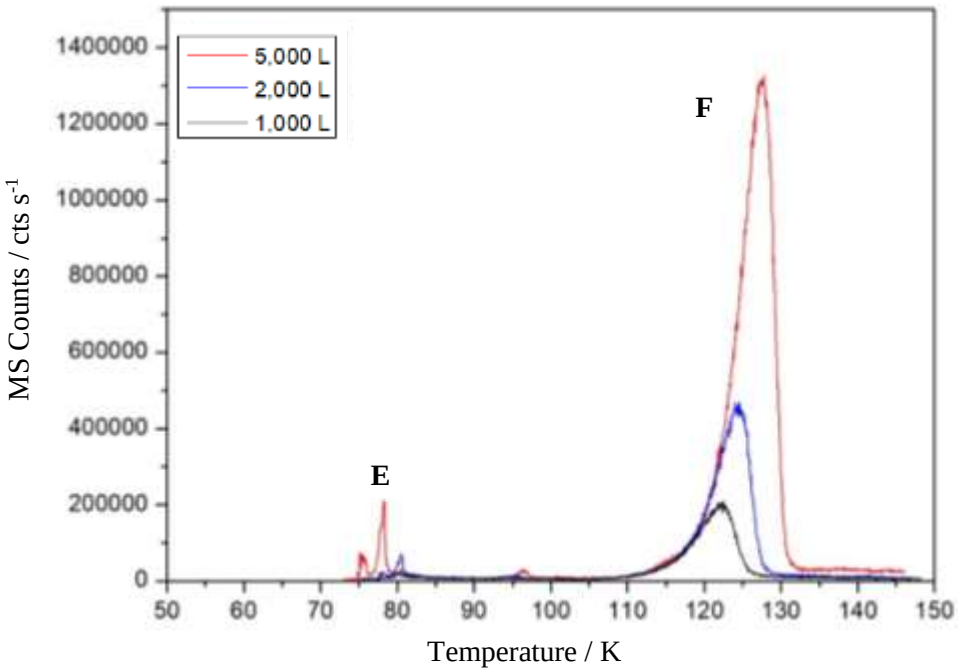

Figure 4.27: TPD spectra for MF (1,000 L, 2,000 L and 5,000 L) deposited on the aSiO_2 coated copper substrate at base temperature (14.5 K). Two features are observed, labelled Peak **E** and Peak **F**. There is perhaps the same evidence of desorption induced by crystallisation entropy release (Peak **E**) *i.e*. Peak **C** in **Figure 4.26**.

The trend established by **Peak B** in **Figure 4.25**, and continued in **Figure 4.26** (**Peak D**), continues in **Figure 4.27** (**Peak F**). The TPD here shows multilayer desorption with zero-order kinetics, as inferred by the common leading edges and the increase in peak temperature with increasing coverage. The order of desorption is confirmed by using Leading Edge Analysis (LEA). By plotting $\ln(r_{des})$, the desorption rate, against $\ln(\Theta)$, the coverage, the gradient yields the order of desorption. Zero order desorption for **peak D** in **Figures 4.26** and **Peak F** in **Figure 4.27** is confirmed by the LEA presented in **Figures 4.28** through to **4.29**. **Figure 4.28** provides the LEA results for 1 ML to 10 ML with a resulting average kinetic order of 0.02 ± 0.02. **Figure 4.30** completes the set with the data for 10 ML to 50 ML where the average value of the kinetic order is 0.0 ± 0.0.

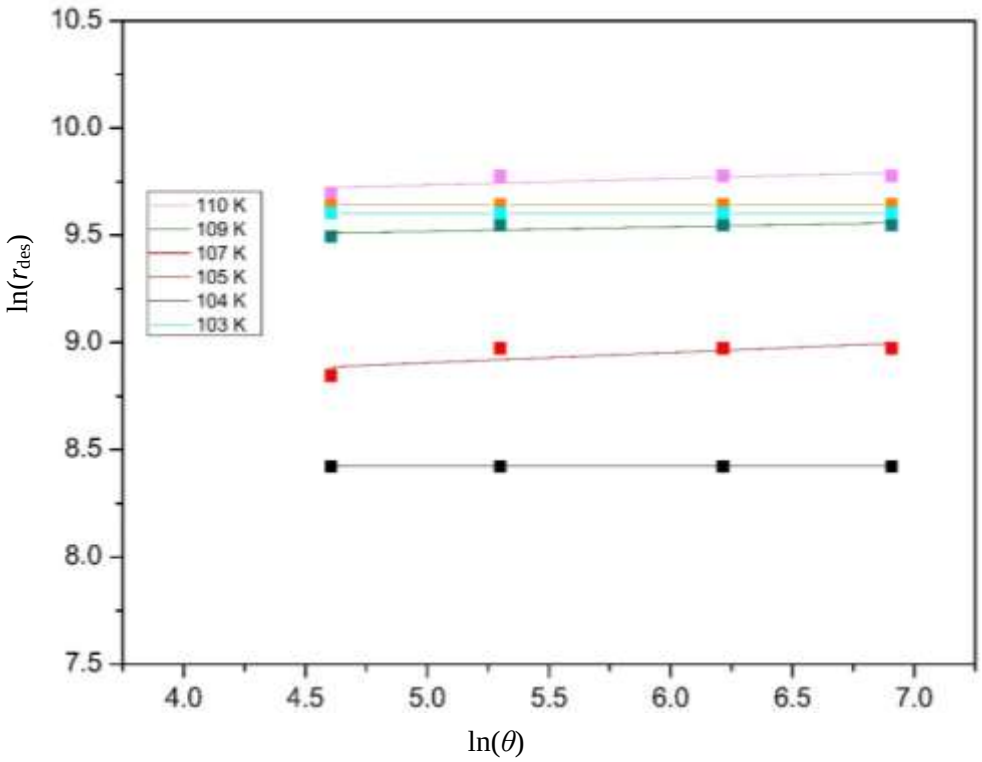

Figure 4.28: Leading-edge analysis of the 1 ML to 10 ML TPD of MF from an $aSiO_2$-coated copper substrate.

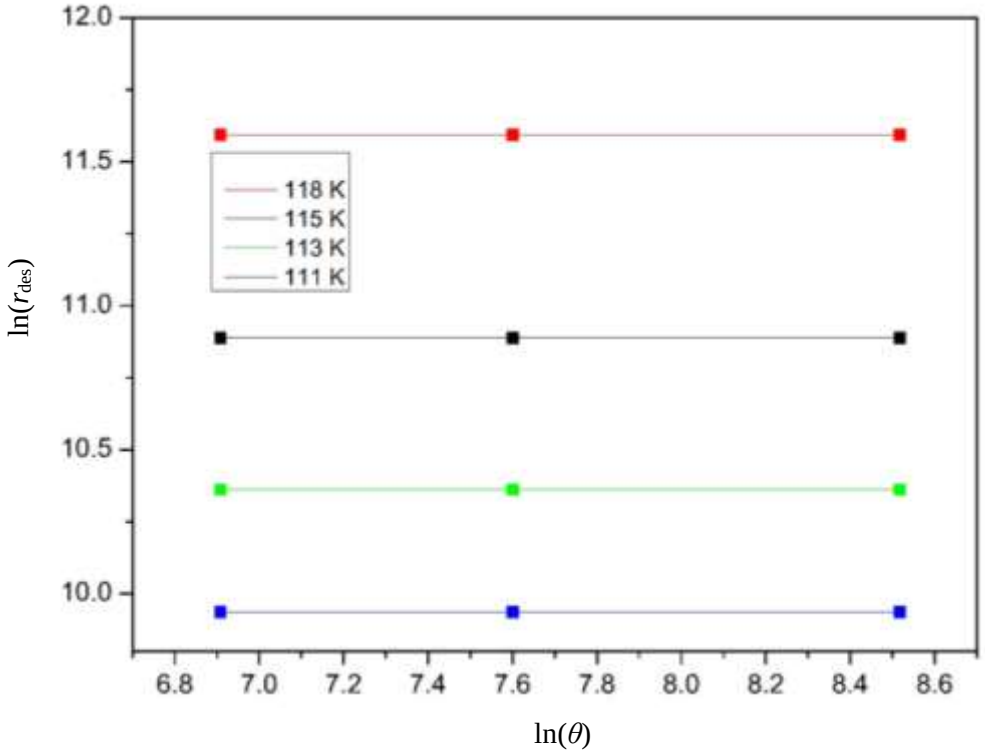

Figure 4.29: Leading-edge analysis of the 10 ML to 50 ML TPD of MF from an $aSiO_2$-coated copper substrate.

As an average over all multilayer coverages, the desorption order is 0.002±0.02. This clearly establishes that the rate law for desorption of multilayer films of MF is zero order and can be written as **Equation 7**:

$$r_{\mathrm{des}} = \upsilon_{\mathrm{des}} e^{-\frac{E_{\mathrm{des}}}{RT}} \qquad \textbf{(E7)}$$

A simple Arrhenius Analysis can then be used to establish E_{des}, as shown in **Figure 4.30**, which shows the required plot ln(r_{des}) *versus* 1/*T* in the case of the TPD of 5,000 L of MF from the $aSiO_2$ coated copper substrate. Similar analyses were performed on all the multilayer systems (**Table 4.2**) and the average activation energy for desorption, E_{des}, was found to be 26.4±5.5 kJ mol^{-1}.

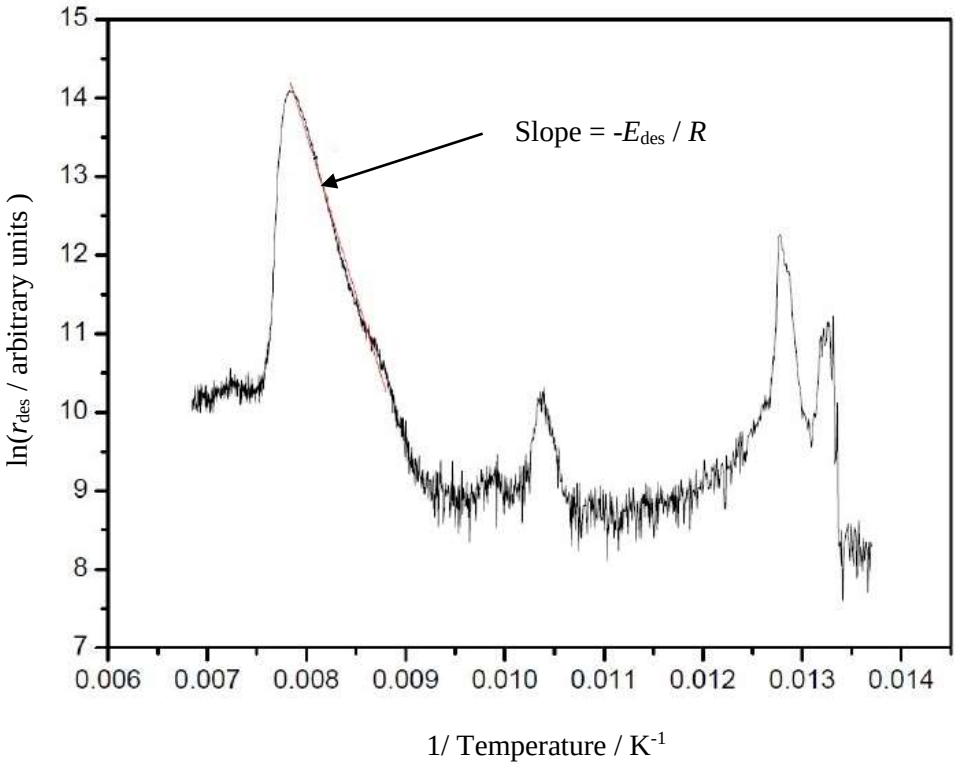

Figure 4.30: Arrhenius Analysis of the TPD of 5,000 L of MF from the $aSiO_2$ surface. The red line indicates the relevant region of the data from which the activation energy for desorption, E_{des}, of the film can be extracted.

Coverage / ML	E_{des} / kJ mol^{-1}
2	20.2
5	22.9
10	25.3
20	29.6
50	33.9
Average E_{des}	26.4 ± 5.5 kJ mol^{-1}

Table 4.2: E_{des} *versus* coverage for multilayer coverages of MF using Arrhenius Analysis.

To calculate E_{des} for the monolayer coverages, Redhead analysis is used [43]. The starting point is the Polanyi-Wigner equation (**Chapter 2, Equation 13**) and for first order kinetics assuming that the activation parameters are independent of the surface coverage, it follows that:

$$E_{\mathrm{des}} = RT_{\mathrm{max}}\left[\ln\left(\frac{\nu_{\mathrm{des}}T_{\mathrm{max}}}{\beta}\right) - \ln\left(\frac{E_{\mathrm{des}}}{RT_{\mathrm{max}}}\right)\right] \quad \textbf{(E8)}$$

The term $\ln\left(\frac{E_{\mathrm{des}}}{RT_{\mathrm{max}}}\right)$ is typically small and assumed to be equal to 3.64 if $\nu_{\mathrm{des}} / \beta$ lies in the range 10^8 to 10^{13} K^{-1} and so the final expression is [41, 43].

$$E_{\mathrm{des}} = RT_{\mathrm{max}}\left[\ln\left(\frac{\upsilon_{des}T_{\mathrm{max}}}{\beta}\right) - 3.64\right] \quad \textbf{(E9)}$$

where ν_{des} is 10^{12} s^{-1}, and T_{max} and β are calculated using **Figure 4.26**. **Table 4.3** shows the calculated desorption energies for the monolayer coverages of MF. The average E_{des} is 29.8 ± 0.1 kJ mol^{-1}.

Coverage / ML	E_{des} / kJ mol^{-1}
0.40	29.7
0.50	29.78
0.60	29.9
0.70	29.8
0.80	29.7
0.90	29.9
Average E_{des}	29.8±0.1

Table 4.3: The E_{des} values for sub-monolayer coverages of MF using Redhead analysis [43].

The E_{des} for monolayer MF is only slightly higher than the E_{des} for the multilayer. This would indicate that MF coupling to $aSiO_2$ is weak and only slightly stronger than MF coupling to itself. This has also been observed in the work by Schwaner *et al.* [44] which investigated MF adsorption from Ag(111). The CKS stochastic integration package was then used to model the sub-monolayer and multilayer coverages (**Figure 4.26**). This approach has been used to aid the fit and analysis of the experimental TPD and is based on a simple three-step process:

$$HCOOCH_3(\text{s-multilayer}) \rightarrow HCOOCH_3(g) \quad \textbf{(R1)}$$

$$HCOOCH_3(\text{s-monolayer}) \rightarrow HCOOCH_3(g) \quad \textbf{(R2)}$$

$$HCOOCH_3(g) \rightarrow HCOOCH_3\,(p) \quad \textbf{(R3)}$$

which involves 4 different species of MF: adsorbed solid MF as monolayer(s-monolayer) and multilayer(s-multilayer); gaseous (g); and pumped (p) MF. CKS relies on stochastic integration of differential equations, which treat each species as a generic entity, with no chemical characterisation. The CKS model for the multilayer and monolayer is set up using E_{des} values calculated using the AA and Redhead Analysis as discussed above. For each simulation, individual experimental temperature ramps are used. This results in slight offset in the simulations but reflects the experimental reality (**Figure 4.33**). The surface concentration for monolayer is taken as 10^{15} molecules cm^{-2} as is typically assumed for a monolayer [35, 41].

First only desorption from sub-monolayers coverages is considered. The results of the model are compared with experimental data and the pre-exponential factor is adjusted until a good fit between the model and experimental data is achieved. **Figure 4.31** shows the sub-monolayer coverages and best fit CKS simulations. The resulting simulations are in good agreement with the experimental data.

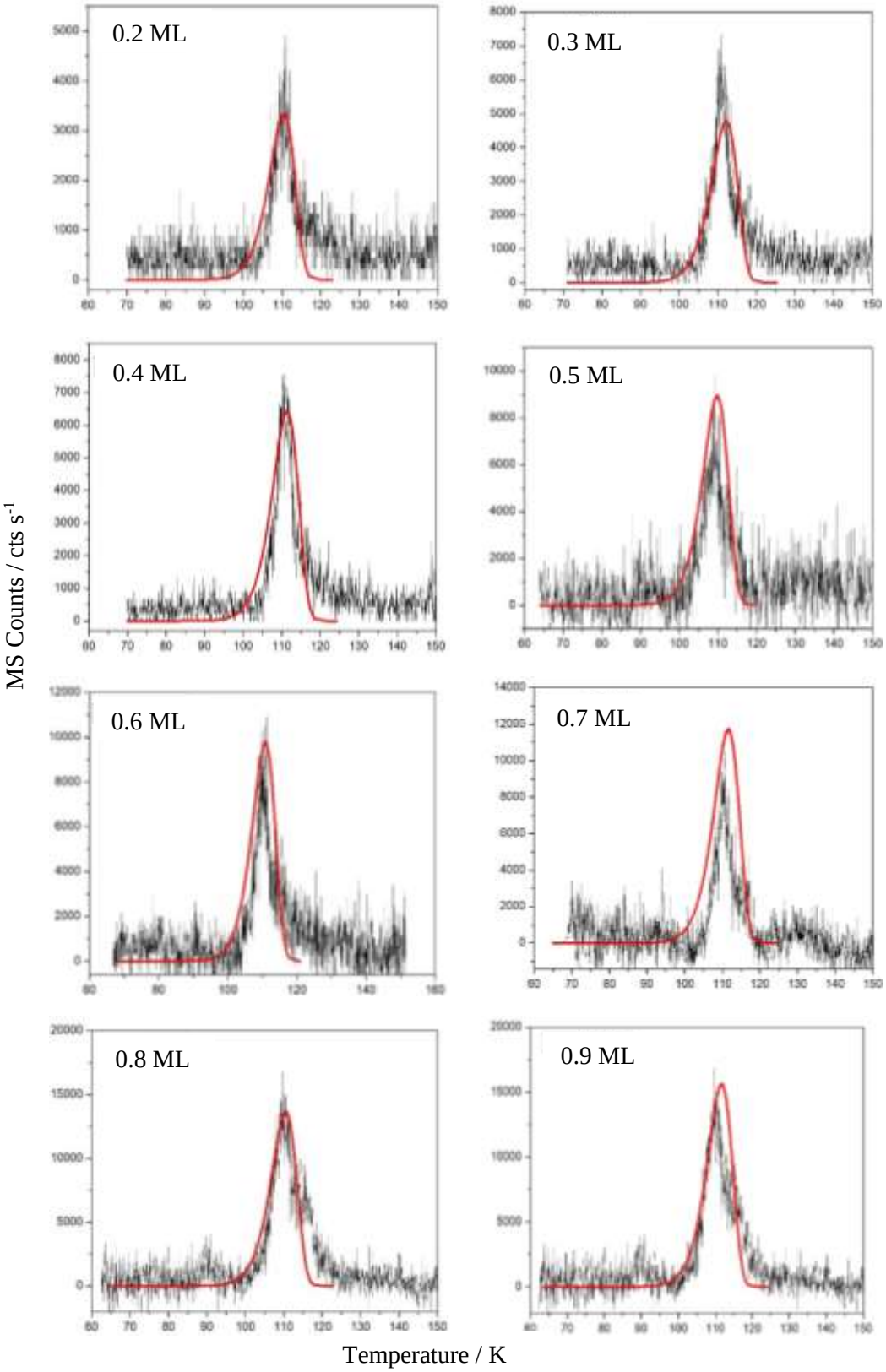

Figure 4.31: The TPD results (black experimental data) with the CKS model simulations (red line) for sub-monolayer coverages 0.20 ML through to 0.90 ML.

To simulate the multilayer coverages using CKS, the same approach was used. The E_{des} is fixed and the surface concentration is fixed for each coverage and the pre-exponential factor is varied until good fit is achieved between the experimental and CKS model. **Figure 4.32** shows a multilayer coverage of 50 ML, TPD (black) and the best fit CKS model (red) and **Figure 4.33** shows the 2 ML coverage.

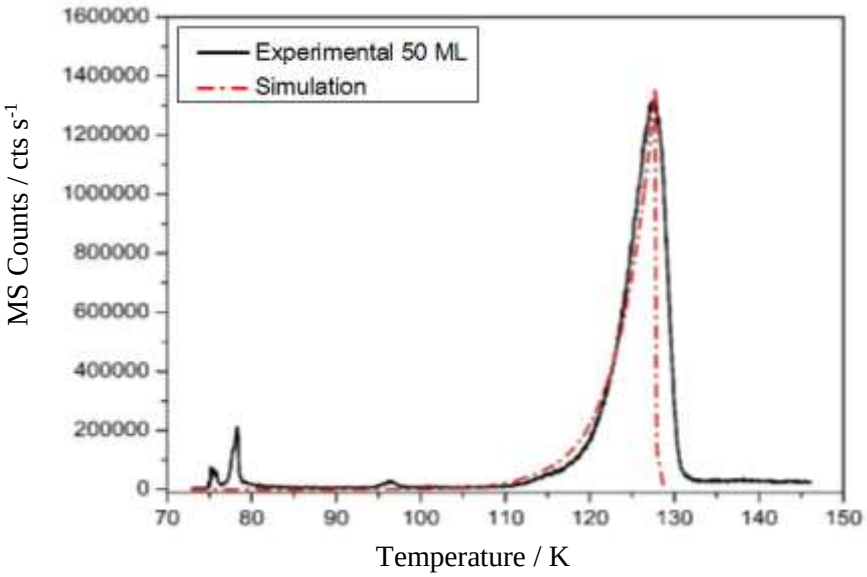

Figure 4.32: The figure shows the TPD data of 50 ML dosing onto aSiO_2 (black) with the best fit CKS model (red).

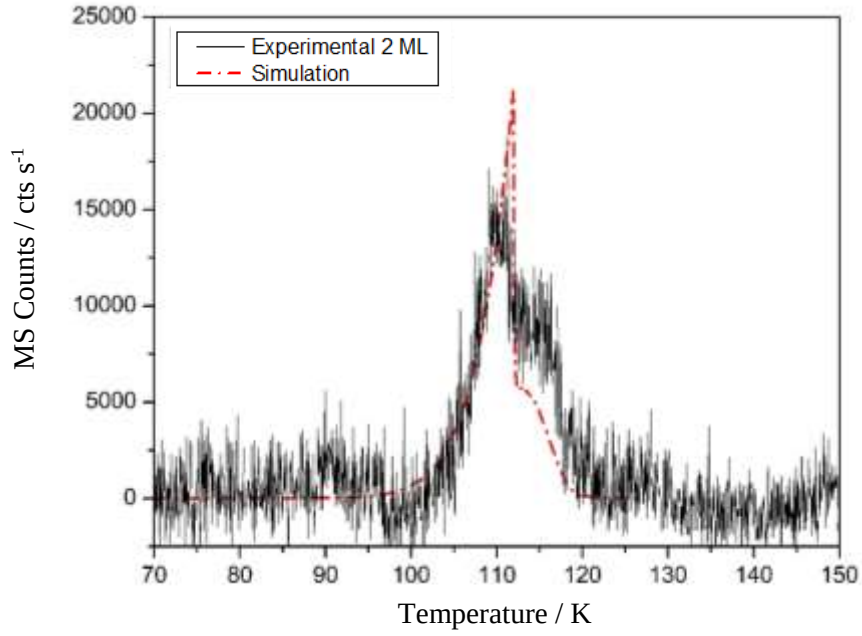

Figure 4.33: The figure shows the TPD data of 2 ML dosing onto aSiO_2 (black) with the best fit CKS model (red).

Table 4.5 and **4.6** show the sub-monolayer and multilayer coverages and the corresponding best fit pre-exponential factors. The E_{des} is fixed for all coverages and the pre-exponential factor is determined through an iteration process until best fit is achieved of experimental and modelled data. From **Table 4.3** the pre-exponential factor for the monolayer is $3.0\pm0.8 \times 10^{12}$ s^{-1}.

Coverage / ML	**υ_{des} / s^{-1}**
0.2	3.0×10^{12}
0.3	2.0×10^{12}
0.4	2.5×10^{12}
0.5	4.5×10^{12}
0.6	3.0×10^{12}
0.7	2.5×10^{12}
0.8	3.5×10^{12}
0.9	3.3×10^{12}
Average	$3.0\pm0.8 \times 10^{12}$

Table 4.4: Sub-monolayer coverages of MF and optimized pre-exponential factor obtained from CKS Analysis.

Coverage / ML	**υ_{des} /molecule cm^{-2} s^{-1}**
2	3.16×10^{28}
5	3.17×10^{28}
10	3.12×10^{28}
50	3.17×10^{28}
Average	$3.15\pm0.02 \times 10^{28}$

Table 4.5: Multilayer coverages of MF and optimized pre-exponential factor obtained from CKS model analysis.

Table 4.6 compares the results from this work with previously published data. The work by Brown and co-workers [42] was carried out on the HOPG surface and is zero order and the work by Schwaner *et al*. [44] is on a Ag(111) surface. Agreement between our data and the literature is good.

	This work		Literature	
	E_{des} / kJ mol^{-1}	υ_{des} / s^{-1}	E_{des} / kJ mol^{-1}	υ_{des} / s^{-1}
Monolayer	29.80±0.12	3.04±0.78x10^{12}	37.4 [44]	
	E_{des} / kJ mol^{-1}	υ_{des} / cm^{-2} s^{-1}	E_{des} / kJ mol^{-1}	υ_{des} / cm^{-2} s^{-1}
Multilayer	26.40±5.50	3.15±0.02x10^{28}	35±0.6 [42], 34 [44]	8±1x10^{28} [42]

Table 4.6: The kinetic parameters from this work and in the literature for MF TPD. The work by Brown and co-workers [42] is on the HOPG surface and the work by Schwaner *et al*. [44] is on a Ag(111) surface.

The results from TPD (**Figure 4.26-28**) demonstrate that MF wets the surface as MF forms weaker intermolecular bonds compared to those between MF and the $aSiO_2$ surface. This wetting is also observed in the work of Brown and co-workers (**Figure 4.34**) [42].

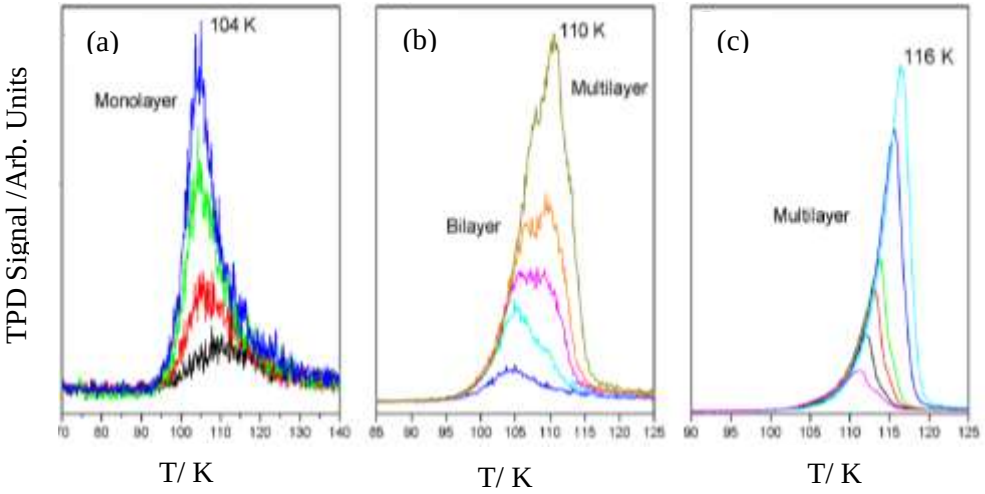

Figure 4.34: TPD spectra for MF adsorbed on HOPG at 23 K (**a**) the monolayer coverages (0.1-0.7 ML), (**b**) the bilayer and multilayer coverages (0.7-5 ML) and (**c**) multilayer coverages (7- 50 ML) (Reproduced from [42]).

4.3.2 RAIRS of Methyl Formate on $aSiO_2$

Assignment of IR Spectra

The full RAIR spectrum of 10,000 L MF deposited on our $aSiO_2$ surface is shown in **Figure 4.35**. The inset in this figure illustrates that the ν_{CO} stretching frequency exhibits clear evidence of splitting. This splitting could result from conformational isomerism and / or LO-TO splitting. Other bands show similar behaviour. This is

in contrast to the literature IR transmission spectrum reported in **Figure 4.36**. **Table 4.5** summarises the assignment and comparison with literature spectra [42, 45].

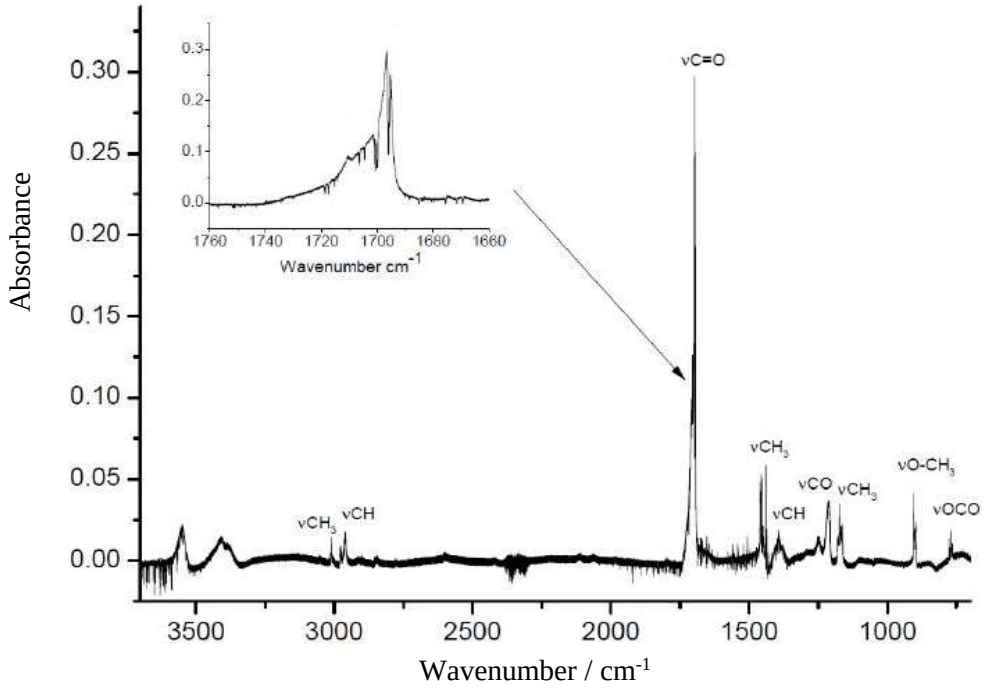

Figure 4.35: RAIRS spectrum for 10,000 L of MF deposited 100 K on an $aSiO_2$ film on a copper substrate. The peak assignment is given.

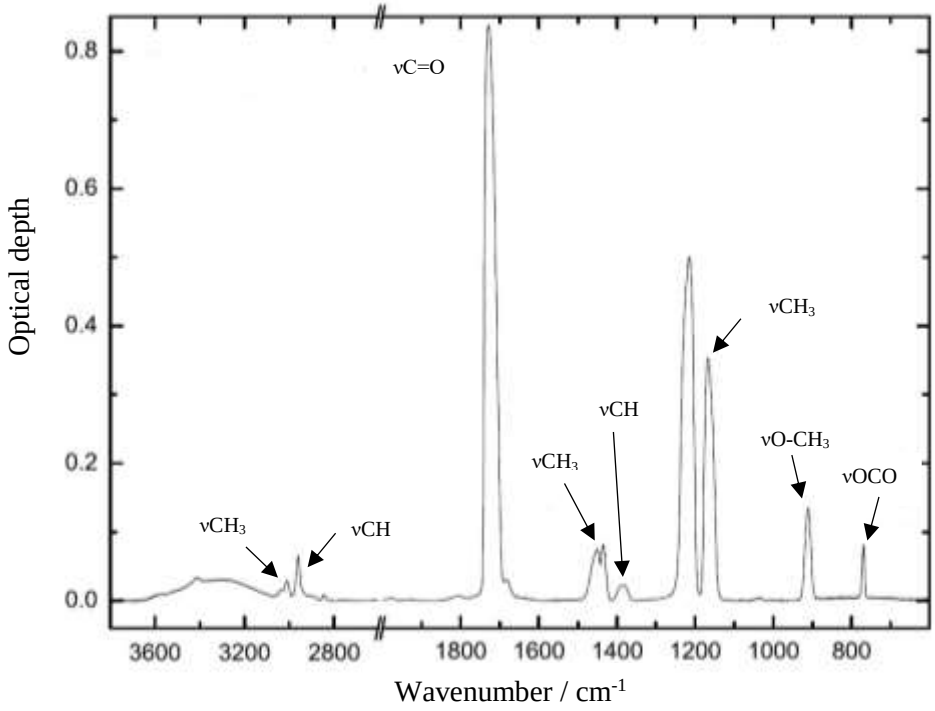

Figure 4.36: IR transmission spectrum of MF deposited and recorded on KBr at 16 K with assignment (Reproduced from [45]).

(a)	Amorphous MF peak positions / cm^{-1}		
Vibration	**Literature [45]**	**Literature [45]**	**This work (±2)**
CH_3 stretch	3038,3010	3015	3011
CH stretch	2960	2964	2959
ν_{CO} stretch	1720	1736	1734,1720
CH_3 deformation	1450,1453	1450,1460	1453
CH bend	1383	1388	1389
C–O stretch	1210	1228	1212
CH_3 rock	1164	1173	1171
O–CH_3 stretch	910	910	913
OCO deformation	768		769

(b)	Crystalline MF peak positions / cm^{-1}		
Vibration	**Literature [42]**	**Literature [42] (±2)**	**This work (±2)**
CH_3 stretch		3013, 3019	3012
CH stretch		2963, 2978	2961, 1976
ν_{CO} stretch	1713,1707	1724, 1706	1717,1706,1710,1697
CH_3 deformation	1450,1453	1440,1451,1459,1472	1440,1454,1460
CH bend		1394	1392
C–O stretch	1210	1214, 1234	1213
CH_3 rock	1164	1164, 1177	116, 1173
O–CH_3 stretch	910	901, 906	899, 905
OCO deformation	768		770, 776

Table 4.7: The vibrational assignment of the infrared spectrum of solid MF. A comparison of work carried out in this thesis with that of Palumbo and co-workers [45] and Brown and co-workers [42]: (**a**) amorphous MF films deposited at 16 K [45], 26 K [42] and 18 K [1] in this thesis and (**b**) the spectra of crystalline MF deposited at 110 K [45], 105 K [42] and 108 K in this thesis [1]. The uncertainty in the line positions is dependent of the resolution of the measurement. In this work, 1 cm^{-1} resolution was employed and we are confident that the positions are defined to within ±0.5 cm^{-1}.

Investigation of Conformational Isomerism in MF

Keolopile and Gutowski have reported on the conformational isomerism of MF using coupled cluster level-theory with single and double excitations (CCSD / aug-cc-pVTZ (ATZ) [1]. **Figure 4.37** shows the electronic structure energy profile and identifies two minima corresponding to *cis*-MF and *trans*-MF. Harmonic vibrational constants for the MF ν_{CO} stretch mode and anharmonic corrections were calculated and are given in **Table 4.8.** These data together tell us that solid MF is likely composed on *cis*-MF as the Boltzmann population is negligible in the temperature range of interest (**Figure 4.20**) and there is no evidence of spectral

features due to the ν_{CO} stretching of *trans*-MF at 1750 cm^{-1} as predicted by the computational work. It is concluded therefore that MF film is exclusively *cis*-MF. Thus, the splitting we observe must be LO-TO splitting.

	Computed ν_{CO} / cm^{-1}				
Structure	**CCSD(H)**	**MP2(H)**	**MP2(AH)**	**δMP2(AH)**	**CCSD(H) + δMP2(AH)**
cis	1827.0	1769.5	1738.5	-31.0	1796.0
trans	1869.1	1807.1	1778.5	-28.5	1840.6

Table 4.8: Computed harmonic (H) ν_{CO} vibrational frequency, anharmonic (AH) correction to the 0 - 1 transition, and anharmonic 0 - 1 transition (cm^{-1}) in *cis*-and *trans*-MF and δMP2 (AH) represents the anharmonic correction obtained at the MP2 level [1].

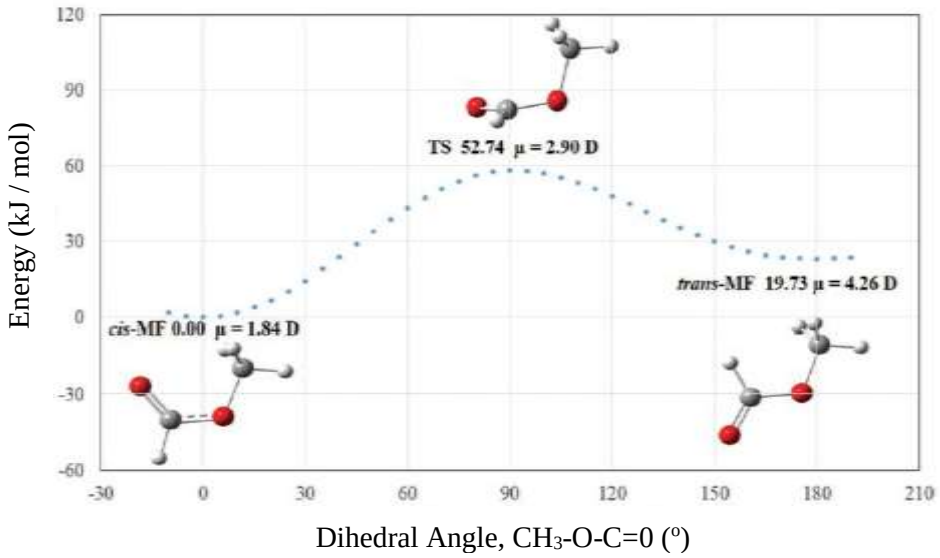

Figure 4.37: The electronic structure energy profile for MF around the dihedral CH_3-O-C = O. Note that the dipole moment increases from *cis*-MF through the transition state (TS) to *trans*-MF (Reproduced from [1]).

Infrared Spectroscopy of cis-MF Thin Films

The spontelectric effect in *cis*-MF is investigated using RAIR spectroscopy. **Figures 4.38** and **4.39** show the full RAIR spectra of 10,000 L of *cis*-MF on $aSiO_2$ from base temperature (14.5 K) to 75 K (**Figure 4.38**) and from 80 to 110 K (**Figure 4.39**). Below 95 K, the spectra are broadly consistent with a material in an amorphous phase. Above 95 K, the spectral features sharpen up in a way which is consistent with crystallisation, such that above 100 K *cis*-MF is crystalline.

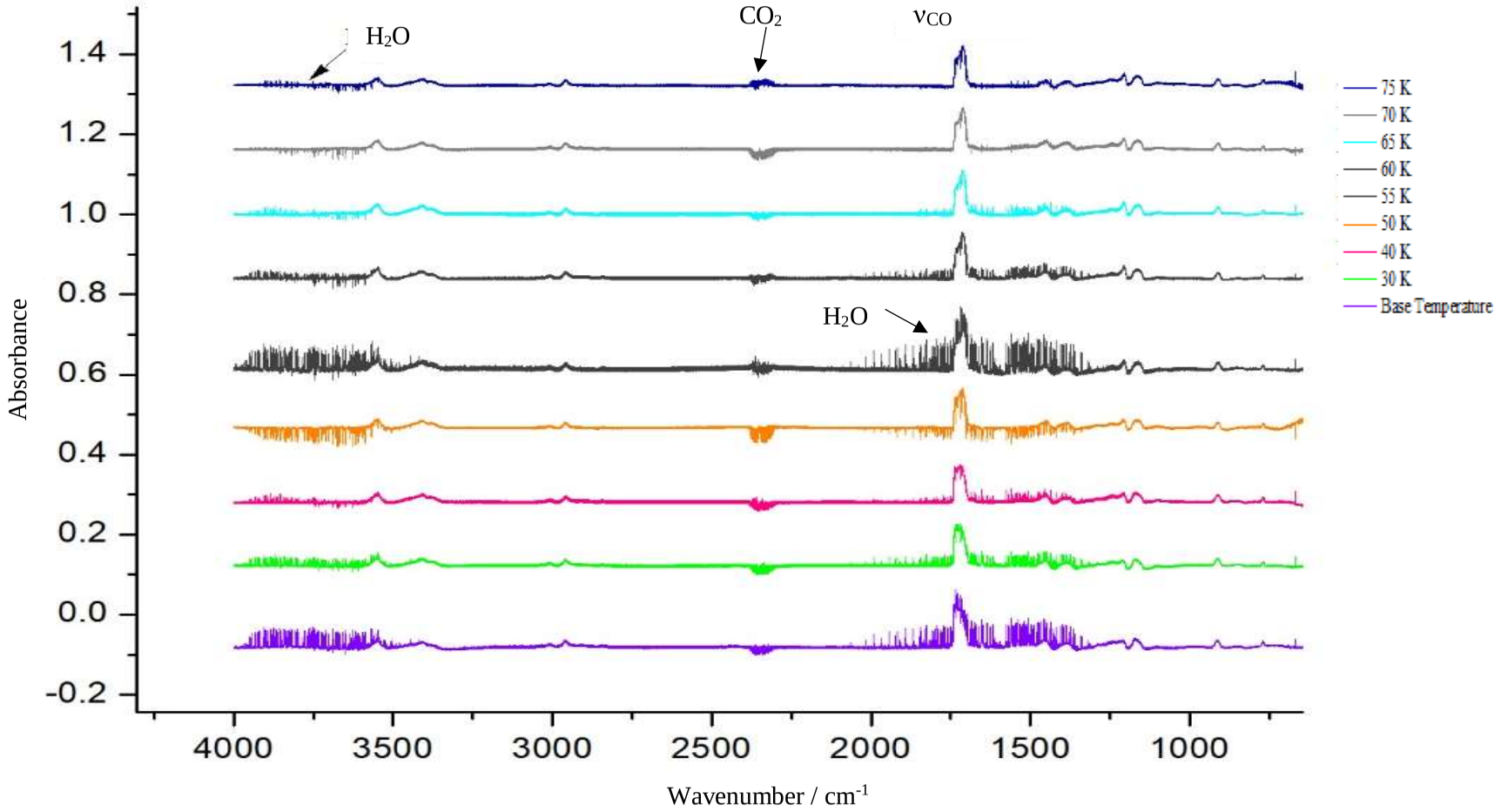

Figure 4.38: The full RAIR spectra for 10,000 L *cis*-MF films deposited on an $aSiO_2$ coated copper substrate at temperatures from base temperature (14.5 K) to 75 K.

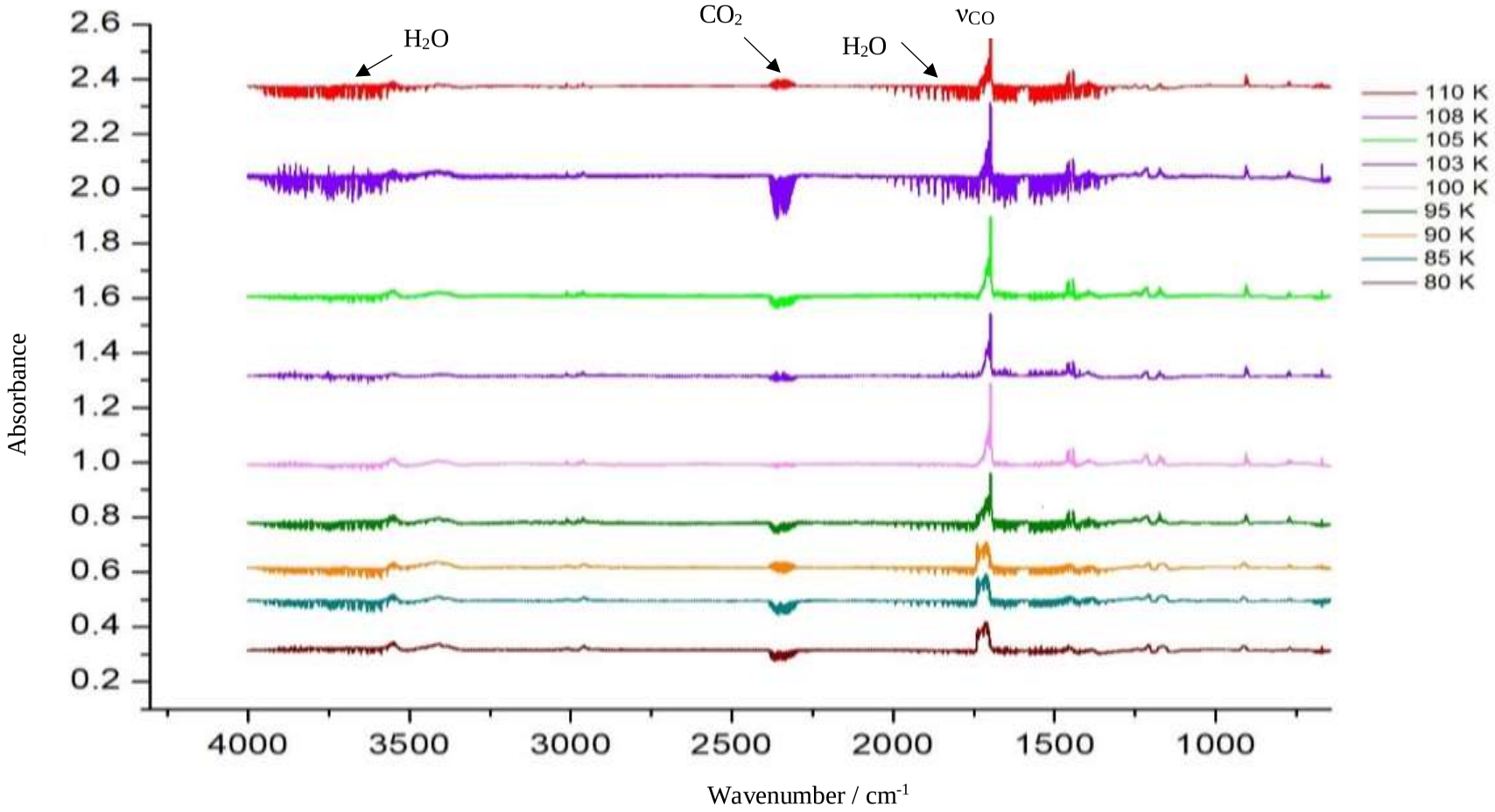

Figure 4.39: The full RAIR spectra for 10,000 L *cis*-MF films deposited on an $aSiO_2$ coated copper substrate at temperatures from 80 to 110 K.

This is perhaps easier to see in the spectra of the ν_{CO} band in the range 1850 to 1600 cm^{-1} region in **Figures 4.40** and **4.41**. These results are consistent with the work in the literature [42, 45] suggesting that at higher deposition temperatures the resulting film is crystalline in nature.

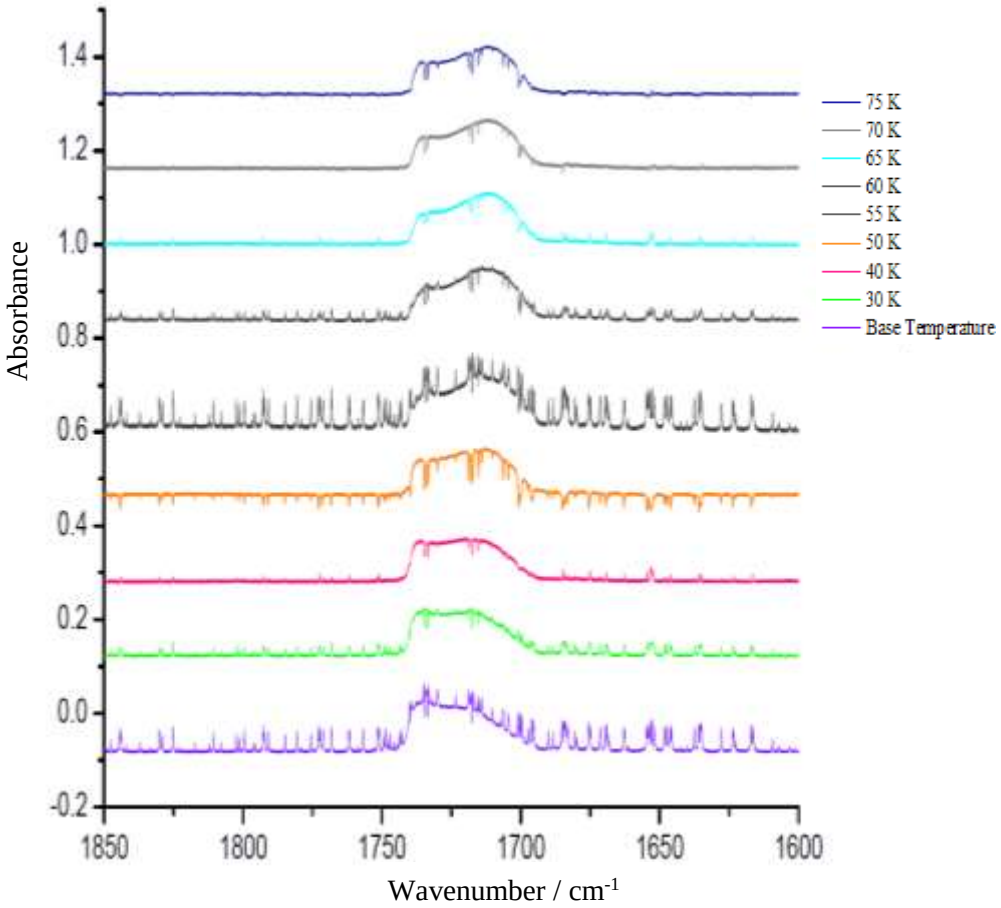

Figure 4.40: The 1600 - 1850 cm^{-1} spectral window of the RAIR spectrum of *cis*-MF (10,000 L) deposited at the indicated temperatures.

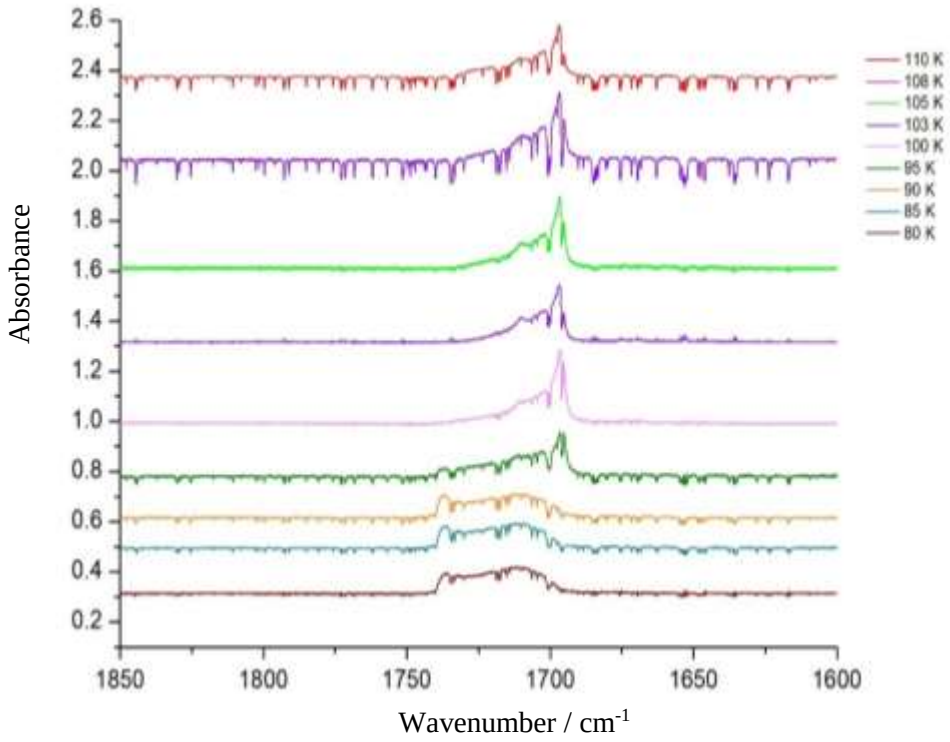

Figure 4.41: The 1600 - 1850 cm^{-1} spectral window of the RAIR spectrum of 10,000 L MF deposited on an $aSiO_2$ coated copper substrate at temperatures ranging from 80 to 110 K.

There is also clear evidence in both **Figures 4.40** and **4.41** of LO-TO splitting in the ν_{CO} band. A simple preliminary analysis given in **Figure 4.42** suggests the absence of any contraction or expansion of the LO-TO splitting of the ν_{CO} band with deposition temperature for temperatures above 95 K. This suggests that crystalline MF is not spontelectric, which is consistent with the spontelectric data on *cis*-MF shown in **Figure 4.43** [13].

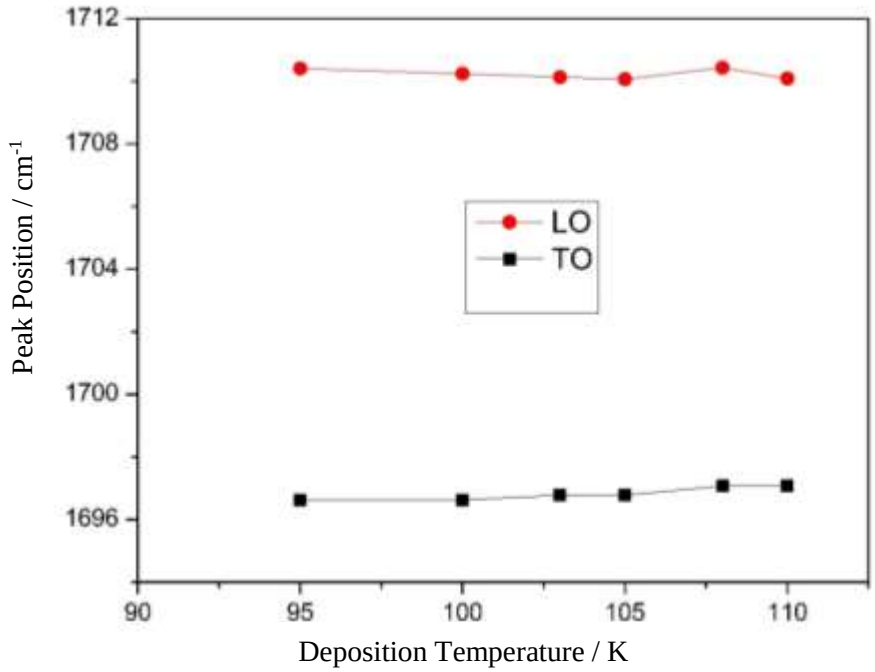

Figure 4.42: Visually estimated peak position of the ν_{CO} band LO and TO modes for a 10,000 L *cis*-MF film on aSiO_2 from **Figure 4.41**.

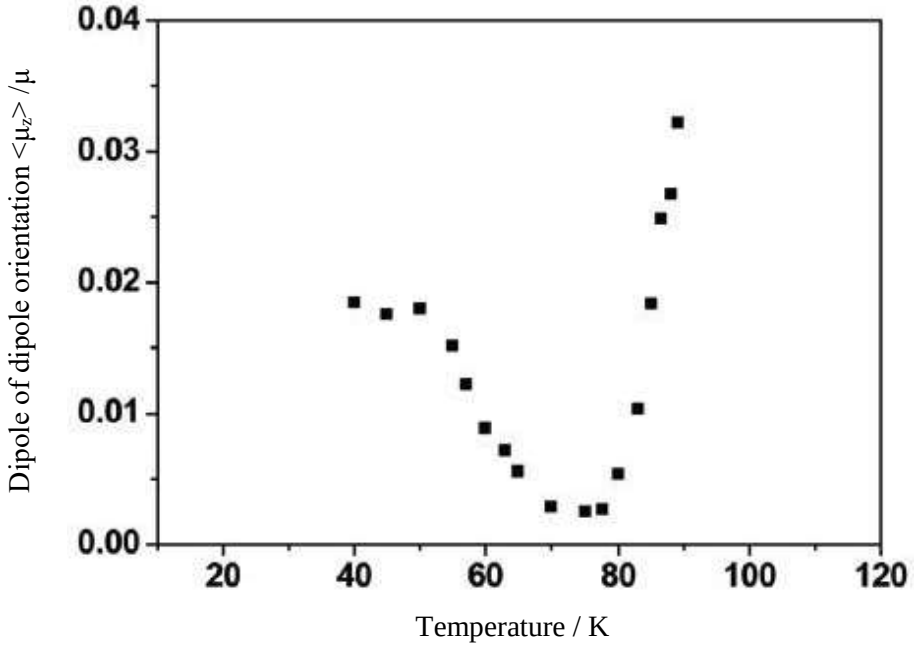

Figure 4.43: The variation of the degree of dipole alignment as a function of deposition temperature for *cis*-MF (Reproduced from [1]).

Assigning a Crystalline Structural Motif

Table 4.7 shows the assignment of the infrared spectrum of *cis*-MF along with reported literature values. **Figure 4.44** compares the ν_{CO} stretching features of

crystalline phase with the work by Palumbo and co-worker [45] and Brown and co-workers [42] with the work done at Heriot-Watt University [2].

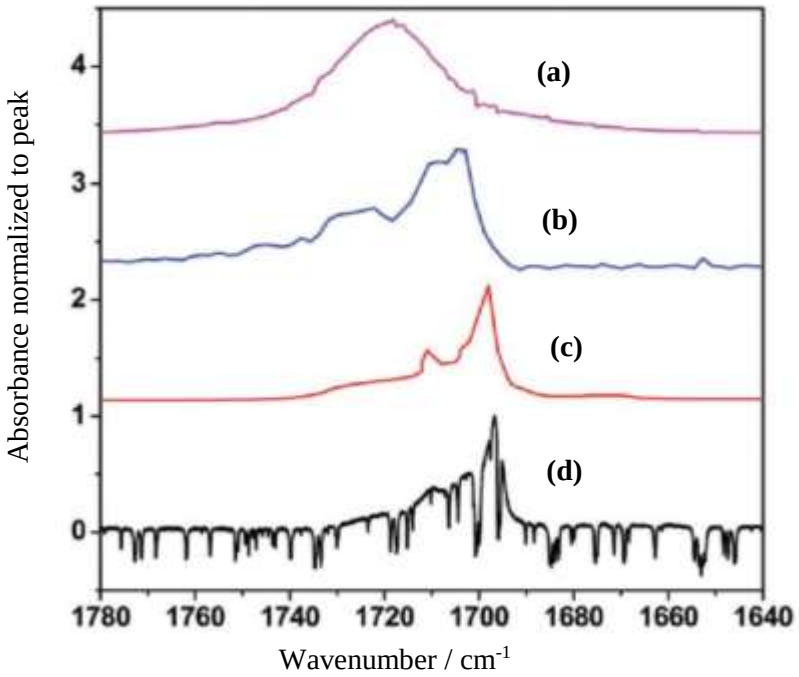

Figure 4.44: ν_{CO} stretching features of cis-MF; (**a**) Liquid MF; (**b**) RAIRS study by Brown and co-workers (95 K) [42], (**c**) The work done by Palumbo and co-workers (16 K) [45], and (**d**) crystalline *cis*-MF from the work done at Heriot-Watt University (108 K) [2].

The liquid phase spectrum lacks any fine structure and demonstrates the situation of truly randomly orientated dipoles. The RAIR spectrum displays measurements made on a graphite substrate and which are therefore subject to the metal surface selection rule. Hence, only the LO mode of the LO-TO split pair is observed. The RAIR spectrum, **Figure 4.44d** from this work, and the transmission spectrum, **Figure 4.44c** from Palumbo and co-worker [42], are very similar in showing several components in the ν_{CO} stretching mode**.** The narrow features in **Figure 4.44d** are due to variations in the gas phase water content of the air used to purge the external optics attached to the spectrometer and the UHV system. This makes fitting the data difficult, but **Figure 4.46c** demonstrates even with the narrow water features, the RAIR spectrum in **Figure 4.44d** can still be fitted to four components corresponding to LO-TO splitting of the ν_{CO} stretching mode. The question arises how to explain the extra LO-TO pairs along with the absence of the spontelectric field in the crystalline phase? The presence of both of the *cis*- and *trans*-rotational isomers is not observed in the crystalline phase. Comparing their computed

anharmonic frequencies (**Table 4.8**) with observed frequencies in the crystalline phase indicates that there is a shift around 45 cm^{-1} between *cis*- and *trans*-isomer ν_{CO} stretching modes. This is far greater than observed in the experimental spectra and hence the additional LO-TO pair is unlikely to be linked with the presence of *trans*-MF. It is suggested that the neighbouring *cis*-MF molecules in the crystalline phase take part in cyclic hydrogen bonding and thus couple to carbonyl groups [1]. The additional doubling of the band is then probably due to the presence of two MF molecules in the cyclic dimers in the solid. This gives rise to in–phase and out-of-phase ν_{CO} stretch modes; each of which is LO-TO split.

As a result of forming hydrogen-bonded dimers (**Figure 4.45**), the monomer ν_{CO} stretching frequency appears as a symmetric and antisymmetric combination of frequencies. Also, in this dimer configuration, the overall dipole moment is cancelled or reduced due to the opposite orientation of the monomer dipoles making up the dimer. The lack of dipole moment associated with the dimer structure explains the absence of a spontelectric field in the crystalline phase [1]. Computational investigations carried out by Keolopile and Gutowski of ring dimer structures of MF support this hypothesis. Keolopile and Gutowski have shown the three most stable dimers of MF, D1-D3 in **Figure 4.45**, are ring dimers [1]. D1 and D3 are symmetric (C_{2h}) and the difference in stability (1.35 kJ mol^{-1}) is due to the difference in proton donors (*e.g.* CH_3 and CH) [1].

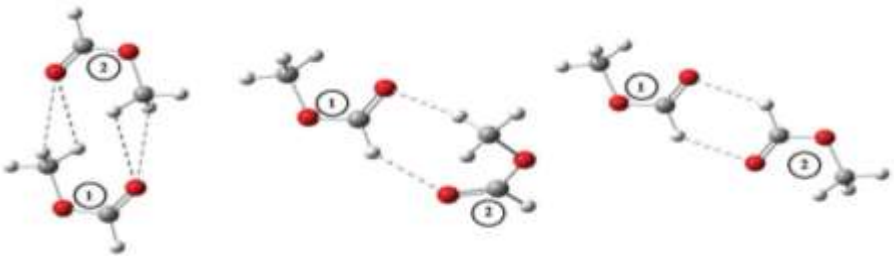

D1, C_{2h}, 0.00 kJ mol^{-1} D2, C_1, 0.10 kJ mol^{-1} D3, C_{2h}, 0.23 kJ mol^{-1}

Figure 4.45: The three most stable dimers of MF, where the monomers are labelled as 1 and 2 (Reproduced from [1]).

The computational results show that the splitting of the symmetric and antisymmetric coupled ν_{CO} vibrations in the ring structures D1, D2 and D3 are 10 cm^{-1}, 14 cm^{-1} and 13 cm^{-1} respectively. However, the experimental RAIR data

presented in **Figure 4.46c** shows a broad ν_{CO} stretch band that can be decomposed into four separate peaks around 1719 cm^{-1}, 1710 cm^{-1}, 1703 cm^{-1} and 1697 cm^{-1}. These peaks have been grouped into two LO-TO pairs and they represent the symmetric and anti-symmetric split modes. A LO-TO pair of 1719 cm^{-1} and 1703 cm^{-1} gives a midpoint of 1711 cm^{-1}, while 1710 cm^{-1} and 1697 cm^{-1} give a midpoint at 1704 cm^{-1} [1]. These results are consistent with the positions from work of Palumbo and co-workers [45] at 110 K (1713 cm^{-1} and 1707 cm^{-1}) and the positions for the LO peaks from the work of Brown and co-workers [42]. Hence the corresponding experimental splitting of the symmetric and anti-symmetric modes is 7 cm^{-1} and this is consistent with the value of 10 cm^{-1} calculated for the structure D1.

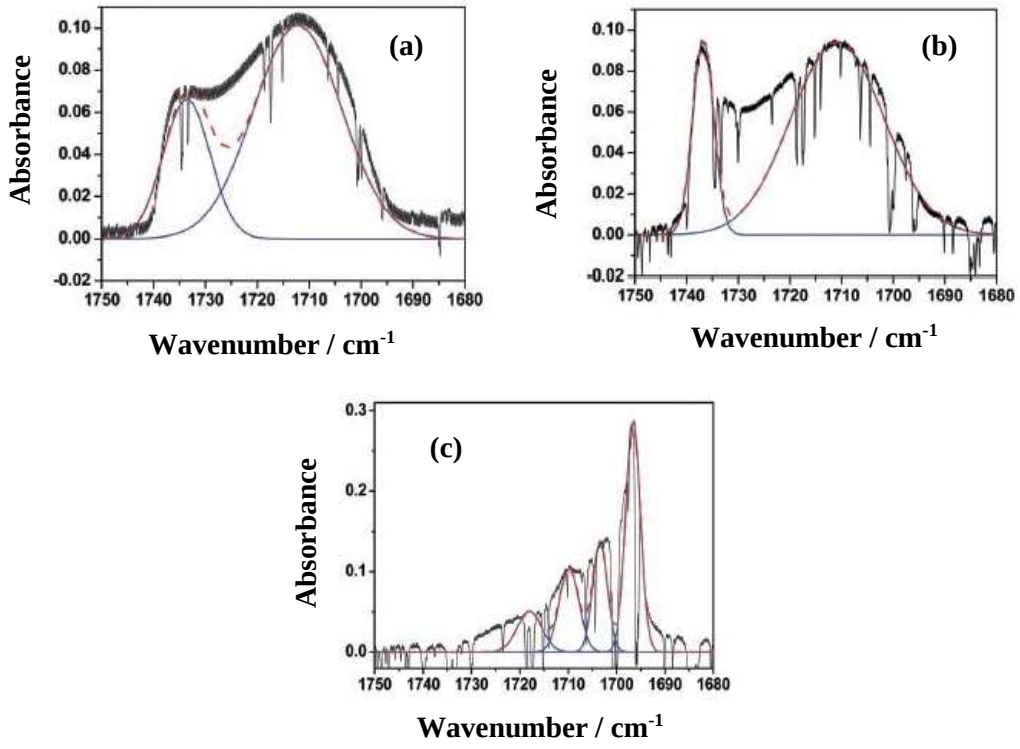

Figure 4.46: The RAIR spectra of solid *cis*-MF on an $aSiO_2$ substrate (black lines) for films of a few 10's of ML. The sharp spectral features are helpful wavelength markers and are due to the residual water vapour in the gas purge of the external optics. The spectra are recorded at deposition temperatures of (**a**) 70 K, (**b**) 90 K and (**c**) 108 K, and are the result of co-adding 512 scans using RAIRS at a resolution of 0.1 cm^{-1}. In the amorphous phase, below 90 K, a single LO-TO pair is observed. However, in the crystalline phase, above 90 K, the extra features are consistent with a second LO-TO pair (Reproduced from [1]).

Figures 4.46a and **4.46b** show that, below 90 K, there are changes in the LO-TO splitting which are correlated with the presence of the spontelectric field. This can be explained by the vibrational Stark Effect [2]. However, at temperatures above 90 K, the spontelectric field disappears as the LO-TO splitting remains constant. **Table 4.9** summarises all the results of fitting the νCO band of *cis*-MF as a function of deposition temperature. **Figure 4.47** plots this data.

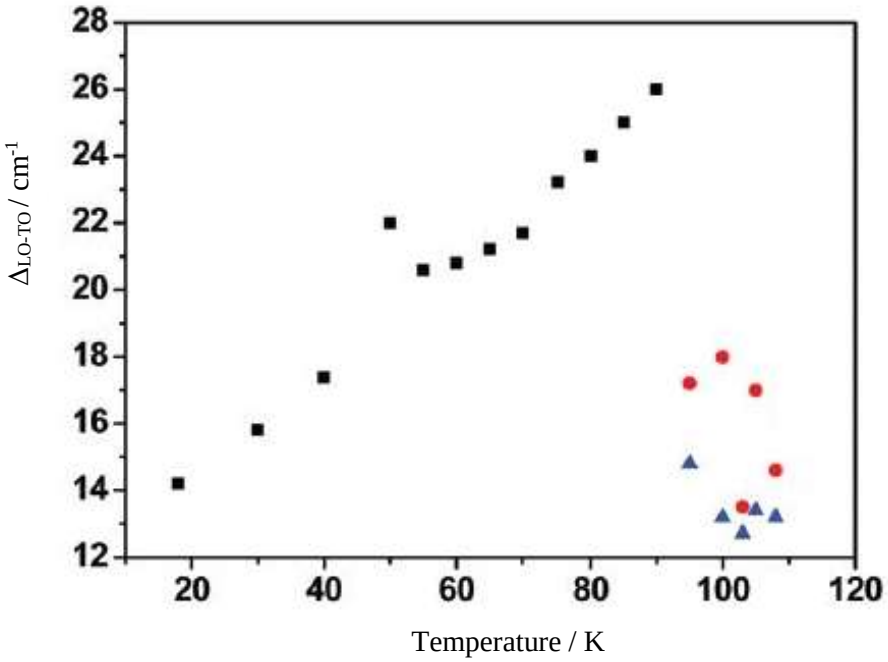

Figure 4.47: The variation of LO-TO splitting (Δ_{LO-TO}) as a function of deposition temperature for an equivalent film of *cis*-MF. The black squares show the splitting for the single ν_{CO} mode, which is observed in the amorphous phase of *cis*-MF, while the red / blue triangles represent the pair of ν_{CO} stretching modes which are seen in the crystalline phase (Reproduced from [1]).

90 K (**Figure 4.46b**) represents a phase transition point, where the crystalline solid phase presents a lattice motif in which the molecular dipoles are in a centrosymmetric structure. It is thought that as the dipolar characteristics of a molecule increase, so does the tendency for antiparallel molecular arrangements *e.g.* centrosymmetry [46]. However, a study by Whitesell *et al.* [47] concluded that the preference for organic molecules to crystallise in one of the centrosymmetric arrangements cannot be due to the molecular dipole-dipole interactions but the authors concluded that local electrostatic interactions between molecules are still

important. The opinion seems to be that while large/small molecular dipole moments may not correlate with the presence or absence of an inversion centre, local dipoles can influence molecular assembly [46]. The behaviour of other MF vibratonal modes *e.g*. the O-CH_3 stretch (906 cm^{-1}) and the OCO deformation (769 cm^{-1}) modes is consistant with that of the ν_{CO} stretch in showing evidence of LO-TO splitting. **Figure 4.48** shows an intial attempt to fit another part of the MF RAIR spectrum and further work is needed on these observations.

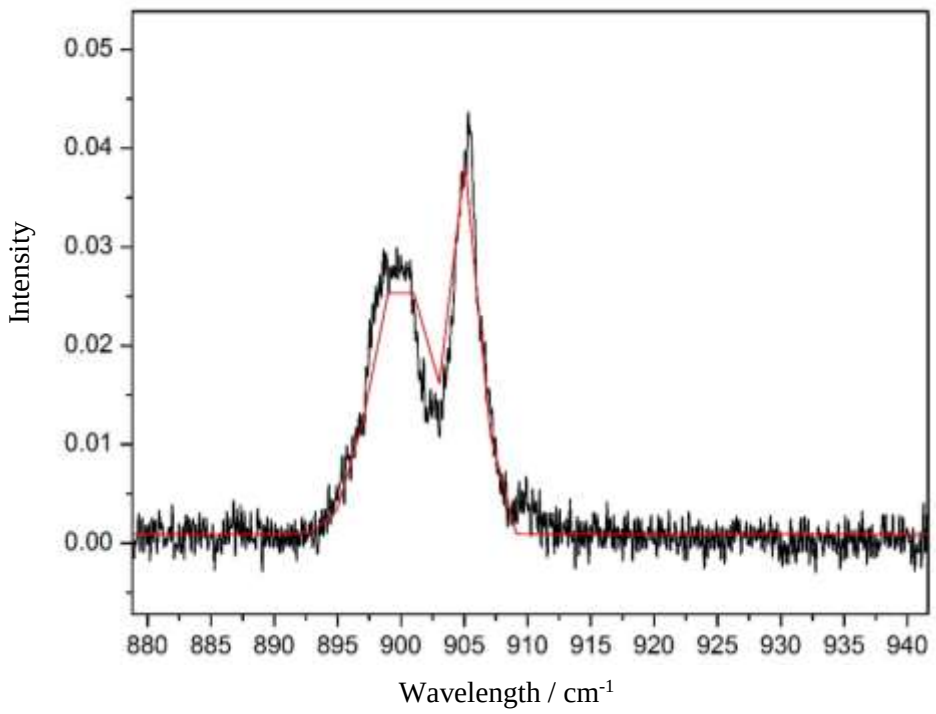

Figure 4.48: RAIR spectrum of the O-CH_3 stretch band of 10,000 L of solid *cis*-MF deposited at 108 K on amorphous silica showing LO-TO splitting. The red curve is a preliminary attempt at Gaussian fitting to the original spectrum.

It is assumed that a film which is deposited at increasing temperatures would show less orientation and hence a lower spontelectric field as a result of thermal agitation. This has been observed in a number of species including N_2O, toluene, propane and iso-pentane [3]. Using the RAIRS data for cis-MF, it can be shown that the non-linear and non-local characteristics of the spontelectric state can result in the increase of the degree of dipole orientation and electric field rising temperature of deposition. This is supported by earlier work by Field *et al*. [3] and Plekan *et al*. [4] using data from measurements of surface polarisation potential via the electron beam technique.

Analysis of the cis-MF data undertaken by a project student for reference 2 yields. This in turn allows the predication of the observed qualitatively distinct increase in the spontelectric field for depo sition temperatures above 77 K, as observed in **Figure 4.24** and **Table 4.9** for the given $\langle \mu_z \rangle / \mu$ values [2].

Deposition Temperature / K	ν_L / cm^{-1}	ν_T / cm^{-1}	$\Delta\nu$ / cm^{-1}	$\Delta_{LO\text{-}TO}$ / cm^{-1}	$\langle \mu_z \rangle / \mu$
55	1733.8±0.4	1713.2 ± 1.6	20.6 ± 1.6	19.2	0.0152
60	1733.6±0.4	1712.8 ± 1.0	20.8 ± 1.1	20.6	0.0089
65	1733.2±0.8	1712.0 ± 0.8	21.2 ± 1.1	22.0	0.0056
70	1722.7±0.6	1712.0 ± 0.2	21.7 ± 0.6	20.9	0.0029
75	1734.8±0.4	1711.6 ± 0.2	23.2 ± 0.4	20.3	0.0025
80	1735.6±0.6	1711.6 ± 0.2	24.0 ± 0.8	25.8	0.0054
85	1736.4±0.2	1711.4 ± 0.2	25.0 ± 0.3	24.3	0.0184
90	1736.8±0.2	1710.8 ± 0.4	26.0 ± 0.4	26.1	0.0322

Table 4.9: The increase in LO-TO splitting at higher deposition temperatures and illustrates the trend of increasing vibrational Stark Effect [2].

The model fails below 55 K, and this is most likely due to the presence of a different phase of *cis*-MF at low temperatures. Hence the discussion is limited to temperatures of deposition above 55 K along with the anomalous behaviour of *cis*-MF above 77 K. Looking at the current RAIRS data for *cis*-MF for temperatures between 55 and 90 K shows the new data support the counter-intuitive behaviour of the spontelectric field (**Figure 4.24a**) and the degree of dipole orientation, as shown in **Table 4.9**.

The LO-TO splitting is a result of the intrinsically different vibrational frequencies which are associated with LO and TO modes plus an additional contribution due to the vibrational Stark Effect. Hence, the values of $\Delta\nu$ are a combination of $\Delta\nu_B$, the intrinsic splitting of which is essentially independent of the temperature of deposition, and $\Delta\nu_s$, the Spontelectric Stark term which is a function of temperature due to the temperature dependence of the Spontelectric Field. The intrinsic splitting is determined mainly by the size of the unit cell [2, 48] and this size is assumed to remain initially roughly constant with temperature; the phase change notwithstanding. The value of $\Delta\nu_B$ can be estimated from the spectra of the crystalline phase which is formed by deposition above 90 K, at which the temperature of the solid is no longer spontelectric and hence there is no spontelectric contribution to the LO-TO splitting, this gives $\Delta\nu_B$ as 13.5 cm^{-1} [2].

Further detailed analysis given in reference 2 gives the variation of LO-TO splitting *versus* deposition temperature as seen in **Figure 4.49**. The biggest source of numerical uncertainty in the calculations of LO-TO splitting is the uncertainty in the value of $\Delta\nu_B$, the inherent LO-TO splitting. In fact, the value of $\Delta\nu_B$ may take on a different value from the average observed value for temperatures above 90 K of 13.5 cm^{-1}, since $\Delta\nu_B$ is structure dependent and *cis*-MF crystallises at above 90 K [42, 45]. The dependence of the LO-TO splitting on $\Delta\nu_B$ logically contains the total derivative governing the variation of the degree of dipole orientation with temperature (**Equation 3)**. **Figure 4.49** shows two estimates of the LO-TO splitting for $\Delta\nu_B$ of 10 and 13.5 cm^{-1}. The lower value of $\Delta\nu_B$ is consistent with a larger unit cell in amorphous *cis*-MF rather than crystalline *cis*-MF [2].

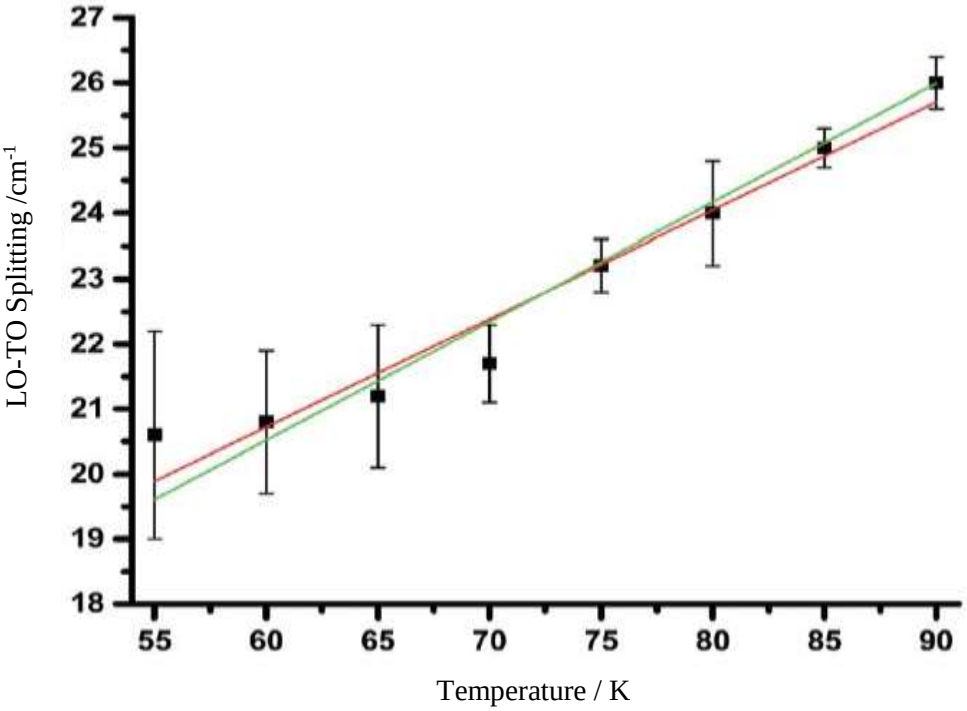

Figure 4.49: Compares the simulations using the method in [2] for $\Delta\nu_B$ of 10 (green) and 13.5 cm^{-1} (red) with the observed LO-TO splitting (black squares) *versus* deposition temperature as a test of model sensitivity. (Reproduced from [2]).

4.4 Conclusion

The aim of the chapter was to characterise thin films of MF using TPD, RAIRS and *ab initio* calculations. The low coverage TPD of MF on $aSiO_2$ is consistent with first-order desorption of the first layer, suggesting that MF wets the silica surface. The higher coverage data displayed in **Figure 4.27** (**Peak F**) follows the behaviour established by Peak **B** in **Figure 4.25** for zero desorption of a multilayer ice. The trend established by **Peak B** in **Figure 4.25**, and continued in **Figure 4.26** (**Peak D**), also continues in **Figure 4.27** (**Peak F**). The TPD here show multilayer desorption with zero order kinetics, as inferred by the common leading edges and the increase in peak temperature with increasing coverage. Zero-order desorption is confirmed by the Leading Edge Analysis (LEA) presented in **Figures 4.28 - 4.29**. **Figure 4.28** provides the LEA results for 100 - 1,000 L (2 – 10 ML) with a resulting average kinetic order of 0.02 ± 0.02. **Figure 4.29** completes the set with the data for 1,000 – 5,000 L (10-50 ML) where the average value of the kinetic order is 0.0 ± 0.0. Redhead Analysis was used to calculate the E_{des} for the monolayer of MF, 29.8±0.1 kJ mol^{-1} and Arrhenius Analysis was used to calculate the E_{des} for multilayer MF as of 26.4±5.5 kJ mol^{-1}. The E_{des} for the monolayer is slightly higher than the E_{des} for the multilayer, which indicates that MF coupling to the $aSiO_2$ surface is weak and only slightly stronger MF coupling to itself. CKS Analysis results for E_{des} and υ_{des} for the multilayer simulate experimental data (**Table 4.6**) well and compare favourably with literature data [42, 47].

The RAIRS data taken at a variety of deposition temperatures has revealed details of the structure of MF thin films. **Figures 4.38** and **4.39** show the full RAIR spectra of 10,000 L of MF on amorphous silica from base temperature (14.5 K) to 75 K (**Figure 4.38**) and from 80 to 110 K (**Figure 4.39**). Below 95 K, the spectra are broadly consistent with material in an amorphous phase. Above 95 K, the spectral features sharpen up in a way that is consistent with crystallisation, such that above 100 K MF is crystalline. This can be seen in the spectra of the ν_{CO} band (the 1850 to 1600 cm^{-1} region) in **Figures 4.40** and **4.41**. There is also clear evidence in both **Figures 4.40** and **4.41** of LO-TO splitting in the ν_{CO} band. This is perhaps most clearly seen in the spectrum of the crystalline phase in **Figure 4.41**, where at least two features are found

in the ν_{CO} band. A simple preliminary analysis suggests from the absence of any contraction or expansion of the ν_{CO} band LO-TO splitting above 90 K crystalline MF is not spontelectric, consistent with the spontelectric data on MF. MF was subject to conformational isomerism around both the methyl-oxygen and formyl-oxygen bonds. The internal rotation about the formyl-oxygen bonds is the most significant and the electronic structure results are shown in **Table 4.8** and indicate that *cis*-MF is 19.7 kJ mol^{-1} more stable than *trans*-MF, where the separating barrier is 52.7 kJ mol^{-1}. Boltzmann analysis indicates that the *trans*-form makes up less than 1 part in 10^6 of the total in the gas phase up to 120 K. Hence the spontelectric measurements and IR spectroscopy mainly probe *cis*-MF in the thin films.

The combination of measurements of the spontaneous dipole orientation, IR spectroscopy and computational chemistry support the idea that basis motif of the lattice in crystalline *cis*-MF is a ring dimer structure. The additional LO-TO pair and absence of a spontelectric field in the crystalline phase can be explained *via* the RAIRS and computational work. Comparing the experimental RAIR data and the anharmonic frequencies in **Table 4.8,** the computed frequencies in the crystalline phase demonstrate a shift between *cis*- and *trans*-isomer ν_{CO} stretch modes that is much larger than that observed in the experimental RAIR data. Hence, the extra LO-TO pair is not due to the additional presence of the *trans*-MF. The conclusion of this work is that the neighbouring *cis*-MF molecules in the crystalline phase engage in cyclic hydrogen bonding and thus couple two carbonyl groups. In forming these hydrogen-bonded dimers (**Figure 4.45**), the monomer ν_{CO} stretching frequency appears as a symmetric and antisymmetric combination of frequencies. Additionally, the overall dipole moment is cancelled or reduced. The lack of dipole moment associated with the dimer structure accounts for the absence of the spontelectric field in the crystalline phase and the computational work on ring dimer structures of MF supports this hypothesis. MF has unique spontelectric properties. One aspect of this work was to provide independent data on this phenomenon of the observed growth of the dipole order with rising temperature, as reported in the literature [3, 4]. The data reported in this chapter, employed in developing the publications in references 1 and 2, which also provide additional interpretation of the data on *cis*-MF from Field and co-workers [3] as taking their data, it is possible to reproduce the observed

deposition temperature dependence of the LO-TO splitting in cis-MF thin films as illustrated in **Figure 4.49**.

4.5 References

[1] M. Roman, A. Dunn, S. Taj, Z. G. Keolopile, A. Rosu-Finsen, M. Gutowski, M. R. S. McCoustra, A. M. Cassidy and D. Field, *Phys. Chem. Chem. Phys*., 2018, **20**, 29038.

[2] M. Roman, S. Taj, M. Gutowski, M. R. S. McCoustra, A. C. Dunn, Z. G. Keolopile, A. Rosu-Finsen, A. M. Cassidy and D. Field, *Phys. Chem. Chem. Phys*., 2018, **20**, 5112.

[3] D. Field, O. Plekan, A. Cassidy, R. Balog, N. C. Jones and J. Dunger, *Int. Rev. Phys. Chem*., 2013, **32**, 345.

[4] O. Plekan, A. Cassidy, R. Balog, N. C. Jones, D. Field, *Phys. Chem. Chem. Phys*., 2012, **14**, 9972.

[5] O. Plekan, A. Cassidy, R. Balog, N. C. Jones and D. Field, *Phys. Chem. Chem. Phys.*, 2011, **13**, 21035.

[6] R. Balog, P. Cicman, N. C. Jones and D. Field, *Phys. Rev. Lett*., 2009, **102**, 073003.

[7] F. A. van Broekhuizen, I. M. N. Groot, H. J. Fraser, E. F. van Dishoeck and S. Schlemmer, *Astron. Astrophys.*, 2006, **451**, 723.

[8] R. Resta and D. Vanderbilt, in *Physics of Ferroelectrics: A Modern Perspective*, Edited by K. M. Rabe, C. H. Ahn and J.-M. Triscone, (Springer, Berlin, Germany, 2007).

[9] J. C. Burfoot, *Ferroelectrics* (van Nostrand Co. Ltd, London, UK, 1967).

[10] L. M. Blinov, V. M. Fridkin, V. M. S. P. Palto, A.V. Bune, P. A. Dowben and S. Ducharme, *Open Access Research Paper in Physics and Astronomy Digital Commons* (University of Nebraska, Nevada, USA, 2000).

[11] V.V. Shvartsman and A.L. Kholkin, *J. Appl. Phys*., 2010, **108**, 042007.

[12] Y. Akishige and Y. Kamishina, *J. Phys. Soc. Jpn*., 2001, **70**, 3124.

[13] J. Lasne, A. Rosu-Finsen, A. Cassidy, M. R. S. McCoustra and D. Field, *Phys. Chem. Chem. Phys*., 2015, **17,** 30177.

[14] M. P. Collings, J. W. Dever and M. R. S. McCoustra, *Phys. Chem. Chem. Phys*., 2014, **16**, 3479.

[15] H. D. Nissen, N. J. Cunningham, M. Gustafsson, J. Bally, J. -L. Lemaire, C. Favre and D. Field, *Astron. Astrophys*., 2012, **540**, A119.

[16] L. E. Kristensen, T. L. Ravkilde, G. Pineau des Forets, S. Cabrit, M. Gustafsspn, S. Diana, J. L. Lemaire and D. Field, *Astron. Astrophys*., 2008, **477**, 203.

[17] C. Lada, M. Lombardi and J. F. Alves, *Astrophys. J*., 2010, **724**, 687.

[18] G. Parmentier, J. Kaufmann, T. Pillai and K. M. Menten., *Mon. Not. Roy. Astr. Soc*, 2011, **416**, 783.

[19] D. Field, Private correspondence.

[20] E. Cohen de Lara and J. Vincent-Geisse, *J. Phys. Chem.*, 1976, **80**, 1922.

[21] B. L. Maschhoff and J. P. Cowin, *J. Chem. Phys*., 1994, **101**, 8138.

[22] D. Fernandez-Torre, O. Kupiainen, P. Pyykko and L. Halonen, *Chem. Phys. Lett*., 2009, **47**1, 239.

[23] A. Cassidy, M. R. V. Jørgensen, A. Rosu-Finsen, J. Lasne, J. H. Jørgensen, A. Glavic, V. Lauter, B. B. Iversen, M. R. S. McCoustra and D. Field, *J. Phys. Chem. C*, 2016, **120**, 24130.

[24] C. Kittel, *Introduction to Solid State Physics, 3rd Edition* (Wiley, New York, USA, 2005).

[25] http://rsl.eng.usf.edu/Documents/Tutorials/TutorialsKelvinProbe.pdf (last accessed 3/5/16).

[26] https://www.slideshare.net/ahmedelsayes/kelvin-probemicroscop(last accessed 15/3/19).

[27] R. A. Baragiola, *Planet Space Sci.*, 2003, **51**, 953.

[28] C. Bu, J. Shi, U. Raut, E. H. Mitchell and R. A. Baragiola, *J. Chem. Phys*., 2015, **142**, 134702.

[29] K. Kutzner, *Thin Solid Films*., 1972, **14**, 49.

[30] L. Onsager, D. L. Staebler, and S. J. Mascarenhas, *J. Chem. Phys*., 1978, **68**, 3823.

[31] M. J. Iedema, M. J. Dresser, D. L. Doering, J. B. Rowland, W. P. Hess, A. A. Tsekouras and J. P. Cowin, *J. Phys. Chem. B*., 1998, **102**, 9203.

[32] I. Gavra, A. N. Pilidi, and A. A. Tsekourasa, *J. Chem. Phys*., 2017, **146**, 104701.

[33] E. Elliott, T. I. Pritchard, M. J. Hampshire and R. D. Tomlinson, *Vacuum*, 1969, **19**, 366.

[34] D. Berreman, *Phys. Rev*., 1963, **130**, 2193.

[35] A. Rosu-Finsen, *PhD Thesis* (Heriot-Watt University, Edinburgh, UK, 2016).

[36] http://enacademic.com/pictures/enwiki/77/Methyl-formate-3Dballs.png (last accessed 17/3/19).

[37] M. L. Senent, M. Villa, F. J. Melendez and R. Dominguez-Gomez, Astrophys. J., 2005, **627**, 567.

[38] Y. Horowitz and M. Asscher, *J. Chem. Phys*., 2012, **136**, 134701.

[39] CKS, (IBM Almaden Research Centre, IBM Corporation, USA, 1995).

[40] F.A. Houle and W.D. Hinsberg, *Surf. Sci.*, 1995, **338**, 329.

[41] D. Marchione, *Ph.D. Thesis* (Heriot–Watt University, Edinburgh, UK, 2015).

[42] D. J. Burke, F. Puletti, P. M. Woods, S. Viti, B. Slater and W. A. Brown, *J. Phys. Chem. A*., 2015, **119**, 6837.

[43] P. A. Redhead, *Vacuum*, 1962, **12**, 203.

[44] A. L. Schwaner, Jeffrey E. Fieberg, and J. M. White, *J. Phys. Chem. B.*, **1997,** 101, 11112.

[45] P. Modica and M. E. Palumbo, *Astron. Astrophys.*, 2010, **519**, A22.

[46] A. Dey and G.R.Desiraji, *Chem. Commu*n, 2005., **0**, 2486.

[47] J. K. Whitesell, R. E. Davis, L. L. Saunders, R. J. Wilson and J. P. Feagins, *J. Am. Chem. Soc*., 1991, **113**, 3267.

[48] L. H. Jones and B. I. Swanson, *J. Phys. Chem*., 1991, **95**, 2701.

Chapter 5

Surface Heterogeneity and Inhomogeneous Broadening of Vibrational Line Profiles

5.1 Introduction

This chapter reports on the results of probing the surface heterogeneity of amorphous silica ($aSiO_2$) using coverage dependent temperature programmed desorption (TPD) and reflection-absorption IR (RAIR) spectroscopy with carbon monoxide (CO) as probe molecule. First, the chapter reports the use of inversion analysis in recovering the distribution of binding site energies, $E_{des}(\theta)$. This distribution is then used in an environmentally broadened vibrational line profile synthesis. Comparison of synthetic line profiles with RAIRS experiments allows the vibrational relaxation mechanism to be investigated. The work presented in this chapter is a result of a number of contributions:

- TPD and RAIRS measurements; and inversion recovery of the $E_{des}(\theta)$ distribution on $aSiO_2$ were carried out by S. Taj.
- Line profile synthesis was carried out by S. Taj and an undergraduate project student (D. Baird) using a spreadsheet developed by M. R. S. McCoustra.
- RAIR spectra of CO on p-ASW were recorded by A. Rosu-Finsen.

and was published as [1].

5.1.1 CO as a Probe of Surface and Solid Phase Environments

Dust surfaces play a key role in astrochemistry. Dust grains are composed of refractory materials, mainly carbon, silicon *etc*., as well as compounds of hydrogen and abundant gases such as oxygen. There is no one type of grain, rather a mixture of different types formed under different physical conditions. The leading materials are silicates and carbonaceous (carbon-bearing) materials, with volatile ices such as H_2O or CO condensed on their surfaces (*i.e.* ice mantles). These are discussed in further detail in **Chapter 1**.

The vibrational frequency and line shape of CO are sensitive to the environment of the CO. This makes CO an excellent probe of surfaces and the solid state, *e.g*. it can be used to identify polar and apolar environments [2, 3]. This is because the CO vibrational frequency and CO vibrational line profile are very sensitive to the strength of intermolecular forces holding the CO on the surface or exerted by the surrounding

solid. The absorption features for CO thus vary according to ice analogue compositions.

The CO molecule can be adsorbed on to a surface either by physisorption or chemisorption. The type of adsorption can be identified *via* the molecular activation energy for desorption. The activation energy of desorption, E_{des}, is equal to the binding energy of the adsorbate to the surface, E_b. This energy can be determined through the use of TPD data, as discussed later in this chapter. In physisorption, the interaction between the adsorbate and adsorbent is weak and is associated with van der Waals interactions. Typically, the binding energies are less than 50 kJ mol^{-1} and the adsorbed molecule is weakly perturbed. In chemisorption, there is an exchange of electrons between the adsorbate and adsorbent, which can be discussed in terms of covalent, ionic or metallic bonding. The perturbation of the adsorbate is much greater than with physisorption, and the binding energies are typically greater than 100 kJ mol^{-1}.

The surface physics and chemistry of dust grains are not well understood. Thus, there is a need to build grain models to probe their surfaces for comparison against observations. In the laboratory, TPD and RAIRS can be used to study adsorption and desorption processes on model grain material surfaces. TPD allows us to investigate the surface heterogeneity of model grain surfaces by revealing the distribution of binding energies felt by CO molecules at these surfaces. RAIRS reveals how that heterogeneity impacts on the positions, shape and width of spectral features associated with CO on these surfaces.

A number of studies have been carried out focusing on CO on or in amorphous and crystalline water environments, as the most directly relevant to observational data. When CO interacts with an ASW surface, the resulting absorption feature produces two peaks, as shown in **Figure 5.1.** These two peaks for CO in a water film have been observed by a number of authors [4-7]. The CO band profile shows a main feature around 2138 cm^{-1} and secondary feature around 2152 cm^{-1}. Some attribute the 2138 cm^{-1} feature to substitution of CO into the matrix [4].

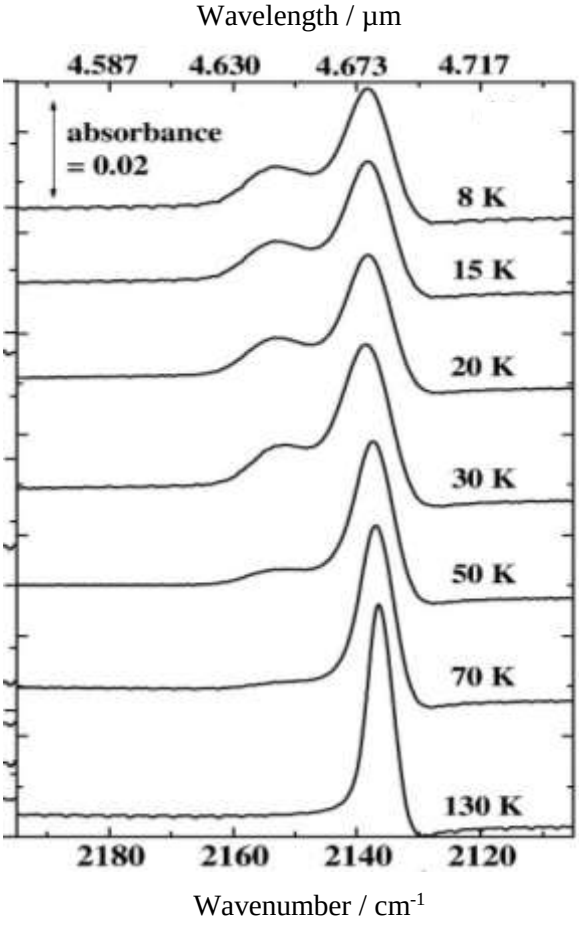

Figure 5.1: RAIR spectrum for CO adsorbed onto ASW. There are two characteristic peaks at low temperature due to the CO interacting with the surface *via* two different bonding configurations (Reproduced from [8]).

However, others have suggested [9-10] that both bands are due to CO molecules in micropores. The 2152 cm^{-1} band is due to CO molecules interacting with dangling OH groups at the pore surface and the 2138 cm^{-1} band has been attributed to CO molecules interacting with oxygen atoms of the pore-surface water molecules [10]. RAIR spectra of CO which are of astrophysical relevance have been reported by Collings and co-workers on water and with other molecular solid surfaces [8, 11] and by Fraser and co-workers on zeolite [12]. Pontoppidan *et al*. [13] described three features of solid CO at 2143.7 cm^{-1}, 2139.9 cm^{-1} and 2136.5 cm^{-1}. The first two features were attributed to the bulk CO in the interstellar medium. The feature at 2136.5 cm^{-1} is identified as being inconsistent with what was previously thought to originate *via* a CO-H_2O interaction [2, 3]. The 2136.5 cm^{-1} band has been assigned to CO mixed in methanol (CH_3OH), which is the final product of CO hydrogenation [14]. Given the experimental uncertainties, Collings *et al*. [3] reported an alternative

assignment of CO being directly bound to the silica surface, as in **Figures 5.8** and **5.9**. The presence of iron and magnesium ions, *i.e*. a silicate matrix, could introduce shifts in this position due to modification of the silica-CO interaction. The work of Manuter *et al*. [15] illustrates this for CO adsorbed on to meteorite silicate nanoparticle surfaces. The resulting spectra show broad absorption features for the CO with a large linewidth, due to the heterogeneity of the model silicate nanoparticle surfaces, which give rise to inhomogeneous broadening, as shown in **Figure 5.2.**

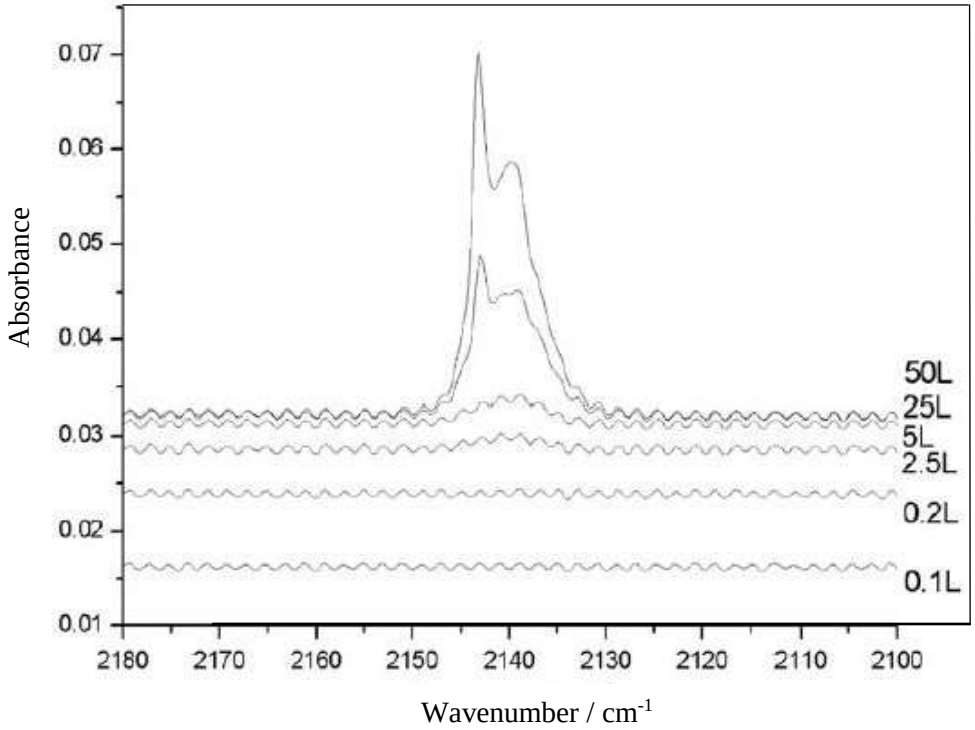

Figure 5.2: RAIR spectra of CO adsorbed on meteorite nanoparticles (Reproduced from [15]).

Inversion of TPD data allows us to determine the range of binding interactions experienced by CO. But, we need to know the pre-exponential factor, ν. The pre-exponential factor can be considered to be the attempt frequency for desorption *i.e*. it is associated with the vibration of the adsorbate-substrate bond along with the reaction coordinate associated with desorption. This simple model yields a typical value for the pre-exponential factor in the order of 10^{12} to 10^{13} s^{-1}, which is appropriate for desorption of atoms and small molecules [3, 16, 17]. In the case of physisorption, the pre-exponential factor is 10^{12} s^{-1} while 10^{13} s^{-1} is typical for chemisorption [17]. Having a good estimate of the pre-exponential factor is key when

analysing desorption data, as well as when building astronomical models which include desorption process from dust grains within the ISM.

In the work of Collings *et al*. [2], CO was used as a molecule in investigating the interactions with model astrophysical surfaces. The interactions of CO at sub-monolayer coverages were studied to focus on CO-surface interactions rather than the CO-CO interactions that occur in multilayer films. The CO interacts with these various model surfaces *via* the C atom, O atom or in a π-bonded configuration. The interaction can occur *via* linear or T-shaped configurations (**Figure 5.3**).

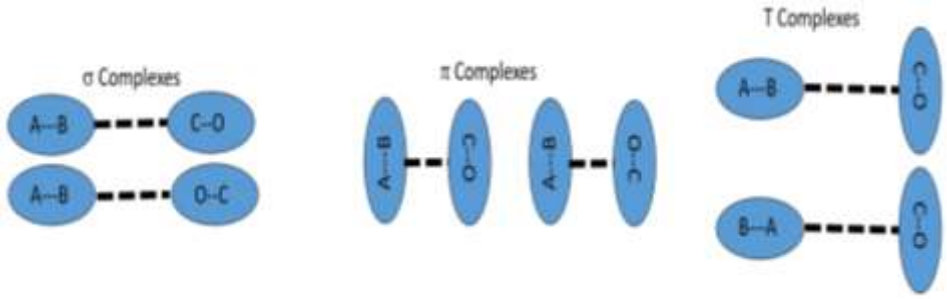

Figure 5.3: Structures of CO complexes, where σ_c complexes are the most common.

The different interaction orientations for CO were studied using *ab initio* calculations. It was found that each type of interaction had a different effect on the vibrational frequency and binding energy of CO on the surface [2]. The experimental results coupled with the *ab initio* calculations support correlations between the CO vibrational frequency and the way the CO orientates itself to interact with these various model surfaces. Where the CO molecules interact with the surface *via* the C atom, the frequency, $\tilde{\nu}_{CO}$, is higher than is the case for isolated CO; and where the interaction takes place *via* the O atom, the frequencies are lower than those of the isolated molecule. The extent to which their frequencies are shifted when compared with isolated CO monomer frequency depends on the surface type [2]. This is shown in **Figure 5.4**. Vibrational frequencies shift reflecting changes in both force fields, because of intermolecular interaction induced changes in electron density distributions around vibrational chromophores, and mass distributions. Combination of experimental observations and modest quantum chemical calculations has confirmed this for CO on various molecular surfaces and in simple complexes [2].

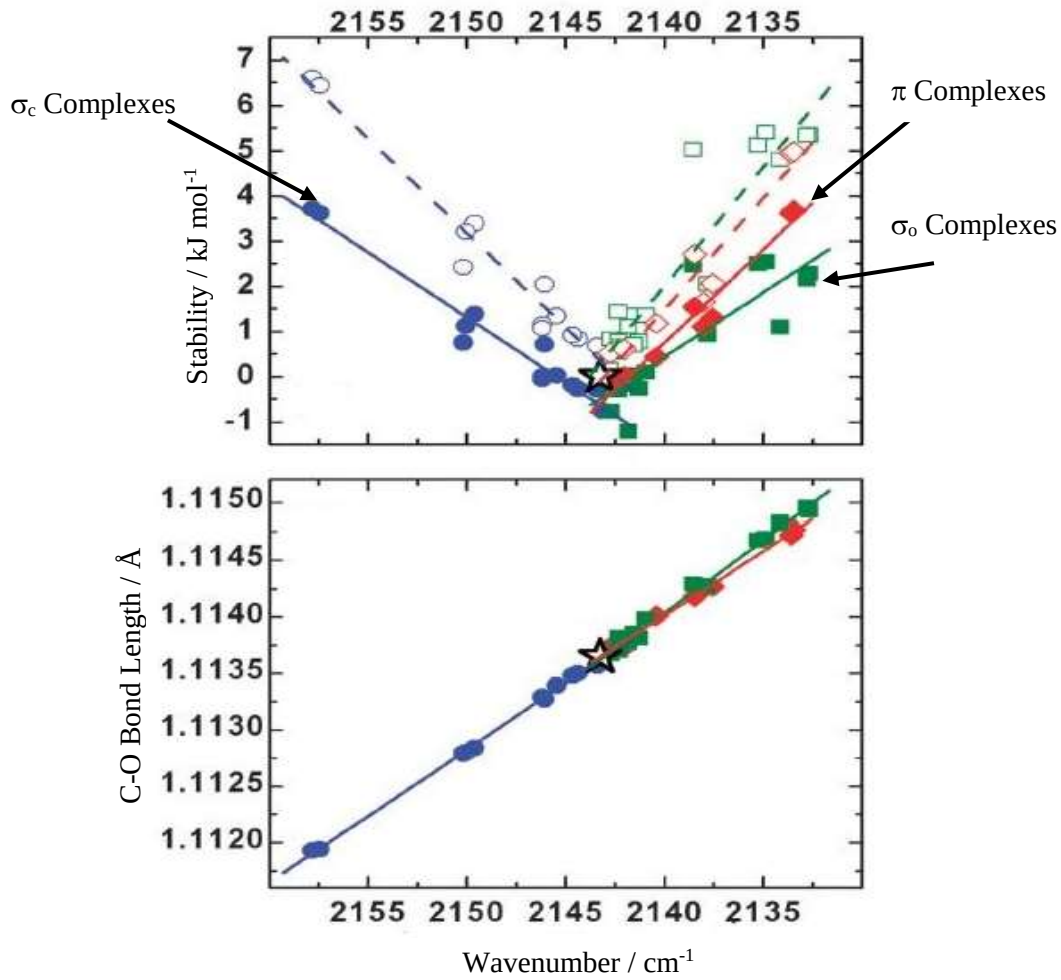

Figure 5.4: (**a**) Stability and (**b**) C≡O bond length for complexes at local minimum geometries in *ab initio* calculations as a function of predicted $\tilde{\nu}_{CO}$. Circles: C_{CO}-bonded complexes; diamonds: O_{CO}-bonded complexes; squares: π-bonded complexes; solid symbols: Basis set superposition error (BSSE) corrected stabilities, hollow symbols: uncorrected stabilities, filled symbols; lines of best fit to the BSSE correxcted (solid) and uncorrected (dashed) data are provided to guide the eye. The large hollow star symbols mark the values for the CO monomer (Reproduced from [2]).

These shifts, $\Delta\tilde{\nu}_{CO}$ can be referenced to the isolated molecule vibrational frequency as shown in **Equation 1**:

$$\Delta\tilde{\nu}_{CO} = \tilde{\nu}_{co(complex)} - \tilde{\nu}_{co(monomer)} \qquad \textbf{(E1)}$$

Collings *et al.* [2] data also determined the relative binding energies, E_b of the complexes with respect to CO monomer. The binding energies, E_b, are a measure of the activation energy for desorption of CO from the corresponding surface, E_{des}. The

ab initio calculations show a trend for the linear σ-interaction of CO with different species. A review of the *ab initio* data indicates that when the binding energy of the complexes of CO with different molecules is increased then the CO vibrational frequency increased. **Figure 5.5** displays $\Delta\tilde{\nu}_{co}$ *versus* E_b for the interaction of CO *via* the C atom. The graph was produced using the data for the complexes of CO with various molecules and the CO bonding configuration occurred *via* the C atom in a linear orientation, shown in **Table 5.1**. The values for $\Delta\tilde{\nu}_{co}$ are positive, since the vibrational frequency for CO interacting *via* the C atom in the CO complexes are blue shifted relative to the CO monomer [2].

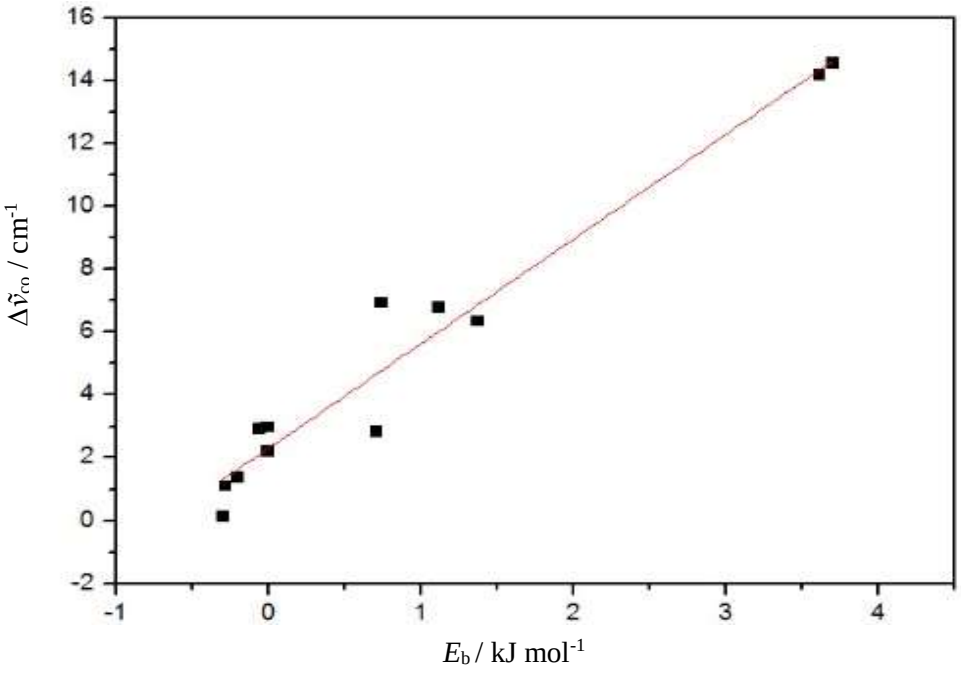

Figure 5.5: $\Delta\tilde{\nu}_{co}$ *versus* E_b for σ-type interaction of CO occurring *via* the C atom using the data from Collings *et al*. [2].

Regression analysis on the data in **Figure 5.5** indicates that there is a strong linear correlation between $\Delta\tilde{\nu}_{co}$ and E_b and hence E_{des}. Indeed, 95.5% of the variation in $\Delta\tilde{\nu}_{co}$ can be attributed to the linear relationship between the two variables as in **Equation 2** as shown in **Figure 5.3**:

$$\Delta\tilde{\nu}_{co}(E_b)/\text{cm}^{-1} = 3.330\ (E_b/\ \text{kJ mol}^{-1}) + 2.308 \qquad \textbf{(E2)}$$

Complex	CO bonding Configuration	E_{des}/ kJ mol^{-1}	$\Delta\tilde{\nu}_{co}$ / cm^{-1}
CO monomer	C_{CO}	-	2.20
O ≡ C---CO_2	C_{CO}	1.374	6.35
O ≡ C---H-NH_2	C_{CO}	1.120	6.78
O ≡ C---H-OCH_3	C_{CO}	3.704	14.56
O ≡ C---H-CH_2OH	C_{CO}	-0.001	2.98
O ≡ C---CH_3OH	C_{CO}	-0.059	2.93
O ≡ C---H-OH	C_{CO}	3.613	14.20
O ≡ C---H-CH_2CH_3	C_{CO}	-0.282	1.11
O ≡ C-H_3C-CH_3	C_{CO}	-0.298	0.12
O ≡ C---H-CH_3	C_{CO}	-0.200	1.39
O ≡ C---H-SH	C_{CO}	0.744	6.93
O ≡ C---H-SH	C_{CO}	0.709	2.82

Table 5.1: The correlation between $\Delta\tilde{\nu}_{co}$ and E_{des} for the σ-C_{co} bonding configuration, adapted from Collings *et al.* [2].

5.1.2 Line Shapes and Lifetimes

Vibrational excitation and relaxation at a surface are of considerable fundamental interest in surface science. Vibrations of molecules at surfaces give details about the chemical identity of the adsorbate; how and where it bonds to the surface; and details of the strength of the internal bonds along with the strength of interactions with other molecules [18]. This can be extracted from a static vibrational spectrum from the line frequencies and intensities. CO is a prototype adsorbate and its vibrational dynamics on metal surfaces have been widely studied [19]. For example, studies of the line shape and width of CO stretching bands on metal surfaces indicate that the creation of electron-hole pairs plays a vital role in energy dissipation of the excited CO stretching mode [20]. Thus, there is clearly a relationship between vibrational line shapes and vibrational dynamics. Microscopic events occurring on a timescale of picoseconds or less will be observable as broadening of spectral lines. However, the linewidths and shapes are not only dominated by non-dynamical effects. Heterogeneity in adsorbate-adsorbate and adsorbate-substrate interactions may contribute [1].

Vibrational dynamics and vibrational line profiles are governed by Fermi's Golden Rule and the Energy-Time Uncertainty Principle. The transition rate depends on the strength of the coupling between the initial and final states of the system and on the number of ways the transition can occur, *i.e.* the density of the final states. The transition probability can take the form shown in **Equation 3**:

$$\lambda_{\mathrm{if}} = \frac{2\pi}{\hbar}|M_{\mathrm{if}}|^2\rho_{\mathrm{f}} \qquad \textbf{(E3)}$$

where λ is the transition probability, which is sometimes also known as the decay probability, and is related to the mean lifetime, τ.

$$\lambda = \frac{1}{\tau} \qquad \textbf{(E4)}$$

M_{if} is the matrix element of the interaction and ρ_{f} is density of the final states. The general form of Fermi's Golden Rule can be applied to a range of situations including atomic transitions and nuclear decay scattering, as well as vibrational transitions [1]. The Energy-Time Uncertainty Principle states that if a system exists in an energy state over a short period of time, δ_{t}, then the energy of the state must be uncertain to a degree δE, as expressed in **Equation 5**:

$$\delta t \times \delta E \sim \frac{h}{2\pi} \qquad \textbf{(E5)}$$

Hence, the transition between the lower level and the excited state will have an energy uncertainty of δE and the broadening will occur over $\delta \nu$, since [21]:

$$\delta\nu = \frac{\delta E}{h} = \frac{h}{2\pi\delta t}.\frac{1}{h} = \frac{1}{2\pi\delta t} \qquad \textbf{(E6)}$$

This results in asymmetric Lorentzian profiles for vibrational transitions in the case of isolated molecules. However, the effect of non-radiative relaxation mechanisms reduces the lifetime of the vibrational excited state. The excited state can either decay by loss of population (energy relaxation) or by loss of coherence (phase relaxation).

- *Phase relaxation* - in the case where there is a dynamical coupling between the considered vibrational mode and other low-frequency modes at certain temperatures, especially where the latter are excited, this results in fluctuations in the normal mode frequency, giving rise to additional broadening [22-26]. The key aspect of this feature is its strong temperature dependence, which will disappear, especially at low temperatures.

- *Energy relaxation* – is a process in which the population distribution of molecules in quantum states of high energy due to an external perturbation returns to a Maxwell-Boltzmann distribution. The process occurs *via* intra- and intermolecular energy transfer, where the excess energy of the vibrational mode is transferred to surrounding molecules. As a result of this process initially excited vibrational modes moves to a vibrational state of a lower energy. This process has been investigated using time-resolved spectroscopy [27].

The linewidth, Γ_{hom}, or half-width at half-maximum (HWHM) of a homogeneously broadened transition is made of two contributions:

$$\Gamma_{\mathrm{hom}} = \frac{1}{2\pi \mathrm{T_2}} = \frac{1}{2\pi}\left(\frac{1}{2\mathrm{T}_1} + \frac{1}{\mathrm{T}_2^*}\right) \qquad \textbf{(E7)}$$

where T_1 is the lifetime of the transition, T_2^* is the dephasing time and T_2 is the overall relaxation time. In inhomogeneous broadening, the overall linewidth includes an additional contribution, Γ_{inhom} :

$$\Gamma_{\mathrm{total}} = \Gamma_{\mathrm{hom}} + \Gamma_{\mathrm{inhom}} \qquad \textbf{(E8)}$$

Homogeneously and symmetrically broadened lines typically have Gaussian or Voigt line profiles. In the gas phase, Doppler broadening and pressure broadening are the main processes resulting in the homogeneous broadening of gas-phase line profiles [24] (**Figure 5.6**).

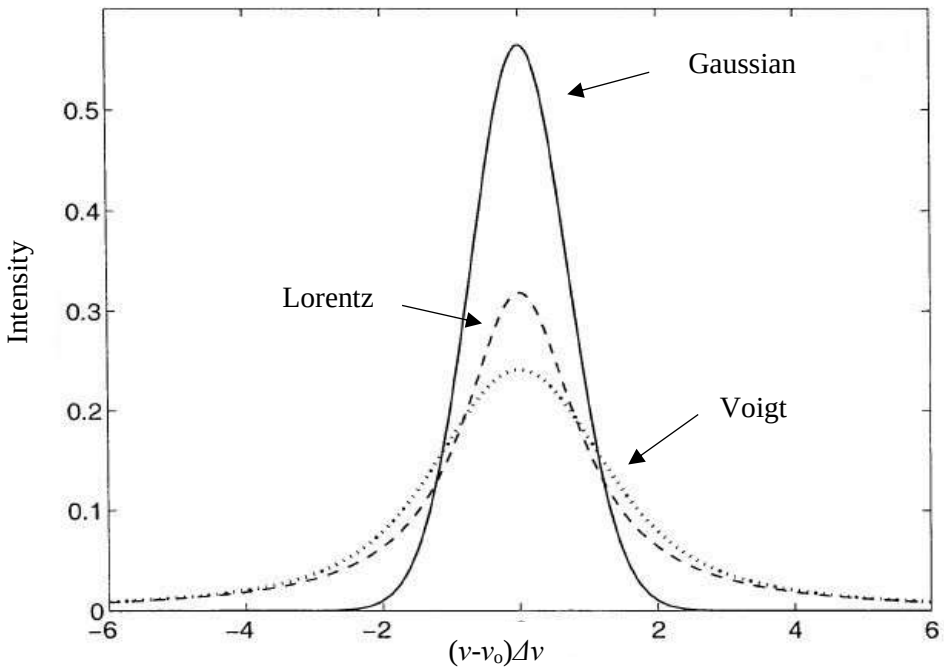

Figure 5.6: A comparison of Doppler, Voigt and Lorentz line shapes (Reproduced from [30]).

In the case of solid surfaces, molecular movement and rotation are restricted and with weakly interacting adsorbates on a simple ionic solids relatively narrow linewidths are displayed. The work of Ewing and colleagues [28, 29] has estimated that the natural linewidth for the vibration of CO on a NaCl (100) surface (at 5 K) to be around 10^{-8} cm^{-1}. The observed linewidth is about 0.07 cm^{-1}, and the difference between observed and estimated linewidths arises from environmental heterogeneity (*i.e.* non-uniformity) of the NaCl surface. On metals, however, an additional relaxation pathway is available. The long-range oscillating dipole field of molecules, or charge oscillations between a molecular ($2\pi^*$) resonance field around a Fermi level and the conduction band, can result in electron-hole pair creation and hence energy dissipation [22, 28-32]. An initial approximation of the electron-hole pair mechanism produces a temperature-dependent Lorentzian peak. The interaction between the vibrational excitation and quasi-continuum of the electron hole pairs should yield a high-frequency tail [22]. CO on Cu (111) has been widely used as a model for investigating the electronic and vibrational properties of chemisorbed molecules on metal surfaces. **Figure 5.7** shows the RAIR spectrum of CO on Cu (100). The spectrum is broadened and deviation from a Lorentzian is evident in the high wavenumber tail. The direct interpretation of these observations is inhomogeneous

broadening and the line shape is described by Gaussian rather than Lorentzian. Intermolecular energy transfer and multi-phonon processes are thought to be an unlikely mechanism of this very fast relaxation.

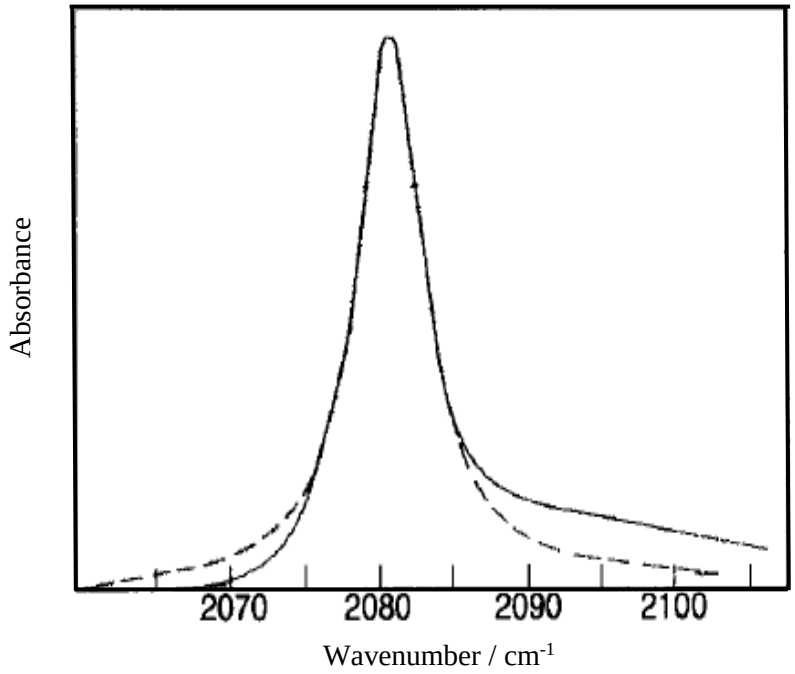

Figure 5.7: RAIR spectrum absorption of an incomplete monolayer at coverage 0.35 of CO on Cu (100) at 100 K. The Lorentzian fit is shown as a dashed line (Reproduced from [30]).

5.2 Experimental

The experiments were all carried out in an ultrahigh vacuum system and details of the sample, dosing and the RAIRS set-up are described in **Chapter 2.** The CO (CK special gases Ltd, 99.997% purity) and H_2O (Fluka, 99.9% purity) were deposited *via* background dosing on to the $aSiO_2$ substrate, which was held at base temperature (18 K). CO coverage of the sample is expressed in monolayers (ML), as estimated from the corresponding exposure and using the assumption of unit sticking probability. The TPD experiments were performed by applying a heating ramp of 0.1 - 0.5 K s^{-1} to a suitable final surface temperature to ensure that all the CO was desorbed from the surface of the $aSiO_2$. Desorbing species were detected *via* quadrupole mass spectrometer (QMS). The IR spectra are recorded at an instrument-limited resolution of 0.1 cm^{-1} by taking 512 scans at base temperature of the UHV

system. The TPD profiles were simulated using a FORTRAN 90 code (**Appendix A**) and are discussed in **Section 5.3.1**.

5.3 Results and Discussion

First, TPD of CO on $aSiO_2$ and p-ASW will be presented and discussed. This is followed by measurement of RAIR spectra of CO on $aSiO_2$ and p-ASW. Finally, the line profile syntheses will be discussed and how CO is deposited on the $aSiO_2$ and p-ASW surfaces will be explained.

5.3.1 TPD of CO from $aSiO_2$ and p-ASW

Up to 20 L exposures CO were deposited on the $aSiO_2$ substrate at base temperature, this allows the identification of the exposure necessary to generate coverage of a monolayer. Using a monolayer or less ensures that only CO-$aSiO_2$ interactions are investigated rather than CO-CO interactions in case of multilayer films. Using the QMS, CO dosing was monitored at m/z = 12, 14 and 28 m_u. Consecutive TPD experiments from 2 to 10 L, were carried out on the same day. The TPD data for CO desorbing from $aSiO_2$ are shown in **Figure 5.8**. The data shows coincident trailing edges at low exposures which would indicate first-order desorption of the first layer and this suggests that CO wets the $aSiO_2$ surface. At higher coverages (**Figure 5.9**), there is a common leading edge which is consistent with zero-order desorption of a multilayer ice. At this stage, this data allows for the identification of the monolayer exposure as 10 L. Hence, 1 ML is equivalent to 10 L. This allows us to convert exposures into coverage.

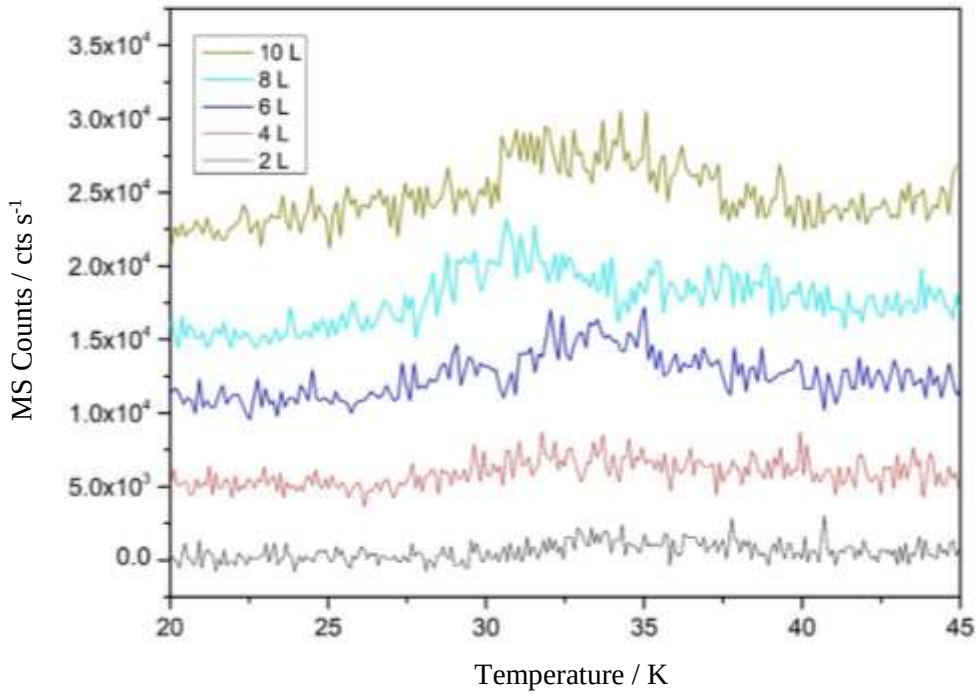

Figure 5.8: TPD data recorded on m/z = 12 m_u for sub-monolayer quantities of CO desorbing from $aSiO_2$ at a range of exposures. The individual traces have been offset for clarity.

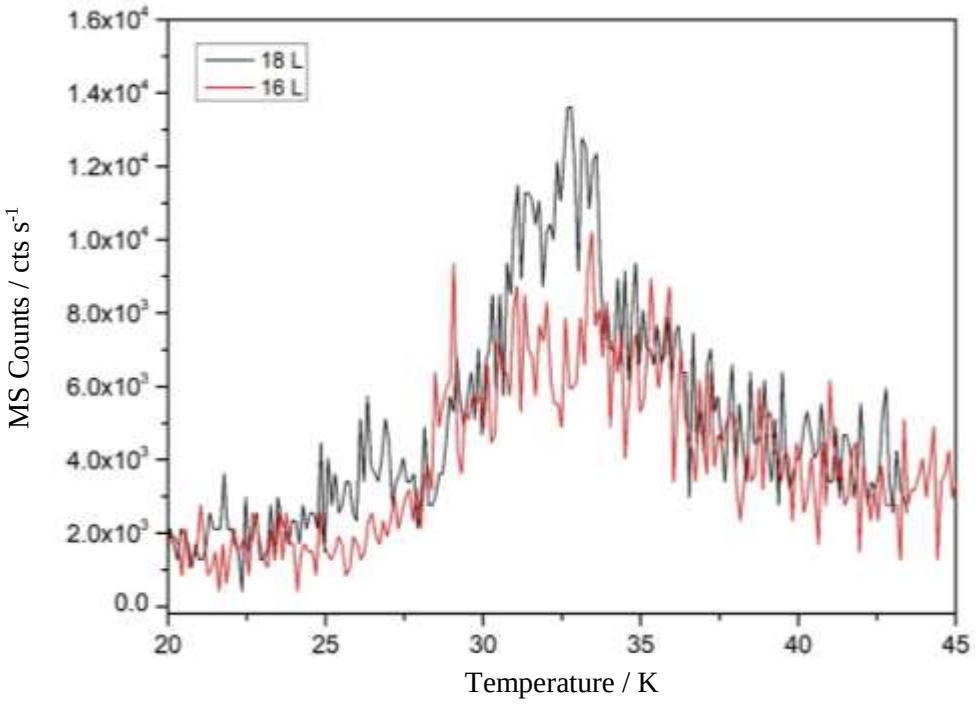

Figure 5.9: TPD data for multilayer coverages of CO desorbing from $aSiO_2$.

The starting point for the inversion analysis of TPD data is that the assumption of a single value for the activation energy of desorption, E_{des}, is no longer valid. The interaction is best represented by a distribution of binding energies on the surface.

We must also assume first order kinetics and a pre-exponential factor which is consistent with physisorption [1]. The analysis of the TPD data is done *via* direct inversion of the Polanyi-Wigner equation:

$$r_{\mathrm{des}} = -\frac{\mathrm{d}N_{\mathrm{ads}}(t)}{\mathrm{d}t} = \upsilon N_{\mathrm{ads}}(t)^{n} e^{-E_{\mathrm{des}}/k_B T} \qquad \textbf{(E9)}$$

where υ is the pre-exponential factor, n is the desorption order, E_{des} is the desorption energy, k_{B} is the Boltzmann constant and T is the surface temperature. This can be used to derive E_{des} as a function of surface concentration at a time t, $N_{\mathrm{ads}}(t)$.

$$E_{\mathrm{des}}\left(N_{\mathrm{ads}}(t)\right) = -k_{\mathrm{B}} T \ln\left(\frac{\frac{dN_{\mathrm{ads}}(t)}{dt}}{\upsilon N_{\mathrm{ads}}(t)^{n}}\right) \qquad \textbf{(E10)}$$

$dN_{\mathrm{ads}}(t)/dt$ is derived from the quadrupole mass spectrometer count rate. The value of $N_{\mathrm{ads}}(t)$ is found by subtracting the total gas-phase concentration at the previous time step from the initial surface concentration, N_{tot}, where N_{tot} is equal to the rate of bombardment, Z_{w}, multiplied by the dosing time, τ, as given by **Equation 10** [24]:

$$N_{tot} = Z_w \tau = \frac{PS\tau}{\sqrt{2\pi \mathrm{m} \mathrm{k}_{\mathrm{B}} T}} \qquad \textbf{(E11)}$$

where m is the mass of one molecule of CO and T is temperature of the CO gas (298 K) and S is taken to be one. The activation energy for desorption is subsequently calculated *via* its dependence on temperature and change in surface concentration of molecules over time. The pre-exponential factor for desorption of CO, ν, is taken to be 1×10^{12} s^{-1}, as indicated by Collings *et al*. [3]. **Figure 5.10** summarises the flow of the inversion process. As a result, plots of E_{des} *versus* N_{ads} (T) are produced for each sub-monolayer CO dose as shown in **Figure 5.11**. **Table 5.2** shows that the range of E_{des} values widens with increasing coverage as observed in the literature [15, 16].

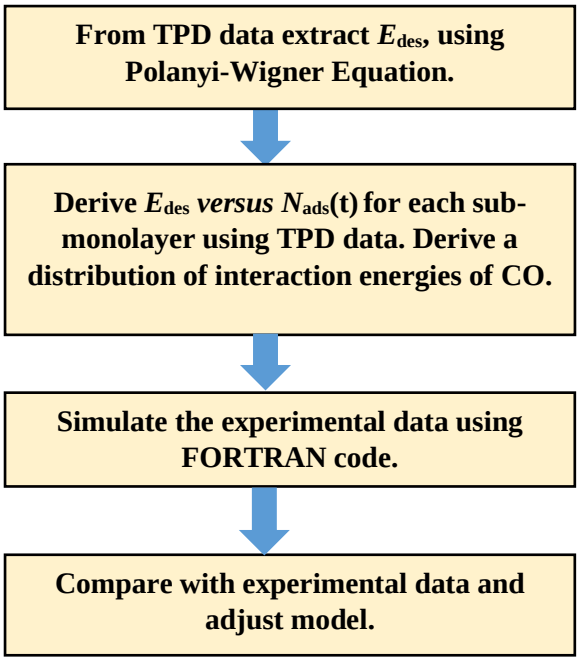

Figure 5.10: Flow chart summarising the inversion process. The process is iterative one and the model data is adjusted until a good fit is achieved with the experimental data.

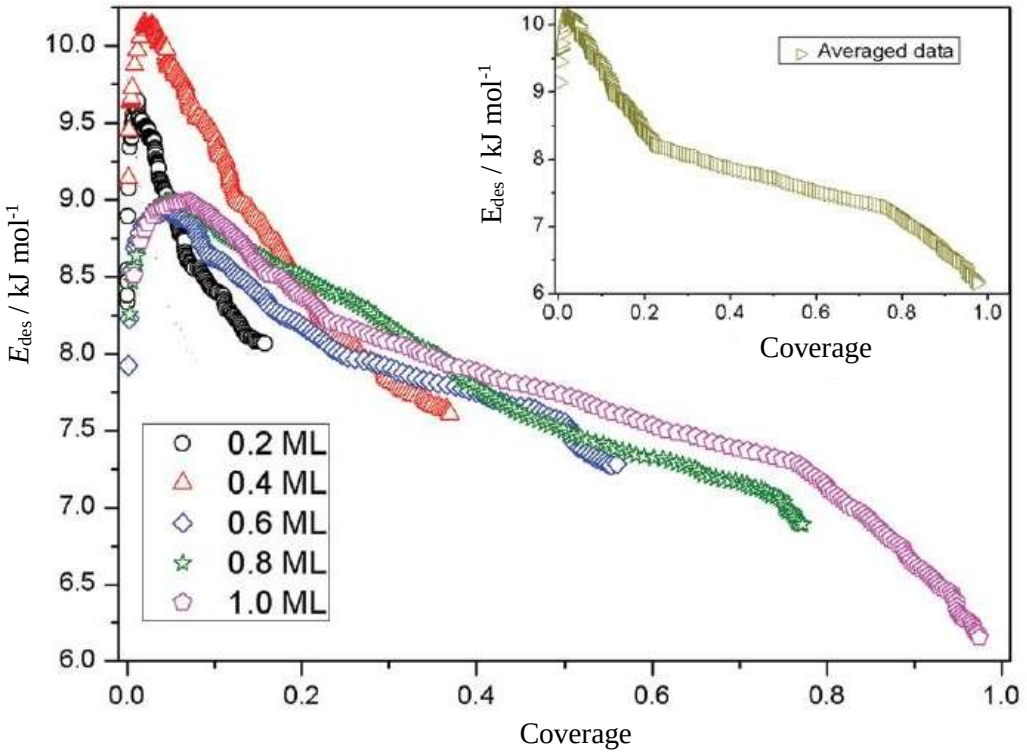

Figure 5.11: E_{des} as function of N_{ads}, the surface concentration of adsorbed CO for background-dosed sub-monolayer coverages of CO on aSiO_2. The average data is displayed in the insert (Reproduced from [1]).

To demonstrate that the distribution recovered and displayed in **Figure 5.11** is consistent with the experimental data, a FORTRAN TPD simulation code was developed based on the work of Thrower [33]. **Figure 5.12** shows TPD data for CO desorbing from $aSiO_2$ in comparison with simulations using this code and the experimentally derived coverage-dependent activation energy $E_{des(\theta)}$.

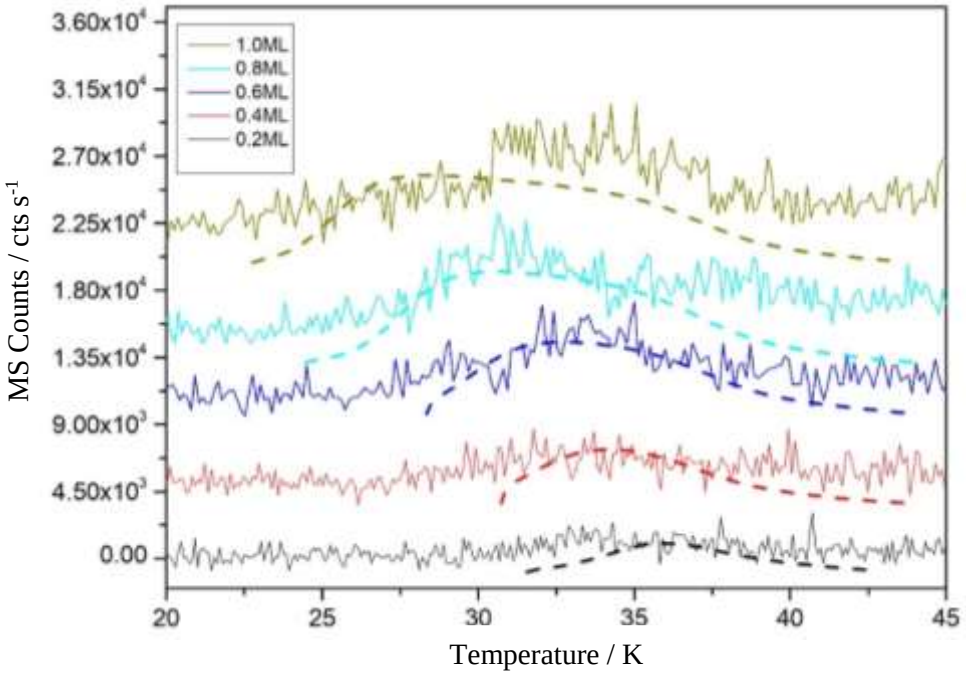

Figure 5.12: Experimental and simulated TPD for sub-monolayers of CO desorbing from $aSiO_2$. The solid lines are the experimental data and the corresponding TPD simulations are presented by dashed lines (Reproduced from [1]).

The FORTRAN 90 code takes the initial number of adsorbed species on the surface, $N_{ads}(0)$, experimental time and temperature as inputs into the calculations. For each time interval, the desorption rate is calculated using the Polyani-Wigner equation at the temperature $T(t)$ using the fitted functional form for $E_{des}(N_{ads})$ derived from inversion of the experimental TPD data. The change in N_{ads} during a time interval is then calculated using that desorption rate. The process is repeated for successive values of t. The output of the code is the original data plus the desorption rate and the calculated surface concentration at each time step [33].

CO coverage / ML	E_{des}±0.5 / kJ mol^{-1}
0.2	8.1-9.6
0.4	7.6-10.2
0.6	7.3-8.9
0.8	6.9-9.0
1.0	6.2-9.0

Table 5.2: Experimental values extracted from the TPD experiments of various coverages CO on $aSiO_2$ [1].

Having established the variation of E_{des} with surface coverage, the next step is to determine the probability distribution of E_{des}, $P(E_{des})$. $P(E_{des})$ is the probability of a CO molecule desorbing from a surface site with a particular E_{des} value. The data in **Figure 5.12** is averaged (see insert) and a single plot produced which is fitted with an easily differentiable function form (in this instance a sum of exponentials). This fitted function is used to convert $E_{des}(\theta)$ to $P(E_{des})$ *via* **Equation 12**:

$$P(E_{\mathrm{des}}) = \frac{\mathrm{d}N_{ads}}{\mathrm{d}E_{\mathrm{des}}} \qquad \textbf{(E12)}$$

The resulting plot of $P(E_{des})$ *versus* E_{des} is shown in **Figure 5.13**. Similar distributions have been reported for CO and other small molecules on a number of heterogeneous surfaces [3,33-36]. **Figure 5.14** shows the $P(E_{des})$ *versus* E_{des} for p-ASW derived from reference [37].

Figure 5.13 sets out the range of interaction energies associated with the surface heterogeneity of the $aSiO_2$ surface and is a key component in the simulation of the vibrational line profiles and this is discussed below [1]. It represents the probability that a CO molecule randomly landing on a $aSiO_2$ surface will find itself in such a environment. **Figure 5.14** does likewise for CO interacting with the p-ASW surface.

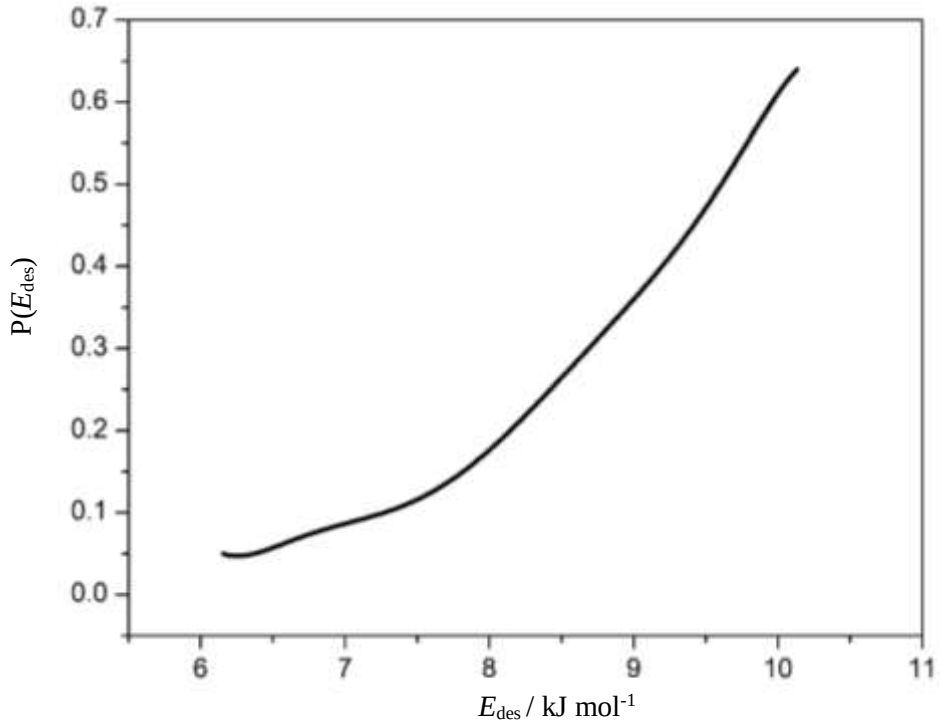

Figure 5.13: *P*(E_{des}) *versus* E_{des} derived from sub-monolayer TPD of CO from an $aSiO_2$ substrate [1].

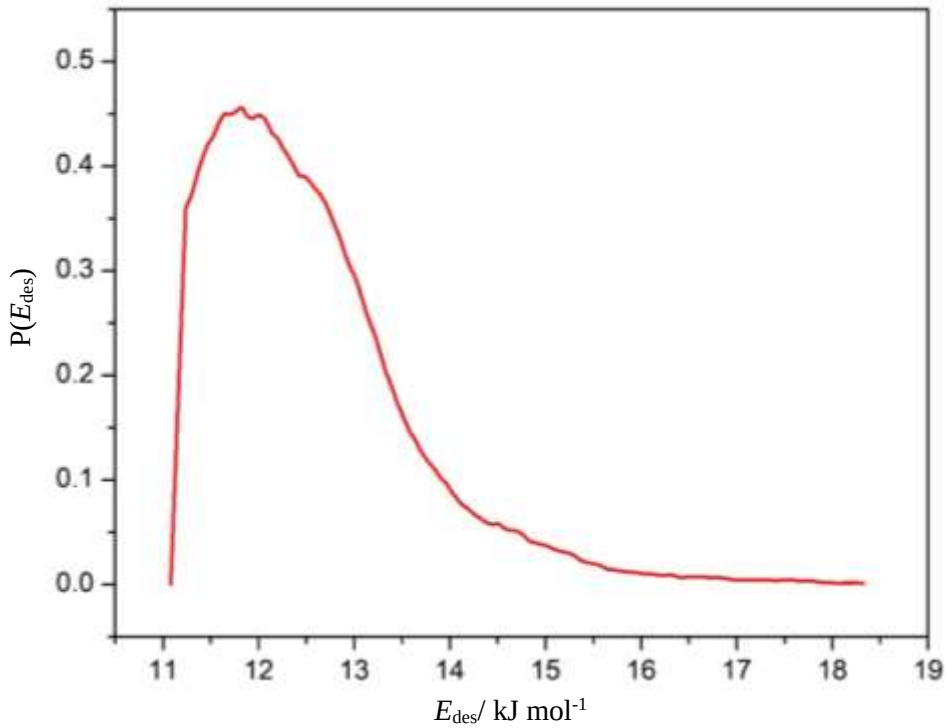

Figure 5.14: *P*(E_{des}) *versus* E_{des} from sub-monolayer TPD of CO from ASW derived from Kay and co-workers data [37].

5.3.2 RAIRS of CO on $aSiO_2$ and p-ASW

Figure 5.15 shows the RAIR spectra of 0.4 to 1.0 ML CO on $aSiO_2$ at 18 K recorded at an instrument–limited resolution of 0.1 cm^{-1}. The line profiles are asymmetric and broad with a full-width-at-half-maximum of 5.6 cm^{-1} which is greater than the instrument-limited resolution of 0.1 cm^{-1} used in recording the spectra. **Figure 5.16** shows the CO RAIR spectrum for 0.6 ML of CO on $aSiO_2$ at 20 K. The CO spectra, and the CO stretching frequency at 2137 cm^{-1}, shows no change when the substrate is annealed from 20 to 22 and 24 K [3]. **Table 5.3** compares the experimental values extracted from the TPD data with the RAIRS linewidths, FWHM and δ, for various CO coverages. The CO vibrational frequency is consistent with observations from Pontoppidan *et al*. [13] and is inconsistent with CO in or on H_2O ice.

CO coverage / ML	E_{des} **±0.5 / kJ mol^{-1}**	**FWHW / cm^{-1}**	**δ / cm^{-1}**
0.2	8.1-9.6	5.0±0.1	2.1±0.05
0.4	7.6-10.2	5.4±0.1	2.3±0.05
0.6	7.3-8.9	5.6±0.1	2.5±0.05
0.8	6.9-9.0	6.5±0.1	2.8±0.05
1.0	6.2-9.0	6.7±0.1	2.9±0.05

Table 5.3: Experimental values extracted from the TPD and RAIRS experiments of various coverages CO on $aSiO_2$, where δ is the linewidth of the ν_{CO} derived from the FWHM using **Equation 15** [1].

There is no reason for the asymmetric profile on an insulator such as $aSiO_2$. The observed line profiles must be determined by a combination of environmental heterogeneity along with homogeneous broadening associated with relaxation of the excited CO vibration *via* its weak mechanical coupling with the vibrations of the $aSiO_2$ substrate.

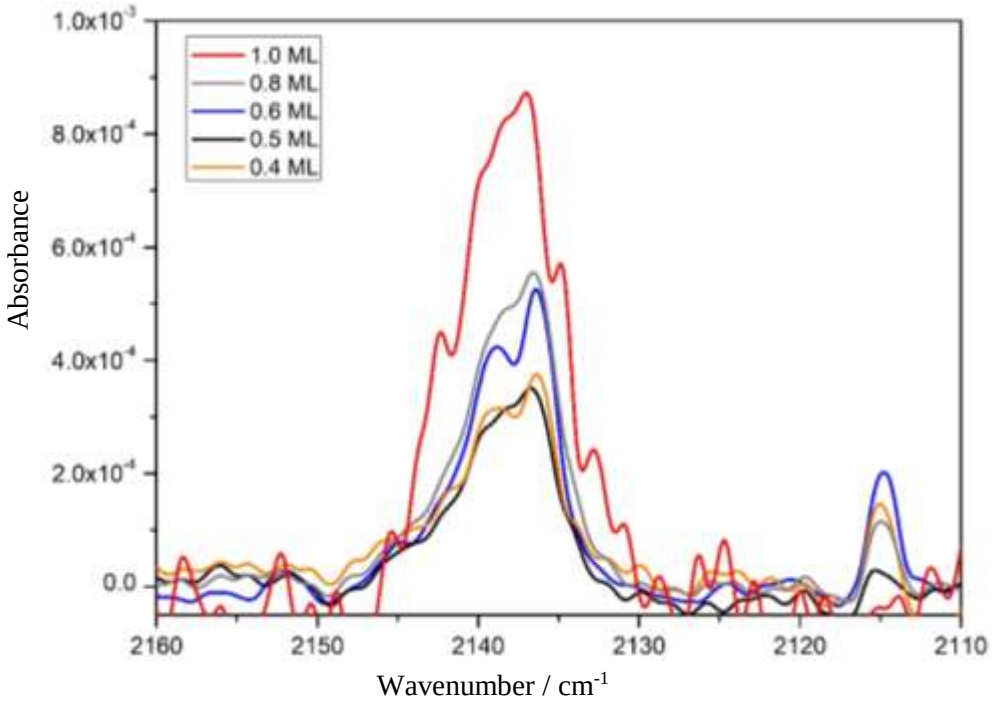

Figure 5.15: RAIR spectra for sub-monolayer quantities of CO on $aSiO_2$. The spectra were recorded at an instrument-limited resolution of 0.1 cm^{-1} at 18 K.

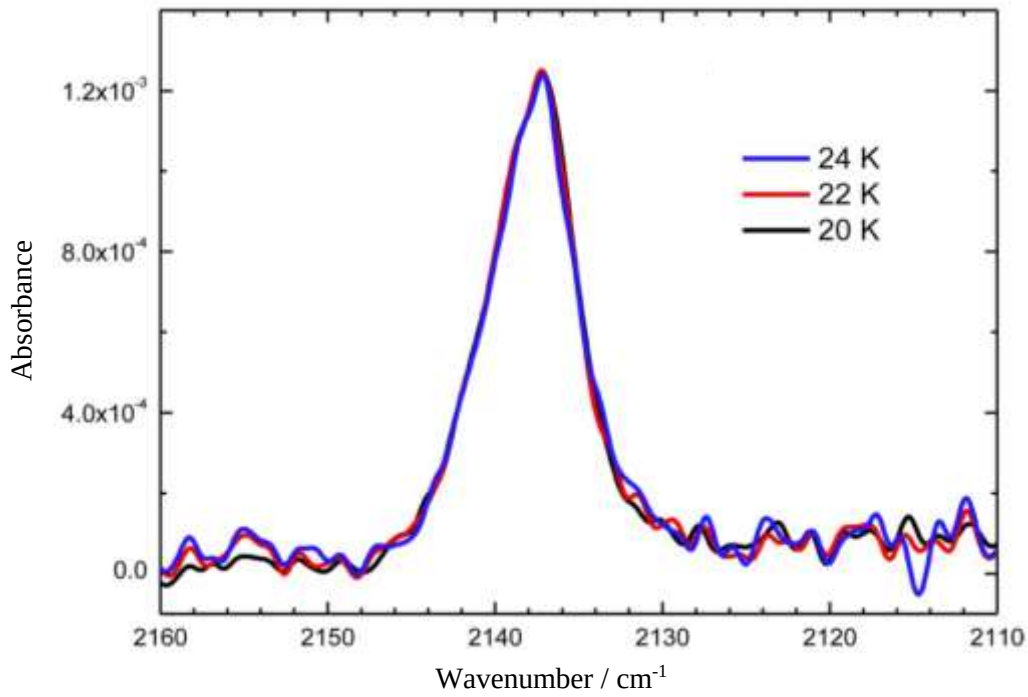

Figure 5.16: The RAIR spectrum spectra of 0.6 ML CO on $aSiO_2$ as a function of temperature. This indicates that CO is free to diffuse at temperature greater than 20 K to sample to most favourable binding sites on the $aSiO_2$ surface. (Reproduced from [3]).

The experimental RAIR data CO on the ASW surface is shown in **Figure 5.17**. The RAIR spectra for CO on ASW produces two absorption features. The most intense peak is due to the π-interaction of CO with the surface, while the smaller peak is due to the linear σ-interaction of the CO with the surface [15, 39].

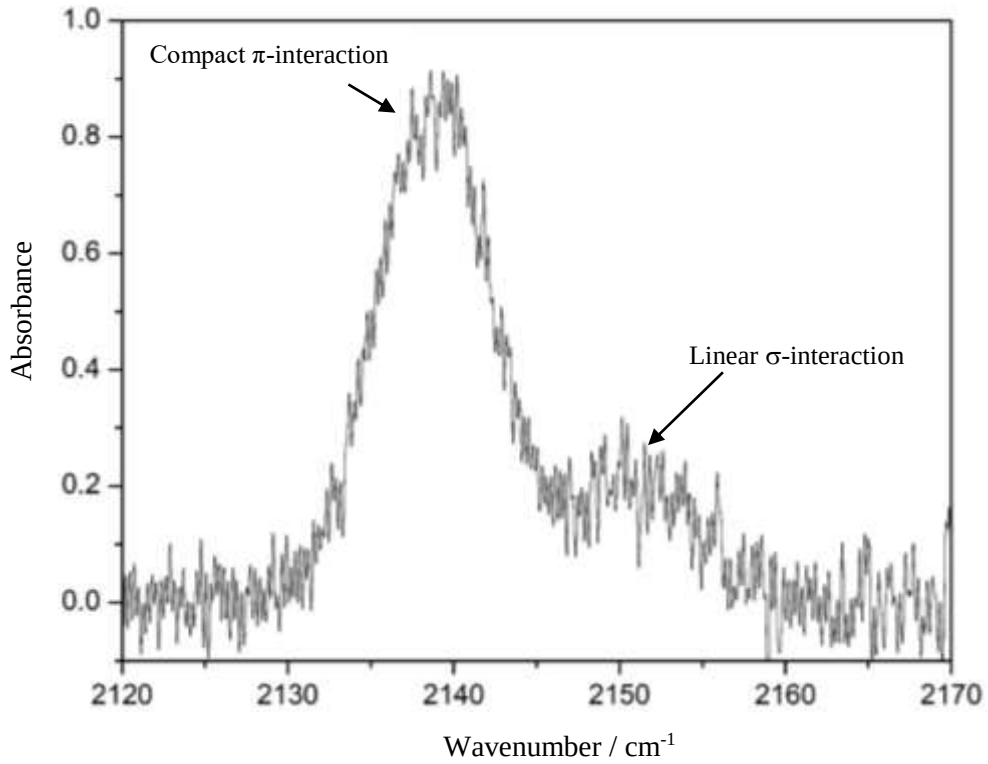

Figure 5.17: Baseline-corrected RAIRS data 15 ML CO on p-ASW, which displays two absorption features due to the π and σ interactions of CO with the surface.

The peak which arises from the σ interaction forms the basis for this work and so this peak was subsequently isolated. This is achieved by fitting a Gaussian to the π-interaction feature. The fitted Gaussian was subsequently subtracted to give the corresponding baseline-corrected spectra. The results of this process are shown in **Figure 5.18**.

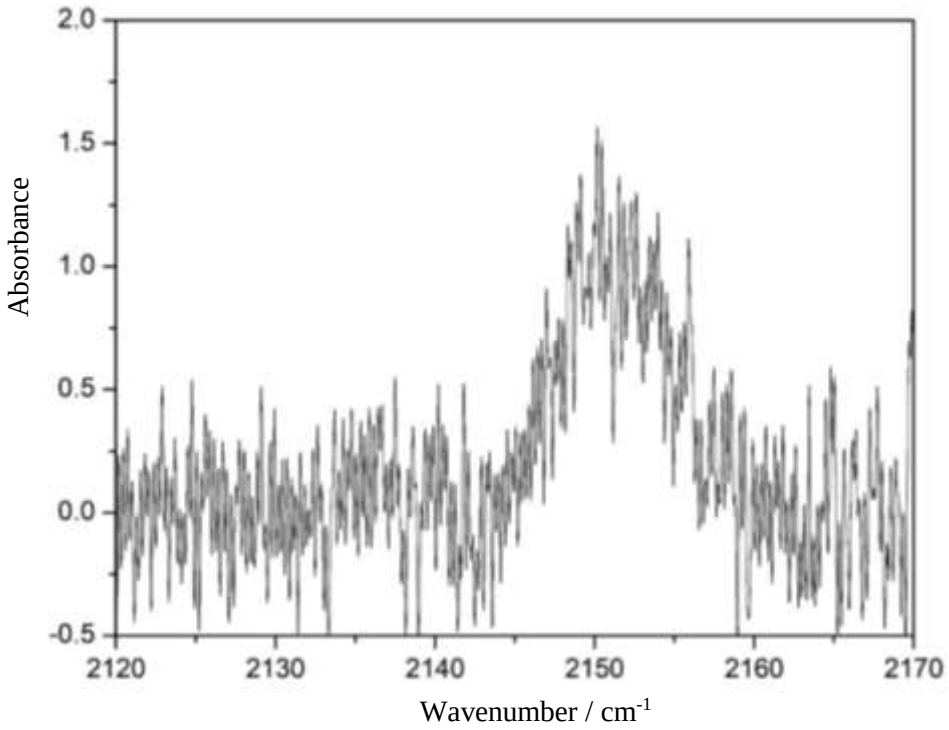

Figure 5.18: The normalised linear σ-interaction of CO with p-ASW.

5.3.3 Line Profile Synthesis

This part of this chapter discusses vibrational line profile synthesis. The line profile synthesis is carried out given [1]:

a) the relevant environmental interaction energies for CO on the $aSiO_2$ and p-ASW surfaces;
b) the variation of the CO stretching frequency with those interaction energies; and
c) assuming Gaussian-line profiles.

This translates to the key steps below:

1. The strength of the interaction experienced by the CO molecule in certain environments E_b is equated with E_{des}. $\Delta\bar{\nu}$, the vibrational shift number from the isolated CO vibrational wavenumber, is given by **Equation 2**.

2. The CO vibrational line position, $\bar{\nu}(E_{des})$, is calculated at each E_{des} according to **Equation 13**, where $\bar{\nu}_o$ is the vibrational origin and which can be viewed as representing the vibrational wavenumber of CO on a non-interacting $aSiO_2$ or p-

ASW surface. Thus, it encompasses the effect of the mass of the silica or solid water surface on the CO vibration.

$$\bar{\nu}(E_{\mathrm{des}}) = \bar{\nu}_0 + \Delta\bar{\nu}(E_{\mathrm{des}}) \quad \textbf{(E13)}$$

The value of $\bar{\nu}_0$ is changed depending on the surface CO is interacting with (e.g. p-ASW or $aSiO_2$) and is determined by varying the value $\bar{\nu}_0$ until the position of the modelled peak for CO is consistent with the position of the experimental RAIRS peak for CO [1, 39]. The input for the model used a set of $\bar{\upsilon}$ values ranging from 2130 cm^{-1} to 2170 cm^{-1}. This set of values was selected due to the CO RAIR features on $aSiO_2$ and p-ASW lying within this range.

3. The vibrational line intensity at each line position, I($\bar{\upsilon}$, E_{des}), is calculated by assuming a simple Gaussian line profile, as shown in **Equation 14**.

$$I(\bar{\upsilon}) = I_0 \sum_{E_{\mathrm{des}}} P(E_{\mathrm{des}})\ e^{-[\bar{\nu}-\bar{\nu}(E_{\mathrm{des}})]^2/2\delta^2} \quad \textbf{(E14)}$$

where I_0 is the intensity scaling factor and the overall line profile is acquired by summing over E_{des}. δ controls the width of the Gaussian. This is sometimes referred to as the Gaussian RMS width. δ is linked to the full-width-half-maximum (FWHM) through **Equation 15**:

$$FWHM = 2\sqrt{2\ln(2)}\,\delta \quad \textbf{(E15)}$$

δ is varied in order to achieve the best fit of the modelled and experimental peaks.

4. The final step is to vary the parameters $\bar{\nu}_0$, I_o and δ until a good reproduction of the experimental line profile is achieved. This modelled data can be used to compare experimental RAIRS data for sub-monolayer coverages of CO on the $aSiO_2$ and p-ASW different surfaces [1].

5.3.4 Ballistic Deposition *versus* Adsorption and Diffusion

There are two limiting deposition behaviours [1] for species adsorbing on a surface;

- Ballistic
- Adsorb and Diffuse

In the case of ballistic deposition, there is no preference for any adsorption site, so within the line synthesis, sites will be sampled according to the $P(E_{\mathrm{des}})$ distribution.

$$I(\bar{\nu}) = I_{\mathrm{o}} \sum_{E_{\mathrm{des}}} P(E_{\mathrm{des}})\ e^{-[\bar{\nu}-\bar{\nu}(E_{\mathrm{des}})]^2/2\delta^2} \qquad \textbf{(E16)}$$

In adsorb and diffuse, the sites are sampled in energetic preference order, with the most strongly bound filling first. Sites are thus sampled according to an inverse Boltzmann weighted $P(E_{\mathrm{des}})$ distribution [1]:

$$I(\bar{\nu}) = \mathrm{I_o} \sum_{E_{\mathrm{des}}} P(E_{\mathrm{des}}) e^{-E\mathrm{des}/RT}\ e^{-[\bar{\nu}-\bar{\nu}(E_{\mathrm{des}})]^2/2\delta^2} \qquad \textbf{(E17)}$$

The following set of figures show the ballistic deposition, and the adsorb and diffusive models compared with experimental RAIR data. **Figure 5.19** shows the ballistic deposition simulation assuming instrument-limited linewidth of 0.1 cm^{-1}. The synthesised line profile (red) has been vertically scaled to provide for direct comparsion with the experimental data (blue). The simulated and experimental clearly do not agree. Thus ballistic disposition cannot be regarded as the deposition mechanism for CO on aSiO_2.

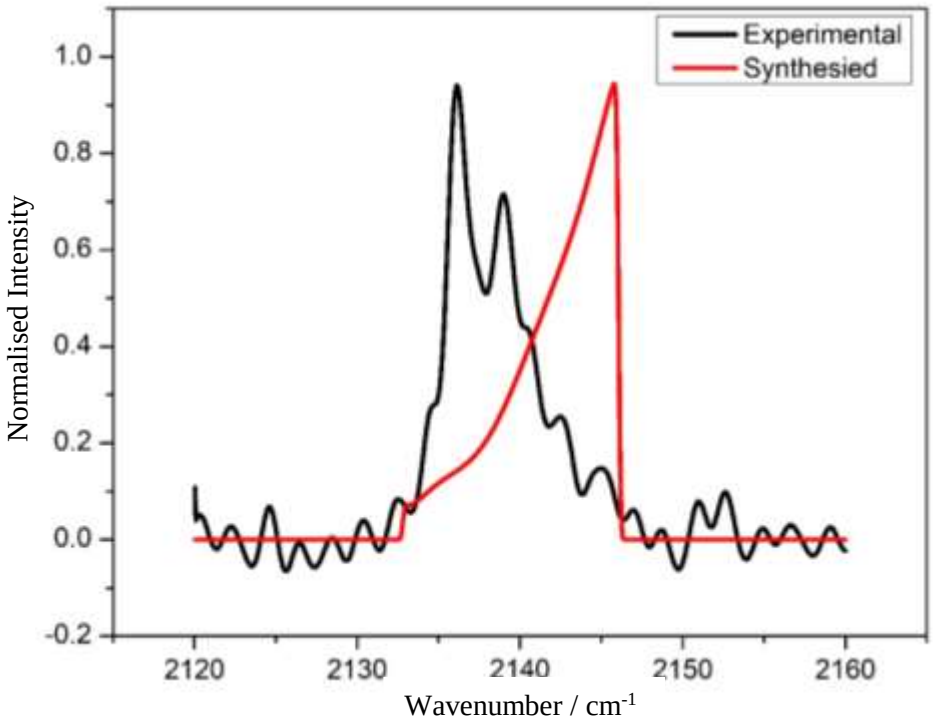

Figure 5.19: Vibrational line profile synthesis for 0.6ML CO on $aSiO_2$ assuming ballistic deposition at instrument limited resolution 0.1 cm^{-1}.

Figure 5.20 shows adsorb-diffuse deposition assuming an instrument-limited linewidth of 0.1 cm^{-1} for CO on $aSiO_2$. Again, this does not produce a good fit. However, optimising the fitting parameters does result in a good fit, and therefore reproduction of the observed line profile as shown in **Figure 5.21**.

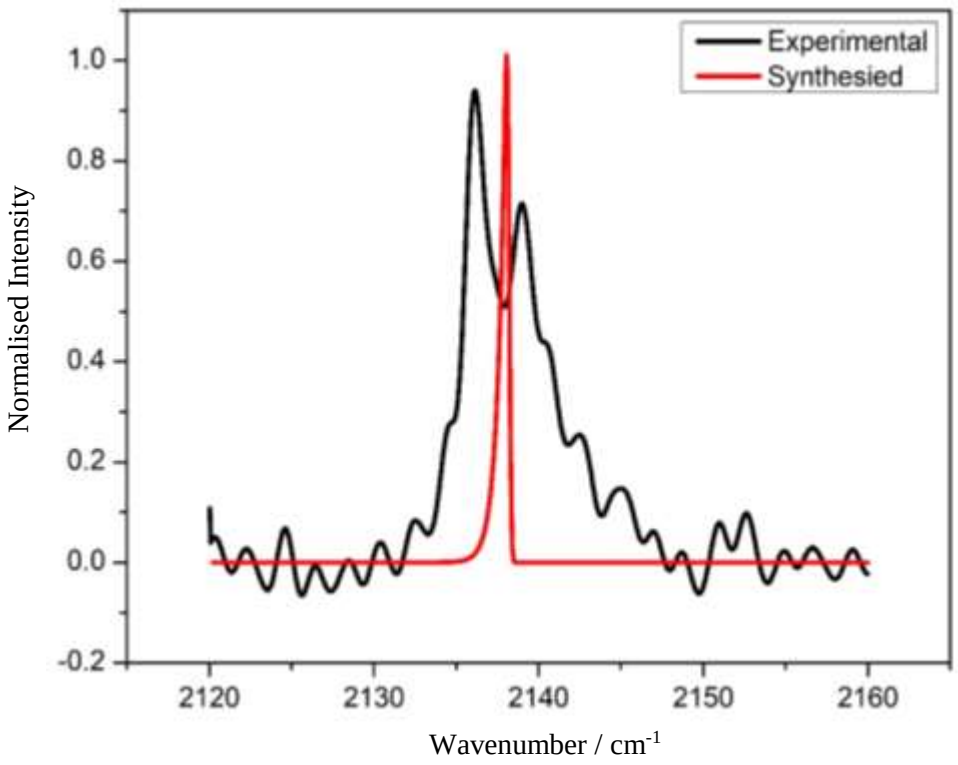

Figure 5.20: Vibrational line profile synthesis assuming the adsorb and diffuse model for 0.6 ML CO on $aSiO_2$ at an instrument limited resolution of 0.1 cm^{-1}.

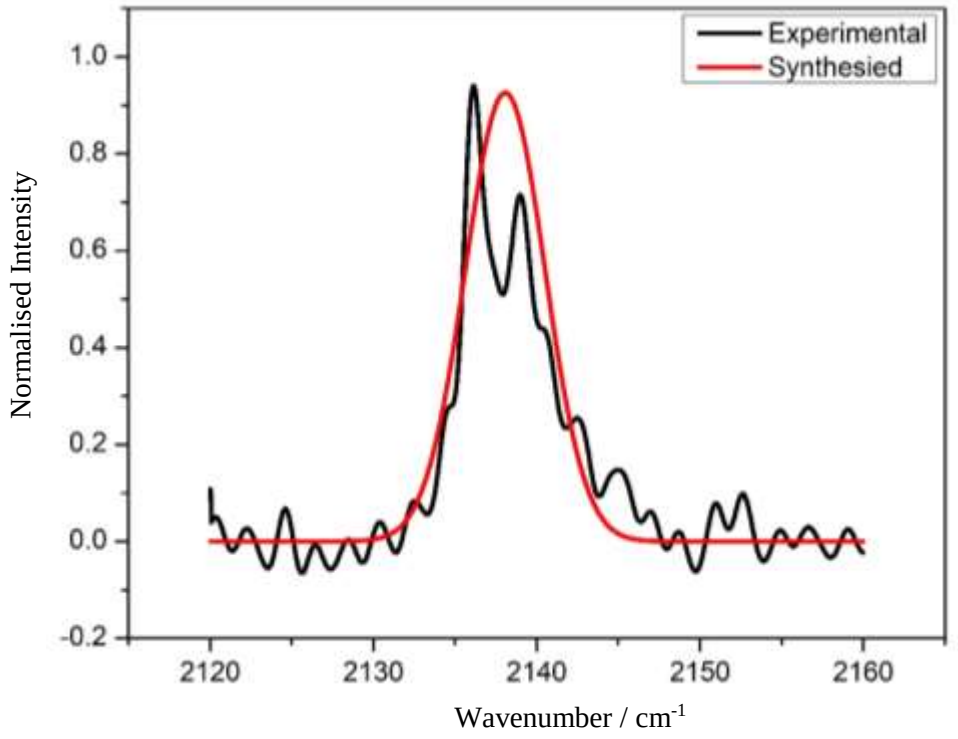

Figure 5.21: Adsorb and diffuse deposition optimised vibrational line profile synthesis at instrument-limited linewidth for 0.6 ML CO on $aSiO_2$.

5.3.5 CO on p-ASW

The process used on the CO aSiO_2 data is now used to simulate the vibrational line profile for CO on p-ASW. The linear interaction of CO molecules with the heterogeneous surface of p-ASW was studied *via* sub-monolayer coverages of CO on p-ASW. The monolayer is greater in CO on p-ASW than CO on aSiO_2 due to the greater surface presented by the p-ASW pores. The modelled RAIR data is compared with the experimental RAIR data at instrument limited linewidth 0.1 cm^{-1} along with the best fit model linewidth. The E_{des} *versus* $P(E_{des})$ for CO on ASW is obtained from the work carried out by Kay and co-workers [37] and is shown in **Figure 5.14**. **Figure 5.22** shows the ballistic deposition model assuming instrument-limited linewidth of 0.1 cm^{-1}, where the experimental data (black) and synthesised line profile (red) are compared. **Figure 5.23** shows adsorb-diffuse deposition assuming an instrument-limited linewidth of 0.1 cm^{-1} for CO on p-ASW. Again, this does not produce a good fit. However, optimising the fitting parameters does result in a good fit, and therefore reproduction of the observed line profile as shown in **Figure 5.24** and **Figure 5.25**.

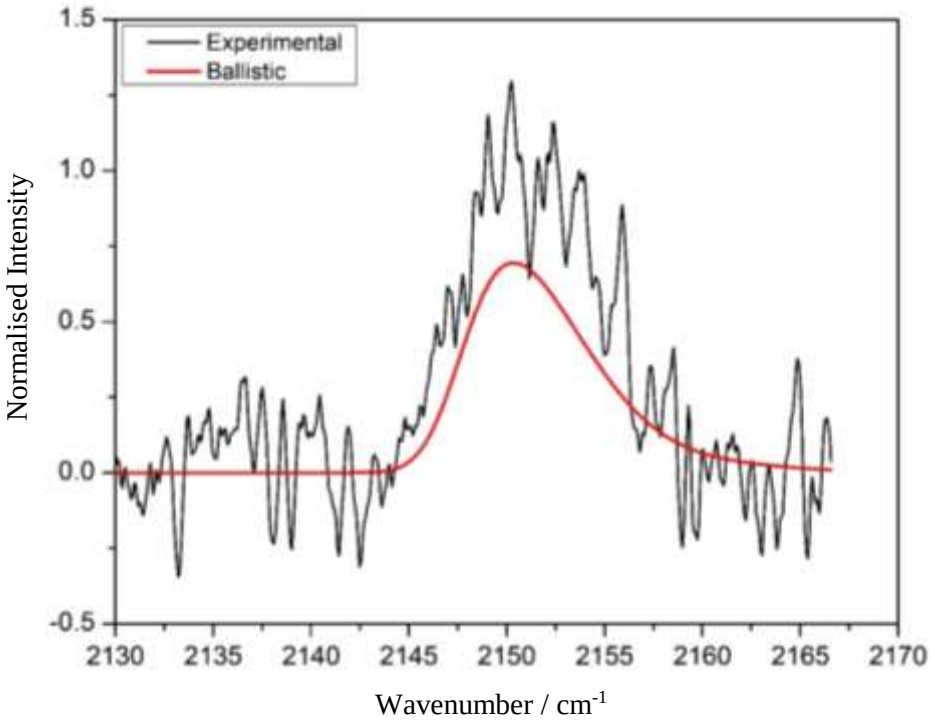

Figure 5.22: Vibrational line profile synthesis for 15 ML CO on p-ASW assuming ballistic deposition at instrument limited resolution 0.1 cm^{-1}.

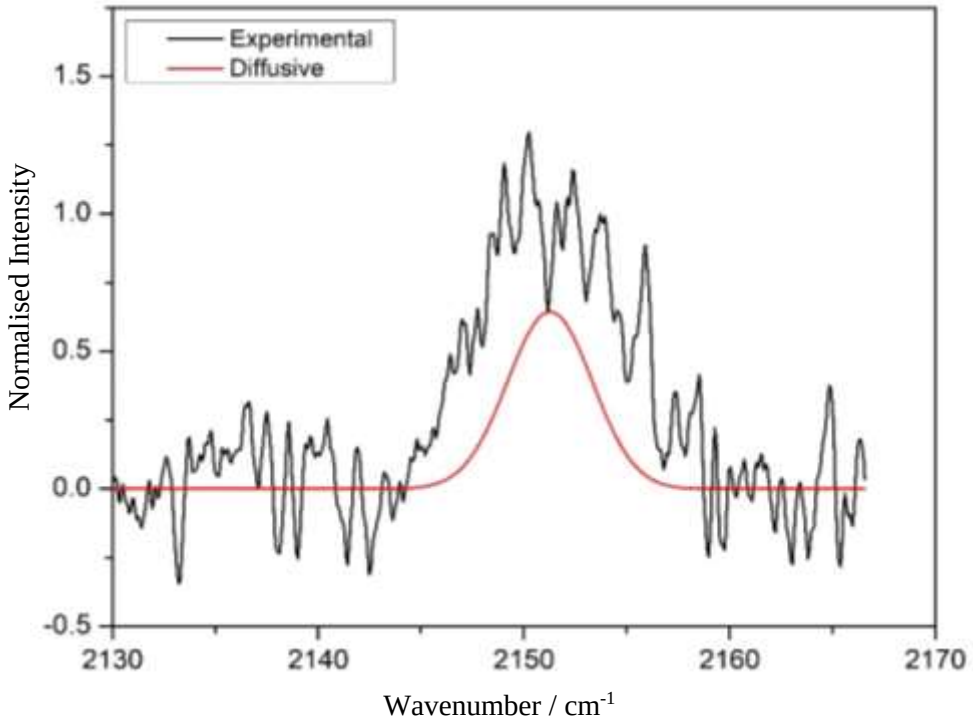

Figure 5.23: Vibrational line profile synthesis for 15 ML CO on p-ASW assuming adsorb and diffuse model for CO on $aSiO_2$ at an instrument limited resolution of 0.1 cm^{-1}.

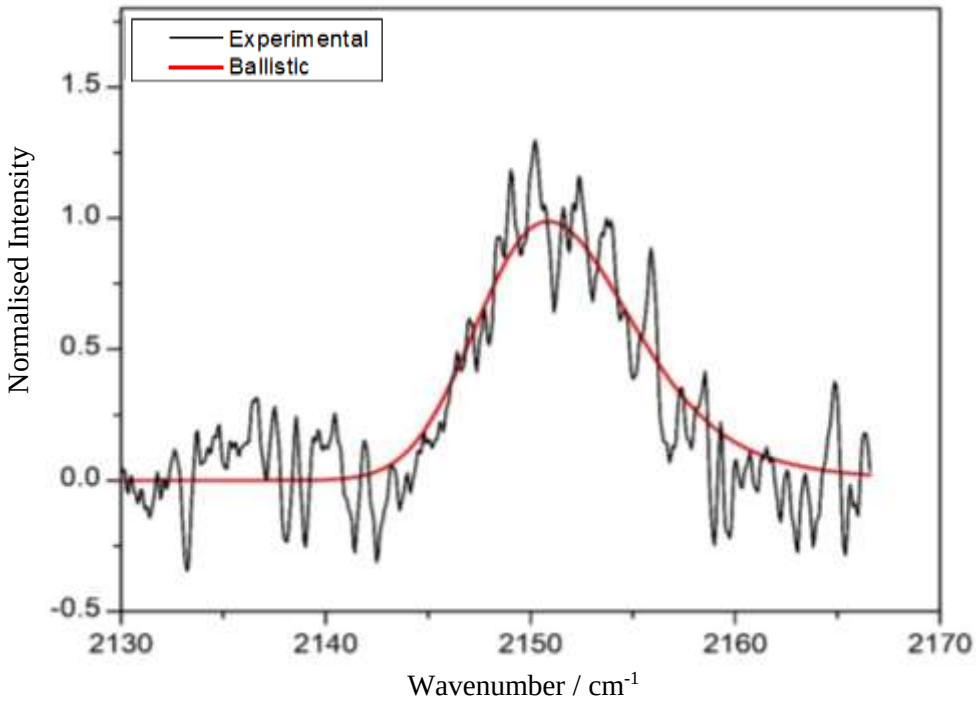

Figure 5.24: The simulated best fit ballistic line profile for linewidth of 2.6 cm^{-1} and experimental CO stretching band for 15 ML of CO on p-ASW on $aSiO_2$ substrate at 18 K at instrument limited resolution of 0.1 cm^{-1}.

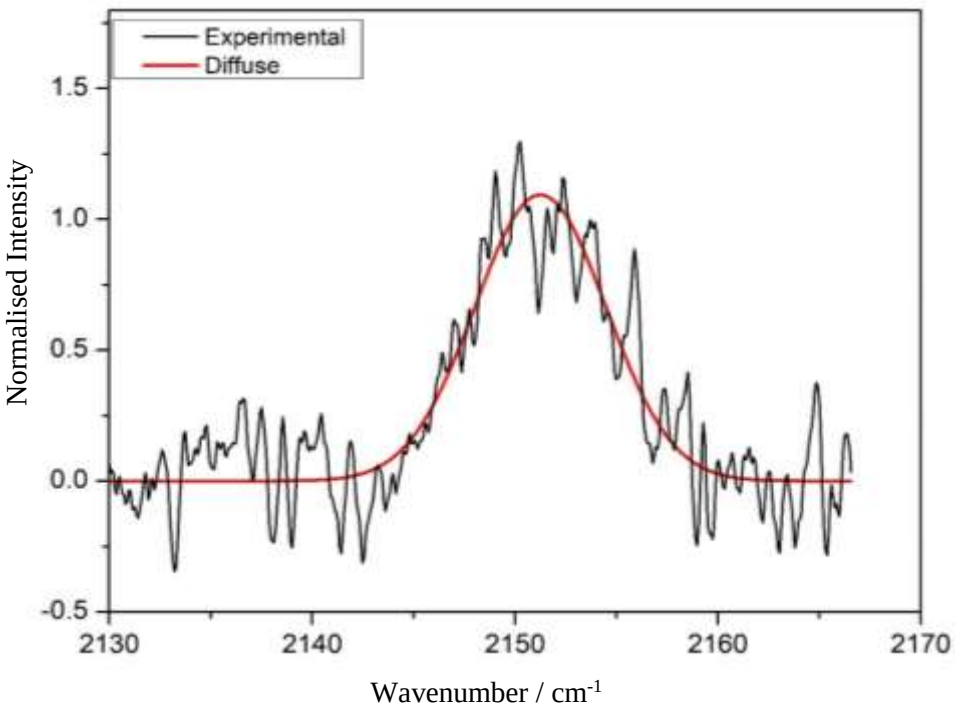

Figure 5.25: The simulated best fit adsorb and diffuse line profile for linewidth of 3.2 cm^{-1} and experimental CO stretching band for 15 ML of CO on p-ASW on $aSiO_2$ substrate at 18 K at an instrument limited resolution of 0.1 cm^{-1}.

Figures 5.24 and **5.25** show the best fit for 15 ML of CO on 1000 L p-ASW RAIR data for ballistic deposition and absorb diffuse models compared with the experimental RAIR data. It appears that both models reproduce the experimental data. Looking at the E_{des} for CO on $aSiO_2$ (6 - 12 kJ mol^{-1}) and CO on a-ASW (11-16 kJ mol^{-1}) this would support the idea that CO is more strongly bound to the water surface than $aSiO_2$. It is thought that the barrier to surface diffusion is in the order of 10-15% of the system's E_{des} [40]. Hence, this results in CO being free to diffuse on $aSiO_2$ compared to p-ASW (**Figure 5.22**). The work in literature [41-43] indicates that CO is relatively free to diffuse compared with only 10% of CO molecules on p-ASW trapped in pores. In this work, the relative amounts of CO that could be trapped or alternatively may not be mobile cannot be estimated. The data in this work supports the idea that the adsorb and diffuse model better represents the experimental data.

5.3.6 CO adsorption on $aSiO_2$ and p-ASW

Table 5.4 summarises the outcome of the line synthesis. In both instances, CO on $aSiO_2$ and p-ASW, evidence from this work and that of others suggests that deposition of CO occurs on these surfaces *via* an adsorb and diffuse mechanism, the reproduction of the experimentally observed CO line profiles being the key piece of supporting evidence from the present work.

	$\bar{\nu}_0$ /cm^{-1} (±0.5)	δ /cm^{-1} (±0.2)	Model FWHM / cm^{-1} (±0.5)	Experimental FWHM / cm^{-1} (±0.1)
CO on $aSiO_2$	2102.5	2.4	4.71	4.66
CO on p-ASW (Ballistic)	2108.0	2.6	9.0	8.0
CO on p-ASW (Diffusive)	2089.0	3.2	7.6	8.0

Table 5.4: Compares the best-fit parameters $\bar{\nu}_0$, δ and $I_{0,}$ along with the corresponding FWHM for the modelled profiles and the experimental CO vibrational line profiles on $aSiO_2$ and p-ASW substrate [1].

When comparing the range of E_{des} for CO for $aSiO_2$ (6 - 12 kJ mol^{-1}) to p-ASW (11-16 kJ mol^{-1}), we see that CO is more strongly bound to the latter. As a rule of thumb, surface diffusion barriers are taken as around 10 to 15 % of the surface binding energy of a species as shown in **Figure 5.26** [40]. Thus diffusion of CO on a p-ASW surface is more likely to be restricted compared to the $aSiO_2$ surface, since the diffusion barrier is lower on the $aSiO_2$ when compared with the p-ASW surface. However, there is work that indicates that CO is relatively free to diffuse over p-ASW with approximately 10% of the CO molecules being trapped, although this does depend on the p-ASW pore size [38-40].

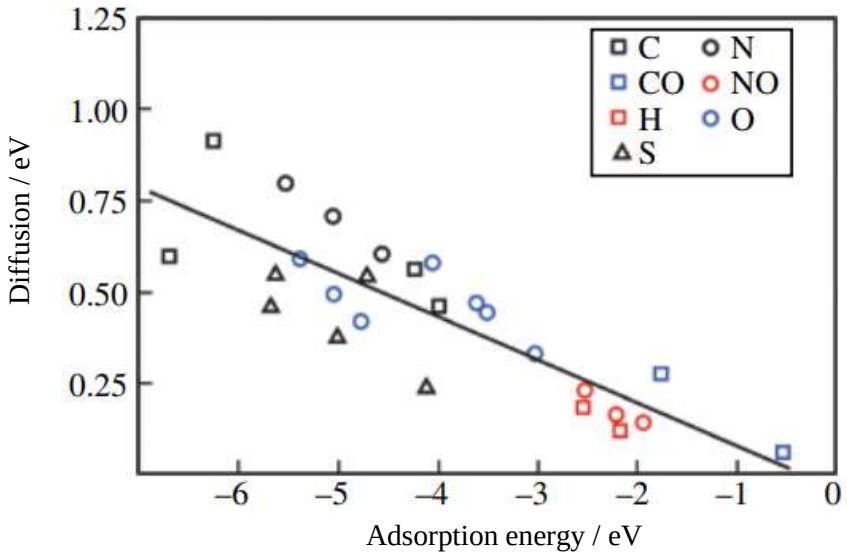

Figure 5.26: Diffusion *versus* adsorption on metal surfaces where the diffusion barriers for a range of different adsorbates are plotted as a function of their adsorption energy (Reproduced from [40]).

Thus diffusion of CO on a p-ASW surface is most likely to be restricted compared to the $aSiO_2$ surface, since the diffusion barrier is lower on the $aSiO_2$ when compared with the p-ASW surface. However, there is work that indicates that CO is relatively free to diffuse over p-ASW with approximately 10% of the CO molecules being trapped, although this does depend on the p-ASW pore size [38-40].

Additionally, this approach allows us to understand the vibrational relaxation of CO on the $aSiO_2$ and p-ASW surfaces. **Table 5.4** lists the best fit linewidths for CO on the two surfaces. If we consider our accepted adsorb and diffuse depletion model then the line width for CO on p-ASW at 3.2±0.2 cm^{-1} is larger than that on $aSiO_2$ at 2.4±0.2 cm^{-1}. This means, of course that the lifetime of vibrational excited CO on p-ASW at 0.7 ps is shorter than that on $aSiO_2$ at 0.94 ps. This time scale is consistent with intermolecular vibrational relaxation (IVR) and the difference points to differences in the efficiency of the IVR process on $aSiO_2$ and p-ASW. This can be readily explained as p-ASW surface provides an underlying continuum of vibrational modes associated with the combination of the H_2O binding vibrational at 1636 cm^{-1} [44] with the p-ASW librational mode at 672 cm^{-1} [44] which can rapidly disperse the excitation of the CO vibrational into the phonon bath of the ASW (**Figure 5.27**). No such spectral overlap is found between the CO vibrational modes in $aSiO_2$ and so the relaxation takes longer.

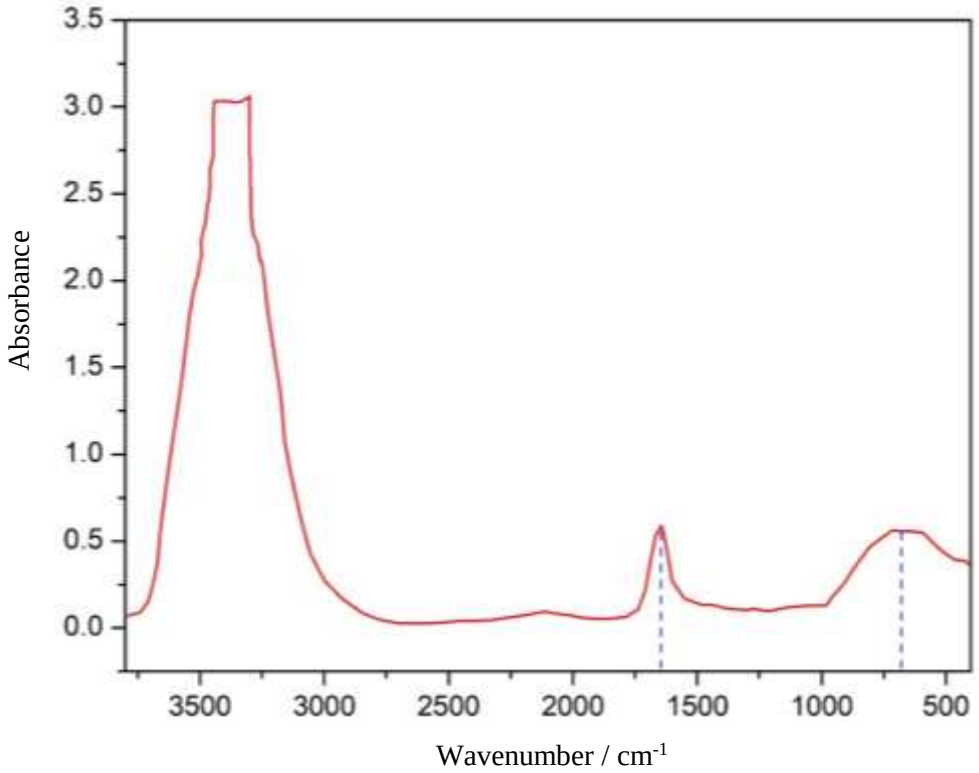

Figure 5.27: IR spectrum of solid H_2O. The broken lines indicate the position of the librational (672 cm^{-1}) and bending modes (1636 cm^{-1}) in solid H_2O [44].

5.4 Conclusion

The work in this chapter has demonstrated a simple method that can be used to synthesise the vibrational line profile of CO on a heterogeneous surface, where the interactions between the CO and the substrate are dominated by weak, non-covalent interactions. The procedure developed allows the conversion of a distribution of E_{des} into a continuous distribution of vibrational frequencies, which can in turn be compared with experimental RAIRS data. A main requirement for synthesis is details of the range of interaction energies along with their weighting as encompassed by the $P(E_{des})$ *versus* E_{des}, which are used in the simulations. In this work, the data was obtained from experimental TPD data, however it may be possible to derive this data using computational chemistry. However, the challenge in using the computational chemistry would be identifying the size of the system to model along which would reproduce the $P(E_{des})$ *versus* E_{des} along with the best computational method to use in modelling that system.

The TPD data for CO desorbing from $aSiO_2$ at low coverages shows coincident trailing edges. This would be consistent with first-order desorption of the first layer and suggests that CO wets the $aSiO_2$ surface. At higher coverages there is a common leading edge, that is consistent with zero-order desorption of a multilayer ice. The $aSiO_2$ surface presents a range of binding sites with different binding energies for adsorption. The trailing edge alignment supports the idea that the molecules are mobile enough on the $aSiO_2$ surface to find the deepest, energetically most favourable binding sites before they desorb. Molecules which are located in the weak binding sites desorb first and this results in desorption peak broadening. Hence, a single value for E_{des} is no longer valid [3, 36].

Figure 5.16 shows the RAIR spectra for 0.6ML CO on $aSiO_2$ and there is no obvious explanation for the asymmetric profile and the observed line profiles hence must be determined by a combination of environmental heterogeneity and homogeneous broadening which is associated with the relaxation of excited CO vibration from its weak mechanical coupling with the vibrations of the $aSiO_2$ substrate. When comparing the range of E_{des} for CO for $aSiO_2$ (6-12 kJ mol^{-1}) to p-ASW (11-16 kJ mol^{-1}), we see that CO is more strongly bound to the latter. As a rule of thumb, surface diffusion barriers are taken as around 10 to 15% of the surface binding energy of a species as shown in **Figure 5.26** [38]. This approach has also been applied to simulating the vibrational line profiles of CO on p-ASW. **Table 5.4** summarises the data and **Figure 5.24** and **5.25** shows the comparison with experimental RAIR data. Finally, the simulations of the line profiles have shown that there is a difference between the vibrational relaxation (*i.e.* p-ASW is more effective than $aSiO_2$). The simulations of the line profiles for CO on $aSiO_2$ and CO on p-ASW have shown vital differences in the vibrational relaxation, where p-ASW is more effective than $aSiO_2$ and surface dynamics where CO can be regarded as being locked in place on p-ASW however CO is free to diffuse on $aSiO_2$ at 18K.

5.5 References

[1] S. Taj, D. Baird, A. Rosu-Finsen and M. R. S. McCoustra, *Phys. Chem. Chem. Phys*., 2017, **19**, 7990.

[2] M. P. Collings, J. W. Dever and M. R. S. McCoustra, *Phys. Chem. Chem. Phys*., 2014, **16**, 3479.

[3] M. P. Collings, V. L. Frankland, J. Lasne, D. Marchione, A. Rosu-Finsen and M. R. S. McCoustra, *Mon. Not. R. Astron. Soc*., 2015, **449**, 1826.

[4] S. A. Sandford, L. J. Allamandola, A. G. G. M.Tielens and G. J. Valero, *Astrophys. J*., 1999 **329**, 498.

[5] B. Schmitt, J. M. Greenberg and R. J. A. Grim, *Astrophys. J*., 1989, **340**, L33.

[6] M. E. Palumbo and G. Strazzulla, *Astron. Astrophys*., 1993, **269**, 568.

[7] M. E. Palumbo, *J. Phys. Chem. A*., 1997, **101**, 4298.

[8] M. P. Collings, J. W. Dever, H. J. Fraser and M. R. S. McCoustra, *Astrophys. Space Sci.*, 2003, **285**, 633.

[9] P. Jenniskens, D. F. Blake, M. A. Wilson and A. Pohorille, *Astrophys. J*., 1995, **455**, 389.

[10] J. P. Devlin, *J. Phys. Chem*., 1992, **96**, 6185.

[11] M. P. Collings, J. W. Dever, H. J. Fraser, M.R.S. McCoustra and D.A. Williams, *Astrophys. J.*, 2003, **583**, 1058.

[12] H. J. Fraser, S. E. Bisschop, K. M. Pontoppidan, A. G. G. M. Tielens, E. F. van Dishoeck, *Mon. Not. R. Astron. Soc*., 2005, **356**, 1283.

[13] K. M. Pontoppidan, H. J. Fraser, E. Dartois, W.-F. Thi, E. F. van Dishoeck, A. C. A. Boogert, L. d'Hendecourt, A. G. G. M. Tielens and S. E. Bisschop, *Astron. Astrophys*., 2003, **408**, 981.

[14] H. M. Cuppen, E. M. Penteado, K. Isokoski , N. van der Marel and H. Linnartz , *Mon. Not. R. Astron. Soc*., 2011, **417**, 2809.

[15] M. N. Mautner, V. Abdelsayed, M. S. El-Shall, J. D. Thrower, S. D. Green, M. P. Collings and M. R. S. McCoustra, *Faraday Discuss*., 2006, **133,** 103.

[16] J. D. Thrower, E. Friis, A. L. Skov, L. Nilsson, M. Andersen, L. Ferrighi, B. Jørgensen, S. Baouche, R. Balog, B. Hammer and L. Hornekær, *J. Phys. Chem. C*, 2013, **26**, 13520.

[17] S. L. Tait, Z. Dohnálek, C. T. Campbell and B. D. Kay, *J. Chem. Phys*., 2005, **122**, 164708.

[18] H. Ueba, Prog. *Surf. Sci*., 1997, **55**, 115.

[19] M. Nagao, K. Watanabe and Y. Matsumoto, *J. Phys. Chem. C,* 2009., **113**, 11712

[20] B. N. J. Persson and M. Persson, *Solid State Commun*., 1980, **36**, 175.

[21] B Sivasankar, *Engineering Chemistry* (Tata McGraw-Hill Education, New Delhi, India, 2008) Chapter 4.

[22] R. Ryberg, *Phys. Rev. B. Condens. Matter Mater. Phys*., 1985, **32,** 2671.

[23] G. Horvath, J. Illenyi, L. Pusztay and K. Simon, *Acta Chim. Hung*., 1987, **124**, 819.

[24] G. C. Pimentel and C. H. Sederholm, *J. Chem. Phys*., 1956, **24**, 639.

[25] P. Atkins and R. Friedman, *Molecular Quantum Mechanics 4th Edition* (Oxford University Press, Oxford, 2005) Chapter 6.

[26] W. Demtroder, *Laser Spectroscopy* (Springer-Verlag, Heidelberg, Germany, 1982) Chapter 3.

[27] https://chem.libretexts.org/Bookshelves/Physical_and_Theoretical_Chemistry_Textbook_Maps/Book%3A_Time_Dependent_Quantum_Mechanics_and_Spectroscopy_(Tokmakoff)/15%3A_Quantum_Relaxation_Processes/15.1%3A_Vibrational__Relaxation (Last accessed 30/5/19).

[28] H.-C. Chang, C. Noda and G. E. Ewing, *J. Vac. Sci. Technol* A, 1990, **8**, 2644.

[29] H.-C. Chang, D. J. Dai and G. E. Ewing, *J. Chin. Chem. Soc*., 1995, **42**, 31.

[30] https://www.researchgate.net/publication/305220662_Development_of_a_NearInfrared_Cavity_RingDown_Spectroscopy_System_for_CO_2_Isotope_Detection (Last accessed 15/5/19).

[31] H. Ueba, *Prog. Surf. Sci*., 1997, **55**, 115.

[32] B. N. J. Persson, and M. Persson, *Solid State Comm*., 1980, **36**, 175.

[33] J. D. Thrower, *PhD Thesis* (Heriot-Watt University, Edinburgh, 2009).

[34] J. D. Thrower, M. P. Collings, F. J. M. Rutten and M. R. S. McCoustra, *J. Chem. Phys*., 2009, **131**, 244711.

[35] J. A. Noble, S. Diana and F. Dulieu, *Mon. Not. R. Astron. Soc*., 2015, **454**, 2636.

[36] J. A. Noble, E. Congiu, F. Dulieu and H. J. Fraser, *Mon. Not. R. Astron. Soc*., 2012, **421**, 768.

[37] R. S. Smith, R. A. May and B. D. Kay, *J. Phys. Chem. B*, 2016, **120**, 1979.

[38] P. Ehrenfreund, A. C. A. Boogert, P. A. Gerakines, D. J. Jansen, W. A. Schutte, A. G. G. M. Tielens and E. F. van Dishoeck, *Aston.Astrophys.*,1996, **315,** L341.

[39] D. Baird, *Undergraduate Project Report* (Heriot-Watt University, Edinburgh, 2016).

[40] J. K. Nørskov, F. Studt, F. Abild-Pedersen and T. Bligaard, *Fundamental Concepts in Heterogenous Catalysis* (Wiley, Hoboken, New Jersey, USA, 2014), p14.

[41] F. Mispelaer, P. Theule, H. Aouididi, J. Noble, F. Duvernay, G. Danger, P. Roubin, O. Morata, T. Hasegawa and T. Chiavassa, *Astron. Astrophys*., 2013, **555**, A13.

[42] L. J. Karssemeijer, S. Ioppolo, M. C. van Hemert, A. van der Avoird, M. A. Allodi, G. A. Blake and H. M. Cuppen, *Astrophys. J*., 2014, **781**, 16.

[43] T. Lauck, L. Karssemeijer, K. Shulenberger, M. Rajappan, K. I. Oberg and H. M. Cuppen, *Astrophys. J*., 2015, **801**, 118.

[44] https://webbook.nist.gov/cgi/cbook.cgi?ID=C7732185&Type=IRSPEC&Index=1(Last accessed 31/5/19).

Appendix A: FORTRAN 90 program to calculate TPD profiles using a distribution of desorption energies.

```
PROGRAM TPDSimulation
!Program to calculate TPD profile using a desorption energy disruption function and experimental heating ramp
!Define variables
IMPLICIT NONE
DOUBLE PRECISION:: ORDER,PREEXP, RATE,PUMP, R, NADS, NGAS, NPUMP, TIMESTEP, SAT, NORM, CONC, STEPRATE, SHIFT
CHARACTER(20):: FILENAME_OUT, FILENAME_IN, FILENAME_DIST
INTEGER::I, J, STEPS, NAMELENGTH, RESTART, IOSTATUS, DISTSTEPS
DOUBLE PRECISION, ALLOCATABLE::TABLE (:,:), TIME(:), TEMP(:), EXPRATE(:), EDES(:)
  double precision numF,numS,numT
  integer num,pos1,pos2
  character(100) :: numchar
!ENSURE THAT  THE PROGRAM PROCEEEDS
RESTART=1
!DO  ALOOP FOR OVERALL PROGRAM OPERATION
DO
   IF (RESTART/=1) exit !Checks to see if program should proceed- will exit of exit is chosen after a calculation
   ! Initialize variables
   RATE = 0 !Desorption rate
   PUMP = 0 !Pumping speed
   NADS = 0 !Surface concentration
   NGAS=0 !Gas phase concentration
   NPUMP = 0 !Pumped concentration
   I=0 !Calculation step
   STEPS=0 !Total number of data points in calculation
   R = 8.314472 !Ideal gas constant
```

```
   NORM=0 !Normalization coefficient
   ORDER=1 !Desorption order
   PREEXP = 1E12 !Pre-Exponential  factor
   SHIFT=0 !Desorption energy shift in KJ/MOL
   call system('cls')  !Clear screen

print*,"*********************************************************"
print*,"**"
print*,"**"                  TPD Simulator 1.2
print*,"**”
print*,"*********************************************************"
   print*,""
   print*,""
   print*,"Kinetic Parameters initialisation"
   print*,""
   print*,"Desorption order = ", ORDER   !Display desorption order
   print*,"Pumping Rate  = ",PUMP         !Display pumping speed
   print*,"Pre-exponential factor: ",PREEXP, "/S"
   print*,"Enter initial coverage in molecules/cm2: "; read*, NADS !Take initial
surface concentration as an input
   print*,""
   print*,"Monolayer saturation is 3.76E13 molecules/cm2" !monolayer saturation
coverage for C6H6
   print*,""
   print*,"Experimental data initiation"
   print*,"-----------------------------"
   print*,""
   print*,"Enter input file name: " !Data file containing experimental data in
columns, TIME, TEMP, RATE
   print*,"(Maximum 20 Characters)"
   print*,"Extension 'csv' will be assumed"; read*, filename_in
   filename_in='data1.csv'
```

```
   print*,""
   print*,""
   print*,"Output Settings"
   print*,"----------------"
   print*,"Enter output file name" !Data file containing calculated TPD profile
   print*,"(Maximum 20 characters)"
   print*,"Extenetion '.csv' will be used;"; read*, filename_out
   print*,"The name the input file is ",filename_in
   !name of data file is data1.csv
   write(*,*)'<debugger>Cez 1'
   !return
   namelength=len_trim(filename_out)  !Set up input file
   filename_out=filename_out(1:namelength) //".csv"
   write(*,*)'<debugger> Filename = ',filename_in
   open(unit=1, file=filename_in)
   open (unit=2, file=filename_out)
   write(2,*) "Time ", "Temperature ", "Experiment ", " EDES ", "Rate ", "NGAS ",
"NPUMP "  !Write column headings to  output file
   !Count lines in put file and swet number of data points in calculation to this value
   IOSTATUS=0
   rewind(1)  !Rewind input file to  start
   do
   write(*,*)'<debugger>Pre Iostatus = ',Iostatus
   if(IOSTATUS<0) THEN
         exit
   endif
   read(1,123,IOSTAT=IOSTATUS)numchar
123 format(a)
   steps=steps+1
   print*,"The number of IOSTATUS is",IOSTATUS
   write(*,*)'Steps read = ',steps
```

```
   write(*,*)numchar
   pos1 = index(numchar, ",")
   pos2 = index(numchar(pos1+1:), ",")
   write(*,*)'pos1 = ', pos1
   write(*,*)'pos2 = ', pos2
   read(numchar(1:pos1-1), *) numF
   read(numchar(pos1+1:pos1+pos2-1), *) numS
   read(numchar(pos1+pos2+1:), *) numT
   write(*,*)numF,numS,numT
   end do
   rewind(1)  !Rewind input file to  start
   steps=steps-1
   write(*,*)'<debugger>Iostatus = ',Iostatus
   write(*,*)'<debugger>Steps = ',steps
   write(*,*)
   !Define size of arrays as number of data points
   allocate(time(steps))
   allocate(temp(steps))
   allocate(exprate(steps))
   allocate(edes(steps))

   IOSTATUS=0
   do i=1, steps
   if(IOSTATUS<0) exit
   read(1,*,iostat=IOSTATUS), time(i),temp(i), exprate(i)
   read(1,124,IOSTAT=IOSTATUS)numchar
124 format(a)
   pos1 = index(numchar, ",")
   pos2 = index(numchar(pos1+1:), ",")
   read(numchar(1:pos1-1), *) time(i)
```

```
read(numchar(pos1+1:pos1+pos2-1), *) temp(i)
read(numchar(pos1+pos2+1:), *) exprate(i)
print*,time, temp
end do
write(*,*)

!Display calculation parameters
print*, ""
print*, "Initializing calculation"
print*, "--------------------------"
write(*,"(A,F8.2,A)")" Starting temperature is:",temp(1), " K"
write(*,"(A,F8.2,A)")" Final temperature is:",temp(steps), " K"
write(*,"(A,F8.2,A)")" Simulation time is:",time(steps), " s"
print*,"Number of steps: ", steps
print*,""
print*,""
!Define output array
allocate(table(steps, 7))
do i=1, steps   !Do loop to  calculate rate for each time step
timestep=(time(i+1)-time(i)) !Work out time increment from experimental data
RATE=0  !Clear Rate Value
EDES=27.42071+14.73463*exp(-NADS/1.7809E13)+2.43792*exp(-
NADS/2.0655E12)+11.515*exp(-NADS/2.6598E14) !Desorption energy
distribution function
EDES=EDES+SHIFT  !Add any desorption energy shift top disruption function
if((EDES(i))<0) then !Check that desorption energy is positive surface
concentration
EDES=0
end if
    if(NADS<=0) then !Check that surface concentration is positive
    RATE=RATE !Rate remains zero if all molecules have desorbed
    else
```

```
      RATE=(PREEXP*NADS**ORDER)*exp((-
EDES(i)*1000)/(RATE*TEMP(i)))  !Calculate rate for non-zero surface
concentration

      end if

      if(NADS>=((RATE*TIMESTEP))) then !Check that sufficient molecules
remain for full desorption implied by  rate and next time increment

      NADS = NADS-(RATE*TIMESTEP) !Calculate new surface concentration

      else

      NADS=0 !set surface concentration to  zero if insufficient molecules remain
for implied desorption

      end if

      !Write calculation results to  output file

      table(i,1)=TIME(i)

      table(i,2)=TEMP(i)

      table(i,3)=EXPRATE(i)

      table(i,4)=EDES(i)

      table(i,5)=RATE

      table(i,6)=NGAS

      table(i,7)=NPUMP


      NGAS=NGAS+(RATE*TIMESTEP)-(PUMP*NGAS*TIMESTEP)

      if(NGAS<0) then

      end if

      ! Calculate pumped concentration for next step

      NPUMP=NPUMP+(PUMP*NGAS*TIMESTEP)

      end do !Repeats for all data points in input file

      !Write output to file

      do i=1, steps

      write(2,*) table(i,:)

      end do

      !Report completion of calculation

      print*,"calculation completed"
```

```
        print*,""
        print*,"output written to ", filename_out    !Report output filename
        print*,""
        print*,"Calculate again? (1:YES 0:NO): " !Ask the user weather new calculation is required
        read*,RESTART
deallocate(TABLE,TIME,TEMP,EXPRATE,EDES) !Clear array for new calculation
    end do
    print*,"Exiting to  command prompt" !Exit program
    print*,""
  call system('pause')   !Display operating system pause prompt
END PROGRAM TPDSimulation
```

Chapter 6

Temperature Programmed Desorption of CO from Astrophysically Relevant Surfaces.

6.1 Introduction

This chapter reports on the temperature programmed desorption (TPD) of carbon monoxide (CO) from astrophysically relevant surfaces. The work has used TPD to measure the desorption characteristics of CO from c-ASW (compact amorphous solid water) where the water is deposited at 100 K; CSW (crystalline solid water) where the water is deposited at 140 K; methanol (CH_3OH) and ammonia (NH_3) deposited on an amorphous silica ($aSiO_2$) substrate. Firstly, there will be a discussion of the different methods which can be used to calculate the pre-exponential factor for the rate of desorption. This is then followed by details of how the Extended Inversion Analysis is carried out, which allows the determination of a more representative value for the pre-exponential factor from a set of experimental TPD data. This is followed by details of the analysis of the experimental results starting with CO on $aSiO_2$, CO on c-ASW, CO on CSW, CO on CH_3OH and finally CO on NH_3. A key aim of this chapter is to investigate what effect the underlying ice has on the desorption of CO adsorbed in the sub-monolayer regime.

Molecules are a key part of the ISM, and within molecular clouds, where they act as coolants and can be used to trace physical conditions including temperature, hydrogen density and the age of a cloud. Simple interstellar molecules are necessary precursors to more complex prebiotic molecules, which are vital for the evolution of life [1]. Within the ISM, the rich gas phase chemistry leads mainly to unsaturated molecules. Saturated molecules are mostly formed on dust grain surfaces *via* the diffusive Langmuir-Hinshelwood mechanism. Hence, diffusion of reactants is a key process on ice mantles [1].

Amorphous solid water (ASW) is the dominant component of interstellar ices, with abundances around 1×10^{-4} with respect to the total H column density. This is equivalent to coverages up to 100 monolayers [2]. It is thought that interstellar H_2O is mainly amorphous in structure [2]. However, the specific morphology of amorphous interstellar H_2O ice is still not clear, especially when it comes to its porosity. Since H_2O is likely to be formed at the grain surface *via* chemical reactions rather than gas phase condensation, it is thought that the structure is similar in nature to that of ice grown by vapour deposition in the laboratory known as Amorphous

Solid Water (ASW). In laboratory experiments, vapour deposited H_2O ices are widely used as analogues for interstellar ice, as the growth can be controlled to obtain amorphous ices of various porosity [4]. The work presented in the chapter focuses on c-ASW and CSW. The structural complexity of solid water has given rise to a number of labels in literature for forms of solid water produced at a range of temperatures and under high and ultrahigh vacuum [5]. In the laboratory, H_2O is usually deposited onto solid surfaces at temperatures around 10 K and it is thought that the film grows *via* ballistic deposition [5]. The incoming H_2O molecules hit and stick to the surface, resulting in a low-density porous amorphous solid H_2O (p-ASW) [6] with short average O-O distance in the ice matrix. Warming of this H_2O ice to temperatures between 30 and 70 K results in collapse of the pores to form high-density, non-porous or compact amorphous solid H_2O (c-ASW). The phase change also sees an increase in the average O-O distance in the solid matrix [7]. Further annealing results in the formation of the cubic crystalline phase at temperature above 140 K. The normal hexagonal phase of ice is not observed at UHV as the ice evaporates before the $I_c \rightarrow I_h$ phase change. **Table 6.1** shows the different names for solid water phases upon deposition under low pressure conditions and the temperatures at which they occur.

Temperature	**< 80 K**	**80 - 120 K**	**120 – 160 K**	**> 160 K**
	Porous Amorphous	Compact Amorphous	Crystalline	Gas
	HAD p-ASW	LDA c-ASW np-ASW	I_c(cubic) I_h (hexagonal) CSW	

Table 6.1: An overview of the different names for solid water phases upon deposition in ultrahigh vacuum [5].

CO is also commonly detected in the solid phase in molecular clouds in the ISM [6, 8]. H_2O is observed in the IR *via* the O-H stretch absorption at 3.07 μm and CO is detected at 4.67 μm *via* the C-O stretching vibration. CO and H_2O typically make up around 90% of the icy mantles which accrete on the grains in dense clouds [8]. Hence understanding the physics and chemistry of H_2O and CO is vital in helping to build an understanding of the many roles played by these icy grains in the physical and chemical evolution of the clouds in which they are hosted. **Chapter 1** has highlighted the importance of ammonia (NH_3) and methanol (CH_3OH) in the

ISM and why they are of interest to the astrophysical community. NH_3 is a vital building block for biological molecules; along with being a valued condensable species in the Solar System. Methanol is the simplest organic molecule found in space, and the gateway to a rich solid-state organic chemistry in ices.

Binding energies of molecules to surfaces and pre-exponential factors for desorption are key quantities but have been derived for only handful of species. This leaves others with highly uncertain estimates of these kinetic parameters [9]. In some studies [10,11], the binding energies were estimated using the polarizability of the molecule or atom, as this provides an estimate of the strength of the van der Waals interaction with the bare grain surface. The work by Penteado *et al.* [9] highlights the effect uncertainties in binding energies have on astrochemical models of a dark molecular cloud using the rate equation approach. Additionally, in most models the diffusion barrier is obtained *via* the binding energy and this is linked to the onset temperature for surface reactions. Typically, diffusion barriers are estimated at 10% to 15% of the binding energy [12]. This will introduce additional uncertainty in models where the rates of surface processes are considered.

Under astrophysical conditions, for example in a hot core, the heating rate is around 1 K century^{-1} [13], which is much slower than values employed in laboratory TPD at around 0.1 K s^{-1}. Hence, by simulating the desorption profiles of the molecule-surface combinations in this work, it is possible to investigate whether surface type and coverage has an impact on the desorption characteristics on astrophysically relevant timescales [2]. The results from the study by Noble *et al.* [2] demonstrate that the molecules CO, CO_2, and O_2 desorb at different times and temperatures. The onset of desorption from ASW and aSiO_2 occurs almost at the same time for CO, CO_2 and O_2. However, desorption from CSW occurs at higher temperatures. This delay in desorption from crystalline surfaces would suggest that in regions where crystalline water dominates, *e.g.* in disc regions, the volatile species will not start to desorb from grain surfaces until significantly later times.

A number of studies have reported binding energies of CO [9, 14]. However, these experiments did not take into account the effects of water or any other substrate. Studies of CO deposited on water ice have demonstrated that CO is substantially

more strongly bound to water-dominated ices compared to pure CO ices. The work by Collings *et al*. [5] showed a 40% higher desorption energy for CO on low-density amorphous water ice compared to pure CO ice. The work by Fayolle *et al*. [15] has shown that CO desorption energies are greatly increased when molecules are desorbing from amorphous water ice surface compared to the pure CO ice as shown in **Figure 6.1**.

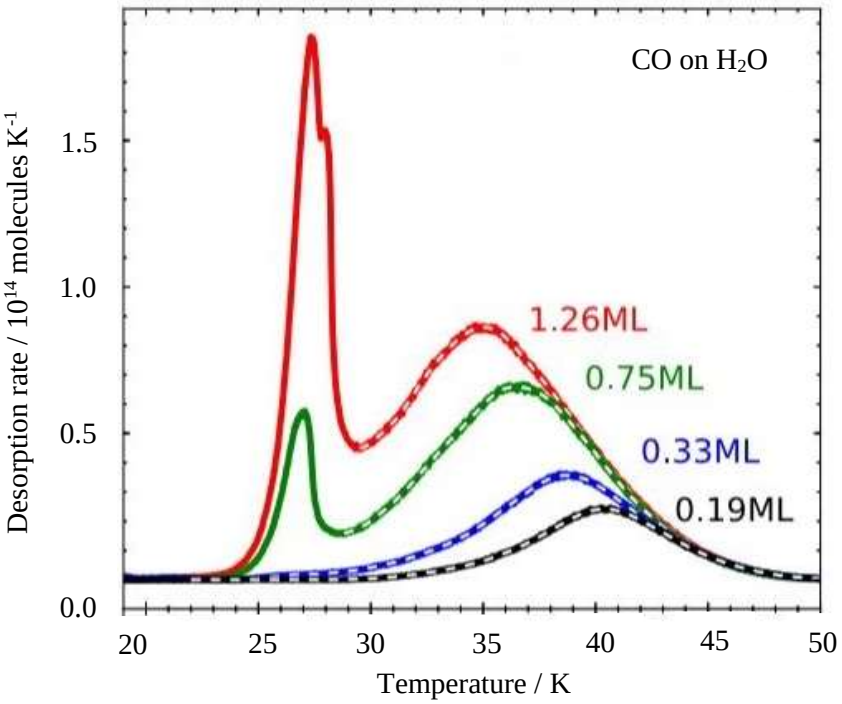

Figure 6.1: The TPD spectra for various coverages of CO from amorphous compact water (Reproduced from [15]).

From **Figure 6.1**, the maximum temperature for desorption (T_{max}) is around 37 K for 0.8 ML coverage for CO and desorption is complete at 49 K. The work of Noble *et al*. [2] reports T_{max} for sub-monolayer CO at around 52 K for CO molecules desorbing from amorphous water. The results from the study by Noble *et al.* [2] show that the desorption energies from crystalline ice are higher than those for the same species desorbing from amorphous water and amorphous silica. A possible reason for this trend is that the ordered structure of the crystalline water surface induces larger scale interactions on the adsorbed molecules. An alternative explanation is that the amorphous surface can impede the build-up of the normal monolayer-multilayer regimes on these surfaces. The work by Collings *et al*. [16] investigated grain model surfaces ($aSiO_2$ and H_2O) with small molecules (CO, O_2

and N_2). The molecules do not dissociate on silica at low temperatures. However, $aSiO_2$ presents a range of binding sites with a range of activation energies for desorption [16,17] as evinced by alignment of the TPD trailing edges (**Figure 2.16**). This indicates that the molecules are mobile enough to find the deepest, energetically most favourable binding sites on the $aSiO_2$ surface. Molecules found in the weaker binding sites desorb first, which results in desorption peak broadening. In the sub-monolayer regime, at the higher end of the binding energy distribution, this implies that the molecules will possess significantly enhanced surface lifetimes allowing the molecules to explore the grain surface more fully [16]. Given a dust grain temperature of 15 K [16], and increasing the binding energy of the sub-monolayer CO on $aSiO_2$ from 8 to 12 kJ mol^{-1}, will increase the lifetime on the surface from $2.3x10^7$ to above 10^{20} years. **Table 6.2** shows the E_{des} and ν for CO on $aSiO_2$ and various water surfaces for monolayer and multilayer coverages of CO. In the case of CO on $aSiO_2$, amorphous and crystalline water, CO wets all three surfaces [2], *i.e.* CO forms a complete monolayer before growth of the multilayer occurs. Non-wetting behaviour results in the formation of 3D islands on the surface (*e.g.* CO_2 on $aSiO_2$) [2].

(a)	**Surface**	ν_{des} **/ s^{-1}**	E_{des} **/ kJ mol^{-1}**	**Coverage**
	ASW (60 K)	$3.5x10^{16}$	11.8	Monolayer [18]
	c-ASW (100 K)	$1.0x10^{11}$	9.6 – 13.1	Monolayer [15]
	CSW (140 K)	$1.0x10^{12}$	11.1 – 8.4	Monolayer [2]
	Non-porous ASW (100 K)	$1.0x10^{12}$	7.2 – 10.7	Monolayer [9]
	$aSiO_2$ (18 K)	$1.0x10^{12}$	9.9 – 11.7 (0.06 ML) 10.7–12.2 (0.03 ML)	Monolayer [16]
	$aSiO_2$ (25 K)	$1.9x10^{13}$	12.5±0.63	Monolayer [19]
	$aSiO_2$ (18 K)	$1.0x10^{13}$	10 – 6	Monolayer [17]
	$aSiO_2$ (18 K)	$1.0x10^{6}$	11.8 – 7.2	Monolayer [2]

(b)	**Surface**	ν_{des} **/ molecules cm^{-2} s^{-1}**	E_{des} **/ kJ mol^{-1}**	**Coverage**
	ASW (120 K)	$7.1x10^{26}$	6.88±0.23	Multilayer [2]
	CSW (140 K)	$7.1x10^{26}$	7.06±0.46	Multilayer [2]
	$aSiO_2$ (18 K)	$7.1x10^{26}$	6.91±0.33	Multilayer [2]
	$aSiO_2$ (18 K)	$1.0x10^{26\pm1}$	7.30±0.30	Multilayer [16]

Table 6.2: Adsorption behaviour of CO on astrophysically relevant surfaces: (**a**) monolayer coverages and (**b**) multilayer coverages. The deposition temperatures are given in brackets.

The mobility of atoms, molecules and radicals on and in icy grain mantles controls ice restructuring, desorption and chemistry in astrophysical environments. Ices are dominated by H_2O and diffusion, on external and internal surfaces of H_2O-rich ices, is a vital process to constrain [20]. Diffusion on and in ices is vital for chemical evolution during star formation, since the ices are a major reservoir of volatiles and ice chemistry is the suggested pathway to both simple volatiles such as CH_3OH and complex organic molecules such as have been observed towards protostars. The efficiencies of the pathways, however, depend mainly on the mobility of the reactants on the ice surfaces and within the bulk of the ices. There have been until recently few laboratory constraints on the diffusion of molecules on top of or inside interstellar ices. The majority of astrochemical models hence parameterise surface and bulk diffusion barriers as fractions (30% - 80%) of the better understood molecular diffusion barriers [20] or as a fraction of the binding energy to the surface [12]. Typically surface diffusion is modelled as a hopping process between different potential minima with a specific barrier or a group of barriers. CO diffusion in H_2O has been the subject of a number of studies due to the interstellar relevance and effectiveness as a model system when evaluating various experimental approaches. The work by Oberg *et al.* [21] calculated a diffusion barrier for CO diffusion out of mixed H_2O-CO ices of 2.49±0.83 kJ mol^{-1} and Mispelaer *et al*. [22] found a barrier of 1.00±1.50 kJ mol^{-1} for CO diffusion through a thick H_2O ice film and into the gas phase. Karssemeijer *et al.* [1] calculated the diffusion of CO out of a CO:H_2O ice mixture through a thick amorphous ice layer and into the gas phase at 32 - 50 K and found a diffusion barrier of 2.49 ±1.41 kJ mol^{-1}.

The work of Karssemeijer *et al.* [1] has shown that for simulations of CO diffusion on amorphous H_2O there are two populations of CO binding sites; the first is described as a strong binding nanopore site and the other is referred to as a weak surface site. These have diffusion barriers of 7.72 and 0.03 kJ mol^{-1} respectively. At low temperatures, CO in strongly bound sites will be completely immobile.

6.2 Gas – Grain interactions

Gas-grain interactions play a vital role in the chemical evolution of the Galaxy. These processes involve the interaction of a chemical species with a solid surface and are governed by potential energy surfaces [14]. If the interaction involves simple electrostatics and dispersion, *e.g.* van der Waals interactions and hydrogen bonding rather than electron exchange, a shallow physisorption well is observed at long range and in this situation, the binding energy (E_b) is equal to the activation energy for desorption (E_{des}) in magnitude but opposite in sign, **Equation 1.**

$$E_b = -E_{\mathrm{des}} \qquad \textbf{(E1)}$$

The presence of a dynamical barrier associated with accommodation of the adsorbate and surface relaxation, E_{act}, which can be thought of as precursor-mediated adsorption, means **Equation 1** no longer holds and hence:

$$E_{\mathrm{b}} = E_{\mathrm{act}} - E_{\mathrm{des}} \qquad \textbf{(E2)}$$

In the first stages of star formation, nearly all the species accrete onto the grains in dense cold cores. The collapse of a cloud converts gravitational potential energy to kinetic energy, most of which would appear a heat unless radiated away. Thus, further into the star formation sequence, when hot cores are formed, the grains are warmed to temperatures such that molecules can start to desorb [23]. As some of these molecules are important coolants during star formation, it is vital to understand their thermal desorption. At temperatures below 300 K, the main coolant is CO, the CO molecules radiate readily in the millimetre and sub-millimetre wavelengths ranges [24]. Desorption is also important in developing models which can be used to determine the current and historical composition of astrophysical bodies including comets, planetary and interplanetary ices [5, 18, 19, 23, 24].

In order to characterise these astrophysical processes quantitatively, it is vital to understand the underlying molecular physics by observing interstellar ice analogues under laboratory conditions. A number of recent publications have shown that even for simple small molecules such a quantification is not a trivial task [4, 14, 25].

There has been a number of studies which have determined the adsorption energies and pre-exponential factors for small molecule desorption from a variety of surfaces *e.g*. graphene-covered Pt(111) as an analogue for carbonaceous surfaces, which are relevant to this problem.

Thermal desorption processes are described in terms of the Polanyi-Wigner Equation, where the rate of desorption, r_{des} is given as:

$$r_{\mathrm{des}} = -\frac{d\theta}{dt} = \nu\theta^{n} exp\left(-\frac{E_{\mathrm{des}}}{k_B T}\right) \quad \textbf{(E3)}$$

where ν is the pre-exponential factor, n is the desorption order, k_{B} is the Boltzmann constant and T is the temperature of the surface. A key assumption made when using the Polanyi-Wigner Equation for data analysis is that the monitored desorption signal is proportional to the rate of desorption. This is only true if the pumping speed of the UHV chamber is high enough to prevent accumulation of desorbed material in the chamber.

The pre-exponential factor is usually assumed to be of the same order of magnitude as the vibrational frequency of the adsorbate against the surface (10^{12} - 10^{13} s^{-1}) [9]. This is fine for small molecules with small adsorption energies. However, with larger and more strongly bound molecules, this value would be inappropriate [26].

Acharyya *et al*. [23] characterised the physical processes involved in the desorption of CO-O_2 ices and this in turn was used to simulate the behaviour of CO-O_2 ices under astrophysical conditions. The pre-exponential factor was approximated by a harmonic oscillator model, **Equation 4**, where ν is the pre-exponential factor for the adsorbed species, N_{s} is the number density, M is the mass of species and E_{b} is the binding energy [25,27].

$$\nu = \sqrt{\frac{2N_s E_b}{\pi^2 M}} \quad \textbf{(E4)}$$

This gives values for the pre-exponential factor around $10^{12} - 10^{13}$ s^{-1}.

Within a Transition State Theory framework, the pre-exponential factor, *v*, depends on the ratio of the partition function of the adsorbate in the physisorption well, and its partition function in the transition state on the path to desorption:

$$\nu = \frac{k_B T}{h}\frac{Q^{\ddagger}}{Q} \qquad \textbf{(E5)}$$

where Q is the partition function for the adsorbed state, $Q^{\ddagger}$ is the partition function for the transition state, k_B is the Boltzmann constant and h is the Planck constant. For weakly interacting species, $Q^{\ddagger}/Q$ is approximately to 1 and this results in ν being 10^{13} s^{-1}. In the case where the adsorption is strong and the adsorbate presents a number of internal degrees of freedom, this ratio can reach significantly larger values. For example, in the adsorption on graphite of functionalized alkanes, alcohols and ethers, ν values are found to be around 10^{19} s^{-1} [26].

Application of Transition State Theory to the Polanyi-Wigner Equation further reveals ν is related to the activation entropy for desorption, $\Delta^{\ddagger}S$ [27]:

$$\nu = \frac{k_B T}{h}\exp\left(\frac{\Delta^{\ddagger} S}{R}\right) \qquad \textbf{(E6)}$$

where R is the gas constant. $\Delta^{\ddagger}S$ is the change in entropy when reactants change from their initial state S^0, to the transition state, $S^{\ddagger}$.

$$\Delta^{\ddagger} S = S^{\ddagger} - S^0 \qquad \textbf{(E7)}$$

Hence, estimating the entropy of activation allows the pre-exponential factor to be calculated [26]. **Figure 6.2** illustrates two limiting situations. In the case of a tight transition state, the entropy of the transition state itself is reduced compared to that of the adsorbed molecule. While in a loose transition state situation, the transition state has extra degrees of freedom and hence higher entropy than the adsorbed molecule. Consequently, ν is typically greater than 10^{13} s^{-1} with a loose transition state and less than 10^{13} s^{-1} with a tight transition state [28].

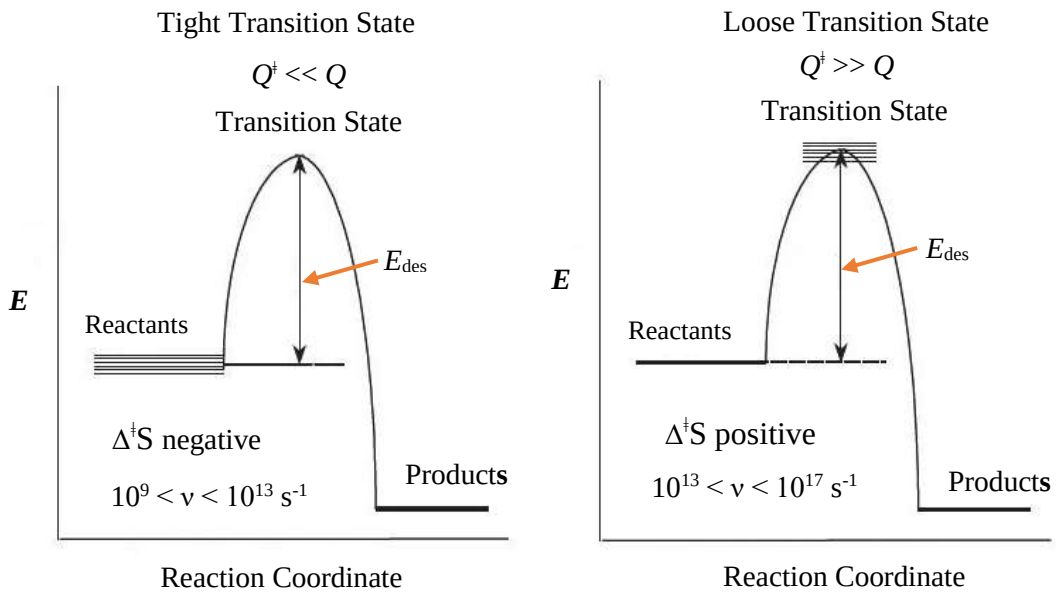

Figure 6.2: Illustrating the extremes of transition state (Reproduced from [28]).

In the neutral case, the entropy of the transition state hardly differs from that of the reactants in the ground state and this gives the standard pre-exponential factor of around 10^{13} s^{-1}. Thus, the influence of the entropy term potentially results in a range of possible pre-exponential factors from 10^9 to 10^{17} s^{-1} [28]. Furthermore, while the pre-exponential factor can vary with both coverage and temperature, it is taken to be constant with both temperature and coverage in most of the literature [27].

The work of Badan [27] illustrates the use of **Equation 6** by considering a completely mobile transition state and immobile adsorbed state. An estimate of the actual pre-exponential factor can be made using:

$$\nu = \frac{k_B T}{h} \exp\left(\frac{S^0_{gas}(T) - S^0_{gas,1\mathrm{D}-trans}(T) - S^0_{ad}(T)}{R}\right) \qquad \textbf{(E8)}$$

where S^0_{gas} is the gas phase entropy, $S^0_{gas,1\mathrm{D}-trans}(T)$ is the entropy associated with the translation perpendicular to the surface and $S^0_{ad}(T)$ is the entropy of the adsorbed state. *T* is the temperature and *R* is the gas constant. The work of Campbell et al. [29] has shown that the entropy correlation shown in **Figure 6.3** (**Equation 9**) can be used to make reliable estimates of the pre-exponential factor in rate constants for adsorbate reactions using Transition State Theory [29].

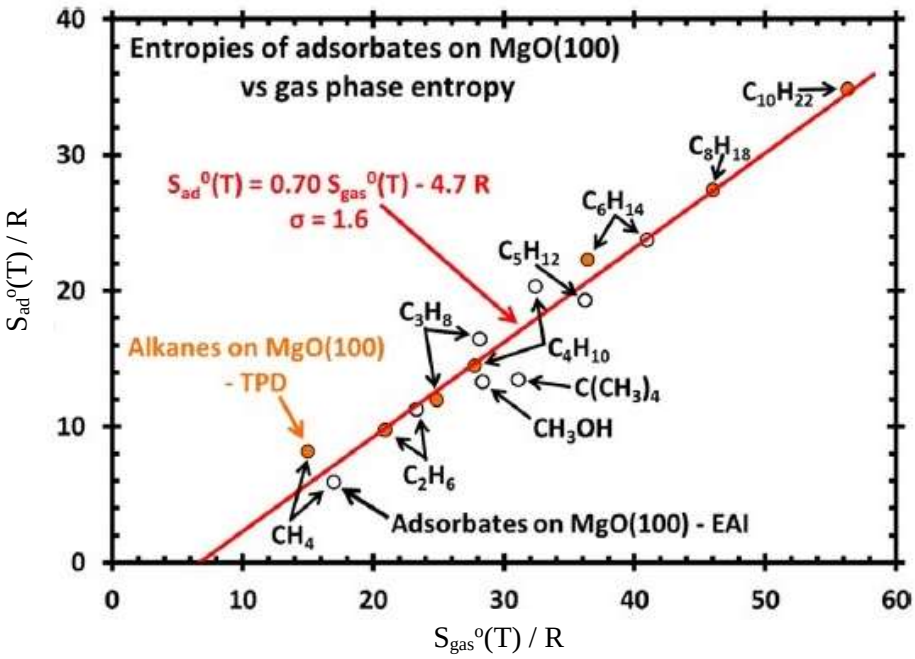

Figure 6.3: A plot of the standard entropies molecular adsorbates ($S_{ad}^0 = S_{gas}^0 + \Delta S_{ad}^0$) on MgO (100) smoke determined by equilibrium adsorption isotherm, plotted versus the standard entropy of the gas-phase molecule at the same temperature (Reproduced from [29]).

$$S_{ad}^0(T) = 0.7 S_{gas}^0(T) - 3.3R \qquad \textbf{(E9)}$$

taking non-activated molecular adsorption with attractive adsorbate-adsorbate interactions. Substituting **Equation 9** into **Equation 8** gives the pre-exponential factor as:

$$\nu_{des} = T k_B/h\ exp\left[\left(0.30 S_{\text{gas}}^0 + 3.3R - S_{\text{gas,1 D-trans}}^0\right)/R\right] \qquad \textbf{(E10)}$$

where $S_{\text{gas,1D-trans}}^0$ can be calculated using **Equation 11**:

$$S_{\text{gas,1D-trans}}^0 = (1/3)\left\{S_{Ar,298\ K}^0 + R\ ln\left[(m/m_{Ar})^{3/2}(T/298\ K)^{5/2}\right]\right\} \qquad \textbf{(E11)}$$

which is derived from the well-known Sackur-Tetrode and where m is the molar mass of the gas and m_{Ar} is molar mass of Argon, and $S_{Ar,298\ K}^0$ is the entropy of Ar gas at 1 bar and 298 K. In effect, the authors are estimating $S_{\text{gas,1 D-trans}}^0$ from a scaling of the Sackur-Tetrode one dimensional translational entropy of Ar at 298 K. This produces **Equation 11** as a working equation scaling back to the mass of Ar

and the surface temperature T. **Figure 6.4** shows a comparison of the predictions of **Equation 10** plotted *versus* experimental desorption pre-exponential factors for the molecules considered in [29]. The results in **Figure 6.4** show good agreement with experimental pre-exponential factors with standard deviation in log (ν / s^{-1}) of only 0.86 [29], confirming the validity of **Equation 10** for estimating the pre-exponential factor.

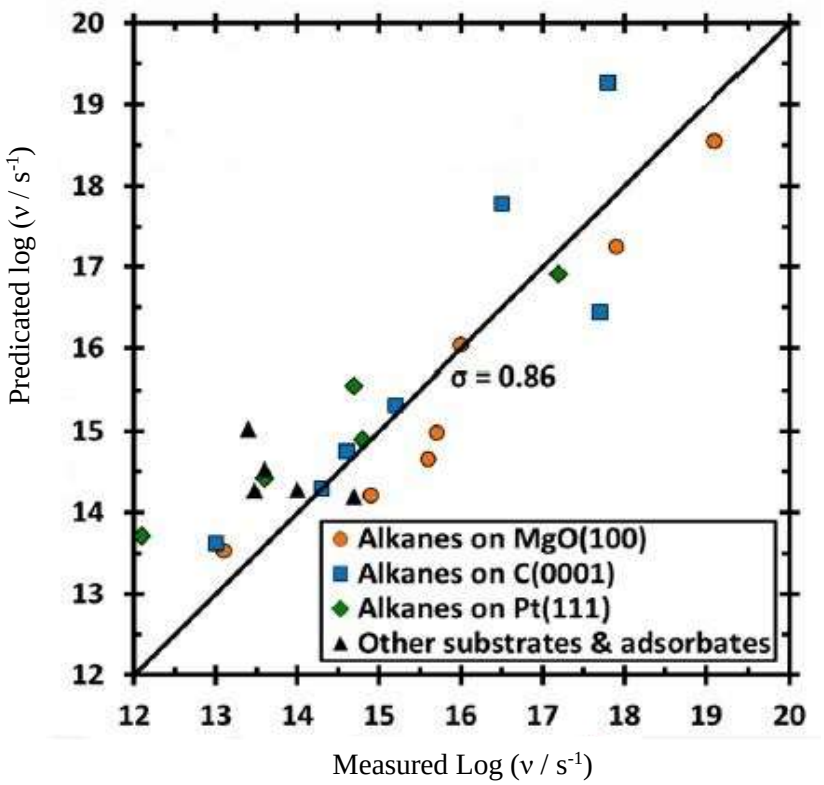

Figure 6 4: The pre-exponential factors for desorption of molecularly adsorbed species as predicted from gas-phase entropies using **Equation 10.** The data are for various molecules on oxide single crystals and for n-alkanes on graphite (0001) and Pt(111). The line shows the expectation based on **Equation 10**, which the data fit with a standard deviation in log(ν / s^{-1}) of 0.86 (Reproduced from [29]).

Table 6.3 summarises desorption parameters of CO from different surfaces. These data can be compared with the astrophysically relevant data in **Table 6.2**. The majority of *v* for CO desorption can be rationalized in terms of the Loose Transition State.

System	ν / s^{-1}	E_{des} / kJ mol^{-1}
CO / Co(0001)	$1.0X10^{14}$	118
CO / Ni(111)	$1.0X10^{15}$	130
CO / Ni(111)	$1.0X10^{17}$	155
CO / Ni(111)	$1.0X10^{15}$	126
CO / Ni(100)	$1.0X10^{14}$	130
CO / Cu(100)	$1.0X10^{14}$	67
CO / Ru(001)	$1.0X10^{16}$	160
CO / Rh(111)	$1.0X10^{14}$	134
CO / Ir(110)	$1.0X10^{13}$	155
CO / Pd(111)	$1.0X10^{15}$	147

Table 6.3: The table shows published values for experimental activation energies and pre-exponential factors for CO desorbing from a range of well-defined crystal surfaces [30].

6.3 Extracting Desorption Kinetics from TPD

6.3.1 Introduction

There are a number of methods which can be used to extract kinetic information from TPD data as discussed in **Chapter 4**. Redhead Analysis (RA, see **Chapter 4**) assumes that the kinetic parameters are independent of surface coverage and that desorption follows first order kinetics. In using this method, a good estimate of the pre-exponential factor is key to the analysis when determining E_{des}. Small variations in estimating the pre-exponential factor can result in significant errors in the E_{des} value. Leading Edge Analysis (LEA) is used to extract coverage and temperature dependent activation parameters. Arrhenius Analysis (AA) using a plot of $\ln(r)$ *versus* $1/T$ gives E_{des} and the pre-exponential factor. The accuracy of the analysis relies upon obtaining high-quality TPD data.

6.3.2 Extended Inversion Analysis

The Extended Inversion Analysis gives coverage-dependent desorption energies by applying the Polanyi-Wigner Equation to a set of TPD data. This method was first presented by Dohnalek *et al.* [31] for CO on the Mg(100) surface. However Tait *et al.* [32] have proposed an inversion optimization method that produces accurate results when multiple desorption features are present in the TPD spectra. Complex desorption traces consist of multiple peaks and shoulders and they have been

interpreted in terms of a set of physically and chemically distinct binding sites each having a characteristic desorption activation energy [33].

Extended Inversion Analysis has been used in a number of studies to determine the optimised pre-exponential factor and the coverage-dependent desorption energy, $E_{des}(\theta)$ [32, 34, 35]. The analysis begins with the Polanyi-Wigner Equation which is rearranged to give the coverage dependent desorption energy, $E_{des}(\theta)$. This simple processes is outlined in the sequence below:

1. Define a pre-exponential factor for a set of experimental TPD data. Typically, values in the range 10^7 to 10^{21} s^{-1} are used as a starting point for the inversion analysis.

2. The analysis of the TPD data is done *via* direct inversion of the Polanyi-Wigner equation where the desorption rate is given by:

$$r_{\mathrm{des}} = -\frac{\mathrm{d}N_{\mathrm{ads}}(t)}{\mathrm{d}t} = \nu N_{\mathrm{ads}}(t)^n e^{-E_{\mathrm{des}}(N_{\mathrm{ads}})/k_B T} \qquad \textbf{(E12)}$$

where T is the temperature, $E_{des}(N_{ads})$ is the desorption activation energy, k_B is Boltzmann constant, ν is the pre-exponential factor and n is the desorption order. The assumption is made that ν is coverage independent and **Equation 12** can be rearranged to give a coverage dependent, $E_{des}(N_{ads})$

$$E_{\mathrm{des}}\big(N_{\mathrm{ads}}(t)\big) = -k_{\mathrm{B}} T \ln\left(\frac{\frac{dN_{\mathrm{ads}}(t)}{dt}}{\upsilon N_{\mathrm{ads}}(t)^n}\right) \qquad \textbf{(E13)}$$

Equation 13 is applied to the experimental TPD data, assuming the constant pre-exponential factor and that desorption is from sub-monolayer coverages and hence n is 1. The assumption of a constant pre-exponential factor is somewhat subjective as the coupling of ν and E_{des} would allow the coverage dependence to be modelled mathematically by either variable. A variation of the pre-exponential factor with coverage can occur if the partition function of the adsorbate varied greatly in different adsorption sites on the surface or as result of adsorbate-adsorbate interactions. The energy will vary with coverage as various adsorption sites are

explored. **Figure 6.5** shows the coverage dependent activation energy for desorption, E_{des}, curves of 2 ML TPD for CH_4 from ASW with pre-exponential factors ranges from 10^{13} to 10^{17} s^{-1} from [18].

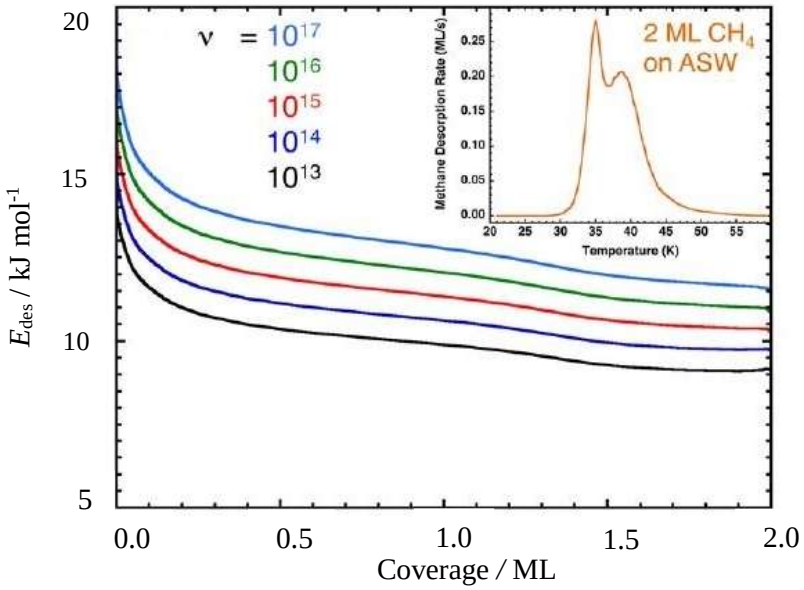

Figure 6.5: Coverage dependent E_{des} obtained by inverting TPD of 2 ML of CH_4 on ASW using ν from 10^{13} to 10^{17} s^{-1}. The inset shows the 2 ML CH_4 TPD data used in the inversion analysis (Reproduced from [18]).

3. Simulations of the experimental data are carried out using a FORTRAN TPD simulation code. The code takes the initial number of adsorbed species on the surface, $N_{ads}(0)$, experimental time and temperature as inputs into the calculations. For each time interval, *i.e.* between t and $t + \Delta t$, the desorption rate is calculated by using the Polyani-Wigner Equation at the temperature $T(t)$ using a fitted functional form for $E_{des}(N_{ads})$ derived from inversion of the experimental TPD data. The change in N_{ads} in the interval Δt is then calculated using that desorption rate. The process is repeated for successive values of t. The output of the code is the original data plus the desorption rate and the calculated surface concentration at each time step. **Chapter 5** reports the FORTRAN code being used to simulate CO TPD profiles in this work [36].

4. The quality of the fit of simulated TPD data to that of the experimental TPD data is defined by calculating χ^2:

$$\chi^2 = \sum_{N_{ads}} \sum_{t} \left[r_{des,obs}(N_{ads}, t) - r_{des,calc}(N_{ads}, t) \right]^2 \qquad \textbf{(E14)}$$

between the simulated and experimental TPD curves as a function of the pre-exponential factor. A plot of χ^2 *versus* pre-exponential factor is constructed and the minimum is calculated from the plot where the solid black line (black) is a quadratic fit to the χ^2 points [18]. This process is repeated using a new value of the pre-exponential factor until the value that best fits the experimental data is achieved. **Figure 6.6** illustrates this using desorption of CH_4 from ASW [18].

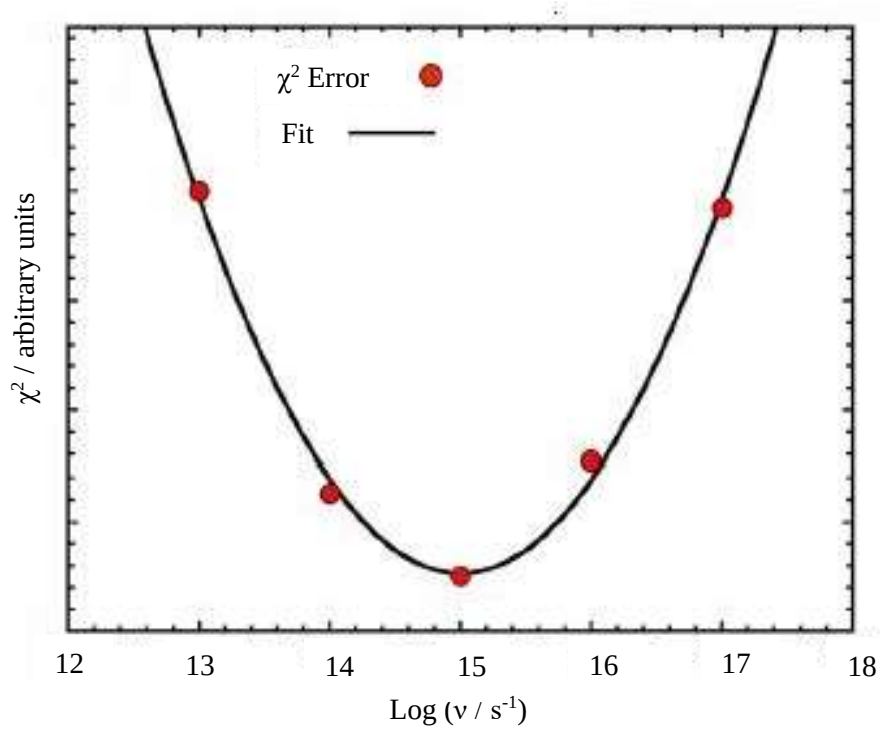

Figure 6.6: The χ^2 (solid red circles) *versus* log(*v*) of the pre-exponential factor for CH_4 desorbing from ASW. The minimum of χ^2 gives the best fit *v* of 9.8×10^{14} s^{-1} (Reproduced from [18]).

5. Finally, the TPD data are simulated using the optimised pre-exponential factor. This is then shown in **Figure 6.7** for desorption of CH_4 from ASW [18].

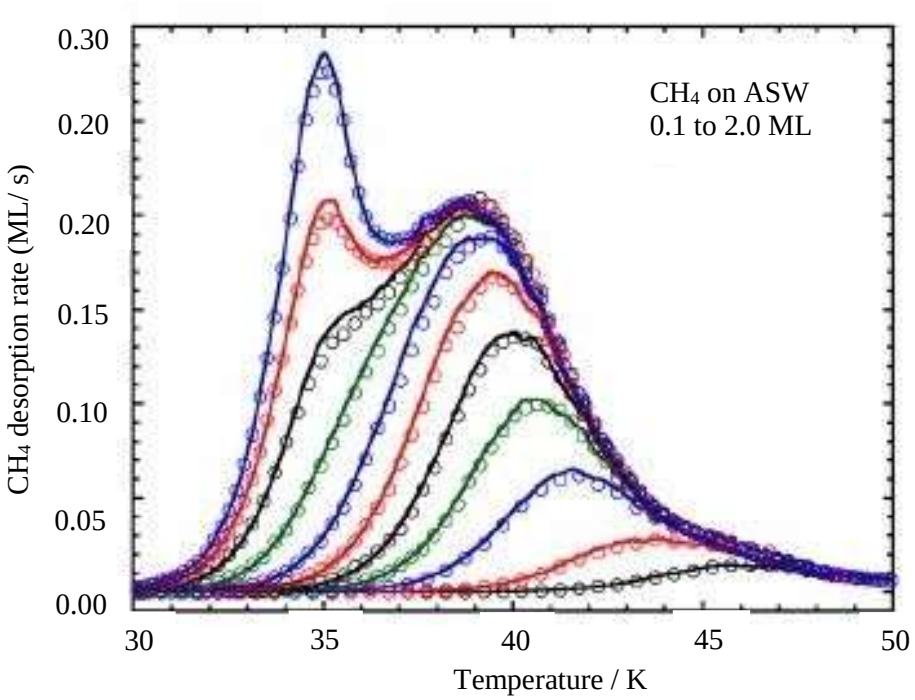

Figure 6.7: A comparison of the experimental data (open circles) and simulated (lines) TPD spectra for 0.7 ML CH_4 coverages 0.1-2.0 ML on ASW (Reproduced from [18]).

Figure 6.8 presents a flow chart summarising the Extended Inversion Analysis used in this work.

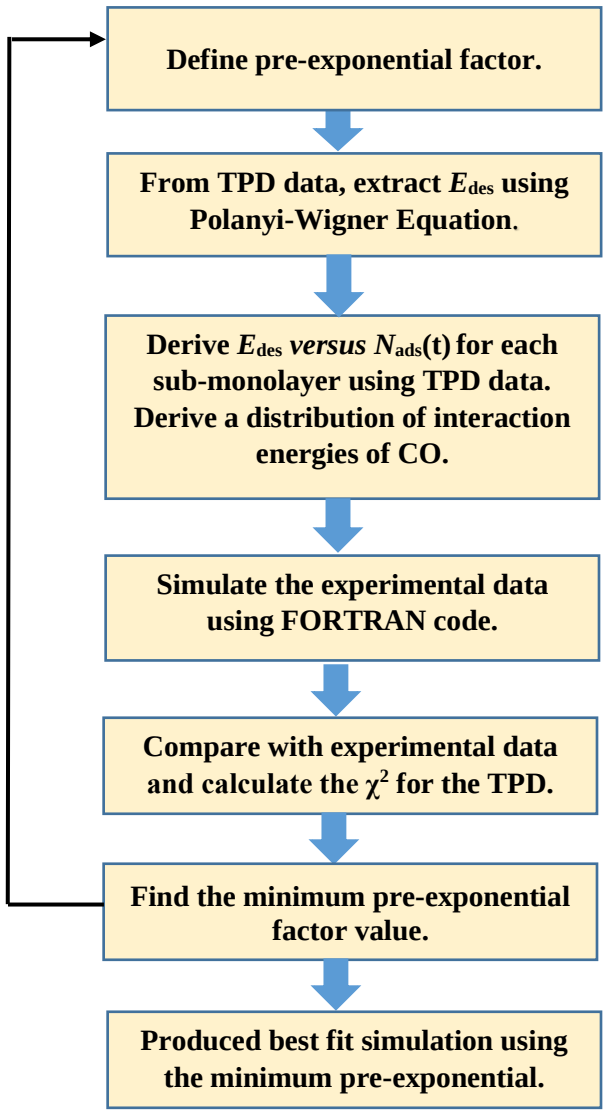

Figure 6.8: Summary of the Inversion process used in analysis of the TPD data in this chapter.

6.4 Experimental

The apparatus used for the experiments is described in **Chapter 2** and only brief details are given below. All the experiments are carried out in an UHV chamber with base pressure of 1×10^{-10} mbar. The deposition of each species is reported as exposures in units of L (1 L ≡ 1×10^{-6} mbar s) where the pressure is determined by

an ion gauge. The surface which is used in these experiments consists of a copper substrate, which is coated with around 300 nm amorphous silica ($aSiO_2$) and is mounted on a closed-cycle helium cryostat. Details of the CO on $aSiO_2$ experiments are discussed in **Chapter 4**. The structure of CO on c-ASW (de-ionised water), CSW (de-ionised water) and CH_3OH (Sigma-Aldrich, 99.9%) and NH_3 (Sigma-Aldrich, 99.99+%) films is shown in **Figure 6.9** and is discussed below:

1. CO on c-ASW and CSW: The water is purified *via* freeze-pump-thaw cycles. The c-ASW experiments were carried out by holding the sample at 100 K then dosing 200 L of H_2O. Then subsequent CO layers (1 to 25 L) are deposited at base temperature (16 K). After each layer is deposited, TPD is carried out. This process is repeated for CSW water, where the sample was held at 140 K during deposition.

2. CO on CH_3OH: CH_3OH is purified *via* freeze-pump-thaw for cycles. Initially a coverage of 200 L of amorphous CH_3OH is deposited at base temperature (16 K) onto the $aSiO_2$ substrate [42]. The dosing lines were pumped out and varying coverages of CO (1 to 25 L) were deposited in order to establish the monolayer and the multilayer. The dosing is carried out *via* background position *via* a rear located leak valve. After each coverage of CO, TPD is carried out by applying a linear heating ramp. The sample position is optimised to achieve the best QMS signal. Temperatures are reported with a precision ±0.5 K.

3. CO on NH_3: a thick layer of amorphous NH_3 (1,000 L) is deposited onto $aSiO_2$ layer at base temperature [42]. The dosing line is pumped out and purged using CO. Varying coverages of CO (1 to 15 L) are then deposited onto the NH_3 at base temperature, in order to establish the monolayer and the multilayer. The dosing is carried out *via* background position *via* a rear located leak valve. After each coverage of CO, TPD is carried out by applying a linear heating ramp. The sample position is optimised to achieve the best QMS signal. Temperatures are reported with a precision ±0.5 K.

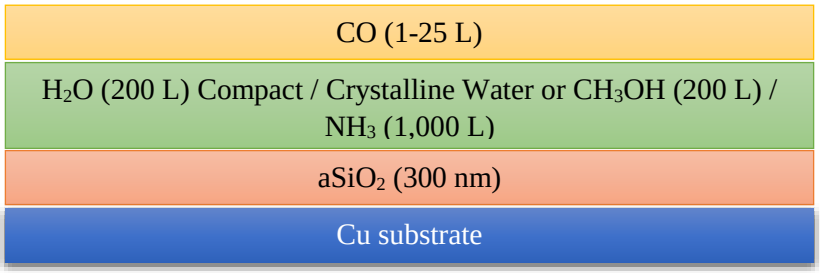

Figure 6.9: Shows the structure of the CO on H_2O, CH_3OH (compact and crystalline) films and NH_3. The experiments are carried out by depositing water at 100 K compact or 140 K crystalline water on the $aSiO_2$ layer. This is then followed by depositing CO.

6.5 Results and Discussion

The interaction of CO with a range of astrophysical surfaces has been investigated using TPD. This will allow a comparisons to be made of how CO interacts with these various astrophysically relevant surfaces. Firstly, the CO on $aSiO_2$ data are reviewed again to derive an optimized pre-exponential factor using the Extended Inversion Analysis. This is followed by investigation of CO desorbing from various astrophysically relevant surfaces using TPD, starting with c-ASW, then looking at CSW, CH_3OH and finally NH_3. The Extended Inversion Analysis is used to determine the coverage dependent activation energies for desorption and ν in each case.

6.5.1 CO on $aSiO_2$

Chapter 5 investigated the interaction of CO on $aSiO_2$ and presents an Inversion Analysis of the TPD using a ν of 1.00×0^{12} s^{-1}, which is typical for the analysis of physisorbed small molecules. The results presented below show analysis of the same TPD data using the Extended Inversion Analysis (**Section 6.3**) in order to find the optimised pre-exponential factor and E_{des} coverage dependence. This will demonstrate and show the importance of using the optimised pre-exponential factor for analysis of TPD spectra, rather than just using the typical value for small molecules. **Figure 6.10** shows the χ^2 error between the experimental and simulated TPD spectra for sub-monolayer coverages *versus* logarithm of the pre-exponential factor used in the Extended Inversion Analysis. The solid line is a polynomial fit to the points and this gives, at the minimum value of χ^2, a ν of $1.74^{+0.75}_{-0.53} \times 10^{21}$ s^{-1}.

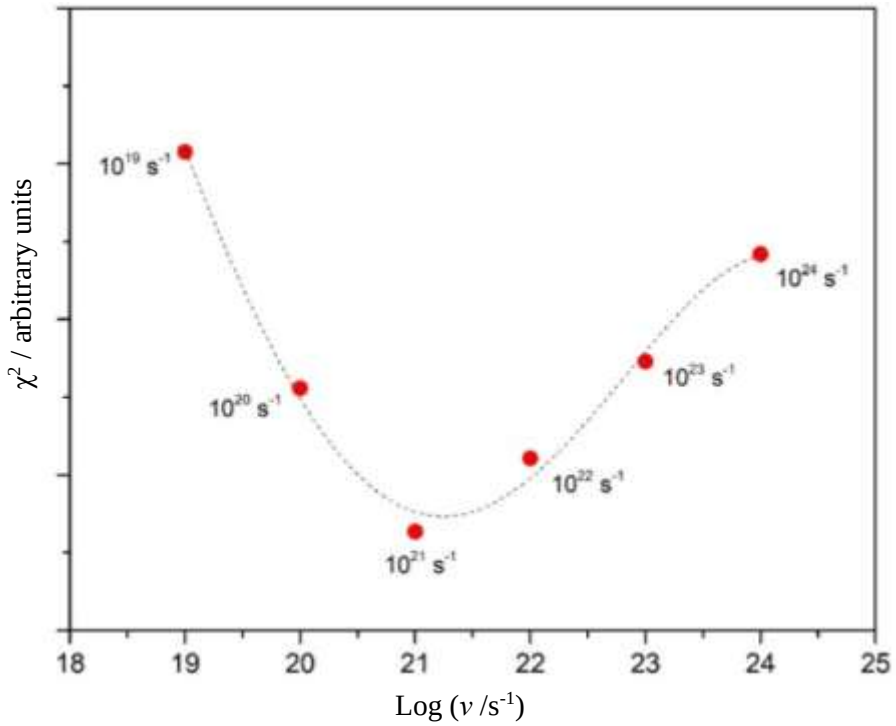

Figure 6.10: The χ^2 between experimental and simulated TPD of CO from $aSiO_2$ for all initial coverages *versus* logarithm of the pre-exponential factor used in the Extended Inversion Analysis. The dashed line in this figure is fourth-order polynomial fit to χ^2 and yields a minimum at a value of 21.24±0.16. A number of different low order polynomial fits were tried. However, the fourth order polynomial proved to give the best fit for the experimental data. Hence, the optimised value of ν is $1.74^{+0.75}_{-0.53} \times 10^{21}$ s^{-1} .

Figure 6.11(a) shows the E_{des} as function of coverage (θ) for sub-monolayer coverages desorbing from $aSiO_2$ derived using the optimised ν of $1.74^{+0.75}_{-0.53} \times 10^{21}$ s^{-1} and in comparison to **Figure 6.11(b)** that derived using 1.00×10^{12} s^{-1}. It can be seen that using a ν of 1.00×10^{12} s^{-1}, as is typical for physisorbed small molecules, results in narrower distribution of interaction energies for CO with the $aSiO_2$ surface (6 – 12 kJ mol^{-1}) in comparison to that obtained using the optimised value of ν (11 – 20 kJ mol^{-1}). This clearly highlights the need to determine ν from the experimental TPD data rather than assuming a value ν of 10^{12} or 10^{13} s^{-1} as currently used in literature. A question arises which analysis method is correct when calculating the distribution of E_{des}?. Both methods are basically derived from the same rate of desorption data. Only independent verification of the E_{des} or ν by other means would confirm which correct analysis is correct.

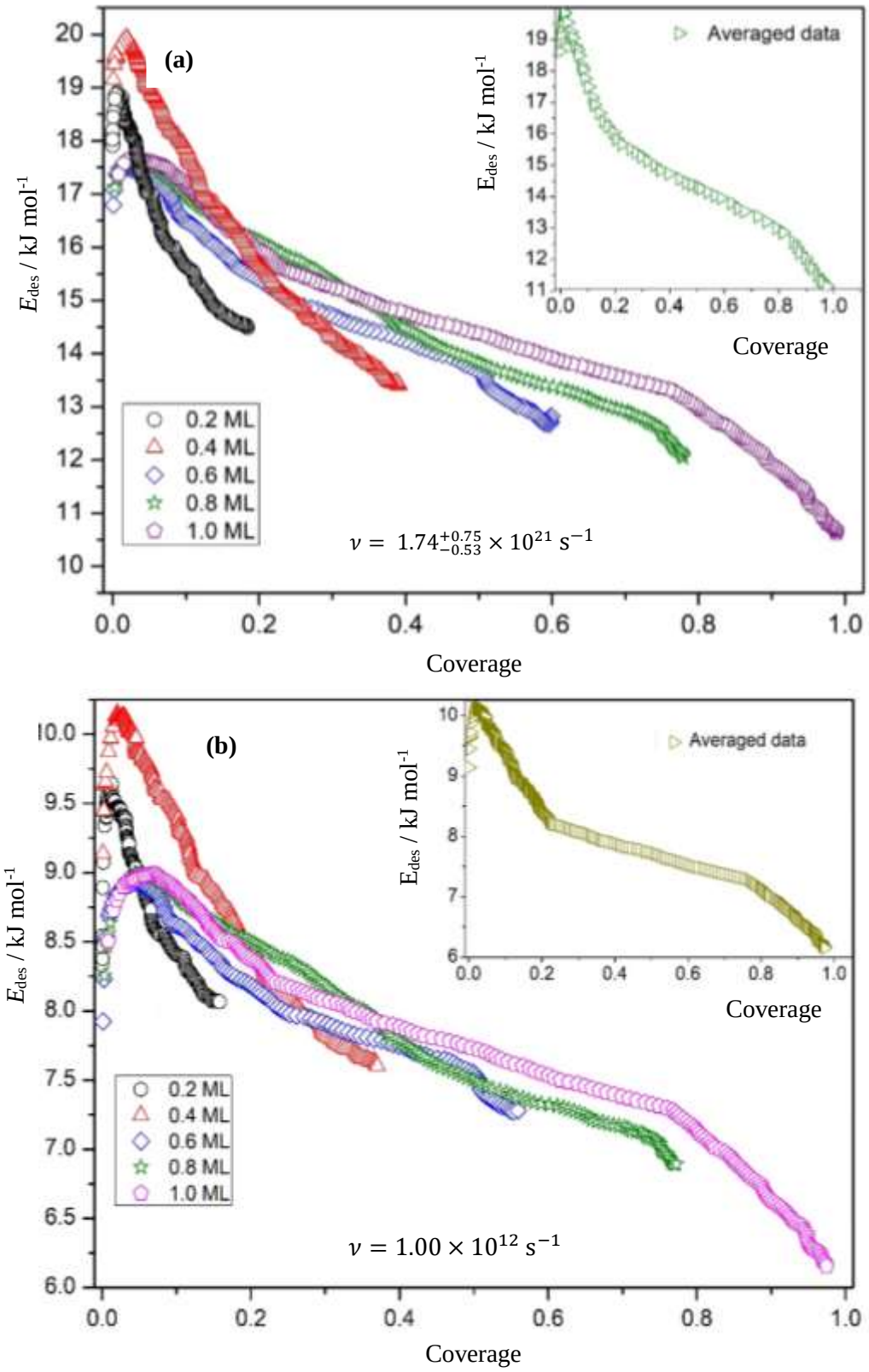

Figure 6.11: **(a)** E_{des} *versus* coverage for sub-monolayers of CO derived using ν of $1.74^{+0.75}_{-0.53} \times 10^{21}$ s^{-1} and (**b**) E_{des} *versus* coverage for sub-monolayers of CO calculated using ν of $1.00X10^{12}$ s^{-1} as in **Chapter 5** [17]. The inset contains the averaged data.

6.5.2 CO on c-ASW

Up to 25 L exposures CO were deposited on c-ASW on the aSiO_2 substrate at 18 K. This allows the identification of the exposure necessary to generate a coverage of a monolayer. Using a monolayer or less ensures that only CO-c-ASW interactions are investigated rather than CO-CO interactions as in case of multilayer films. Using the QMS, CO dosing was monitored at m/z = 12, 14 and 28 m_u. Consecutive TPD experiments from 1 to 25 L were carried out on the same day. **Figure 6.12** and **6.13** shows TPD traces for CO desorbing from c-ASW for coverages 10 to 25 L and 1 to 9 L recorded on m/z of 28 m_u. Both the low and high coverages have a rising background at around 42 K, which is labelled **A**.

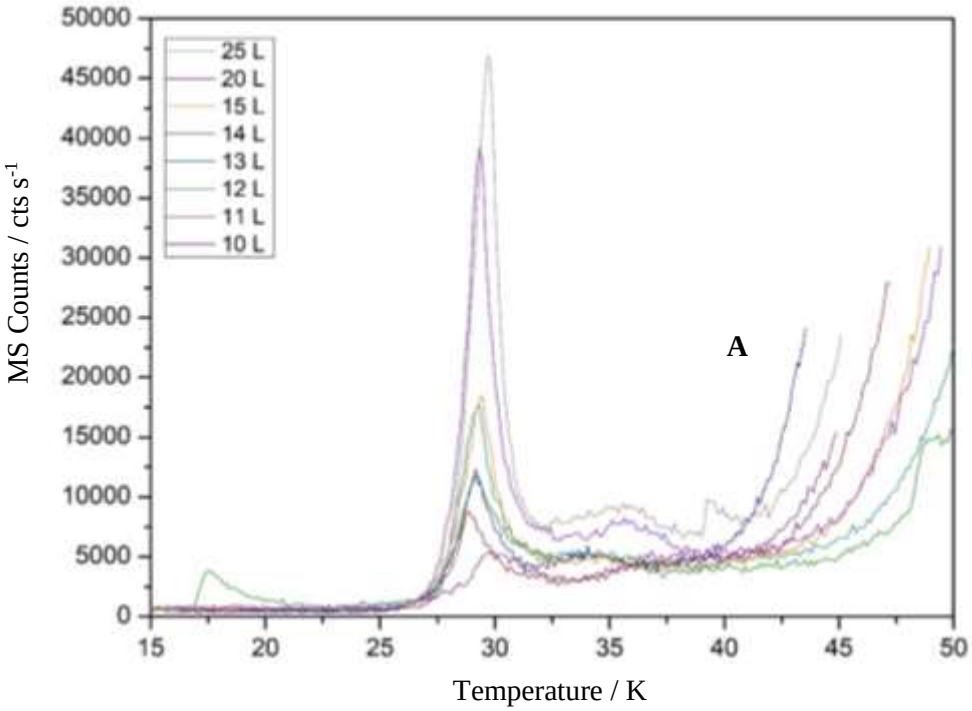

Figure 6.12: TPD traces for CO desorbing from c-ASW for coverages 10 to 25 L, recorded on m/z of 28 m_u. The data has a rising background, labelled A, which is removed in order to use in the data in the Extended Inversion Analysis.

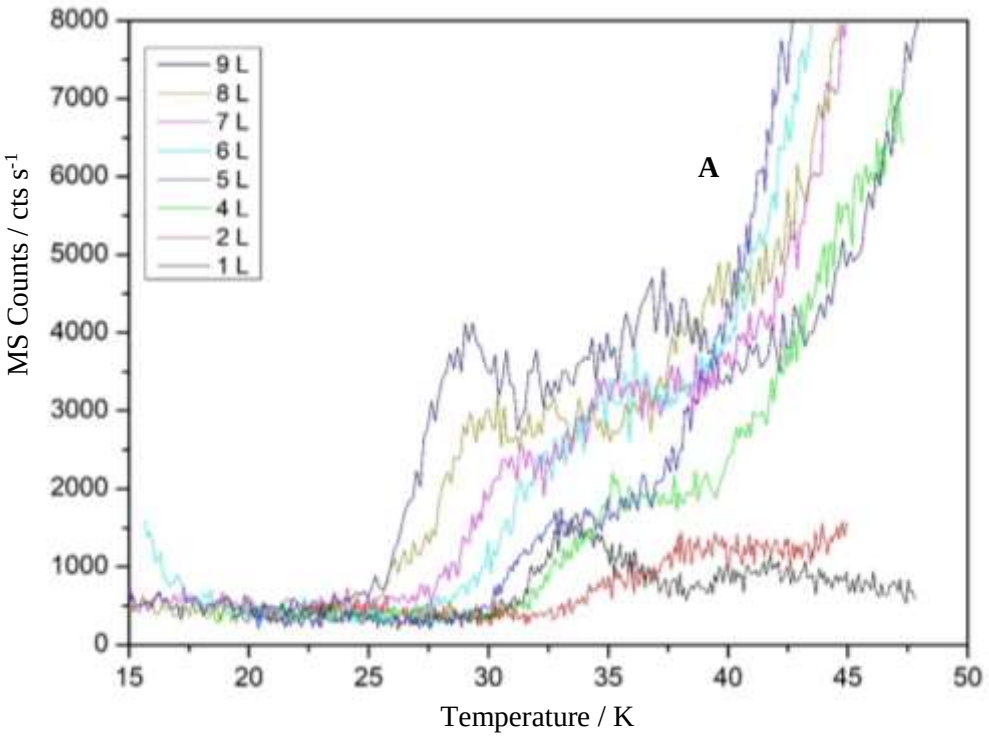

Figure 6.13: TPD traces for CO desorbing from c-ASW for coverages 1 to 9 L, recorded on m/z of 28 m_u. The data has a rising background labelled A, which is removed in order to use in the data in the Extended Inversion Analysis.

In order to remove the background from the experimental TPD spectra, data are selected from regions marked **A** and **B** as shown in **Figure 6.14**. The data is combined and fitted to an exponential function (**Equation 15**), which is then subtracted from the experimental data. The exponential function is used because desorption of the thick film on the cold finger is a multilayer desorption which is know from previous work to have an exponential leading edge. **Figure 6.15** shows the result of this process.The same process was also used in analysing the TPD data for CO from CSW, CH_3OH and NH_3 data.

$$A_1 \times exp^{(T/T_1)} + Y_o \qquad \textbf{(E15)}$$

where A_1, T_1,Y_o are fitting parameters obtained from fitting **Figure 6.15b** with exponential function **Equation 15** and T is the experimental temperature value.

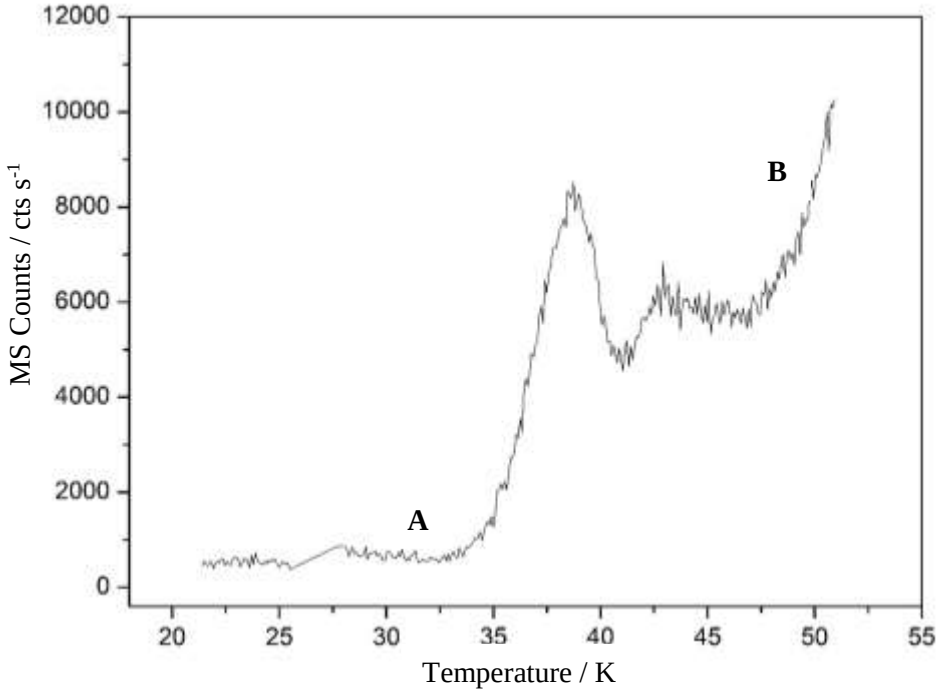

Figure 6.14: Raw TPD spectra for 14 L CO on c-ASW. The regions A and B are used to define the rising background.

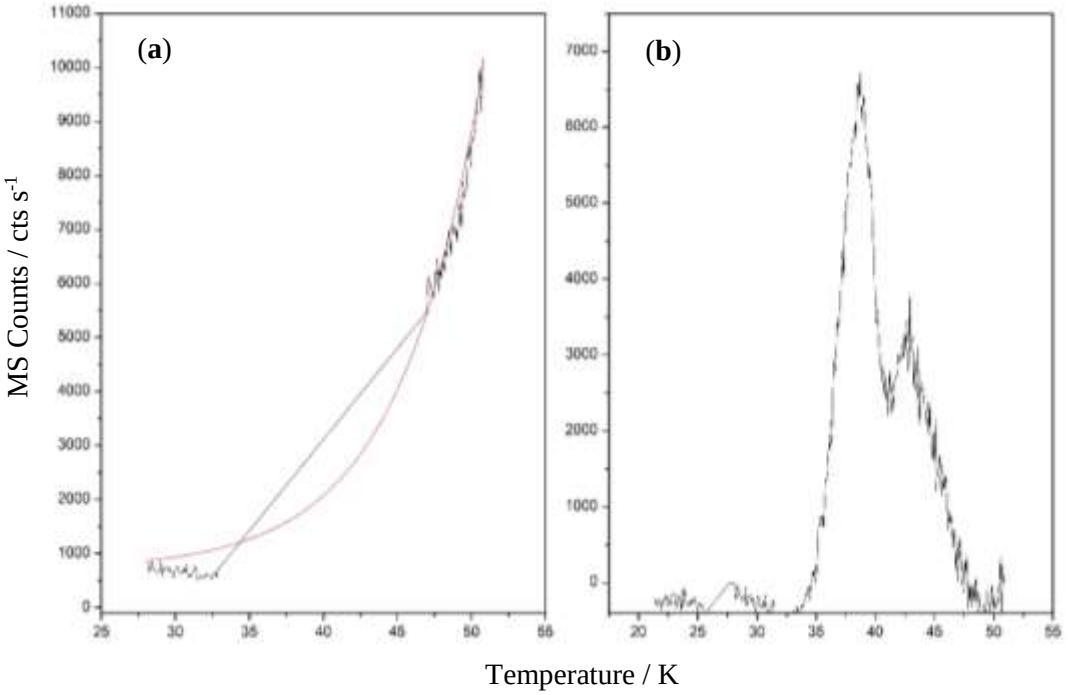

Figure 6.15: Removing the rising background from the experimental TPD data: (**a**) results of fitting an exponential function to data regions A and B in **Figure 6.14**; (**b**) shows 14 L CO on c-ASW TPD data from which the rising background has now been removed.

Figure 6.16 shows the TPD data for 1 to 25 L of CO on c-ASW, after correcting the rising background as shown in **Figure 6.12** and **6.13**. The sub-monolayer

coverages show common trailing edges and a reducing T_{max} with increasing coverage which is characteristic of first order kinetics with a distribution of binding energies.

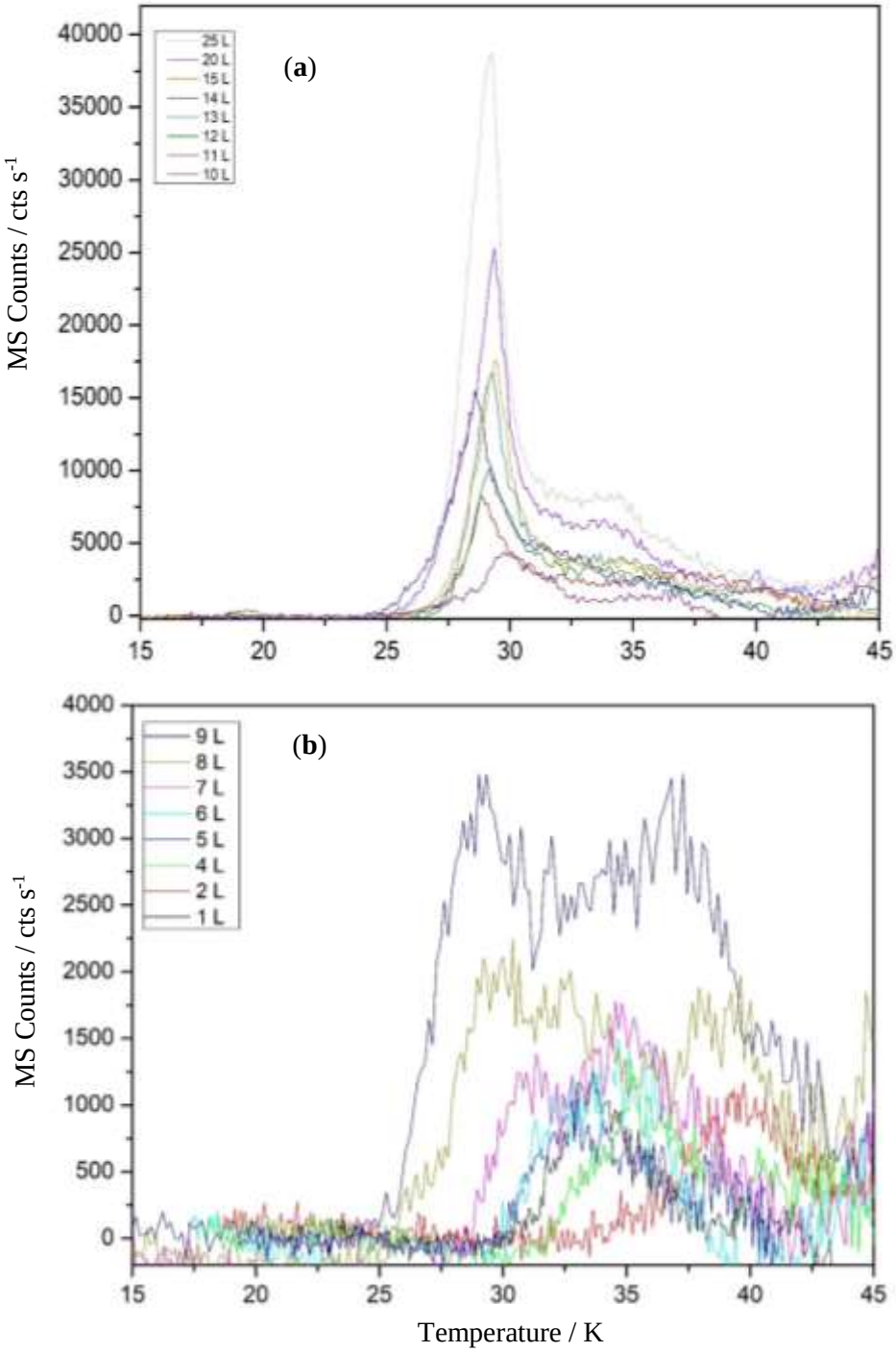

Figure 6.16: TPD data for CO on c-ASW for coverages of 1 to 25 L after correcting for the rising background: (**a**) multilayer 10 to 25 L coverages and (**b**) sub-monolayer 1 to 9 L coverages.

The CO desorption starts around 25 to 33 K and peaks around 30 to 35 K, depending on the coverage. CO fully desorbs around 38 K depending on the coverage. Alignment of the TPD trailing edges is noted up to an exposure of around 9 L. Above this exposure we begin to see evidence of multilayer growth in alignment of the leading edges. Hence, we identify 9 L as the exposure that produces a single monolayer. The alignment of the trailing edges at low exposures would indicate a distribution of binding site energies and that the adsorbates have enough mobility prior to desorption to find the highest energy binding sites. The monolayer TPD peaks on c-ASW at around 34 K (**Figure 6.13**). This occurs at slightly higher temperature than on $aSiO_2$ (**Figure 5.9**, **Chapter 5**). This would indicate that the interaction of CO with $aSiO_2$ is weaker than with c-ASW. Extended Inversion Analysis was carried out on the CO from c-ASW TPD data as described in **Section 6.2** using the corrected TPD data (**Figure 6.16**). **Figure 6.17** shows the χ^2 between the experimental and simulated TPD spectra for sub-monolayer coverages *versus* logarithm of the pre-exponential factor used in the Extended Inversion Analysis. The solid line is a fit to the points and this gives, at the minimum of χ^2, a value of ν of $2.57^{+1.04}_{-1.21} \times 10^{15}$ s^{-1}.

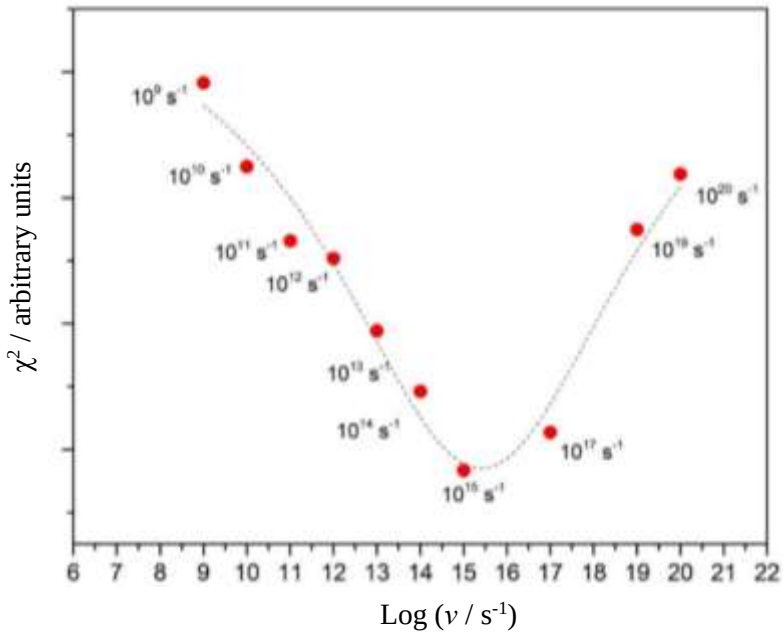

Figure 6.17: The χ^2 between the experimental and simulated TPD CO for c-ASW for all initial coverages *versus* logarithm of the pre-exponential factor used in the Extended Inversion Analysis. The dashed line in this figure is PsdVoigt1 fit to χ^2 and yields a minimum at a value of 2.57±0.28. Hence, the optimised value of ν is $2.57^{+1.04}_{-1.21} \times 10^{15}$ s^{-1}.

Figure 6.18 shows the plot of E_{des} against coverage for each sub-monolayer coverage of CO derived from the experimental data presented in **Figure 6.16** using the best fit value of *v*. The averaged data is shown in the inset and is used to represent the distribution of interactions energies of CO molecules with the c–ASW surface. In **Figure 6.18**, the highest binding energy is around 12.5 kJ mol^{-1} and available at the lowest coverages. The binding energy goes down to 9.5 kJ mol^{-1} at higher coverages. These values are in line with the sub-monolayer values reported by Fayolle *et al*. [15].

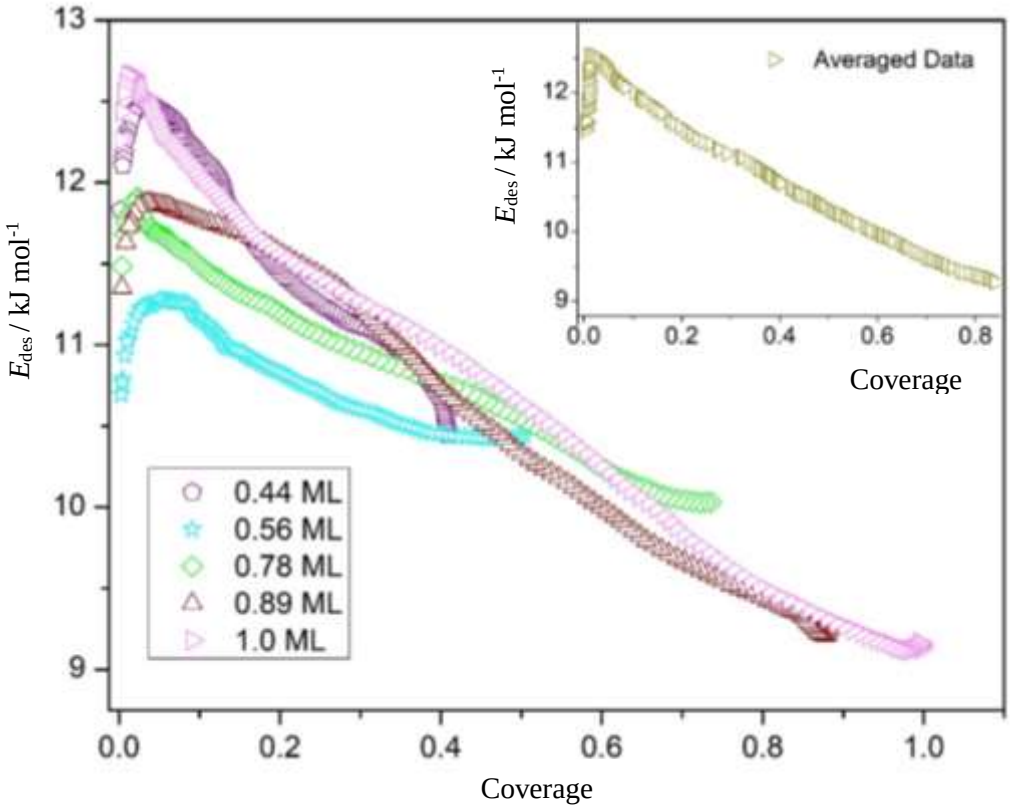

Figure 6.18: E_{des} *versus* coverage for CO sub-monolayers adsorbed on c-ASW and the inset shows the averaged data. The plots were obtained using the optimised ν of $2.57^{+1.04}_{-1.21} \times 10^{15}$ s^{-1} and the inset contains the averaged data.

Figure 6.19 shows some of the simulated and experimental TPD produced using the optimised *v* value of $2.57^{+1.04}_{-1.21} \times 10^{15}$s^{-1} and the E_{des} distribution inset in **Figure 6.18**. The simulated TPD profiles fit the experimental data reasonably well.

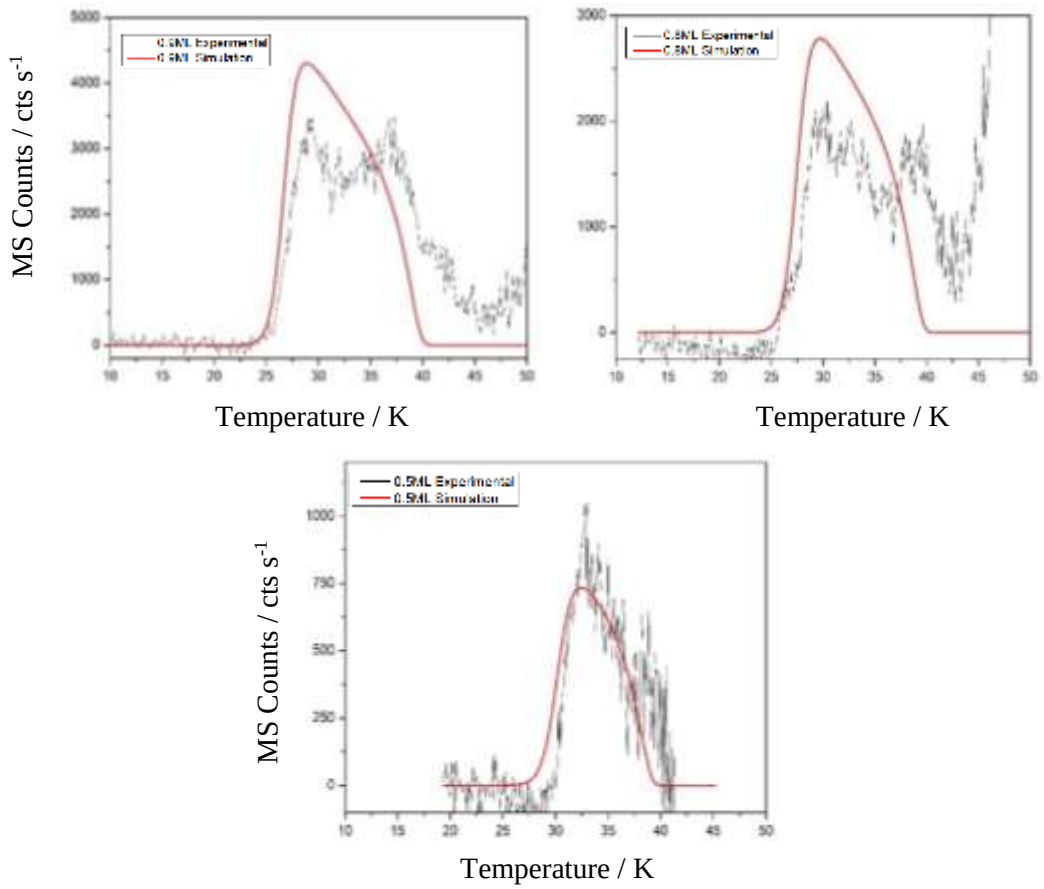

Figure 6.19: A comparison of the experimental (black) and simulated (red) TPD data for sub-monolayer coverages of 0.9 to 0.5 ML CO on c-ASW. The simulated data were obtained using a pre-exponential factor of $2.57^{+1.04}_{-1.21} \times 10^{15}$ s^{-1} and the $E_{des}(\theta)$ distribution presented in the inset in **Figure 6.18**.

6.5.3 CO on CSW

Up to 25 L exposures of CO were deposited on CSW on the $aSiO_2$ substrate at 18 K. CO dosing was monitored using the QMS at *m/z* = 12, 14 and 28 m_u. Again this, allows the identification of the exposure necessary to generate a coverage of a monolayer. Using a monolayer or less ensures that only CO-CSW interactions are investigated rather than CO-CO interactions in case of multilayer films. Consecutive TPD experiments from 1 to 25 L were carried out on the same day. **Figures 6.20** and **6.21** show TPD traces for CO desorbing from CSW for coverages 10 to 25 L and 1 to 9 L, recorded on *m/z* = 28 m_u . Both the low and high coverages have a rising background after 42 K which is labelled **A** and as previously observed in the c-ASW TPD data. This has to be removed in order to use the TPD data in the Extended Inversion Analysis. Removal was done using the process set out for analysing the CO on c-ASW in **Section 6.5.2**.

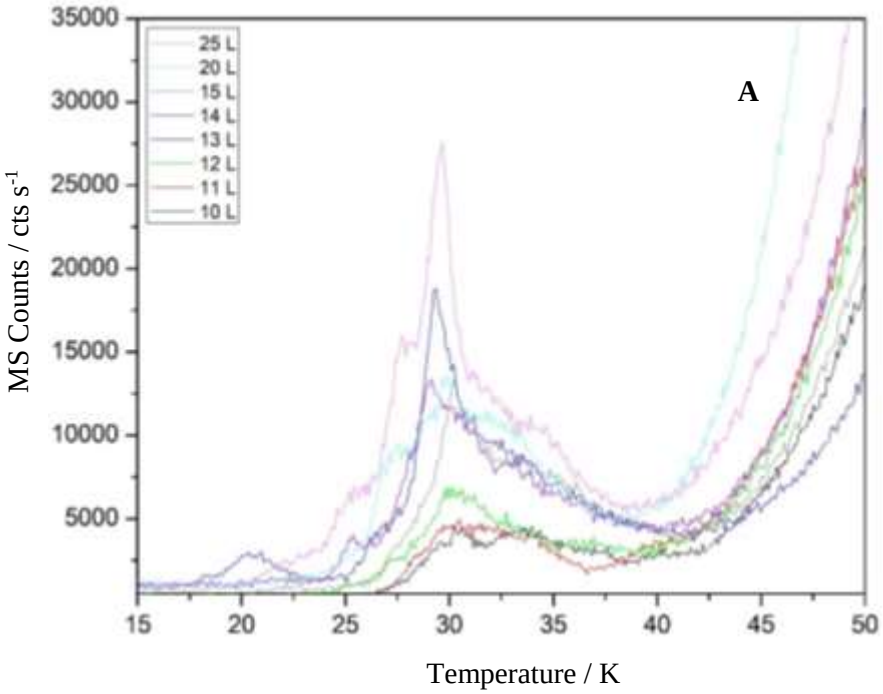

Figure 6.20: TPD traces for CO desorbing from CSW for exposures 10 to 25 L recorded on m/z =28 m_u. The plot has a rising background, labelled A, which is removed in order to use the data in the Extended Inversion Analysis.

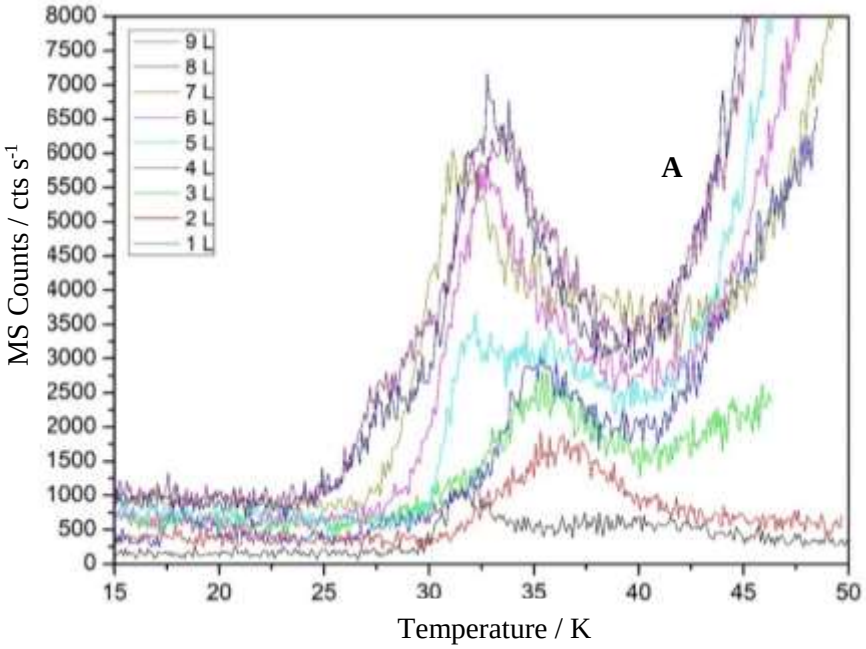

Figure 6.21: TPD traces for CO desorbing from CSW for exposures of 1 to 9 L recorded on m/z = 28 m_u. The plot has a rising background, labelled A, which is removed in order to use the data in the Extended Inversion Analysis.

Figure 6.22 shows TPD data for CO from CSW after background correction as described previously. The TPD displays coincident trailing edges at low exposures

and a common leading edge at higher exposures. The latter is consistent with multilayer growth and hence allows identification of the exposure needed to produce monolayer coverages of CO on CSW.

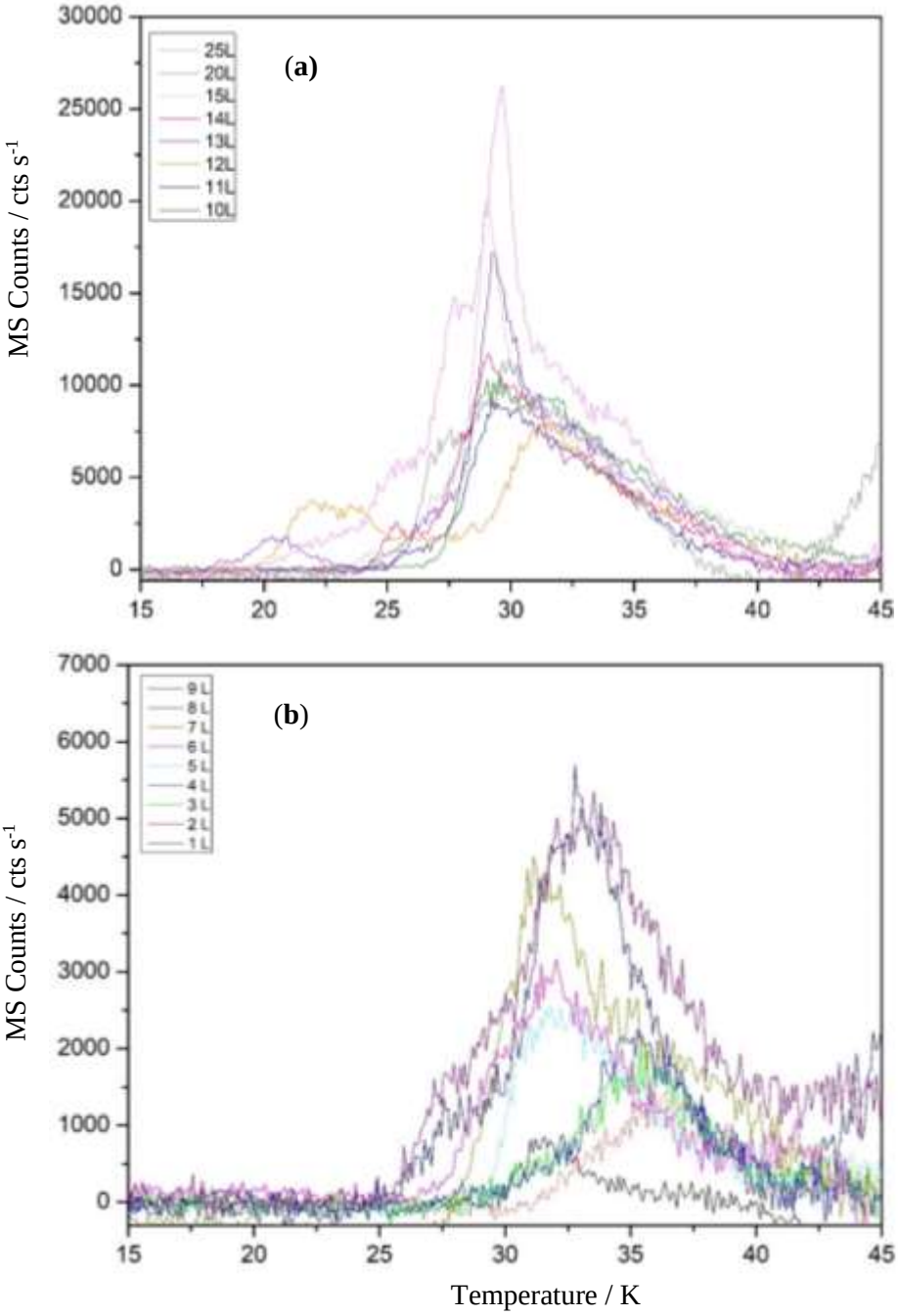

Figure 6.22: TPD data for CO from CSW for CO coverages of 1 to 25 L after correcting for the rising background: **(a)** multilayer 10 – 25 L and (**b**) sub-monolayer 1 to 9 L coverages.

At this stage the monolayer exposure is identified as 9 L. Hence, 1 ML is equivalent to 9 L. This allows us to convert exposures into coverage. Again the data indicates, as in the case of c-ASW, that there is distribution of binding site energies and that the adsorbate molecules have enough mobility prior to desorption to find the highest energy binding sites.

The Extended Inversion Analysis is carried out on the CO from CSW TPD data as described in **Section 6.2**. **Figure 6.23** shows the χ^2 between the experimental and simulated TPD data for sub-monolayer coverages *versus* the logarithm of the pre-exponential factor used in the Extended Inversion Analysis. The solid line is a fit to the points and this gives, at the minimum of χ^2, a value of ν of $2.51^{+1.47}_{-0.93} \times 10^{17} s^{-1}$. The best fit value of the pre-exponential factor determined for CO on CSW is larger than for CO on c-ASW.

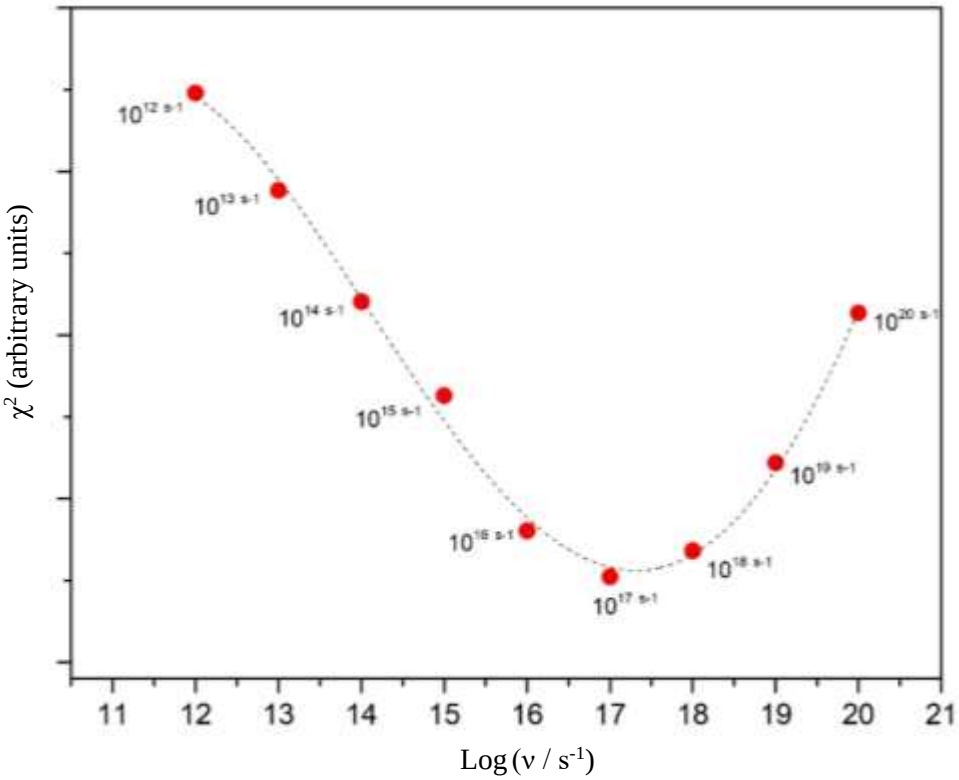

Figure 6.23: The χ^2 between the experimental and simulated TPD of CO from CSW for all initial coverages *versus* logarithm of the pre-exponential factor used in the Extended Inversion Analysis. The dashed line in this figure is fourth-order polynomial fit to χ^2 and yields a minimum at a value of 17.40±0.20. A number of different low order polynomial fits were tried. However, the fourth order polynomial proved to give the best fit for the experimental data. Hence, the optimised value of ν is $2.51^{+1.47}_{-0.93} \times 10^{17}\ s^{-1}$.

Figure 6.24 shows the plot of E_{des} against coverage constructed for each sub-monolayer CO coverage from the experimental data presented in **Figure 6.22** using the Extended Inversion Analysis assuming the optimised ν of $2.51^{+1.47}_{-0.93} \times 10^{17}$ s^{-1}. The averaged data are shown in the inset and is used to represent the distribution of interaction energies of CO molecules with the CSW surface. The highest binding energy is around 14.2 kJ mol^{-1} at the lowest coverage and decreases down to 9.5 kJ mol^{-1} as the coverage approaches 1.0 ML.

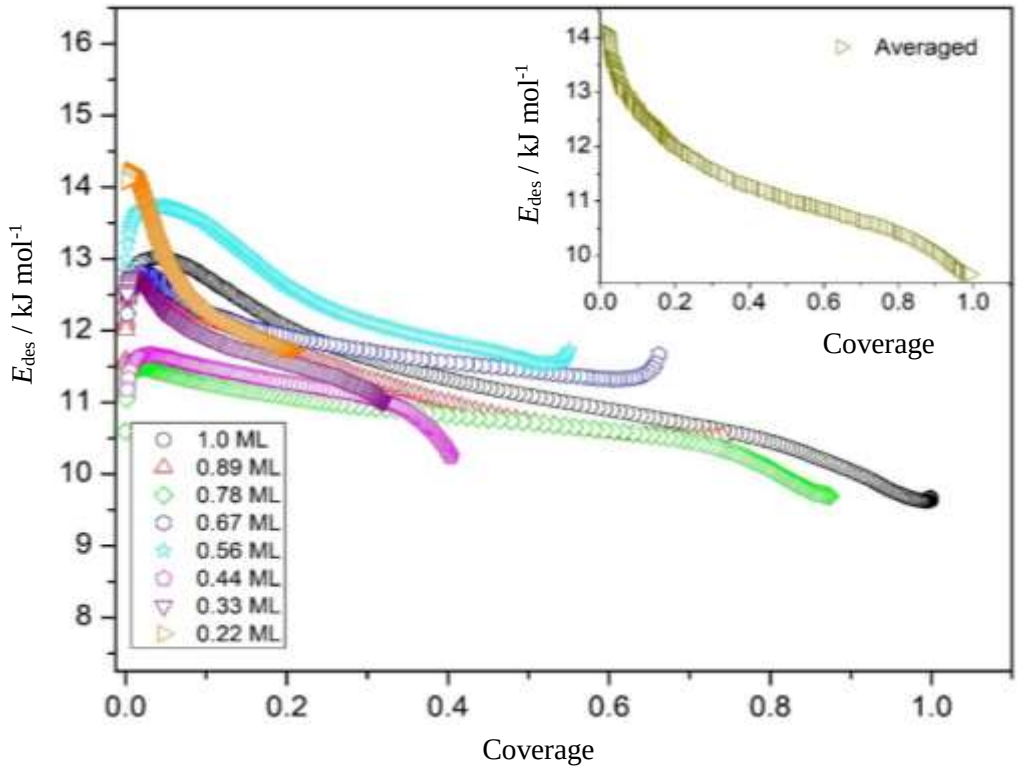

Figure 6.24: E_{des} *versus* coverage for CO sub-monolayers adsorbed from CSW and the inset shows the averaged data. The plots were obtain using with ν of $2.51^{+1.47}_{-0.93} \times 10^{17}$ s^{-1} and the inset contains the averaged data.

These results are line with those reported by Noble *et al*. [1], which range between 11.1 – 8.4 kJ mol^{-1}, and slightly wider in range when compared to the binding energy range for c-ASW (**Figure 6.18**). **Figure 6.25** shows a comparison of some the experimental (black) and simulated (red) TPD data for sub-monolayer coverages of CO on CSW. The simulated spectra were obtained using the $E_{des}(\theta)$ curve obtained with a pre-exponential factor $2.51^{+1.47}_{-0.93} \times 10^{17}$ s^{-1} in **Figure 6.24**. The simulated and experimental TPD profiles are in good agreement, which further validates the chosen value for the optimized pre-exponential factor.

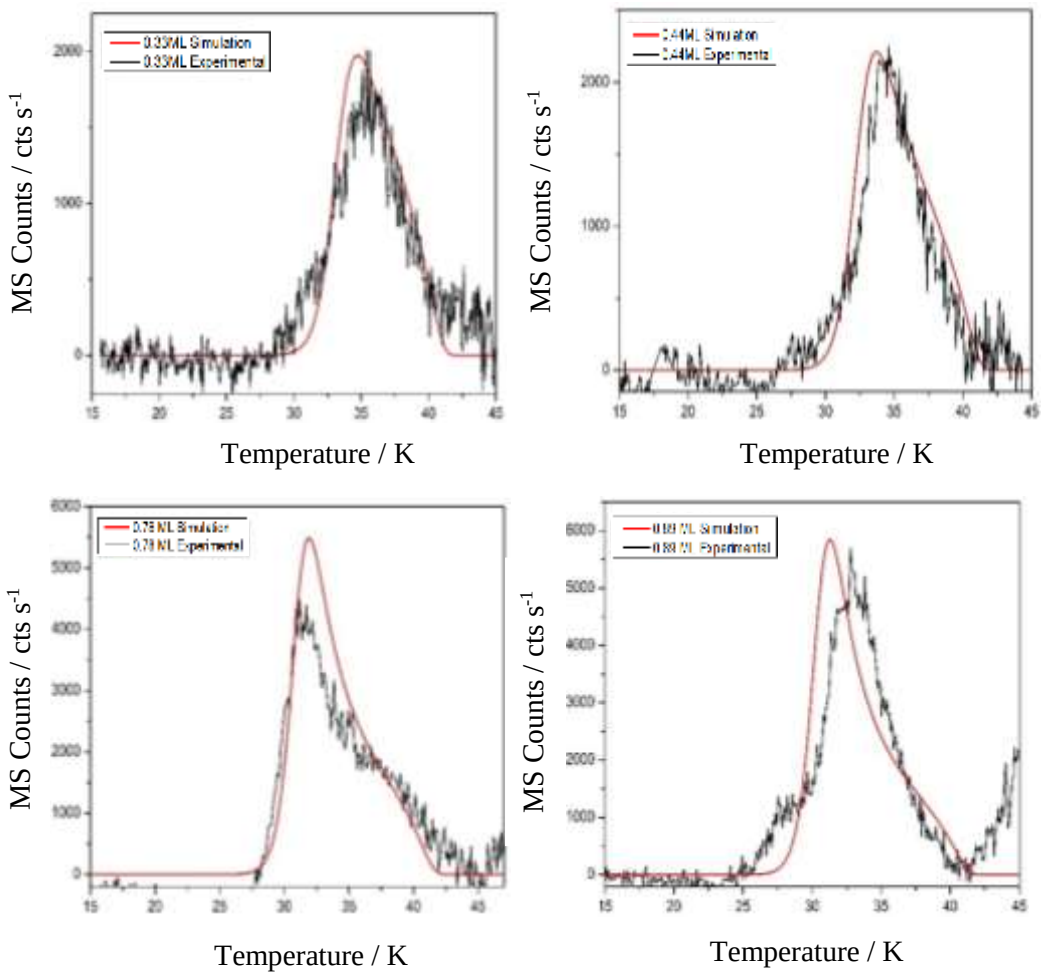

Figure 6.25: A comparison of the experimental (black) and simulated (red) TPD spectra for sub-monolayer coverages of CO on CSW. The simulated spectra were obtained using the $E_{\mathrm{des}}(\theta)$ curve in **Figure 6.24** obtained using a pre-exponential factor of $2.51^{+1.47}_{-0.93} \times 10^{17}\ \mathrm{s}^{-1}$.

Table 6.4 shows a comparison of the E_{des} and ν for CO on c-ASW and CSW with literature data for p-ASW. Comparing the binding energies of CO on p-ASW and c-ASW and CO on CSW, it is found that latter extends to higher binding energies. This difference in the binding energies between the two forms of water suggests that the degree of crystallinity of the material influences the kinetic parameters. The work by Karssemeijer *et al.* [1] has shown that CO mobility is mainly influenced by morphology of the ice substrate. With nanopores on the surface providing strong binding site, that virtually immobilize the adsorbate at low coverages. As the coverages increases, the weaker binding sites are gradually occupied and this leaves a number of admolecules with the ability to diffuse over the surface.

Surface	E_{des} / kJ mol^{-1}	E_{diff} / kJ mol^{-1}	ν / s^{-1}
p-ASW [18]	11.8	1.18	$3.50X10^{16}$
c-ASW	12.5 – 9.5	1.25 – 0.95	$2.57^{+1.47}_{-0.93} \times 10^{15}$
CSW	14.2 – 9.5	1.42 – 0.95	$2.51^{+1.47}_{-0.93} \times 10^{17}$

Table 6.4: Comparison of E_{des} and ν for CO on c-ASW and CSW from this work and from the literature.

The work by Noble *et al.* [2] indicates that this could be due to the ordered structure of the crystalline water being able to form larger scale interactions as suggested by observations of Dohnalek *et al.* [31] . The work by Green *et al.* [37] indicated that the surface type is relatively unimportant but the heating rate and grain size are dominant with regard to desorption kinetics. This work did not, however, take into account the sub-monolayer case. However, the work by Noble *et al.* [2] indicates that the surface type is the dominant factor controlling desorption under sub-monolayer coverage conditions. Hence the definition of the surface type must take into account both the surface material and the degree of crystallinity and not just simply material alone. The data presented by Noble *et al.* [2] shows that the desorption characteristics of molecular species from amorphous water and $aSiO_2$ are similar than those from amorphous water and crystalline water, which are both composed of the same underlying material. The work by Kay and co-workers investigated the desorption of small molecules from p-ASW [18]. The desorption of CO from p-ASW, where the monolayer peaks occur at lower temperature (27 K) compares with CSW at around 33 K and c–ASW around 34 K. This indicates that the interaction of the CO adsorbate with p–ASW is noticeably weaker than the interaction with CSW and c-ASW [18], as shown in **Table 6.4**. Thus p-ASW has a lower diffusion barrier 1.18 kJ mol^{-1} compared to the other surfaces, and thus CO is freer to move over p–ASW than CSW and c–ASW.

6.5.4 CO on CH_3OH

Up to 25 L exposures CO were deposited on CH_3OH on the $aSiO_2$ substrate at 15 K. Using the QMS, CO dosing was monitored at *m/z* = 12, 14 and 28 m_u. This allows identification of the exposure necessary to generate a coverage of a monolayer. Using a monolayer or less ensures that only CO-CH_3OH interactions are investigated

rather than CO-CO interactions as in the case of multilayer films. Consecutive TPD experiments from 1 to 25 L were carried out on the same day. **Figure 6.26** and **6.27** shows TPD traces for CO desorbing from CH_3OH for coverages 10 to 25 L and 1 to 9 L, recorded on m/z = 28 m_u. Both the low and high coverages have a rising background after 42 K which is labelled A. This has been removed using the method used in the analysis of CO desorption from c-ASW as discussed in **Section 6.5.2**.

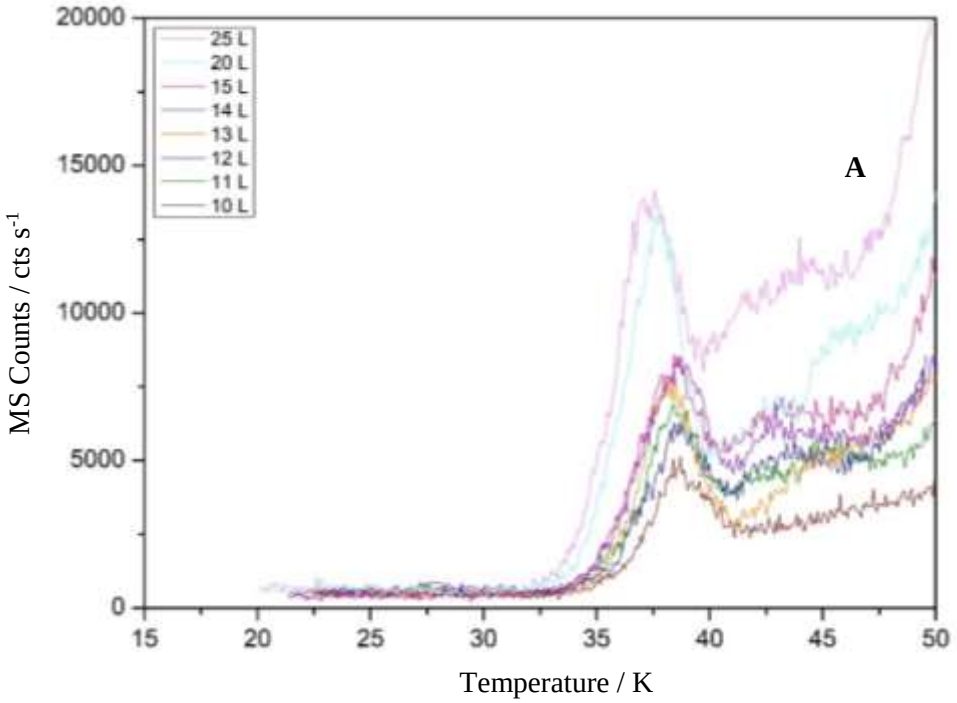

Figure 6.26: TPD traces for CO desorbing from CH_3OH for exposures of 10 to 25 L, recorded on m/z = 28 m_u. The plot has a rising background, labelled A, which is removed in order to carry out Extended Inversion Analysis.

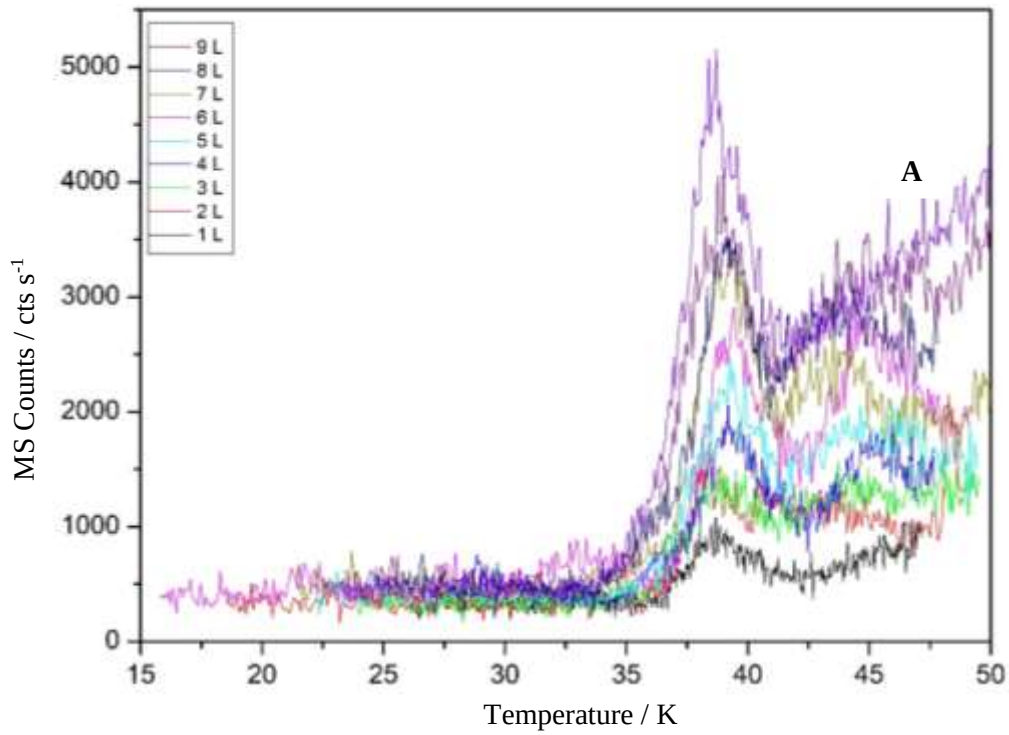

Figure 6.27: TPD traces for CO desorbing from CH_3OH for exposures of 1 to 9 L, recorded on m/z = 28 m_u. The plot has a rising background, labelled A, which is removed in order to use the data in the Extended Inversion Analysis.

Figures 6.28 shows the background corrected TPD data for CO desorbing from CH_3OH.

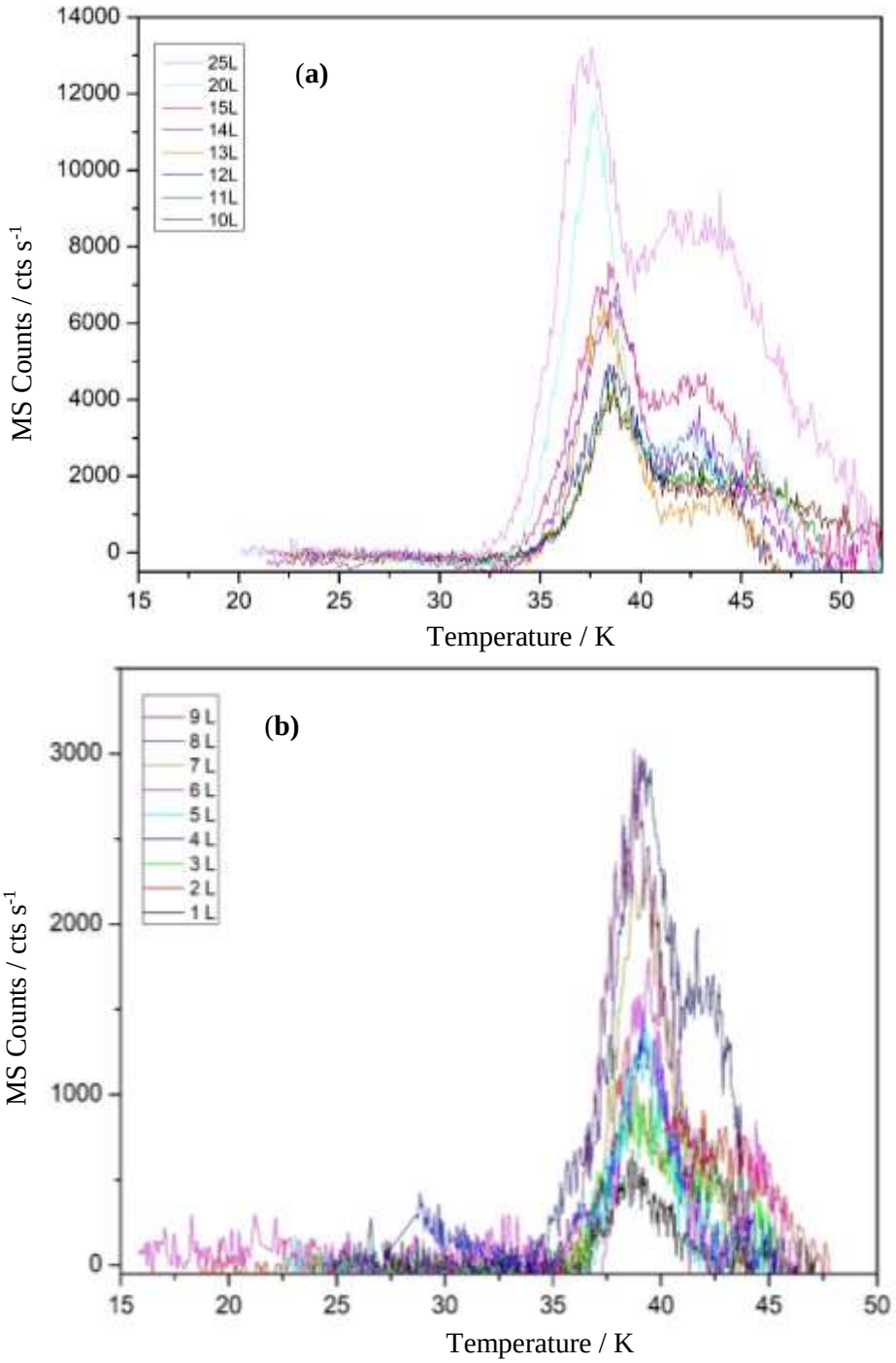

Figure 6.28: TPD data for CO on CH_3OH for coverages of 1 to 25 L after correcting for the rising background: (**a**) multilayer 10 to 25 L coverages and (**b**) sub-monolayer 1 to 9 L coverages.

The desorption kinetics of CO on CH_3OH are different to CO desorption from CSW and c-ASW. The TPD data for exposures up to 9 L again show same alignment of trailing edges but much less progression of T_{max} to lower temperature. This behaviour would suggest a more limited distribution of binding sites energies. Above this exposure, alignment of the leading edges once again points to multilayer growth. We can identify the monolayer equivalent dose at 9 L.

The Extended Inversion Analysis was carried on the TPD data in **Figure 6.28** as described in **Section 6.2**. **Figure 6.29** shows the χ^2 between the experimental and simulated TPD data for sub-monolayer coverages *versus* logarithm of the pre-exponential factor used in the Extended Inversion Analysis. The solid line is a fit to the points and this gives, at the minimum of χ^2, a value of ν of $1.41^{+0.29}_{-0.45} \times 10^{16} s^{-1}$.

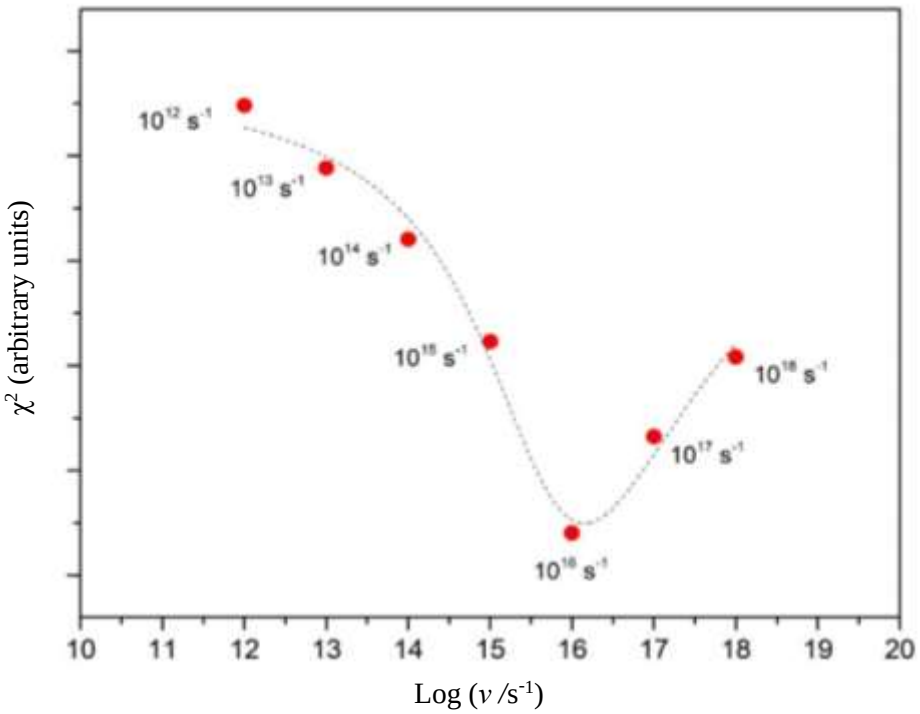

Figure 6.29: The χ^2 between the experimental and simulated TPD of CO from CH_3OH all initial coverages *versus* logarithm of the pre-exponential factor used in the Extended Inversion Analysis. The dashed line in this figure is PsdVoigt1 fit to χ^2 and yields a minimum at a value of 16.41±0.43. Hence, the optimised value of ν is $1.41^{+0.29}_{-0.45} \times 10^{16}\ s^{-1}$.

Figure 6.30 shows the plot of $E_{des}(\theta)$ for each sub-monolayer coverage CO dose from the experimental data presented in **Figure 6.27** using the Extended Inversion

Analysis. The averaged data are shown in the inset and is used to represent the distribution of interaction energies of CO molecules with the CH_3OH surface. The range of binding sites on the CH_3OH surface (**Figure 6.30**) presented is much narrower than for CSW (**Figure 6.24**) and c–ASW (**Figure 6.18**) surfaces. The highest binding energy is 14 kJ mol^{-1} at the low coverages and decreases down to a lower binding energy limit of 12.8 kJ mol^{-1} at 0.8 ML.

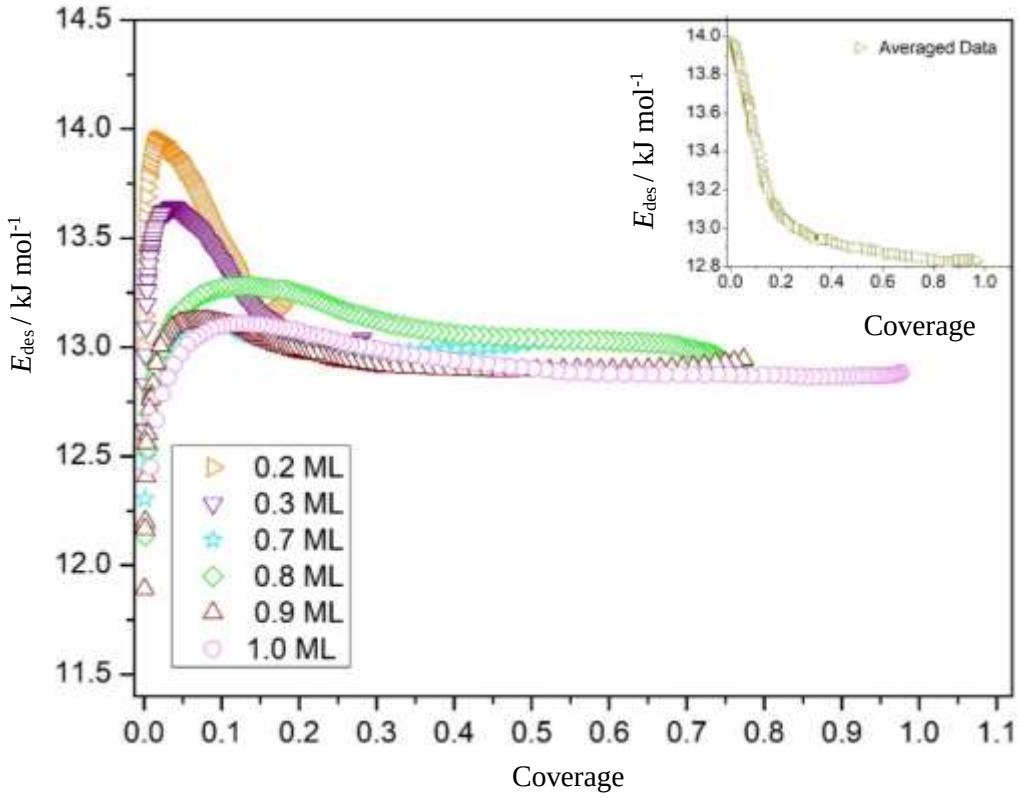

Figure 6.30: E_{des} *versus* coverage for sub-monolayer quantities of CO on CH_3OH. The inset shows the averaged data. The plots were obtained using the optimised ν of $1.41^{+0.29}_{-0.45} \times 10^{16}$ s^{-1} and the inset contains the averaged data.

Figure 6.31 shows an example of the simulated and experimental TPD produced using the optimised pre-exponential factor. The simulated TPD data reproduces the experimental data reasonably well using the optimized pre-exponential factor.

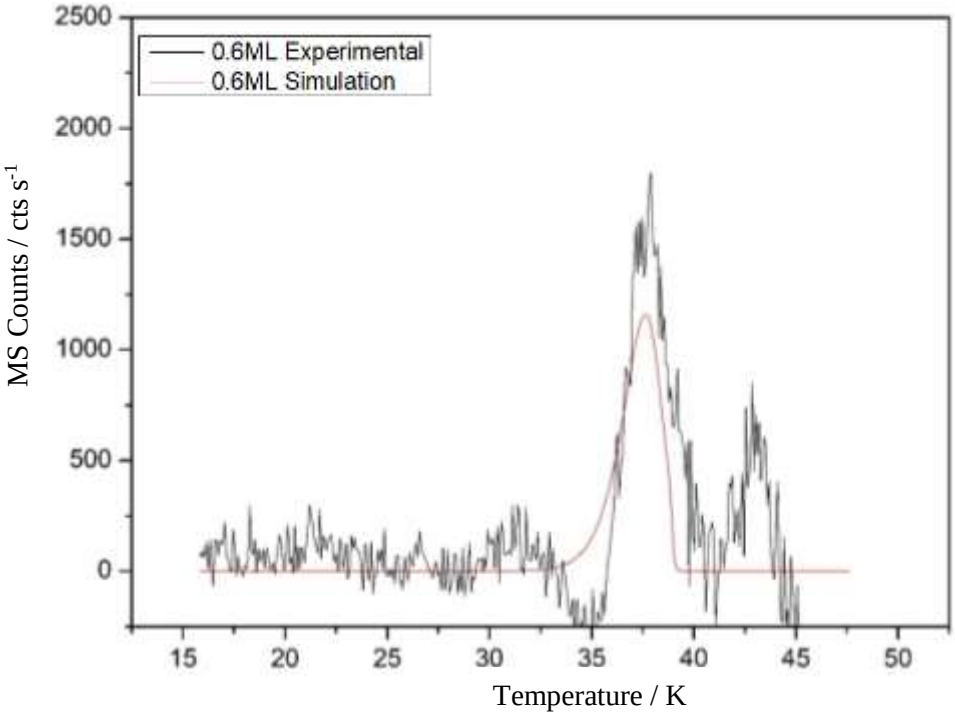

Figure 6.31: A comparison of the experimental (black) and simulated (red) TPD data for sub-monolayer coverages of CO on CH_3OH. The simulated and experimental TPD produced using the optimised pre-exponential factor, ν, of $1.41^{+0.29}_{-0.45} \times 10^{16} s^{-1}$.

6.5.5 CO on NH_3

Coverages in the range of 1 L to 15 L of CO on 1000 L of NH_3 were deposited on the $aSiO_2$ substrate at base temperature. This allows the identification of the exposure necessary to generate coverage of a monolayer. Using a monolayer or less ensures that only CO-NH_3 interactions are investigated rather than CO-CO interactions in case of multilayer films. Using the QMS, CO dosing was monitored at m/z = 12, 14 and 28 m_u. Consecutive TPD experiments from 1 to 15 L were carried out on the same day. **Figure 6.32** and **6.33** shows TPD traces for CO desorbing from NH_3, for coverages 10 to 15 L and 1 to 9 L recorded on m/z = 28 m_u. Both the low and high coverages have a rising background at around 42 K, which is labelled A. This rising background is removed using the method used in the analysis of CO desorption from c-ASW as discussed in **Section 6.5.2**.

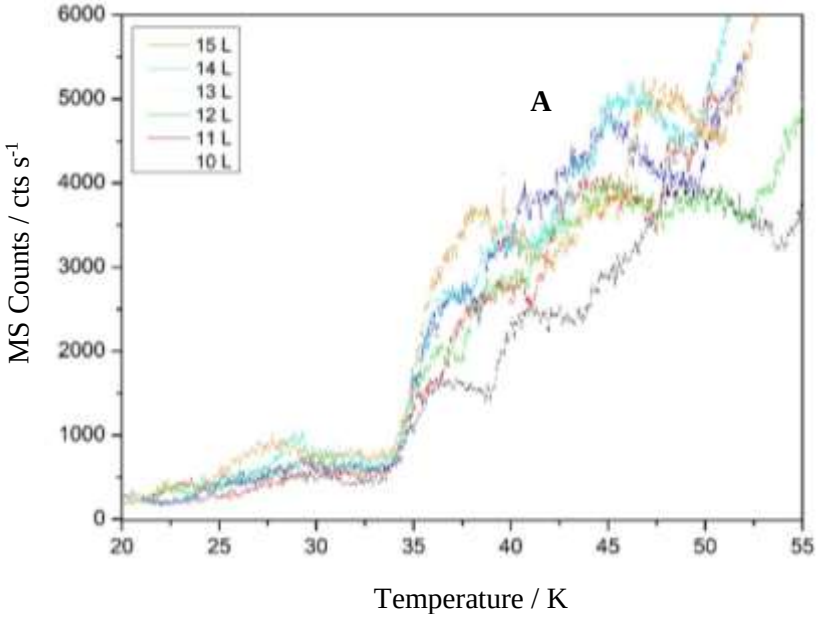

Figure 6.32: TPD traces for CO desorbing from NH_3, for coverages 10 to 15 L, recorded on m/z = 28 m_u. The plot has a rising background, labelled A, which is removed in order to use in the data in the Extended Inversion Analysis.

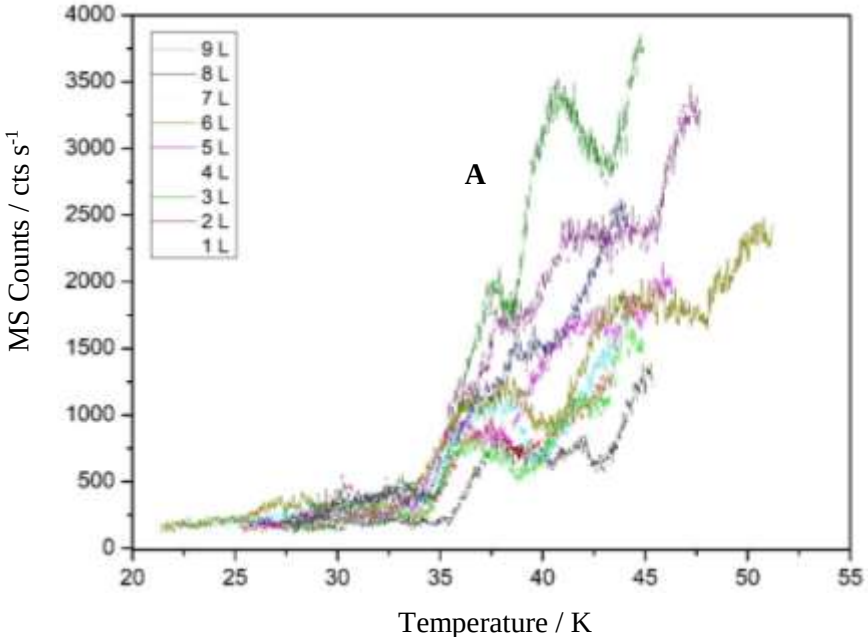

Figure 6.33: TPD traces for CO desorbing from NH_3, for coverages 1 to 9 L, recorded on m/z = 28 m_u. The plot has a rising background, labelled A, which is removed in order to use in the data in the analysis process.

Figure 6.34 show the corrected TPD data for 1 to 15 L of CO on NH_3, after correcting the rising background as shown in **Figure 6.32** and **6.33**. The sub-

monolayer coverages show common trailing edges and a reducing T_{max} with increasing coverage which is characteristic of first order kinetics with a distribution of binding energies. At this stage, we confirm the TPD behaviour and identify the monolayer exposure as 9 L. Hence, 1 ML is equivalent to 9 L. This allows us to convert exposures into coverage.

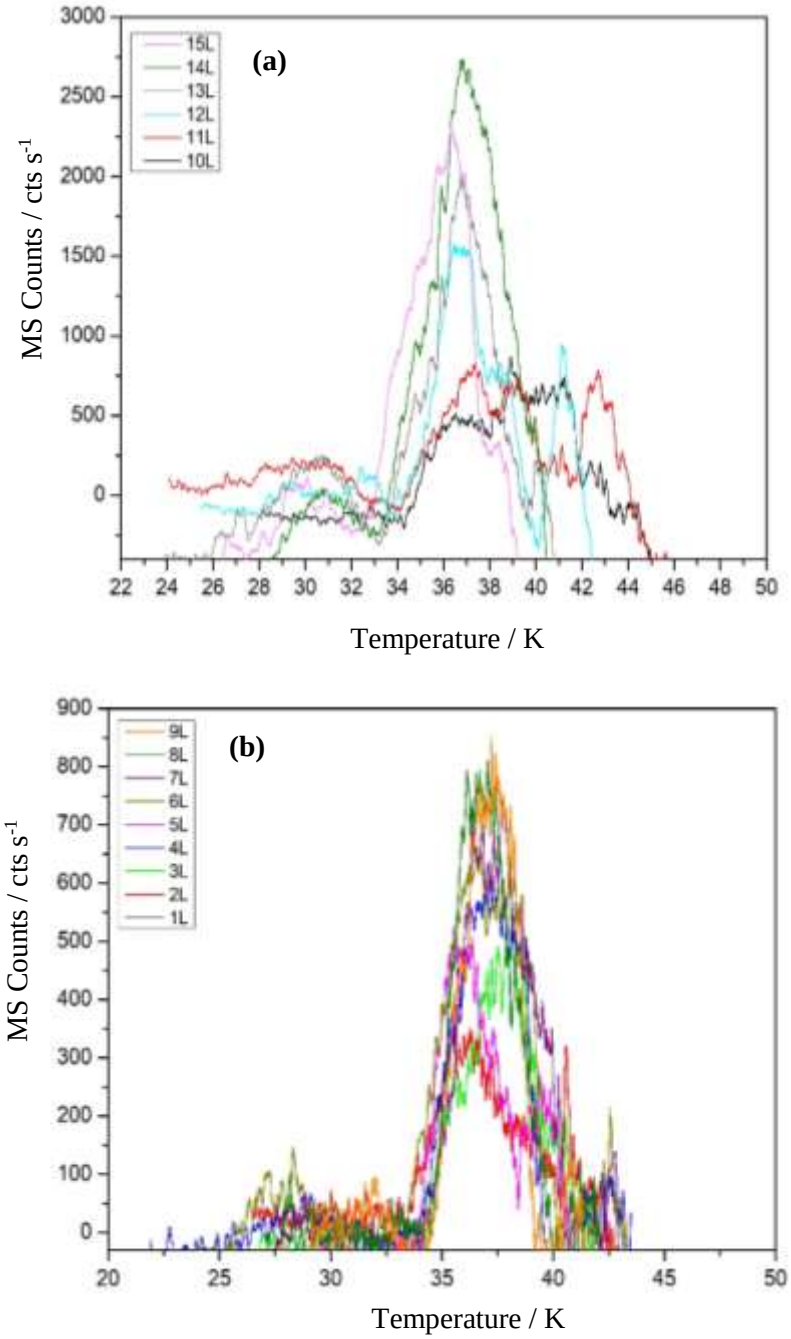

Figure 6.34: TPD data for CO on NH_3 for coverages of 1 to 15 L after correcting for the rising background: (**a**) multilayer 10 – 15 L and (**b**) sub-monolayer 1 – 9 L coverages.

The desorption kinetics of CO on NH_3 are similar to CO on the other surfaces investigated *e.g*. CH_3OH (**Figure 6.28**). The TPD data for exposures up to 9 L again show same alignment of trailing edges but much less progression of T_{max} to lower temperature. This behaviour would suggest a more limited distribution of binding site energies. Above this exposure, alignment of the leading edges once again points to multilayer growth. This suggests that CO wets the NH_3 surface.

The Extended Inversion Analysis was carried on the TPD data in **Figure 6.34** as described in **Section 6.2**. **Figure 6.35** shows the χ^2 between the experimental and simulated TPD data for sub-monolayer coverages *versus* logarithm of the pre-exponential factor used in the Extended Inversion Analysis. The solid line is a fit to the points and this gives, at the minimum of χ^2, a value of ν of $1.51^{+0.46}_{-0.40} \times 10^{12}$ s^{-1}.

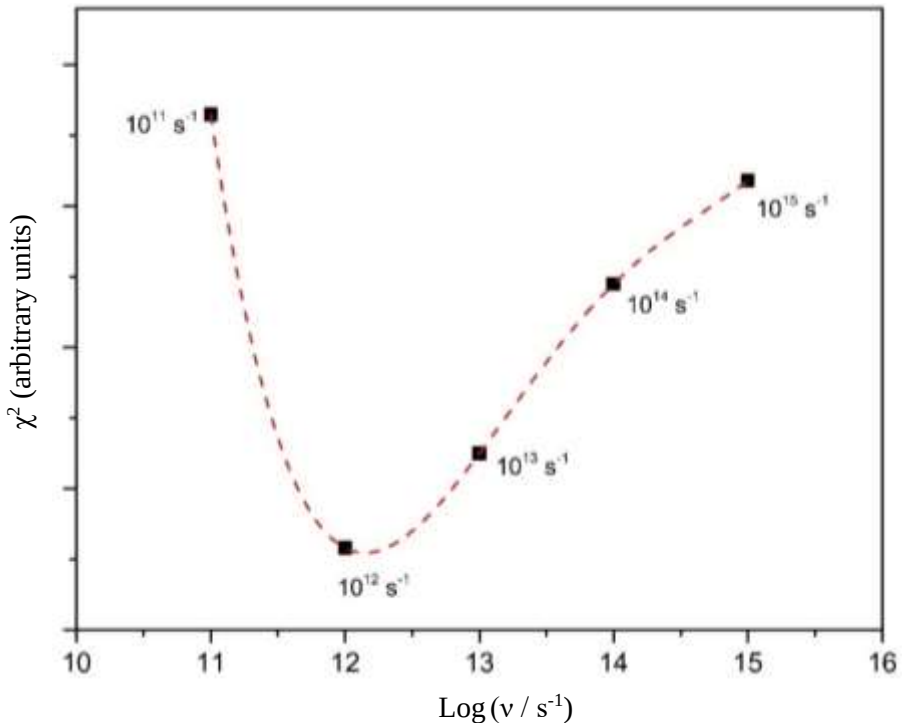

Figure 6.35: The χ^2 between the experimental and simulated TPD CO for NH_3 for all initial coverages *versus* logarithm of the pre-exponential factor used in in the Extended Inversion Analysis. The dashed line in this figure is fourth-order polynomial fit to χ^2 and yields a minimum at a value of 12.18±0.13. A number of different low order polynomial fits were tried. However, the fourth order polynomial proved to give the best fit for the experimental data. Hence, the optimised value of ν is $1.51^{+0.46}_{-0.40} \times 10^{12}$ s^{-1}.

Figure 6.36 shows the plot of $E_{des}(\theta)$ against coverage for each sub-monolayer coverage of CO derived from the experimental data presented in **Figure 6.34** using the best fit value of the pre-exponential factor derived. The averaged data are shown in inset and is used to represent the distribution of interactions energies of CO molecules with NH_3 surface. In **Figure 6.36** the highest binding energy is around 8.50 kJ mol^{-1} and available at the lowest coverages. The binding energy goes down to 8.40 kJ mol^{-1} at higher coverages.

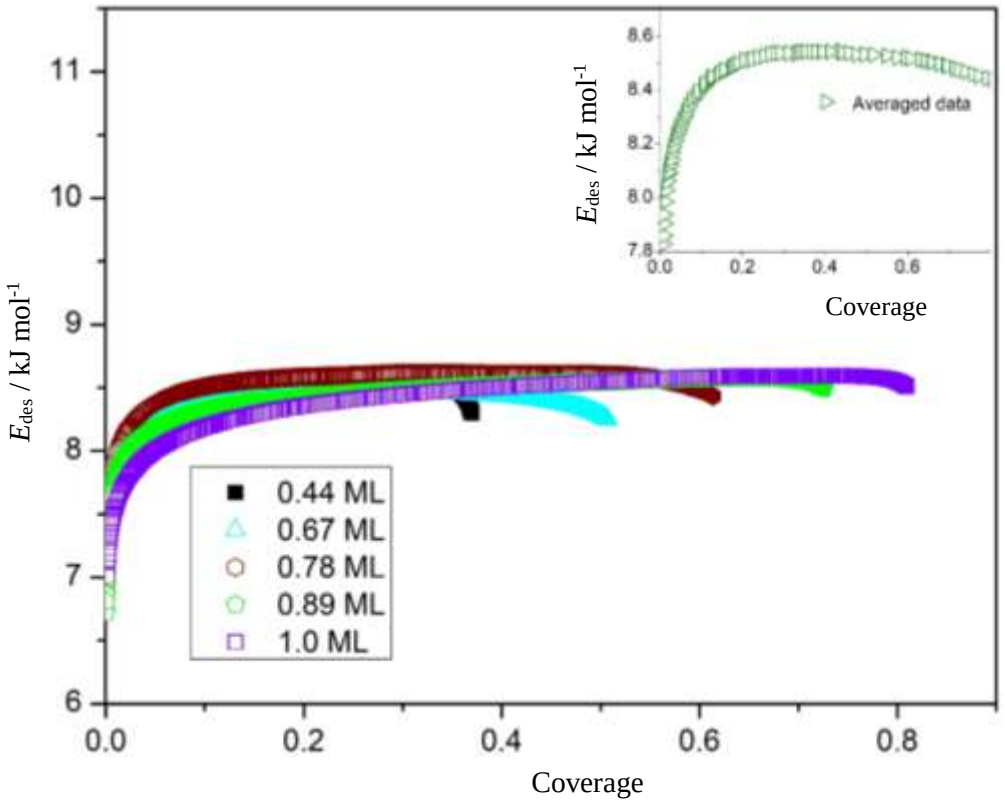

Figure 6.36: E_{des} *versus* coverage for CO sub-monolayers adsorbed on NH_3 and inset shows the average data. The plots were obtained using the optimised ν of $1.51^{+0.46}_{-0.40} \times 10^{12}\ s^{-1}$ and the inset contains the averaged data.

Figure 6.37 shows a comparison of the experimental and simulated TPD spectra for CO on NH_3, the simulated spectra were obtained using the optimised pre-exponential factor ν value of $1.51^{+0.46}_{-0.40} \times 10^{12}\ s^{-1}$. The simulations are slightly narrow when compared with the experimental data and this due in part to the value of the pumping speed used in the FORTRAN code used to carry out the simulations. This could in future work be optimised to reflect the true pumping speed behaviour which is clearly slower than currently in the model.

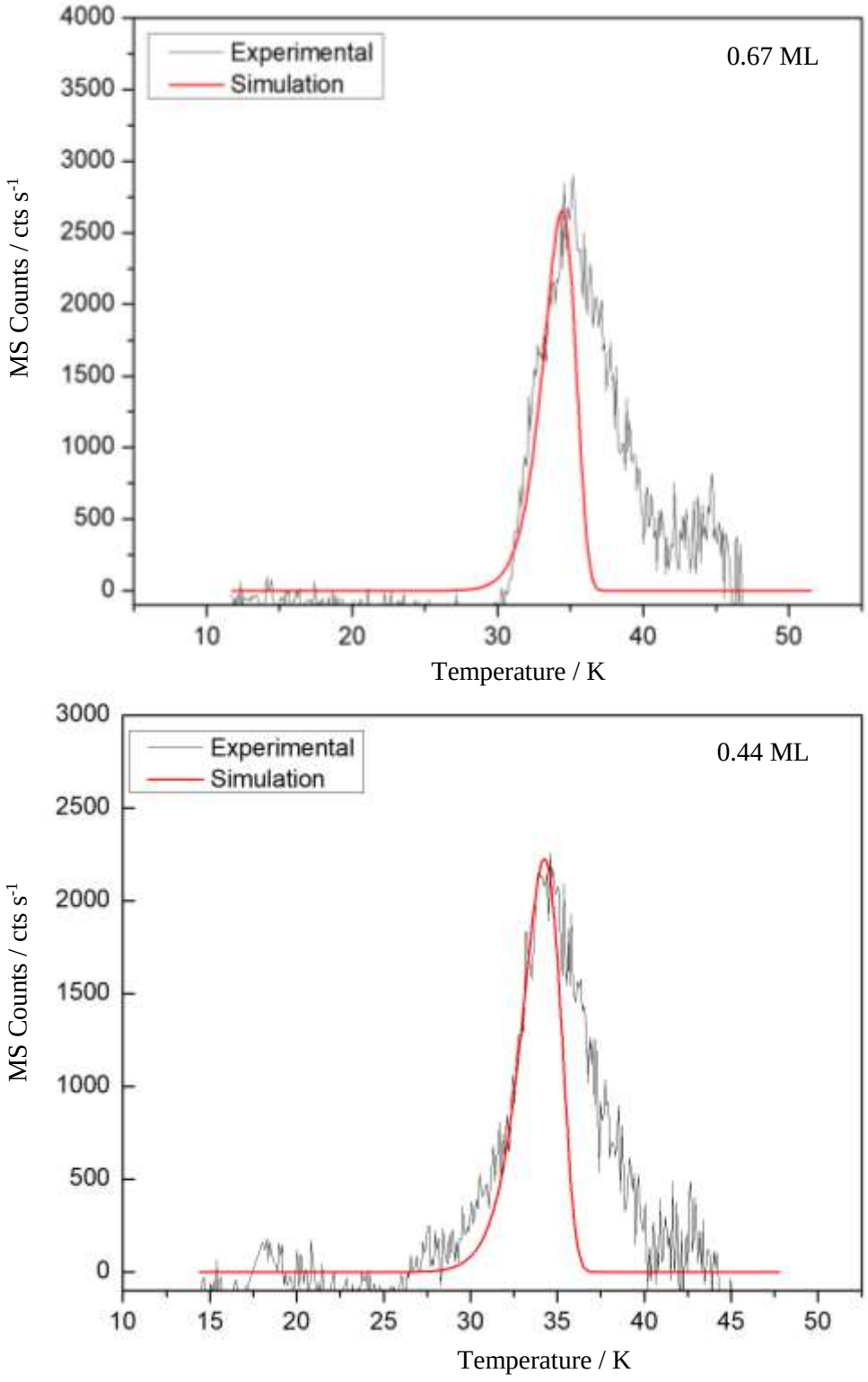

Figure 6.37: A comparion of the experimetnal (black) and simulated (red) TPD spectra for sub-monolayer coverages of 0.44 to 0.67 ML CO on NH_3. The simulated spectra were obtained using the the pre-exponetial factor of $1.51^{+0.46}_{-0.40} \times 10^{12}$ s^{-1}.

NH_3 has the narrowest range of E_{des} range (8.50 – 8.40 kJ mol^{-1}) and hence the smallest diffusion barrier compared to any of the other surfaces investigated. The very narrow E_{des} range indicates that NH_3 provides a very limited number of binding sites when compared to the other surfaces. This, indicates that CO motion is the least restricted on NH_3 compared to any of the other surfaces investigated. The diffusion barrier estimated for NH_3 is lowest 0.85 – 0.84 kJ mol^{-1} of any of the surfaces and this allows for more motion of the CO on NH_3 surface which results in least tightly packed CO layer with the minimum repulsions and hence a very low entropy when compared to all the other surfaces.

6.5.6 CO on $aSiO_2$-Vibrational Line Profiles Revisited

In **Chapter 5**, a simple method was demonstrated which was used to synthesise the vibrational line profiles of CO on $aSiO_2$ using the binding energy distribution derived from TPD data by inversion analysis assuming a value of 1.00×10^{12} s^{-1} for the pre-exponential factor. In this chapter, the optimised pre-exponential factor has been calculated using the Extended Inversion Analysis and a revised binding energy distribution calculated. The work below demonstrates the effect of that revised distribution on the vibrational line profile synthesis. **Figure 6.38(a)** shows the $P(E_{des})$ *versus* E_{des} for CO-$aSiO_2$ which is calculated using ν of 1.00×10^{12} s^{-1} and **Figure 6.38(b)** calculated using ν of $1.74^{+0.75}_{-0.53}\times10^{21}$ s^{-1} which results in a recovered binding energy distribution wider than that reported in **Chapter 4**.

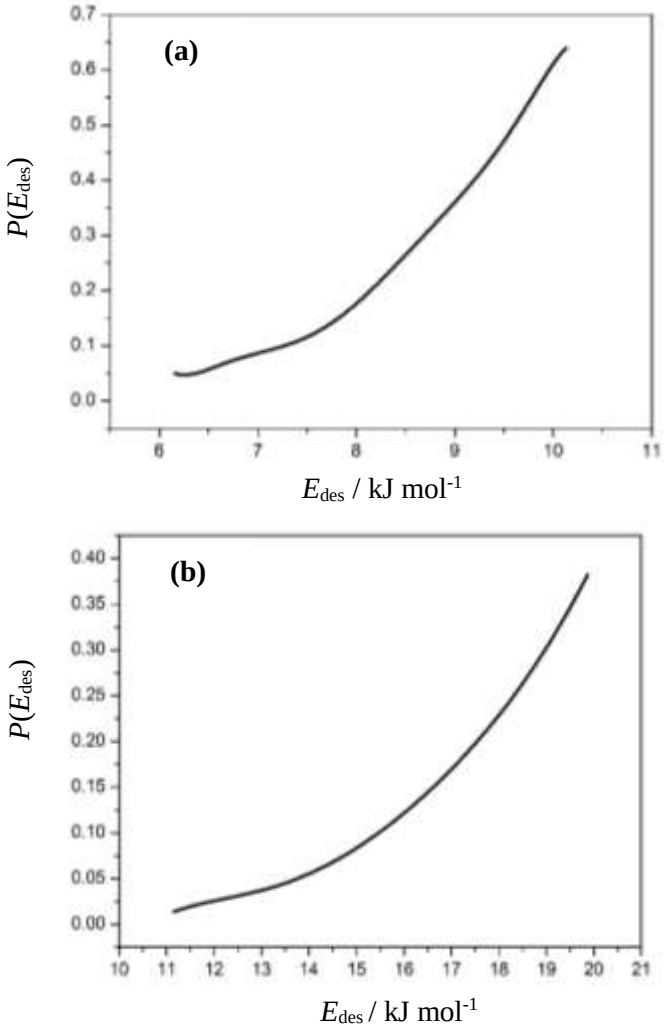

Figure 6.38: $P(E_{des})$ *versus* E_{des} as derived from the sub-monolayer TPD of CO from $aSiO_2$ substrate (**a**) using pre-exponential factor of $1.00X10^{12}$ s^{-1} [17] and (**b**) using optimised pre-exponential factor of $1.74^{+0.75}_{-0.53} \times 10^{21}$ s^{-1}.

Figure 6.39 (**d**, **e**, and **f**) shows the impact of the revised binding energy distribution on the vibrational line profile synthesis for 0.6 ML CO on $aSiO_2$. The figure compares the simulations from **Chapter 5** (**Figure 6.39 a**, **b** and **c**) with the revised simulations. **Figures 6.39(a)** and **6.39(d)** present the situation of ballistic deposition assuming the instrument-limited linewidth of 0.1 cm^{-1}. As in **Chapter 5**, this clearly indicates that ballistic deposition does not explain the observed line profile. Deposition by the adsorb and diffuse mechanism, initially presented in **Figure 6.39(b)** and **6.39(e)** at instrument-limited linewidth, can be optimised as in **Figure 6.39(c)** and **6.39(f)** to reproduce the data. We must conclude therefore that CO deposition on $aSiO_2$ at 18 K follows an adsorb and diffuse mechanism.

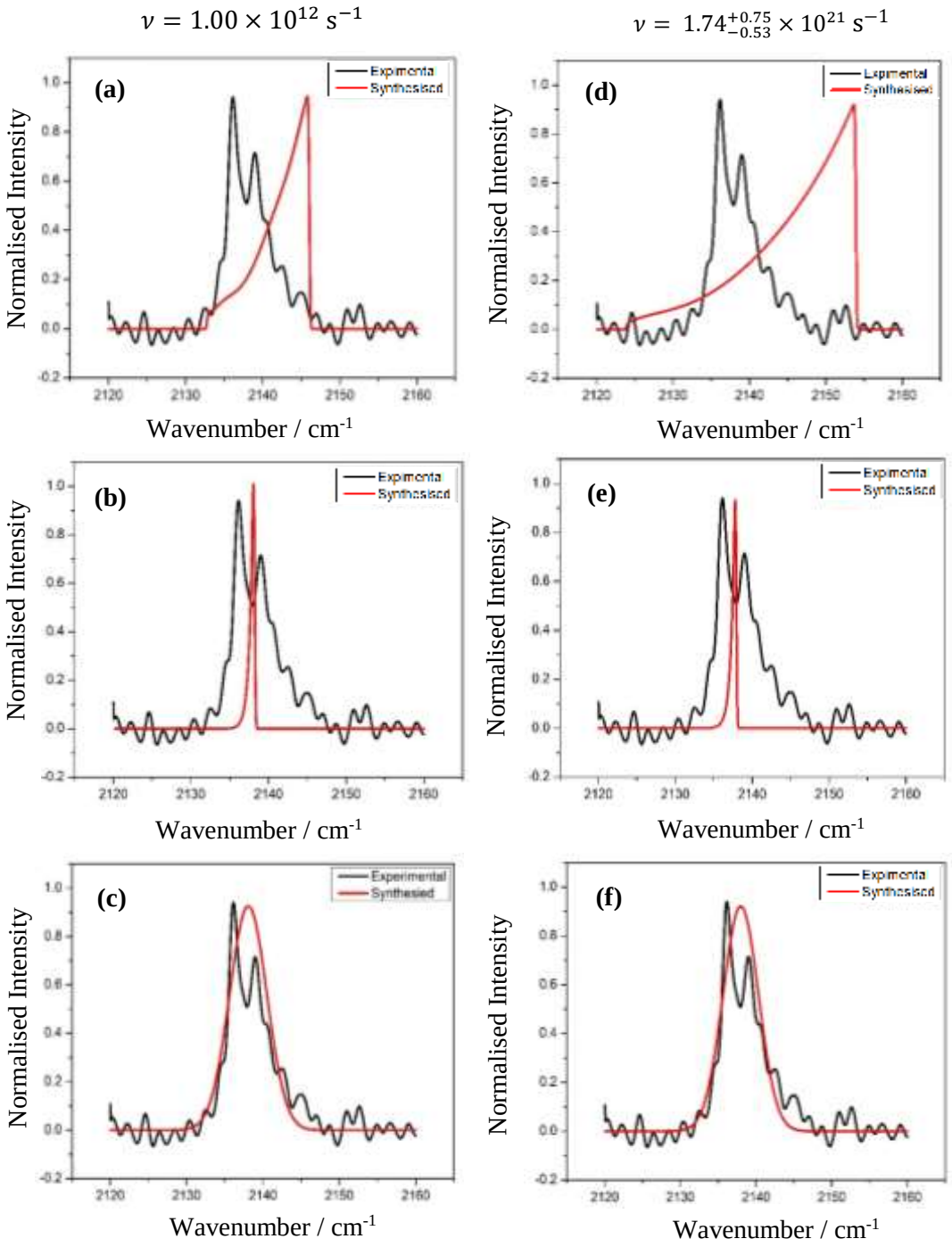

Figure 6.39: Vibrational line profile synthesis for 0.6 ML CO on $aSiO_2$ (**a, d**) assuming ballistic deposition and (**b, e**) adsorb and diffuse deposition at instrument limited linewidth of 0.1 cm^{-1} and (**c, f**) show adsorb and diffuse deposition with optimised linewidth.

Table 6.5 summarises the best fit parameters of the modelled profiles to the experimental CO vibrational line profiles on $aSiO_2$ using the binding energy distribution derived from the pre-exponential factors of $1.00X10^{12}$ s^{-1} and $1.74^{+0.75}_{-0.53} \times 10^{21}$ s^{-1} and compares with those for ASW reported in **Chapter 5**.

	$\bar{\upsilon}_o$ /cm^{-1} (±0.5)	δ /cm^{-1} (±0.2)	Model FWHM / cm^{-1} (±0.5)	Experimental FWHM / cm^{-1} (±0.1)
Chapter 5 analysis $aSiO_2$	2102.5	2.4	5.7	4.7
Revised analysis $aSiO_2$	2069.5	2.3	5.4	4.4
CO on p-ASW (Ballistic)	2108.0	2.6	5.9	5.6
CO on p-ASW (Diffusive)	2089.0	3.2	7.6	8.0

Table 6.5: Compares the best-fit parameters $\bar{\upsilon}_o$, δ and I_0, along with the corresponding FWHM for the modelled profiles and the experimental CO vibrational line profiles on $aSiO_2$ and p-ASW [17].

It is clear from the table that the linewidth δ of the CO on $aSiO_2$ line is significantly narrower than for CO on H_2O, 2.4 cm^{-1} *versus* 3.2 cm^{-1}. The revised analysis strengthens this argument in comparing 2.3 cm^{-1} *versus* 3.2 cm^{-1}. This in turn impacts on the lifetime of the vibrationally excited state of CO which increases from 0.94 ps corresponding to 2.4 cm^{-1} to 0.98 ps with the revised analysis. However, the basic explanation for this remains unaltered from **Chapter 5**. As in both systems CO is likely bound to the substrate *via* weak hydrogen bond interactions with the surface OH groups, we might expect similar relaxation modes for vibrationally excited CO and hence similar linewidth.

Figure 6.40, however, highlights a significant difference between the systems. **Figure 6.40** compares the IR spectra of ASW and $aSiO_2$. The dotted line on the figure represents the position of the CO vibrational frequency on solids. As can be seen, the CO line sits on top of the broad continuous absorption associated with the bending-libration combination mode in the case of ASW. This opens an additional quantum mechanical relaxation pathway on the ASW surface over and above simple mechanical intermolecular energy redistribution (IVR) presented equally by both surfaces. This is Fano Coupling [43,44] between the CO resonance and the underlying ASW continuum. This additional pathway reduces the lifetime of the CO on the ASW surface, hence increasing the linewidth in comparison to CO on $aSiO_2$.

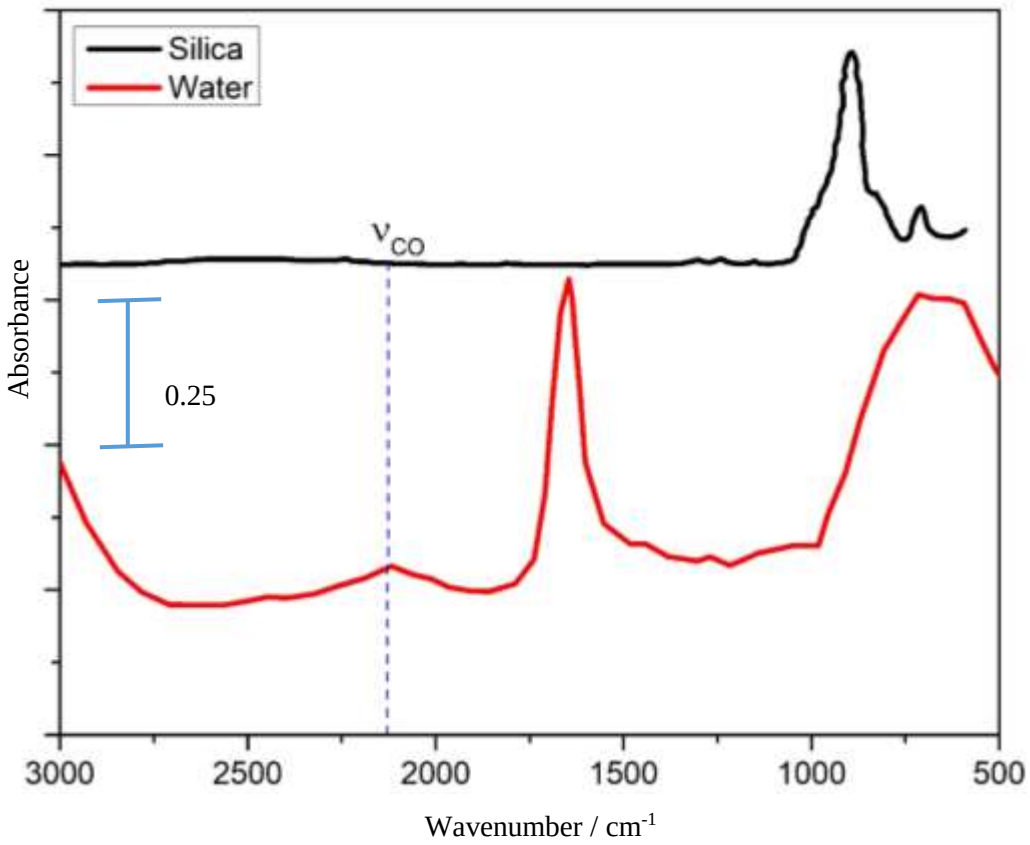

Figure 6.40: IR spectrum of solid $aSiO_2$ [38] and solid H_2O [39].

6.5.7 Pre-Exponential Factors and Entropy of Activation

The entropy of activation ($\Delta^{\ddagger}S$) is calculated by rearranging **Equation 6**:

$$\Delta^{\ddagger}S = R\ln\left(\frac{h\nu}{k_B T}\right) \qquad \textbf{(E16)}$$

where R is the gas constant, h is the Planck constant, k_B is the Boltzmann constant, ν is the pre-exponential factor and T is maximum temperature for desorption for CO on $aSiO_2$, CSW, c-ASW and CH_3OH (**Figures 6.17, 6.23** and **6.29**). **Table 6.6** summarises the results for CO on each surface.

Surface	ν / s^{-1}	$\Delta^{\ddagger}S$ /J K^{-1} mol^{-1}	E_{des} / kJ mol^{-1}	E_{diff} / kJ mol^{-1}
$aSiO_2$	$1.74^{+0.75}_{-0.53} \times 10^{21}$	$178.85^{+1.17}_{-1.03}$	19.5 – 11	1.95 – 1.10
c-ASW	$2.57^{+1.04}_{-1.21} \times 10^{15}$	$67.91^{+1.28}_{-1.11}$	12.5 – 9.5	1.25 – 0.95
CSW	$2.51^{+1.47}_{-0.93} \times 10^{17}$	$106.00^{+1.28}_{-1.11}$	14.2 – 9.5	1.42 – 0.95
CH_3OH	$1.41^{+0.29}_{-0.45} \times 10^{16}$	$81.83^{+1.21}_{-1.05}$	14.0 – 12.8	1.40 – 1.28
NH_3	$1.51^{+0.46}_{-0.40} \times 10^{12}$	$5.59^{+1.21}_{-1.06}$	8.5 – 8.4	0.85 – 0.84

Table 6.6: Summary of the pre-exponential factors, entropy of activation, E_{des} and E_{diff} for CO interactions on $aSiO_2$, c-ASW, CSW, CH_3OH and NH_3. Note the diffusion barrier, E_{diff}, is typically around 10% of the E_{des} [12].

The entropy for activation $\Delta^{\ddagger}S$ can be written as

$$\Delta^{\ddagger} S = S^{\ddagger}_{CO(des)} - S_{CO(ads)} \qquad \textbf{(E17)}$$

and is the difference between the entropy of the transition state for desorption and that of the adsorbed state. If we assume that the former is largely independent of the system then the data in **Table 6.6** is revealing something of the nature of the adsorbed systems.

CO is strongly bound to $aSiO_2$ and diffusion on that surface is likely restricted. This clearly introduces some disorder into the system which is likely to be reinforced by the extensive heterogeneity of the surface and hence, a larger $\Delta^{\ddagger}S$ compared to the other surfaces. If we compare the solid water surfaces, the diffusional barrier estimated for c-ASW is lower than that for CSW. This will allow for more motion of the CO on the c-ASW surface producing a less tightly packed CO layer with minimum repulsions and hence lower entropy than the CSW surface.

If we then compare c-ASW to CH_3OH, the data in **Table 6.6** suggests a larger entropy for the adsorbed system on CH_3OH than on H_2O. Again the higher barrier to diffusion on the former may play a role in restricting heterogeneity of CO on the CH_3OH surface compared to c-ASW.

NH_3 has the lowest diffusion barrier of any of the surfaces investigated. This, indicates that CO is the least restricted on NH_3 compared to any of the other surfaces

investigated, which results in the least tightly packed CO layer with the minimum repulsions and hence a very low entropy when compared to all the other surfaces.

6. 6 Conclusion

This chapter has investigated the interaction of CO with a range of astrophysically relevant surfaces including $aSiO_2$, c-ASW, CSW, CH_3OH and NH_3. In the sub-monolayer regime CO desorption from $aSiO_2$, CSW, c-ASW, CH_3OH and NH_3 follows first order kinetics where the CO molecules are mobile enough to find locate and fill the most favourable binding sites. This is due to the underlying surface offering an array of binding energies, with the highest binding energies available at the lowest coverage. The work in this chapter has demonstrated how the Extended Inversion Analysis can be used to calculate the optimised pre-exponential factor and the distribution E_{des} with coverage; and to estimate E_{diff} and $\Delta^{\ddagger}S$. The results have shown the importance of calculating the optimised pre-exponential factor for a set of experimental TPD data rather than using the widely assumed value for small molecules of $10^{12} – 10^{13}$ s^{-1}, as used in the analysis of CO TPD from $aSiO_2$ in **Chapter 5**. The work by Penteado *et al.* [9] highlights the effect of uncertainties in the binding energies have on astrochemical models of dark molecular clouds using rate equations approach and hence the necessity to determine them accurately.

Table 6.6 shows a summary of the optimised pre-exponential factors, E_{des} ranges, estimated E_{diff} and $\Delta^{\ddagger}S$ for CO on $aSiO_2$, c-ASW, CSW, CH_3OH and NH_3. E_{des} has been calculated using a range of ν values which can be compared to the literature data in **Table 6.2**. In some of the work, ν is often fixed at 10^{12} or 10^{13} s^{-1} and is not optimised for the experimental data. The rate of desorption cannot just be calculated from knowledge of E_{des} alone and a value of ν is required. Previously, ν has often been assumed to be $10^{12} – 10^{13}$ s^{-1}. The measurements in the work and above show this is incorrect.

Of the surfaces investigated, $aSiO_2$ has the broadest E_{des} range (19.5 – 11 kJ mol^{-1}) and the largest diffusion barrier (1.95 – 11 kJ mol^{-1}), which indicates that motion of CO is the more restricted on the $aSiO_2$ surface compared to any other surfaces. Comparing the interaction of CO on the two different water surfaces (c-ASW and

CSW) shows that there is a broader range of binding energies in the case of CO on CSW. While NH_3 has the narrowest range of E_{des} range (8.50 – 8.40 kJ mol^{-1}) and the smallest diffusion barrier compared to any of the other surfaces investigated. The very narrow E_{des} range indicates that NH_3 provides a very limited number of binding sites when compared to the other surfaces.

These results support the idea that the surface is the dominating factor which controls desorption kinetics under sub-monolayer conditions. This is observed in the work by Noble *et al.* [1]. Finally, CO on CH_3OH shows a much narrower range of binding energies when compared to the other surfaces (14 – 12.8 kJ mol^{-1}) and CO binds much strongly to CH_3OH than to c-ASW surface.

The work in **Chapter 5** demonstrated a simple method to synthesise the vibrational line profile of CO on $aSiO_2$ using value of 10^{13} s^{-1} for the pre-exponential factor. In this chapter, the TPD data from **Chapter 5** are re-analysed using the Extended Inversion Analysis. From **Table 6.5**, it can be seen that using the Extended Inversion Analysis produces an optimum value for ν of $1.74^{+0.75}_{-0.53} \times 10^{21}$ s^{-1} and this results in much broader range of E_{des} (19.5 – 11 kJ mol^{-1}) values when compared to the using ν of 1.00×10^{12} s^{-1} (10 – 6 kJ mol^{-1}) as in **Chapter 5**.

The CO on $aSiO_2$ vibrational line profiles were revisited using the Extended Inversion Analysis and **Table 6.5** summarises the best fit parameters. **Figure 6.39** compares the vibrational line profiles derived using the optimised pre-exponential factor or 1.00×10^{12} s^{-1} as in **Chapter 5**.

It can be seen from **Figure 6.39(a, d)** that using the optimised pre-exponential factor or 1.00×10^{12} s^{-1} does not still reproduced the experimental data and the ballistic deposition is entirely inconsistent with line profile. Neither of the deposition cases does the instrument limited linewidth reproduce the observed line profiles, **Figure 6.39 (b, e)**. Only assuming adsorb and diffuse deposition can we optimise the model line profile to the fit the observed profile. **Figure 6.39(c, f)** shows the optimised adsorb and diffuse deposition model using the optimised pre-exponential factor results in narrower fit of the synthesis data compared to using pre-exponential factor

of 1.00×10^{12} s^{-1}. If we consider our accepted adsorb and diffuse model then the linewidth for CO on p-ASW at 3.2±0.2 cm^{-1} is larger than that on $aSiO_2$ at 2.3±0.2 cm^{-1}. This means, of course, that the lifetime of vibrational excited CO on p-ASW at 0.70 ps is shorter than that on $aSiO_2$ at 0.93 ps. This time scale is consistent with intermolecular vibrational relaxation and the difference points to differences in the efficiency of the IVR process on $aSiO_2$ and p-ASW. This can be readily explained as p-ASW surface provides an underlying continuum of vibrational modes associated with the combination of the H_2O bending vibrational at 1636 cm^{-1} [38] with the p-ASW librational mode at 672 cm^{-1} [38] which can rapidly disperse the excitation of the CO vibrational into the phonon bath of the ASW (**Figure 6.40**). No such spectral overlap is found between the CO vibrational modes in $aSiO_2$ (**Figure 6.40**) and so the relaxation takes longer. In a surface, we have Fano-like coupling of the CO vibration on the c-ASW surface.

The Extended Inversion Analysis has shown that it possible to obtain accurate estimates for desorption parameters which can be used in astrochemical models. However, this method relies on good quality TPD data. Further work is needed to improve the quality of the TPD data used as input into the extended inversion analysis. The extended inversion analysis could be used to improve the accuracy of kinetic parameters of a range of astrophysically relevant molecules (*e.g.* $HCOOCH_3$, CO_2 and O_2). Under estimation of the desorption energies has astrophysical implications as models would not be able capture the correct abundances of molecules present in the solid form [2] or when they are released into the gas phase.

6.7 References

[1] L. J. Karssemeijer , S. Ioppolo , M. C. van Hemert, A. van der Avoird, M. A. Allodi, G. A. Blake and H. M. Cuppen, *Astrophys. J*., 2014, **781.** 16.

[2] J. A. Noble, E. Congiu, F. Dulieu and H. J. Fraser, *Mon. Not. R. Astron. Soc*., 2012, **421**, 768.

[3] W. Hagen, A. G. G. M. Tielens and J. M. Greenberg, *Chem. Phys.*, 1981, **56**, 257.

[4] A. Al-Halabi, H. J. Fraser, G. J. Kroes and E. F van Dishoeck, *Astron. Astrophys.*, 2014, **422**, 777.

[5] M. P. Collings, J. W. Dever, H. J. Fraser and M. R. S. McCoustra, *Astrophys. Space Sci*., 2003, **285**, 633.

[6] K. P. Stevens, G. A. Kimmel, Z. Donhalek, R. S. Smith and B. D. Kay, *Science*, 1999, **283**, 1505.

[7] P. Jenniskens, D. F. Blake, M.A. Wilson and A. Pohorile, *Astrophys. J.*, 1995, **455**, 389.

[8] L. J. Allamandola, M. P. Bernstein, S. A. Sandford and R. L. Walker, *Space Sci. Rev*., 1999, **90**, 219

[9] E. M. Penteado, C. Walsh and H. M. Cuppen, *Astrophys. J.*, 2017, **844**, 13.

[10] A. G. G. M .Tielens and W. Hagen, *Astron. Astrophys.*, 1982, **114**, 245.

[11] T. I. Hasegawa and E. Herbst, *Mon. Not. R. Astron. Soc.*, 1993, **263**, 589.

[12] J. K. Nørskov, F. Studt, F. Abild-Pedersen and T. Bligaard, *Fundamental Concepts in Heterogenous Catalysis* (Wiley, Hoboken, New Jersey, USA, 2014), p14.

[13] S. Viti and D. A. Williams, *Mon. Not. R. Astron. Soc.*, 1999, **305**, 755.

[14] S. E. Bisschop, H. J. Fraser, K. I. Öberg, E. F. van Dishoeck and S. Schlemmer, *Astron. Astrophys.*, 2006, **449**, 1297.

[15] E. C. Fayolle, J. Balfe, R. Loomis, J. Bergner, D. Graninger, M. Rajappan and K. I. Öberg, *Astrophys. J*., 2016, **816,** L28.

[16] M. P. Collings, V. L. Frankland, J. Lasne, D. Marchione, A. Rosu-Finsen and M. R. S. McCoustra, *Mon. Not. R. Astron. Soc*., 2015, **449**, 1826.

[17] S. Taj, D. Baird, A. Rosu-Finsen and M. R. S. McCoustra, *Phys. Chem. Chem. Phys*., 2017, **19**, 7990.

[18] R. S. Smith, R. A. May and B. D. Kay, *J. Phys. Chem. B*, 2015, **120,** 1979.

[19] S. A. Sandford and L. J. Allamandola, *Astrophys. J.*, 1993, **417**, 815

[20] T. Lauck, L. Karssemeijer, K. Shulenberger, M. Rajappan, K. I. Öberg and H. M. Cuppen, *Astrophys. J*., 2015, **801**, 118.

[21] K. I. Oberg, E. C. Fayolle, H. M. Cuppen, E. F. van Dishoeck and H. Linnartz, H, *Astron. Astrophys.*, 2009, **505**, 183.

[22] F. Mispelaer, P. Theulé, H. Aouididi, J. Noble, F. Duvernay, G. Danger, P. Roubin, O. Morata, T. Hasegawa and T. Chiavassa, *Astron. Astrophys.*, 2013, 555, A13.

[23] K. Acharyya, G.W. Fuchs, H.J. Fraser, E.F. van Dishoeck and H. Linnartz, *Astron. Astrophys*., 2018, **466**, 1005.

[24] A. Williams and T. W. Hartquist, *Acc. Chem. Res*., 1999, **32**, 334.

[25] M.P. Collings, M. A. Anderson, R. Chen, J. W. Dever, S. Viti, D. A. Williams and M.R.S. McCoustra, *Mon. Not. R. Astron. Soc*., 2004, **354**, 1133.

[26] M. Doronin, M. Bertin, X. Michaut, L. Phillipe and J. H. Fillion, *J. Chem. Phys*., **2015**, 143, 084703.

[27] C. Badan, *PhD Thesis* (University of Leiden, Leiden, Holland, 2016).

[28] https://www.docenti.unina.it/webdocentibe/allegati/materialedidattico/542391 (Last accessed 20/6/19).

[29] C. T. Campbell and J. R. V. Sellers, *J. Am. Chem. Soc*., 2012, **134**, 18109.

[30] V. P. Zhdanov, J. Pavlicek and Z. Knor, *Catal. Rev. Sci. Eng.*, 1989, **30**,501.

[31] Z. Dohnalek, G.A. Kimmel, S. A. Joyce, P. Ayotte, R. S. Smith and B. D. Kay, *J. Phys. Chem. B*, 2001, **105**, 3747.

[32] S. L. Tait, Z. Dohnalek, C. T. Campbell and B. D. Kay, *J. Chem. Phys*., 2005, **122**, 164707.

[33] D. A. King, *Surf. Sci*., 1975, **47**, 384.

[34] Z. Dohnalek, J. Kim, O. Bondarchuk, J. M. White and B. D. Kay. *J. Phys. Chem. B*, 2006, **110,** 6229.

[35] R. S. Smith, Z. J. Li, L. Chen, Z. Dohnalek and B. D. Kay, *J. Phys. Chem*. *B*, 2014, **118**, 8054.

[36] J. D. Thrower, *Ph.D. Thesis* (Heriot–Watt University, Edinburgh, UK, 2009).

[37] S. D. Green, A. S. Bolina, R. Chen, M. P. Collings, W.A. Brown and M. R. S. McCoustra, *Mon. Not. R. Astron. Soc*, 2009, **398,** 357.

[38] https://webbook.nist.gov/cgi/cbook.cgi?ID=C7732185&Type=IRSPEC&Index=1(Last accessed 31/5/19).

[39] https://www.researchgate.net/figure/FT-IR-spectrum-of-SiO2_fig10_258256404 (Last accessed 31/5/19).

[40] C. T. Campbell, L. Aradottir and J. R. V. Sellers, *Z. Phys. Chem.*, 2013, **227**, 1.

[42] B. M. Giuliano, R. M. Escribano, R. Martín-Doménech, E. Dartois and G. M. Muñoz Caro, *Astron. Astrophys.*, 2014, **565**, A108.

[43] J. W. Gadzuk and A. C. Luntz, Surf. Sci., 1984, 144, 429.

[44] D. C. Langreth, Phys. Rev. Lett., 1985, 54, 126.

Chapter 7

Concluding Remarks and Outlook

7.1 Introduction

This thesis is broadly split into three sections:

1. **Chapter 3** focused on the design, construction and testing of a UV/visible reflection-absorption spectrometer which is used to determine the complex refractive index, $\hat{n}$, and the thickness, *d*, of thin films.
2. **Chapter 4** investigated, in ultrahigh vacuum, Methyl Formate ($HOOOCH_3$, MF) thin films using TPD, RAIRS and *ab initio* computational chemistry methods.
3. **Chapters 5** and **6** looked at desorption of CO from a range of astrophysically relevant surfaces including $aSiO_2$, c-ASW, CSW, CH_3OH, and NH_3. Emphasis is given to investigating adsorbate-surface interactions by temperature programmed desorption through the pre-exponential factor (ν_{des}) and activation energy (E_{des}) for desorption.

This chapter will initially present a summary of the conclusions to this work before highlighting future work as there are yet more interesting experiments needed to further our understanding of the results presented in this thesis and of the surface science of the solid state in astrophysical environments.

7.2 Summarising Remarks

7.2.1 Chapter 3

Chapter 3 presented the design, construction and initial results from a UV/visible reflection-absorption spectrometer which will be to determine the complex refractive index, $\hat{n}$, and the thickness, *d*, of ice films. Preliminary results are presented for benzene (C_6H_6) ices on a highly-orientated pyrolytic graphite (HOPG) surface. The preliminary results for *n* (1.43 ± 0.07) and *d* (261±5 nm) for C_6H_6 ice are in good agreement with published data. This demonstrates the proof of concept of the instrument and of the method employed by Harrick [1] to calculate *n* and *d*. The next stage in the analysis is to determine the imaginary part, *k*, of the complex refractive index, which will in turn allow the determination of $\hat{n}$, the complex

refractive index. This work is currently being undertaken at the University of Sussex.

7.2.2. Chapter 4

Chapter 4 investigated the adsorption of Methyl Formate ($HCOOCH_3$, MF) on amorphous silica ($aSiO_2$) at temperatures from 15 to 115 K by means of TPD, RAIRS and *ab initio* quantum chemical calculations. The low coverage TPD of MF on $aSiO_2$ is consistent with first-order desorption of the first layer, suggesting that MF wets the silica surface. The higher coverage data displayed in **Figure 4.27** (**Peak F**) follows the behaviour established by Peak **B** in **Figure 4.25** for zero order desorption of a multilayer ice. The trend established by **Peak B** in **Figure 4.25**, and continued in **Figure 4.26** (**Peak D**), also continues in **Figure 4.27**(**Peak F**). The TPD here show multilayer desorption with zero order kinetics, as inferred by the common leading edges and the increase in peak temperature with increasing coverage. Zero order desorption is confirmed by the Leading Edge Analysis (LEA) presented in **Figures 4.28 - 4.29**. **Figure 4.28** provides the LEA results for 100-1,000 L (2 – 10 ML) with a resulting average kinetic order of 0.02±0.02. **Figure 4.29** completes the set with the data for 1,000 – 5,000 L (10-50 ML) where the average value of the kinetic order is 0.0±0.0. The E_{des} for the monolayer is 29.8±0.1 kJ mol^{-1} and for multilayer MF is 26.4±5.5 kJ mol^{-1}. The E_{des} for the monolayer is slightly higher than the E_{des} for the multilayer, which indicates that MF binding to the $aSiO_2$ surface though weak and is slightly stronger than MF coupling to itself in the solid MF. CKS analysis results for E_{des} and ν_{des} for the multilayer simulate experimental data (**Table 4.6**) well and compare favourably with literature data [2, 3].

RAIRS has revealed details of the structure of MF thin films. Below 95 K, the spectra are broadly consistent with material in an amorphous phase. Above 95 K, the spectral features sharpen up in a way that is consistent with crystallisation, such that above 100 K MF is crystalline. This can be seen in the spectra of the ν_{CO} band in the 1850 to 1600 cm^{-1} region in **Figures 4.40** and **4.41**. There is also clear evidence in both **Figures 4.40** and **4.41** of LO-TO splitting in the ν_{CO} band. This is perhaps most cleanly seen in the spectrum of the crystalline phase in **Figure 4.41**,

where at least two features are found in the ν_{CO} band. A simple preliminary analysis suggests from the absence of any contraction or expansion of the ν_{CO} band LO-TO splitting above 90 K that crystalline MF is not spontelectric, which is consistent with the known spontelectric data on MF [4].

MF is subject to conformational isomerism around both the methyl-oxygen and formyl-oxygen bonds. The internal rotation about the formyl-oxygen bonds is the most significant and the results of electronic structure calculations shown in **Table 4.8** and indicate that *cis*-MF is 19.7 kJ mol^{-1} more stable than *trans*-MF. The barrier between the isomers is 52.7 kJ mol^{-1}. The combination of measurements of spontaneous dipole orientation, IR spectroscopy and computational chemistry support the idea that the basis motif of the lattice in crystalline *cis*-MF is a ring dimer structure. Comparing the experimental RAIR data and the anharmonic frequencies in **Table 4.8,** the computed frequencies in the crystalline phase demonstrate a shift between *cis*- and *trans*-isomer ν_{CO} stretch modes that is much larger than that observed in the experimental RAIR data. Hence, the extra IR features are not due to the additional presence of the *trans*-MF. The conclusion of this work is that the neighbouring *cis*-MF molecules in the crystalline phase engage in cyclic hydrogen bonding and thus couple two carbonyl groups. In forming these hydrogen bonded dimers (**Figure 4.45**), the monomer ν_{CO} stretching frequency appears as a symmetric and antisymmetric combination of frequencies. Additionally, the overall dipole moment is zero in this configuration. The lack of dipole moment associated with the dimer structure accounts for the absence of the spontelectric field in the crystalline phase and the computational work on ring dimer structures of MF supports this hypothesis. MF has unique spontelectric properties. One aspect of this work was to provide independent data on this phenomenon of the observed growth of the dipole order with rising temperature, as reported in the literature [5, 6]. The data reported in this chapter, employed in developing the publications in references 7 and 8, which also provide additional interpretation of the data on *cis*-MF from Field and co-workers [5] as taking their data, it is possible to reproduce the observed deposition temperature dependence of the LO-TO splitting in cis-MF thin films as illustrated in **Figure 4.49**.

7.2.3 Chapters 5 and 6

The work in **Chapters 5** and **6** looks at the interaction of CO with a range of astrophysically relevant surfaces including $aSiO_2$, c–ASW, CSW, CH_3OH and NH_3. The TPD data for CO desorbing from $aSiO_2$ at low coverages shows coincident trailing edges. This would be consistent with first order desorption of the first layer and suggests that CO wets the $aSiO_2$ surface. At higher coverages, there is a common leading edge; that is consistent with zero order desorption of a multilayer ice. The $aSiO_2$ surface presents a range of binding sites with different binding energies for adsorption. The trailing edge alignment supports the idea that the molecules are mobile enough on the $aSiO_2$ surface to find the deepest, energetically most favourable binding sites before they desorb. Molecules which are located in the weak binding sites desorb first and this results in desorption peak broadening. Hence, a single value for E_{des} is no longer valid [9, 10].

Figure 5.16 shows the RAIR spectra for 0.6 ML CO on $aSiO_2$. There is no obvious explanation for the asymmetric profile. However, the observed line profile hence must be determined by a combination of environmental heterogeneity and homogeneous broadening associated with the relaxation of excited CO vibration from its weak mechanical coupling with the vibrations of the $aSiO_2$ substrate. When comparing the range of E_{des} for CO for $aSiO_2$ (6 – 12 kJ mol^{-1}) to that for p-ASW (11 – 16 kJ mol^{-1}), we see that CO is more strongly bound to the latter. As a rule of thumb, surface diffusion barriers are taken as around 10 to 15 % of the surface binding energy of a species as shown in **Figure 5.26** [11]. The work in **Chapter 5** then demonstrated a simple method that can be used to synthesise the vibrational line profile of CO on a heterogeneous surface, where the interactions between the CO and the substrate are dominated by weak, non-covalent interactions. The procedure developed allows the conversion of a distribution of E_{des} into a continuous distribution of vibrational frequencies, which can in turn be compared with experimental RAIRS data. A main requirement for the synthesis is the range of interaction energies along with their weighting as encompassed by $P(E_{des})$ *versus* E_{des}. In this work, this data was obtained from experimental TPD data. However, it may be possible to derive this data using computationally. The challenge in using the computational methods would be identifying the size of the system to model

which would reproduce $P(E_{des})$ *versus* E_{des} along with the best computational method to use in modelling that system.

Table 7.1 summarises the parameters recorded from fitting the line profile data as illustrated in **Figure 5.24** and **5.25**. The simulations of the line profiles for CO on $aSiO_2$ and CO on p-ASW has shown significant differences in the vibrational relaxation of the CO. p-ASW is more effective than $aSiO_2$ in relaxing ν_{CO}.

	$\bar{\upsilon}_o$ /cm^{-1}	δ /cm^{-1}	Model / FWHM	Experimental / FWHM
CO on $aSiO_2$	2102.5±0.5	2.4±0.2	4.71±0.5	5.6±0.1
CO on p-ASW (Ballistic)	2108.0±0.5	2.6±0.2	9.0±0.5	8.0±0.1
CO on p-ASW (Diffusive)	2089.0±0.5	3.2±0.2	7.6±0.5	8.0±0.1

Table 7.1: Compares the best-fit parameters $\bar{\upsilon}_o$, δ and $I_{0,}$ along with the corresponding FWHM for the modelled profiles and the experimental CO vibrational line profiles on $aSiO_2$ and p-ASW substrate.

Chapter 6 continues the work from **Chapter 5** by looking at the interaction of CO with range of astrophysically relevant surfaces which include c-ASW, CSW, CH_3OH and NH_3. The analysis of CO on $aSiO_2$ TPD spectra was carried out in **Chapter 5** using a pre-exponential factor 10^{12} s^{-1} as widely used for small molecules. **Chapter 6** demonstrates how using an extended inversion analysis allows the determination of a more representative value for the pre-exponential factor and E_{des} for a set of experimental TPD data. **Table 7.2** shows a summary of the pre-exponential factor values, $\Delta^{\ddagger}S$, E_{des} and E_{diff} for CO interactions on a range of astrophysically relevant surfaces.

Surface	ν / s^{-1}	$\Delta^{\ddagger}S$ /J K^{-1} mol^{-1}	E_{des} / kJ mol^{-1}	E_{diff} / kJ mol^{-1}
$aSiO_2$	$1.74^{+0.75}_{-0.53} \times 10^{21}$	$178.85^{+1.17}_{-1.03}$	19.5 – 11	1.95 – 1.10
c-ASW	$2.57^{+1.04}_{-1.21} \times 10^{15}$	$67.91^{+1.28}_{-1.11}$	12.5 – 9.5	1.25 – 0.95
CSW	$2.51^{+1.47}_{-0.93} \times 10^{17}$	$106.00^{+1.28}_{-1.11}$	14.2 – 9.5	1.42 – 0.95
CH_3OH	$1.41^{+0.29}_{-0.45} \times 10^{16}$	$81.83^{+1.21}_{-1.05}$	14.0 – 12.8	1.40 – 1.28
NH_3	$1.51^{+0.46}_{-0.40} \times 10^{12}$	$5.59^{+1.21}_{-1.06}$	8.5 – 8.4	0.85 – 0.84

Table 7.2: Summary of the ν, $\Delta^{\ddagger}S$, E_{des} and E_{diff} for CO interactions on $aSiO_2$, c-ASW, CSW, CH_3OH and NH_3. Note the diffusion barrier is typical 10% of the E_{des} [11].

From **Figure 6.11**, it can be seen that using a ν of 10^{12} s^{-1}, which is typically used for small molecules, results in narrow distribution of interaction energies of CO with the $aSiO_2$ surface (6 – 12 kJ mol^{-1}). However, using the optimised value of ν ($1.74^{+0.75}_{-0.53} \times 10^{21}$ s^{-1}), this results in broader distribution of interaction energies (11.0 – 19.5 kJ mol^{-1}) (**Table 7.2**). This clearly highlights the needs to calculate the ν from a set off experimental TPD data rather than simply assuming the value of 10^{12} - 10^{13} s^{-1} for small molecules as used in literature.

CO on c–ASW shows a narrower distribution of binding energies, compared to CO on $aSiO_2$ and these values are line with the sub-monolayer values reported by Fayolle *et al*. [12]. CO on CSW shows a broader distribution of binding energies compared to CO on c–ASW. Comparing the binding energies between CO on c–ASW and CO on CSW, it is found that latter has higher binding energies. This difference in the binding energies between the two forms of water suggests that degree crystallinity of the material influences the kinetic parameters. The work by Noble *et al.*[10] indicates that this could be due ordered structure of the crystalline water being able to form larger scale interactions based on the observations by Dohnalek *et al*. [14]. The work by Green *et al*. [13] indicated that the surface type is relatively unimportant but the heating rate and grain size are dominant with regard to desorption kinetics. However, this work did not take into account the sub-monolayer case. The work by Noble *et al*. [10] indicates that the surface type is the dominant factor which controls desorption under sub-monolayer coverage conditions. Hence the definition of the surface type must take into account both the surface material and the degree of crystallinity and not just material alone.

The desorption kinetics of CO from CH_3OH are different when compared to CO on CSW and c–ASW, the sub-monolayer coverages align far greater on a single curve (**Figure 6.28**) than in the case of CSW and c–ASW, which indicates first order desorption. The highest biding energy is 14 kJ mol^{-1} at low coverages and decreases down to lower binding energy of 12.8 kJ mol^{-1} at 0.8 ML. Compared to biding energy c–ASW (12.5 kJ mol^{-1}) the binding energy of CH_3OH (14 kJ mol^{-1}) is higher which indicates that CO binds more strongly to CH_3OH than c–ASW. NH_3 has the narrowest range of E_{des} range (8.50 – 8.40 kJ mol^{-1}) and the smallest diffusion barrier compared to any of the other surfaces investigated. The very narrow E_{des} range indicates that NH_3 provides a very limited number of binding sites when compared to the other surfaces. This, indicates that CO is the least restricted on NH_3 compared to any of the other surfaces investigated. The diffusion barrier estimated for NH_3 is lowest 0.85 – 0.84 kJ mol^{-1} of any of the surfaces and this allows for more motion of the CO on NH_3 surface which results in least tightly packed CO layer with the minimum repulsions and hence a very low entropy when compared to all the other surfaces.

In **Chapter 5**, a simple method was demonstrated which was used to synthesise the vibrational line profiles of CO on $aSiO_2$ using the binding energy distribution derived from TPD data by inversion analysis assuming a value of 1.00×10^{12} s^{-1} for the pre-exponential factor. In **Chapter 6**, the optimised pre-exponential factor has been calculated using the Extended Inversion Analysis and a revised binding energy distribution calculated. **Figure 6.38(a)** shows the $P(E_{des})$ *versus* E_{des} for CO-$aSiO_2$ which is calculated using ν of 1.00×10^{12} s^{-1} and **Figure 6.38(b)** calculated using ν of $1.74^{+0.75}_{-0.53}\times10^{21}$ s^{-1} which results in a recovered binding energy distribution wider than that reported in **Chapter 5**. **Figure 6.39** shows the impact of the revised binding energy distribution on the vibrational line profile synthesis for 0.6 ML CO on $aSiO_2$. The figure compares the simulations from **Chapter 5** with the revised simulations. **Figures 6.39(a)** and **6.39(d)** present the situation of ballistic deposition assuming the instrument-limited linewidth of 0.1 cm^{-1}. As in **Chapter 5**, this clearly indicates that ballistic deposition does not explain the observed line profile. Deposition by the adsorb and diffuse mechanism, initially presented in **Figure 6.39(b)** and **6.39(e)** at instrument-limited linewidth, can be optimised as in **Figure**

6.39(c) and **6.39(f)** to reproduce the data. We must conclude therefore that CO deposition on $aSiO_2$ at 18 K follows an adsorb and diffuse mechanism. **Table 6.5** summarises the best fit parameters of the modelled profiles to the experimental CO vibrational line profiles on $aSiO_2$ using the binding energy distribution derived from the pre-exponential factors of $1.00X10^{12}$ s^{-1} and $1.74^{+0.75}_{-0.53} \times 10^{21}$ s^{-1} and compares with those for ASW reported in **Chapter 5**.

It is clear from **Table 6.5** that the linewidth δ of the CO on $aSiO_2$ line is significantly narrower than for CO on H_2O, 2.4 cm^{-1} *versus* 3.2 cm^{-1}. The revised analysis strengthens this argument in comparing 2.3 cm^{-1} *versus* 3.2 cm^{-1}. This in turn impacts on the lifetime of the vibrationally excited state of CO which increases from 0.94 ps corresponding to 2.4 cm^{-1} to 0.98 ps with the revised analysis. However, the basic explanation for this remains unaltered from **Chapter 5**. As in both systems CO is likely bound to the substrate *via* weak hydrogen bond interactions with the surface OH groups, we might expect similar relaxation modes for vibrationally excited CO and hence similar linewidth. **Figure 6.40**, however, highlights a significant difference between the systems. **Figure 6.40** compares the IR spectra of ASW and $aSiO_2$. The dotted line on the figure represents the position of the CO vibrational frequency on solids. As can be seen, the CO line sits on top of the broad continuous absorption associated with the bending-libration combination mode in the case of ASW. This opens an additional quantum mechanical relaxation pathway on the ASW surface over and above simple mechanical intermolecular energy redistribution (IVR) presented equally by both surfaces. This is Fano Coupling between the CO resonance and the underlying ASW continuum. This additional pathway reduces the lifetime of the CO on the ASW surface, hence increasing the linewidth in comparison to CO on $aSiO_2$

7.3 Outlook for Future Work

7.3.1 Chapter 3

The next stage in the present work is to determine the imaginary part *k* of the complex refractive index, which will in turn allow the determination of $\hat{n}$, the complex refractive index. This work is currently being undertaken at the University

of Sussex. Future work will likely explore the optical constants for a wide range of small organic molecules with common chromophores as found interstellar ices. The goal will be to explore how the optical constants of ices change with irradiation as either single component ices or a mixtures. The latter, of course brings us to a current limitation of the understanding of optical constants in how to consider those of mixtures. Parallel computational chemistry effort is likely to be necessary to approach this goal. Dust is widespread within the Universe and impacts on most areas of astronomy, hence it is vital to understand the interaction between light with dust and ice [15, 16, 17]. The radiative transfer problem describes the interaction between radiation and matter and is described using **Equation 7** and **10, Chapter 3**. Solving the radiative transfer equation is a challenging task (**Chapter 3**) in part due to poor understanding of optical properties of dust and ice [18]. By determining the optical properties of a range of astronomically relevant materials (*i.e.* dust and ices), this will help to reduce the difficulties in solving **Equation 10, Chapter 3** and enable the astronomically community to develop a better understanding of how light interacts with relevant materials.

7.3.2 Chapter 4

As discussed in **Chapter 4**, the work of Bu *et al*. [19] investigated p-ASW films and determined the electric field present using a Kelvin Probe (KP). A KP has been mounted on the UHV chamber and further work in the field of spontelectric effect will involve the use of this KP to measure the surface potential. Initial test work will involve thick MF films as a well characterised spontelectric system.

The combination of IR spectroscopy, computational chemistry and dipole orientation measurements have been used successfully demonstrated in structural identification in the solid state, as in the case of MF. It has shown that spontelectric effect can be used to aid the identification of new structures in the solid materials. Fundamentally, however, we still don't know what makes a species grow as a spontelectric film. A programme coupling bottom-up studies of film growth combining local probe methods and deposition simulations with top-down exploration of the chemical motifs that produce spontelectric behaviour in thin films is currently under development.

The spontelectric effect may play a role in astrophysics and this needs further work, for example spontelectric CO. Since interstellar dust grains acquire a polarization charge on the grain surface, the polarization charge could attract electrons or ions to the surface, thus changing the gas phase abundance of electrons. The depletion of gas phase electrons could influence the abundance of chemical species in the interstellar medium [4]. Since molecular species play a key role in cooling a cloud undergoing gravitational collapse and their reduction could influence star formation rates. The above indicates that, by including the spontelectric grains, this could influence the chemistry and physics of gravitational collapse of protostellar cores [4]. However, this needs further investigation.

7.3.3 Chapters 5 and 6

Chapter 5 demonstrated a simple method that can be used to synthesise the vibrational line profile of CO on a heterogeneous surface, where the interactions between the CO and the substrate are dominated by weak, non-covalent interactions. The procedure developed allows the conversion of a distribution of E_{des} into a continuous distribution of vibrational frequencies, which can in turn be compared with experimental RAIRS data. This can extended to investigate other astrophysically relevant molecules on a range of surfaces.

The work in **Chapter 6** used the Extended Inversion Analysis to calculate the optimal pre-exponential factor for set of experimental TPD data along with the distribution of binding energies, diffusion barrier and entropy of activation for CO on a range of astrophysical relevant surfaces, including c-ASW, CSW, CH_3OH and NH_3. This work could be extended to calculate these kinetic parameters for other relevant astrophysical molecules and surfaces, as there is a lack of data on these molecules and surfaces in the literature, as analysis of small molecules typically uses, $\nu = 10^{12}$ s^{-1} – 10^{13} s^{-1}. The accuracy of kinetic parameters (ν, $\Delta^{\ddagger}S$, E_{des} and E_{diff}) could be further improved by developing computational methods to calculate in particular the pre-exponetial factor, as this value greatly impacts the accuracy of $\Delta^{\ddagger}S$ (**Chapter 6, Equation 16**). Uncertainties in the kinetic parameters result in inaccuracies in astrochemical models, as the work of Penteado et al. [20] demonstrates. Uncertainties

in both binding energies and pre-exponential factors can have a marked effect on the rate estimates used to model astrophysical environments.

The work of Badan [21] (**Chapter 6, Equation 6**) and Campbell *et al*. [22] (**Chapter 6, Equation 10**) has shown that it is possible to calculate the pre-exponential factor using measurements of the entropies of adsorbates. This could be developed further using computational chemistry and this in turn could lead to more accurate determination of $\Delta^{\ddagger}S$. Since adsorbed molecules are involved in many reactions on solid surfaces which is of significant value. Hence, being able to predicate reaction rates and equilibrium constants, has drawn considerable interest. However, calculations of the rate and equilibrium constants for such reactions needs accurate values of entropy and enthalpy of the adsorbed molecules [22].

In the CO on CH_3OH experiments, the simulated TPD spectra are narrow and do not fit the experimental data as well as CO on p-ASW and c-ASW. This is in part due to value used for the pumping speed and the simulations need to be repeated again using a more optimized value for when pumping speed. The FORTRAN code was used to simulate the TPD profiles and astrophysical implications of the results was discussed. However, these simulations could be repeated using the FORTRAN code to take into account interstellar conditions (e.g. heating rates of 1 K/century and 1 K/millennium) for CO on each substrate ($aSiO_2$, c–ASW, CSW, CH_3OH, NH_3).

The Extended Inversion Analysis has shown that it possible to obtain accurate estimates for desorption parameters which can be used in astrochemical models. However, this method relies on good quality TPD data. Further work is needed to improve the quality of the TPD data used as input into the extended inversion analysis. The Extended Inversion Analysis could be used to improve the accuracy of kinetic parameters of a range of astrophysically relevant molecules (e.g. $HCOOCH_3$, CO_2 and O_2). Under estimation of the desorption energies has astrophysical implications as models would not be able capture the correct abundances of molecules present in the solid form or when they are released into the gas phas

7. 4 References

[1] N. J. Harrick, *Appl. Opt.*, 1971, **10**, 2344.

[2] D. J. Burke, F. Puletti, P. M. Woods, S. Viti, B. Slater and W. A. Brown, *J. Phys. Chem*. *A*., 2015, **119**, 6837.

[3] J. K. Whitesell, R. E. Davis, L. L. Saunders, R. J. Wilson and J. P. Feagins, *J. Am. Chem. Soc*., 1991, **113**, 3267.

[4] J. Lasne, A. Rosu-Finsen, A. Cassidy, M. R. S. McCoustra and D. Field, *Phys. Chem. Chem. Phys*., 2015, **17,** 30177.

[5] D. Field, O. Plekan, A. Cassidy, R. Balog, N. C. Jones and J. Dunger, *Int. Rev. Phys. Chem*., 2013, **32**, 345.

[6] O. Plekan, A. Cassidy, R. Balog, N. C. Jones, D. Field, *Phys. Chem. Chem. Phys*., 2012, **14**, 9972.

[7] M. Roman, A. Dunn, S. Taj, Z. G. Keolopile, A. Rosu-Finsen, M. Gutowski, M. R. S. McCoustra, A. M. Cassidy and D. Field, *Phys. Chem. Chem. Phys*., 2018, **20**, 29038.

[8] M. Roman, S. Taj, M. Gutowski, M. R. S. McCoustra, A. C. Dunn, Z. G. Keolopile, A. Rosu-Finsen, A. M. Cassidy and D. Field, *Phys. Chem. Chem. Phys*., 2018, **20**, 5112.

[9] M. P. Collings, V. L. Frankland, J. Lasne, D. Marchione, A. Rosu-Finsen and M. R. S. McCoustra, *Mon. Not. R. Astron. Soc*., 2015, **449**, 1826.

[10] J. A. Noble, E. Congiu, F. Dulieu and H. J. Fraser, *Mon. Not. R. Astron. Soc*., 2012, **421**, 768.

[11] J. K. Nørskov, F. Studt, F. Abild-Pedersen and T. Bligaard, *Fundamental Concepts in Heterogenous Catalysis* (Wiley, Hoboken, New Jersey, USA, 2014), p14.

[12] E. C. Fayolle, J. Balfe, R. Loomis, J. Bergner, D. Graninger, M. Rajappan and K. I. Öberg, *Astrophys. J.*, 2016, **816,** L28.

[13] S. D. Green, A. S. Bolina, R. Chen, M. P. Collings, W.A. Brown and M. R. S. McCoustra, *Mon. Not. R. Astron. Soc*, 2009, **398**, 357.

[14] Z. Dohnalek, G.A. Kimmel, S. A. Joyce, P. Ayotte, R. S. Smith and B. D. Kay, *J. Phys. Chem. B*, 2001, **105**, 3747.

[15] W. R. M. Rocha and S. Pilling, *Spectrochim. Acta A.*, 2014, **123**, 436.

[16] D. M. Hudgins, S. A. Sandford, L. J. Allamandola and A. G. G. M. Tielens, *Astrophys. J. Suppl. Ser.*, 1993, **86**, 713.

[17] W. R. M. Rocha, S. Pilling, A. L. F. de Barros, D. P. P. Andrade, H. Rothard and P. Boduch, *Mon. Not. R. Astron. Soc.*, 2017, **464**, 754.

[18] G. Leveque and Y. Villachon-Renard, *Appl. Opt*., 1990, **29**, 3207.

[19] C. Bu, J. Shi, U. Raut, E. H. Mitchell and R. A. Baragiola, *J. Chem. Phys*., 2015, **142**, 134702.

[20] E. M. Penteado, C. Walsh and H. M. Cuppen, *Astrophys. J.*, 2017, **844**,13.

[21] C. Badan, *PhD Thesis* (University of Leiden, Leiden, Holland, 2016).

[22] C. T. Campbell and J. R. V. Sellers, *J. Am. Chem. Soc*., 2012, **134**, 18109.